THÈSE

En vue de l'obtention du

DOCTORAT DE L'UNIVERSITÉ DE TOULOUSE

Délivré par : *l'Université Toulouse 3 Paul Sabatier (UT3 Paul Sabatier)*

Présentée et soutenue le *09/04/2015* **par :**

JUAN PABLO ÁLVAREZ ZÚÑIGA

Analytical and numerical study of the Superfluid - Bose glass transition in two dimensions

---

JURY

MONSIEUR DAVID GUERY-ODELIN	Président
MONSIEUR XAVIER WAINTAL	Rapporteur
MONSIEUR GEORGES BATROUNI	Rapporteur
MONSIEUR ERIK SØRENSEN	Examinateur
MONSIEUR GABRIEL LEMARIÉ	Examinateur

École doctorale et spécialité :
SDM : Physique de la matière - CO090
Unité de Recherche :
Laboratoire de Physique Théorique de Toulouse
Directeur de Thèse :
Nicolas LAFLORENCIE
Rapporteurs :
Georges BATROUNI et *Xavier WAINTAL*

A mi abuelina y mi mamá...

"Do not worry about your difficulties in Mathematics. I can assure you mine are still greater."

Albert Einstein

"Natural science, does not simply describe and explain nature; it is part of the interplay between nature and ourselves."

Werner Heisenberg

"Physics is like sex: sure, it may give some practical results, but that's not why we do it."

Richard P. Feynman

Acknowledgements

Having finally arrived to the point where I need to think about who do I have to thank for achieving this goal, I can not help myself from wanting to shout out loud: "EUREKA!"

First of all I want to thank from the heart my advisor Nicolas Laflorencie for his excellent guidance through the maze a Ph. D can become at times. Many thanks for your availability, good advise and patience. Secondly, I would like to thank Gabriel Lemarié for all his teachings and the time spent explaining them to me, as well as for accepting to be part of my jury. I would also like to thank Georges Batrouni and Xavier Waintal for kindly accepting to read in detail this manuscript and fighting the french strikes to be able to make it to my defence. I extend this to the remaining members of the jury David Guéry-Odelin and Erik Sørensen.

To the excellent people in the FFC group at the LPT: Didier, Pierre, Mathieu, Sylvain, Fabien, Revaz, Aleksandra and Zoran, many thanks for all the knowledge and good times shared. A special mention to the non-permanents of the entire LPT: Fabrizio, Leonardo, David S., Carlos, Yasir, Luca, Helder, Anil, Daniel, Medha, Thibault, Fred, Maxime, Marlene, Giuseppe, Stefano, Nader, Gao, David L., Sumiran... thank you guys for making this journey the most pleasant it could have been.

A heartfelt special thank you goes to Malika Bentour for helping me with all the administrative craziness involved in a research laboratory everyday live.

On a more personal note, I would like to thank everyone that has made the achievement of this childhood dream become a reality throughout the years, starting with my brothers from El Portón de Cali: Carlangas, W., Manuel Alejandro and Pablo. I am also very grateful with people at the Lycée Français Paul Valery, Laura, Catherine, Marcela, Sergio, Juan David and Laura.

My thanks must also go to everyone that made the transition into a new (older) world in France for a 17 year old Colombian smoother than I could have hoped, starting from the people in La Martinière Monpaisir in Lyon: Etienne, Caroline, Emilie, Johann, Maël, Michael and most specially the families of Fabien (Alain, Na-

dine and Stephane) and Thomas (Claire, Luc and Paco: The Bourguis). This can be extended to the excellent people from the ENS Lyon: Madded, Rééééémy, Sonic, Maxime, Lou Lou, Ahmed, Bruuuuuuuno, Roméo, Ivan, Adrien, Alex, Alex, Anh Thy, Aisling, Hugo, Julia, Fabián, Maxime T., Titi et Claire, Timothée, Elaine, and all the Erasmus exchange students from around Europe I had the chance to share my time at Normale Sup'.

Furthermore, the crazy people from Toulouse: Les Gens Cool, Julia, Daniel (Esooo weeeey!), Aurélien, Elisa, Flo (Corentin?), Margaux, Fabien and everyone involved in Le Printemps Étudiant, many thanks for making me fall in love with Toulouse.

I would like to give a special thanks from the bottom of my heart to "el Parche" in Toulouse: Anita, Marcela, Anita Osorio, Jorge, Carlos, the bureau of Guayabo Colectivo, the girls from La Guaïra Cinética and the crazy musicians (past and present) of Los Guayabo Brothers y Su Pachanga Mohánica! without whom I may have lost my mind during the completion of this thesis.

My family in Colombia and my adoptive family (Carlos Andrés, Jorge Alberto y Doña Chela) deserve a very special mention here. I need to thank my mom Martha for making me the man I am today: ¡Lo logramos ma!

The best for the last, Livia words cannot describe the gratitude and love you make me feel, without you I would not have been able to make it through this test. TVB figa!

Contents

Chapter I

Introduction

The physics of condensed matter systems has attracted huge interest along its history. These systems, where the low energy properties are investigated, present an important amount of spectacular phenomena which defy physical intuition and therefore constitute an excellent playground for fundamental investigations, both experimentally and theoretically, such as superfluidity, superconductivity or Bose-Einstein condensation [1, 2]. The low energy regimes became accessible at the beginning of the 20th century as the technological advances allowed lower and lower temperatures to be probed. In this regime, the quantum effects become important and give rise to new physics never before seen in experiments, which needed to be explained by theory. It was soon realized that many-body effects were responsible for some of these amazing features, *i.e.* interactions play a huge role and cannot be neglected. This is also true for some classical systems.

At the same time, disorder, *i.e.* impurities, is intrinsic to any realistic system. Although the theories developed at first completely neglected the effects of disorder they are inevitable in the experiments and they were found to give rise to new phenomena such as Anderson localization [3–5] among others. It is known that non-interacting electrons get localized by arbitrarily weak disorder in dimensions one and two but repulsive interactions can stabilize a delocalized state in 2D [5, 6]. The interplay between interactions and disorder received a great deal of attention in the following years.

The question of interacting disordered bosons was brought to day by experiments on superfluid Helium in porous media [7]. The loss of superfluidity in these systems raised new theoretical questions. A series of theoretical studies followed [6, 8–12] discovering that the quantum ($T = 0$) onset of superfluidity in random media has to be treated as a fluctuation-driven quantum phase transition between a delocalized superfluid and a localized Bose glass phase, the Bose-Hubbard model becoming the paradigmatic model to study the interplay of interactions and disorder. Huge theoretical and experimental efforts have been put in determining the phase diagram of this model in one, two and three dimensions. In 2D, it was shown that bosons with repulsive interactions present superfluidity which is robust to weak disorder [6].

The remaining of this introductory chapter will present some of the most important results obtained for the Superfluid - Bose glass (or superfluid - insulator) transition both experimentally and theoretically.

1 Experimental realizations of the transition

In this section we present a number of experimental realizations of the Superfluid-Bose glass transition, starting with the first that presented a transition to an insulating state and motivated the study of the interplay between disorder and interactions, namely Helium adsorbed on porous media. We will also present the superfluid to insulator transition in disordered superconducting thin films, cold atoms on optical lattices and magnetic insulators under a magnetic field. The list of results and methods is not meant to be exhaustive.

1.1 He^4 in porous media

The study of superfluid helium in porous media has a long standing history, beginning at the time of the discovery of superfluidity itself. As a matter of fact, one of the first demonstrations of superfluidity was Allen and Jones's "fountain effect" experiment where they showed a frictionless flow of helium through the fine channels of a packed powder [13]. Of more relevance were the studies of the superfluid fraction in experiments of He^4 adsorbed on Vycor glass [14, 15], or on aerogel glass [7, 16–18], where the disorder is quenched (*i.e.* fixed in time) and varying the helium coverage is equivalent to changing the chemical potential [6]. Vycor is prepared in two steps: first, phase separation is induced in a borosilicate glass through heat treatment. Then the boron-rich phase is removed by a leaching process and the remainder is a complex sponge of material rich in silica where open pores "occupy" some 30% of the total volume. Levitz *et al.* [19] showed that Vycor glass has no hierarchical structure and a narrow distribution of pore sizes. In contrast, aerogel glasses have low densities and are created through a sol-gel process followed by a hypercritical drying. The porous structure occupies as little as 1% of the volume. Some groups studied aerogels via small-angle scattering and found they have a fractal-like structure with self-similar structures with length scales ranging from a few to hundreds of nanometers [20, 21]. For low enough coverages, the system can be considered as quasi-2D.

The superfluid density in such experiments is measured by a torsional oscillator technique [22], which gives access to the resonant period of the oscillator and is proportional to the moment of inertia of the oscillator + the helium. Two measures are carried out for each sample, one with the Helium giving a period P_f, and another one for the empty cell P_e. The difference in the two periods $P_f - P_e$ is then proportional to the helium moment of inertia. At high temperatures $T > T_c$, the resonant period of the filled cell is roughly a constant ($\bar{P}$) with temperature when all the helium

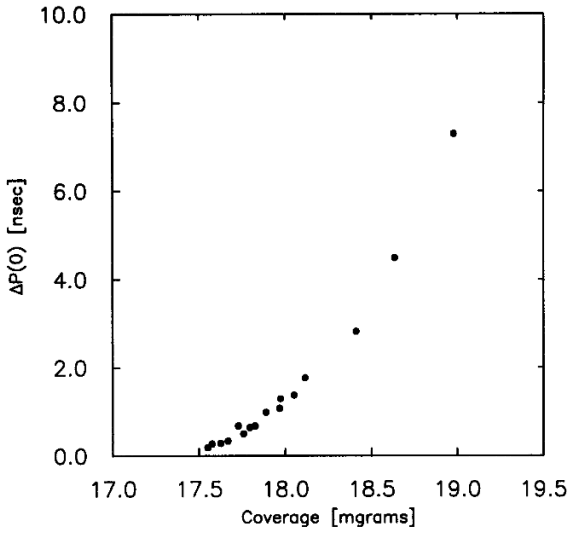

Figure I.1: *Period shift extrapolated to zero temperature* $\Delta P(0)$ *as a function of coverage near the critical coverage for the onset of superfluidity for He adsorbed on Vycor. Superfluidity emerges following a power law near the critical coverage as predicted for localized bosons by Fisher et al. [6], cf. eq.*(I.1). *Taken from Ref. [16].*

mass is in the normal state[7, 16], hence subtracting this value gives the period shift $\Delta P(T) = P_f - P_e - \bar{P}$ which is proportional to the superfluid density [16]. The data for $\Delta P(T)$ can be extrapolated to zero temperature and plotted against the coverage of the pores as shown in figure I.1.

Building on the zero-temperature findings for boson localization in the disordered Bose-Hubbard model (*cf.* section 2), Fisher *et al.* extended the hyperscaling relations to predict the behaviour of the zero temperature superfluid density with the distance to the critical chemical potential μ_c at which superfluidity emerges [6]. In the experiments of adsorbed He^4 in porous media, this distance is proportional to the distance to the critical coverage of the pores n_c [6, 18], yielding:

$$\rho_{\rm sf}(T=0) \sim (\mu - \mu_c)^{\zeta} \sim (n - n_c)^{\zeta} \quad , \quad \zeta = \nu(d + z - 2), \tag{I.1}$$

where d is the spatial dimension and z the dynamical exponent and ν the correlation length exponent. The localized bosons scenario of Fisher *et al.* predicts such a power-law dependence and explains the experimental results indicating that He in porous media is indeed a realization of the bosonic Superfluid-Insulator transition. Indeed, for coverages $n < n_c$ the He^4 bosons are localized due to repulsive interactions and the random media, but upon increasing n the substrate potential is smoothed by the adsorbed bosons in the pores which form layers. Once the critical coverage is reached delocalized states appear and superfluidity is present [7].

1.2 Disordered superconducting thin films

Disordered superconducting thin films present a transition from a superconducting to an insulating phase at low temperatures. There are various kinds of such films among which we find amorphous indium oxyde films (InO) [23–25], polycrystalline titanium nitride films (TiN) , niobium titanium nitride films (NbTiN) [26] and niobium nitride (NbN) films [27–30]. Polycrystalline TiN films are produced by magnetron sputtering of a target from pure titanium Ti in a nitrogen plasma. On the other hand, InO_x films are prepared by using electron-beam evaporation of high-purity ($\sim$99.998%) In_2O_3 onto SiO_2 in an O_2 background and disorder is controlled by the film thickness and a low temperature annealing [31].

These systems present a wealth of striking phenomena such as activated behaviour of resistivity in the insulating phase [23, 32–35], nonmonotonic magnetic field dependence of the activation temperature and the voltage threshold behaviour [34, 36–38] and nonmonotonic temperature and magnetic field dependence of the resistance [23, 33, 39, 40]. These features have been explained by disorder-induced spatial inhomogeneities in the superconducting order parameter [8, 25, 30, 38, 41], but several other questions remain open. The mechanism of the destruction of superfluidity is an example. If the mechanism is fermionic, the Cooper pairs are destroyed by disorder before the electrons localize hence the system passes through a badly conducting metallic phase before becoming an insulator at higher disorder [42]. The bosonic mechanism is accomplished if the Copper pairs remain bound through the transition and superfluidity is destroyed by the pairs themselves becoming localized, the system having a direct superfluid to insulator transition [43].

The existence of Cooper pairs at short length scales can be directly revealed by the observation of a superconducting gap in the density of states (DOS) [44, 45] using scanning tunnelling microscopy (STM) [46]. Sacépé *et al.* [25] studied two disordered InO_x films with thicknesses 150 and 300 Å, at different temperatures. Their results are shown in figure I.2: the least disordered sample (panels *a* and *c*) has the opening of a gap in the DOS at its critical temperature T_c signalling the appearance of bound Cooper pairs. When cooled further down coherence peaks develop at exactly the gap value $\pm\Delta$ indicating a global superconducting state [25]. These peaks grow as the temperature is lowered. The strongly disordered sample (panels *b* and *d* in figure I.2) presents the same opening of a gap in the DOS at T_c, so Cooper pairs are indeed present in the sample but no coherence peaks appear to the lowest probed temperatures. Therefore, the Copper pairs do not condense to a delocalized state and are localized, making the sample insulating [25]. This proves that for these disordered superconducting films the destruction of superconductivity is brought about by the localization of bosonic Cooper pairs.

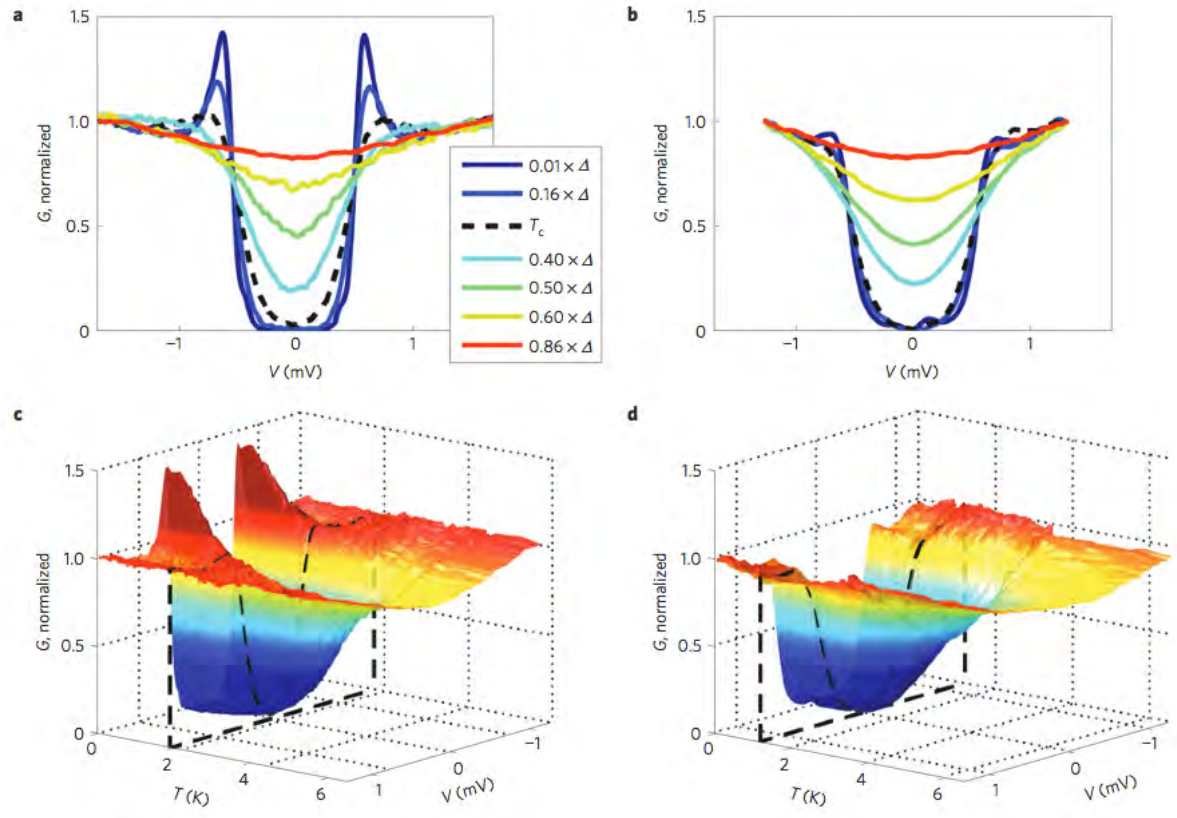

Figure I.2: *Evolution of the local tunnelling conductance G with temperature T and bias voltage V at two different locations of the disordered sample. Panels a-c: Low disorder sample with spectral gap $\Delta = 560\mu eV$. A gap Δ near $V = 0$ opens exactly at $T \leq T_c$ indicating Copper are present in the sample, and distinct coherence peaks develop at $V = \pm\Delta$, growing for lower temperatures, the sample is then superconducting. Panels b-d: Highly disordered sample with spectral gap $\Delta = 500\mu eV$. A similar gap opens in exactly the same way as for the low disorder sample but no coherence peaks develop, indicating the presence of localized preformed Cooper pairs in the insulating film. Taken from Ref. [25].*

As a side note, it is worth noting that disordered bosonic models has been pointed out as relevant in the study of High-T_c superconducting cuprates via a mapping of vortex trajectories onto bosonic world lines [47, 48], although the pairing mechanism in such systems has not been determined and there is an ongoing debate on whether it is a bosonic or a fermionic one (see for example Ref. [49]). The link is further enphasized by the fact that a peudo-gap in the density of states even above the superconducting transition temperature T_c is a well known property of under-doped

high-T_c superconductors [29, 50], also present for the superconducting films discussed here (*cf.* figure I.2) [25].

1.3 Cold atoms in optical lattices

Cold atoms constitute a somewhat recent and rapidly evolving field of physics which make it possible to produce Bose [51, 52] and Fermi gases [53, 54] and manipulate them with incredible tunability and measurement possibilities [55–57]. They already have allowed for the first observations of Bose-Einstein condensation [58, 59], which are described by the Gross-Pitaevskii equation in the weak coupling regime [60, 61], and other condensed matter physics phenomena like Anderson localization of matter waves [62–65] and the transition from a Superfluid to a Mott Insulator phase [66–71] proving that they can be accurate quantum simulators [66] of the many-body physics [72].

Since cold atoms in optical lattices can be described by the Bose Hubbard model [73] it is then natural to use them as quantum simulators for the interplay between disorder and interactions. The latter can be fine tuned via Feshbach resonances [74, 75] while disorder can be included in the optical lattice by speckle potentials [76–83], two-colored superlattices [84–88], or different atomic species mimicking random impurities [89–91].

It is worth noting that the harmonic confinement in the experiments results in finite-size inhomogeneous systems and changes the nature of the problem, transforming the quantum phase transitions into crossovers and leading to a coexistence of different phases in the system [88]. Therefore, the experimental system is always compressible which makes it impossible for such experiments to distinguish between the Bose glass and Mott Insulating phases.

D'Errico *et al.* studied a quasi-1D cold gas of ^{39}K atoms in a quasi periodic optical lattice superimposed by a second one, the depth of which fixes the disorder strength Δ and studied the effect of disorder and interactions on its coherence and transport properties [88]. They measured the coherence of the gas by the root-mean-square width of the momentum distribution Γ obtained through absorption imaging after a free flight. A low Γ means a high coherence and its dependence on disorder and interaction strengths is plotted in panel *a* of figure I.3. A coherent phase (blue region) and another region with low coherence are visible. The mobility of the system is measured via the momentum δp accumulated in a fixed time by the sudden application of a finite shift of the harmonic confinement (figure I.3 panel *b*). In the clean case (black triangles) the mobility is high for small U and smoothly decreases as U increases reaching a Mott insulating state for strong interactions. Disorder turns the weakly interacting regime from conducting to insulating (squares and circles) but at intermediate interaction strengths the mobility is high again, the

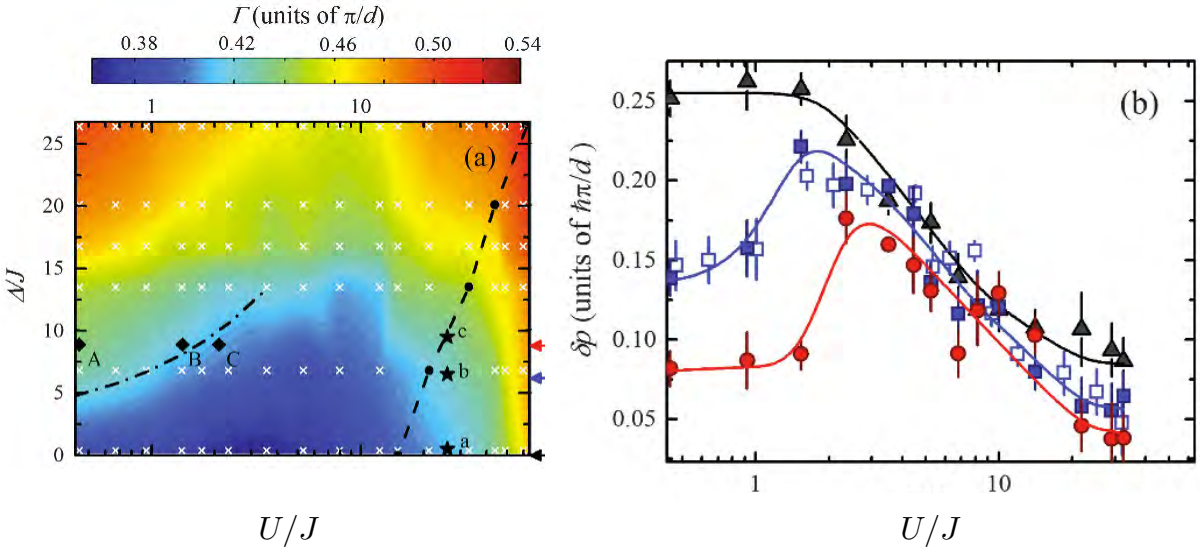

Figure I.3: *Panel a) Map of the width of the momentum distribution* Γ *as a function of disorder strength* Δ/J *and interaction strength* U/J*, built with 94 data points (white crosses) having standard deviations from 2% to 5%. A MI is present only to the right of the dashed line (cf. text) and the dashed-dotted line follows* $\Delta - 2J = nU$*, where* n *is the density. The SF phase corresponds to the blue region. Panel b) Momentum transferred to the system by an impulse as a function of interaction strength for three different disorder strengths* $\Delta = 0$ *(black triangles),* $\Delta = 6.2J$ *(blue squares) and* $\Delta = 8.8J$ *(red circles). Full symbols depict data obtained at a temperature* $k_B T = 3.1(4)J$ *and open symbols at* $k_B T = 4.5(7)J$*. Error bars are the std of five measurements. Taken from Ref. [88].*

system becomes conducting again before going to a strongly interacting insulating state. These measurements confirm the insulating nature of the incoherent regions.

The shape of the phase diagram agrees with the theoretical picture of a weakly interacting Bose glass phase at small U/J values going through a phase transition to a Superfluid phase at intermediate interaction and disorder strengths. Finally, there is a strongly interacting Mott insulating phase present at commensurate densities, to the right of the dashed line in fig I.3 *a*, as calculated by DMRG for the same model at $T = 0$ [92]. The other insulating region is then a Bose glass phase, as confirmed by further measurements by D'Errico *et al.* [88], which we do not show here for lack of space.

1.4 Magnetic insulators in the presence of an external magnetic field

Magnetic insulators are great new materials to test condensed matter physics phenomena. Gapped quantum magnets with non-magnetic ground-states have been proven to show a field-induced phase transition to a Bose-Einstein condensed phase of magnetic triplon excitations [93, 94] (for a review *cf.* [95, 96]). In particular, organic transition metal halogenides have been showed to be disorder-free realizations of quantum spin models [97–100], their magnetic energy scales making them much more accessible to experimental realizations than the historic oxide systems. If randomness is present, disordered quantum magnets have shown a wide range of interesting phenomena such as the the order-by-disorder mechanism induced by impurities in spin-gap compounds [101–103], the random-singlet phase [104, 105], and non-trivial excitations [106–111] and transport [112, 113] properties.

Disorder is introduced in these systems via doping of the parent compound, *i.e.* by a low concentration chemical modification of the parent compound, as illustrated in figure I.4 for DTN where Cl^- anions are replaced by Br^- ones in the crystalline structure, yielding a modified coupling between the Ni^{2+} cations. Transition metal halogenides with organic ligands with very different structures, geometries and dimensionalities, on which such dopings are possible have been discovered. Among these there are spin chains [115–120], spin ladders [121–126], 2D [99, 127–131] and 3D [132] spin networks, and even geometrically frustrated systems [133], making

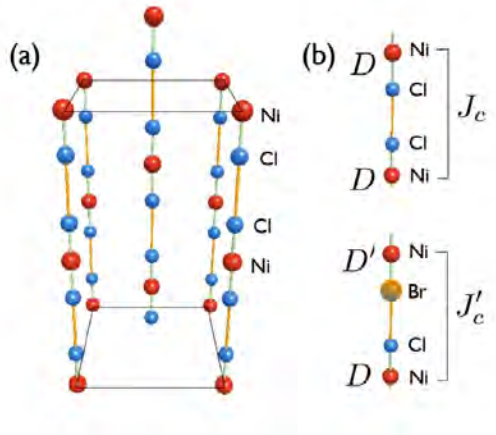

Figure I.4: *Panel a): Body-centered tetragonal arrangement of $S = 1$-carrying Ni^{2+} and the Cl^- ions connecting them in DTN. Panel b) Doping of DTN by Br^- ions which randomly replace Cl^- ions, creating an random effective coupling $J_c^{'} \neq J_c$ between the Ni^{2+} ions . Taken from Ref. [114] .*

magnetic insulators very powerful and versatile quantum simulators of disordered physics. Furthermore, one distinct advantage of magnetic insulators is that cold neutron scattering studies [134] can be performed on them giving direct access to the complex BEC order parameter, in particular its square modulus which is proportional to the antiferromagnetic Bragg peaks [114].

Three organic materials where a magnetic Bose glass phase has been observed are $(CH_3)_2CHNH_3CuCl_3$ ($IPACuCl_3$), $(C_4H_{12}N_2)Cu_2Cl_6$ (PHCC) and $NiCl_2{\cdot}4SC(NH_2)_2$ (DTN). $IPACuCl_3$ is a system of weakly coupled strung-rung spin ladders [126] with a critical magnetic field for long-range magnetic ordering $H_c \sim 10$T [135] and triclinic symmetry. It has been studied by electron spin resonance (ESR) [136], thermodynamic measurements [135], neutron diffraction [137] and neutron spectroscopy [138]. Its triclinic symmetry makes it potentially subject to a U(1) symmetry-breaking anisotropy which could make it impossible to see a magnetically long-range ordered state [139]. DTN, on the other hand, is a $S = 1$ system with large easy-plane single-ion anisotropy with tetragonal crystalline structure so the axial U(1) symmetry is preserved when the magnetic field is applied along the c axis, *cf.* figure I.4.

There are evidences of a magnetic Bose glass phase in Br doped $IPACuCl_3$ [140, 141] and DTN [142, 143]. This Bose glass phase has no magnetic long-range order (equivalent to an insulating phase) and finite magnetic susceptibility (equivalent to a finite compressibility). Figure I.5 shows the magnetization and magnetic susceptibility as a function of the applied magnetic field (panel a) at 500mK for the clean $IPACuCl_3$ (solid lines) and the Br-doped $IPACuCl_3$ with doping parameter $x = 0.05$ (symbols). The antiferromagnetic Bragg peak intensity *vs.* the magnetic field at 600mK for the same systems is shown in panel b with the same graphical conventions. The clean $IPACuCl_3$ susceptibility is vanishing (or very small) for magnetic fields up to $H_c = 9.8$ T, and jumps abruptly to a finite value for larger magnetic fields. The appearance of the Bragg peak happens at exactly the same magnetic fiield $H = H_c$. There is then a gapped phase with no transverse long-range order for fields $H < H_c$, equivalent to a Mott Insulating phase. For higher fields $H > H_c$ a long-range ordered phase with finite susceptibility *i.e.* a BEC phase is present. The situation is not the same for the Br-doped $IPACuCl_3$: for low fields there is an almost vanishing susceptibility up to $H = H_c$, but it smoothly increases up to a saturation value at $H = H' = 11$ T, while no Bragg peak develops in the interval $H \in [H_c; H']$. For higher magnetic fields, an antiferromagnetic Bragg peak with intensity growing in the same way as for the clean $IPACuCl_3$ is present and there is a finite magnetic susceptibility: the system is in the BEC phase. Coming back to the system for intermediate fields $H_c < H < H'$, there is a finite susceptibility, *i.e.* a finite compressibility, and no transverse long-range order: the system is in the Bose glass phase.

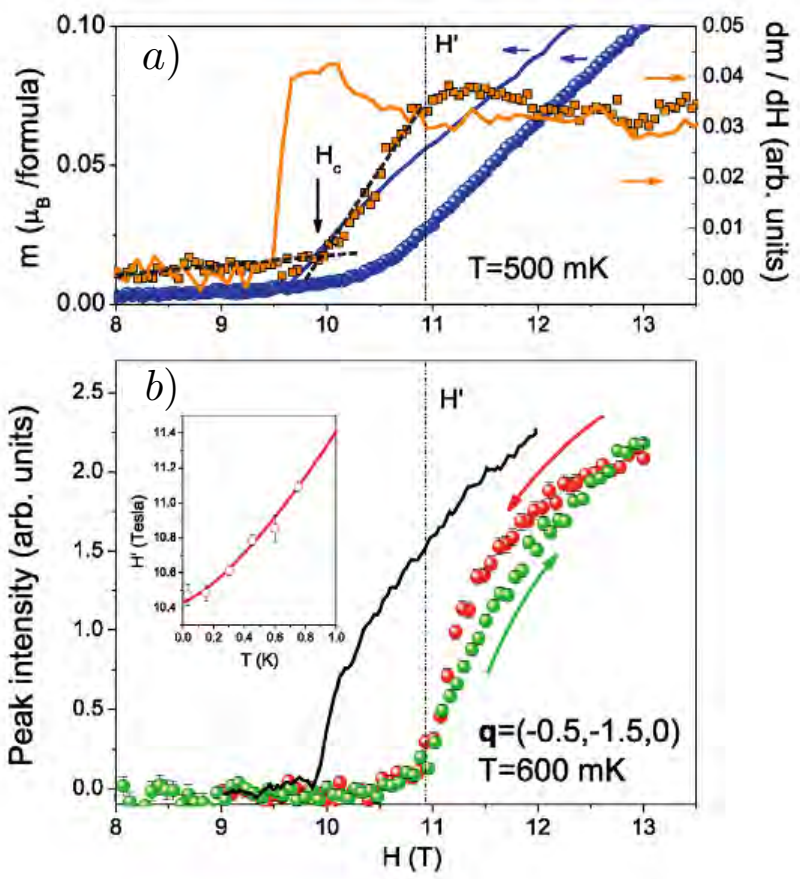

Figure I.5: *Panel a): Field dependence of magnetization (Boson density), in blue, and susceptibility (compressibility of the Bose gas), in orange, as measured in the clean $(CH3)_2CHNH_3CuCl_3$ (solid lines) and the doped $(CH3)_2CHNH_3Cu(Cl_{(1-x)}Br_x)_3$, $x = 0.05$ (symbols) magnetic insulators. Panel b) Field dependencies of intensity of the antiferromagnetic Bragg peaks (square of the BEC order parameter) in the two respective materials. Data obtained in Ref. [140]. The figure is taken from Ref. [114].*

2 Theoretical results

In this section we will explore some of the main theoretical considerations, predictions and findings that followed the discovery of the Superfluid - Insulator transition discovery in 2D as reported in the previous section. First, we will briefly introduce the paradigmatic model capturing the effects of interactions in clean bosonic systems, namely the Bose Hubbard model. Following this, we will explain the different questions relative to the inclusion of disorder in the model, yielding the disordered Bose-Hubbard model. It is worth mentioning that some of the results presented have

been obtained with two related models. One is the Quantum Rotors model which is the equivalent of the Bose-Hubbard model in the limit of very large integer fillings [144]. The second one is hard-core Bose-Hubbard model, *i.e.* the limit of infinite on-site repulsion between the bosons ($V \to \infty$ in (I.2)), which we will actually use in our study of the SF-BG transition in the subsequent chapters of this thesis work.

2.1 Bose-Hubbard model phase diagram in the clean system

The clean Bose-Hubbard model describes the physics of interacting bosons in a lattice. It has two competing ingredients: *(i)* the kinetic energy, which tends to delocalize the bosons and is characterised by a hopping parameter J. It tends to stabilise the superfluid phase. *(ii)* Interactions, in the form of on-site interactions characterized by a parameter V. They tend to localize the bosons on each site stabilizing a Mott insulating phase at strong interactions. We stress the very important fact that interactions are short-ranged in this model (on-site repulsion), the case of Coulomb interactions (long-range) is in a different universality class [6, 145, 146]. Following Fisher *et al.* [6], we can write the model by the Hamiltonian:

$$H_{\mathrm{BH}} = -\sum_i (\mu + \delta\mu_i)\, n_i + \frac{V}{2}\sum_i n_i(n_i - 1) - \frac{J}{2}\sum_{<i,j>} \left(b_i^\dagger b_j + b_j^\dagger b_i\right), \qquad \text{(I.2)}$$

where b_i ($b_i^\dagger$) is the bosonic annihilation (creation) operator on site i, $n_i = b_i^\dagger b_i$ is the bosonic number operator on site i, and the chemical potential has an average μ fixing the average occupation and a random component $\delta\mu_i$ for each site i modelling disorder. In the clean system $\delta\mu_i = 0$. Disorder is introduced by $\delta\mu_i$ uniformly distributed in $[-\Delta; \Delta]$, the parameter Δ controlling the disorder strength (*i.e.* the impurity concentration in an experiment).

Fisher *et al.* established the phase diagram of the clean Bose-Hubbard model (I.2) finding two different phases. A compressible and delocalized superfluid phase for dominant kinetic energy regimes (large J/V) and a series of localized incompressible Mott insulating phases with integer fillings at large interaction values. The phase diagram they find is shown in panel *a* of figure I.6. The successive Mott lobes with fixed $n_i = 1, 2, 3, \ldots$ (controlled by the average chemical potential μ) for low enough J/V are visible. If the system has sites with N bosons and others with $N + 1$, N being an integer number, the "excess" particles (*i.e.* on sites with $N+1$ bosons) can hop around in the lattice without energy cost, regardless of the strength of J so at $T = 0$ those particles (or holes) will Bose condense and be in the superfluid state. This happens at chemical potentials such as $\mu/V = N$ and the SF phase exists for arbitrary J at this values of μ/V. Similarly, the excitations in the Nth Mott lobe are the addition of a particle (hole) to the system by increasing (decreasing) μ/V, and for a given $J > 0$ the kinetic energy gained by delocalizing an extra particle above the insulating background with N bosons per site will eventually exceed the

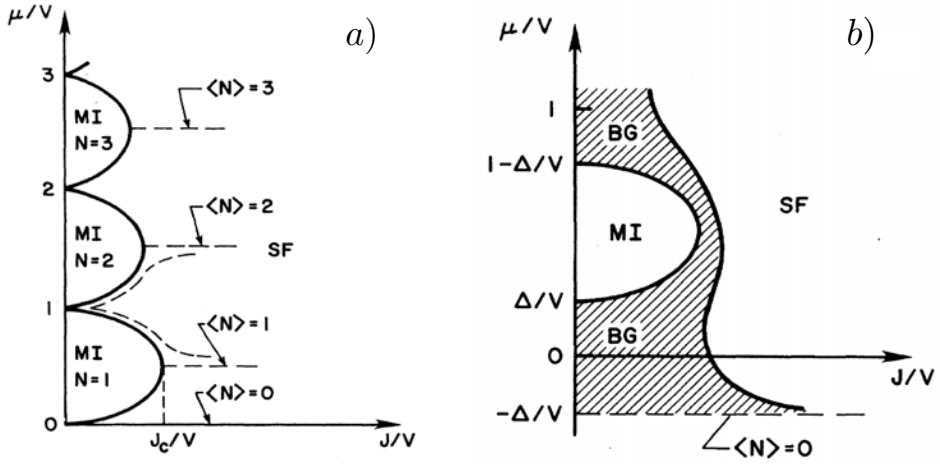

Figure I.6: *Panel a: Qualitative phase diagram of the clean Bose-Hubbard model* (I.2) *in the $\mu - J$ plane . Panel b: Most likely qualitative phase diagram of the disordered Bose-Hubbard model with with disorder on the chemical potential $\mu + \delta\mu_i$, with μ the average chemical potential and $\delta\mu_i$ uniformly distributed in $[-\Delta; \Delta]$. Taken From Fisher et al. [6].*

associated potential energy cost. This will occur more rapidly (*i.e.* a smaller increase in μ/V) as J is bigger and hence the lobe form of the Mott Insulating phases and the presence of a a finite energy gap for particle (hole) excitations in the Mott lobe which decreases with increasing J and vanishes at the tip of the lobe. This also means that the phase transition between the MI and the SF states occurs at continuous density variations.

2.2 Direct Superfluid - Mott Insulator transition in presence of disorder?

In their seminal paper Fisher *et al.* [6] also depicted some qualitative features of the disordered Bose-Hubbard model. They showed that the bounded disorder $\delta\mu_i \in [-\Delta; \Delta]$ only reduces the spread of the ideal Mott lobes at $J = 0$ from $[N-1; N]$ to $[N - 1 + \frac{\Delta}{V}; N - \frac{\Delta}{V}]$ for the Nth lobe. Another insulating phase (because everything is localized at $J = 0$), namely the Bose glass [11] fills-in the phase diagram and extends also for small hoppings. As a consequence, in the case of strong enough disorder $\Delta > V/2$ the Mott phase completely disappears at $J = 0$ and there is only a transition from Bose glass to superfluid as J/V increases. It is worth mentioning that $V/2$ is the half-width of the energy gap of the disorder-free Mott Insulator at $J = 0$, $E_{g/2}(J = 0)$. The strong disorder regime for $J > 0$ is such that $\Delta > E_{g/2}(J)$ which decreases with J (*cf.* section 2.1).

In the case of weak disorder $\Delta < E_{g/2}(J)$, the possibility of a direct Mott Insulator – Superfluid transition is not ruled out. At the boundary of the Mott lobe the discussion for the clean case in section 2.1 still holds and there still is a finite energy gap for particle-hole excitations and so the superfluid correlations decay exponentially at the boundary too. Just outside the boundary the excess bosons (holes) have very low densities and are spaced by more than the superfluid correlation length of the background (of density N) and do not interact though it, occupying only low lying excited states which are localized by the disorder. This means the transition is to a localized Bose glass phase.

Nevertheless, there remains the question of the vicinity of the tip of the Mott lobes which are multi-critical points. At exactly the tip of the lobes the particle-hole excitations gap vanishes and just outside the tip these excitations could create a superfluid state, although Fisher *et al.* claim this is very unlikely leaving the most likely scenario of an intervening Bose glass phase even for weak disorders , as shown in panel *b* of figure I.6.

These qualitative results called for more quantitative studies to check the relevance of weak disorder (in the renormalization-group sense) for the pure Mott insulator – Superfluid transition. A number of teams carried out such studies using real space renormalization-group schemes and found that strong disorder is relevant [147, 148] in agreement with Fisher *et al.* [6]. In the decade following the appearance of Ref. [6] a big controversy around the possibility of a direct MI-SF transition developed with many studies observing a direct transition via numerical results such as QMC [149, 150] and DMRG [151], and via approximative methods [147, 148, 152–154]. Another number of teams observed an absence of direct transition by strong coupling expansions [155], analytical dual theory studies [156, 157], renormalization-group analysis [158], QMC simulations [159–164] and double ϵ expansions [165]. It was argued that the observation of a direct transition in QMC simulations come from the finite-size of the systems considered which are too small to be able to capture rare regions effects.

This debate was settled by Pollet *et al.* in 2009, exactly one decade after Fisher *et al.* original work. In their paper [166] they demonstrated the existence of the so called "Theorem of inclusions" which states that for any disorder-driven phase transition between phase A at weak disorder and phase B at strong disorder, depending on the bound and the distribution function of disorder, there are always arbitrarily large (although exponentially rare) regions of phase A in phase B and vice versa, hence the name of theorem of inclusions. The main supposition of the theorem, based on the existence of Lifshitz regions [167] near the transition, is that the position of the critical disorder depends on the distribution of disorder [168], characterized by a generic parameter λ (*e.g.* one of its cumulants, like the variance or its spatial correlations). Inside the strong disorder phase B, there are local regions were disorder is smaller than the bound and will locally be in phase A, these regions

are exponentially rare and exponentially large [167]. The fact that the location of the transition point depends on λ ensures that close to the transition but inside phase A, it is always possible to define a model with slightly different disorder distribution (*i.e.* a different λ') such that the transition point is shifted towards lower values ($\Delta_c(\lambda') < \Delta_c(\lambda)$) and the system is locally in phase B for the new model. As a consequence, if the phase A is gapless, phase B will be gapless as well since it has exponentially large regions inside of it that are in the gapless phase A. This rules out the possibility of a transition between the gapless superfluid and the gapped Mott Insulator even for an *arbitrarily weak disorder*. The Bose glass phase always intervenes and the qualitative phase diagram by Fisher *et al.* in figure I.6 *b* is the correct one.

It is worth noting that the theorem of inclusions forbids transitions between gapped and gapless phases, so it would seem that the transition from Bose glass to Mott Insulator is not possible. This apparent contradiction is lifted by the fact that this transition does not fulfil the main supposition of the theorem and hence the latter does not apply in this case [166, 168]. The MI-BG has to be [166, 168] of the Griffiths' type [169, 170], as originally conjectured by Fisher *et al.* [6], and there are evidences that it should happen for a disorder strength $\Delta = E_{g/2}(J, V)$ [166, 168], which does not depend on the disorder distribution. The fact that the transition is of the Griffiths type necessarily means that macroscopically large systems have to be studied by definition of the Griffith's regions, which makes it impossible for present day simulations and experiments to observe the MI-BG transition [168, 171].

2.3 Critical exponents for the SF-BG transition

In their seminal work, Fisher *et al.* extended the Josephson relations [172] for classical phase transitions driven by thermal fluctuations to get a hyperscaling relation for quantum ($T = 0$) phase transitions where quantum fluctuations drive the system from one phase to the other, yielding:

$$2\beta = (d + z - 2 + \eta)\nu \tag{I.3}$$

with β the order parameter exponent, z the dynamical exponent, d the dimensionality, η the anomalous exponent and ν the correlation length exponent. It is worth noting that compared with classical Josephson relations [172], the dimensionality d is replaced by $d + z$ here [6]. Some bounds for the critical exponents of the SF-BG transition were derived and this section will briefly present their arguments using the notations in Ref. [6]. In particular, δ will denote the distance to the critical point.

2.3.1 Correlation length exponent ν and anomalous exponent η

i) The Correlation length exponent ν

The correlation length exponent is defined by the power law divergence near the critical point of the correlation length:

$$\xi \sim \delta^{-\nu}. \tag{I.4}$$

An important question addressed by Harris in the seventies is to know whether the inclusion of disorder will induce a smearing of the transition, instead of the sharp well-behaved transition for the pure system [173]. Let us consider a disordered system at a distance δ from its critical point. This fixes the correlation length of the system as in equation (I.4), and the system can be thought of as independent subsystems of volume ξ^d (provided interactions are short-ranged and correlations decay faster than a power-law), each having a critical parameter, say a critical temperature T_c^i. By virtue of the central limit theorem, the spread of such critical temperatures ΔT_c scales as $\Delta T_c \sim \xi^{-d/2}$. Now, for the system to have a sharp phase transition, it is required that the spread of critical temperatures ΔT_c goes to zero faster than δ when approaching the transition, *i.e.* :

$$\lim_{\delta\to 0} \frac{\Delta T_c}{\delta} = 0 \Leftrightarrow \lim_{\xi\to\infty} \frac{\Delta T_c}{\delta} = 0. \tag{I.5}$$

Since

$$\frac{\Delta T_c}{\delta} \sim \frac{\xi^{-d/2}}{\xi^{-1/\nu}} = \xi^{-d/2+1/\nu}, \tag{I.6}$$

is required to vanish as $\xi \to \infty$ the exponent has to be negative: $-d/2 + 1/\nu < 0$, which yields a lower bound for the correlation length exponent

$$\nu \geq \frac{2}{d}. \tag{I.7}$$

This inequality is known as the Harris criterion [173]. This criterion was later extended to the case of quantum phase transitions and shown to hold as well by Chayes *et al.* [174] for any system with independent bond or site disorder.

In a more recent work, Pázmándi *et al.* note that this criterion actually concerns the finite size scaling exponent $\nu_{\rm FS}$ related to a new diverging length scale. This length scales is introduced by the standard averaging procedure which produces a noise and $\nu_{\rm FS}$ may be unrelated to the intrinsic exponent ν of the system under investigation. They claim that when $\nu > 2/d$ the standard procedure can access the intrinsic ν and when the intrinsic $\nu < 2/d$, typically $\nu_{\rm FS} = 2/d$ and there is a break-down of self-averaging [175].

ii) Concerning the anomalous exponent η

The anomalous exponent is defined by the power in the power law divergence at criticality of the order-parameter susceptibility

$$\bar{\chi}(r,\tau) \equiv \overline{\langle T_\tau \Phi_r(\tau)\Phi_0^\dagger(0)\rangle} - \overline{\langle \Phi_r(\tau)\rangle\langle\Phi_0(0)\rangle}, \tag{I.8}$$

where $\Phi_r(\tau)$ is the order-parameter field at point r and imaginary time τ, $\langle\mathcal{O}\rangle$ is the ground-state expectation value of operator $\mathcal{O}$ and the overbar denotes average over disorder. This susceptibility scales at criticality, for long distances $r \to \infty$ and long times $\tau \to \infty$, as:

$$\bar{\chi}(r,\tau) \sim r^{-(d+z-2+\eta)} g(r/\xi, \tau/\xi^z) \tag{I.9}$$

with g a universal scaling function. The following analysis is based on the behaviour of the single-particle density of states at energy ϵ, $\rho_1(\epsilon)$ which related to the imaginary time Green's function by a Laplace transform [6]. It can then be shown that in the entire Bose glass phase $\rho_1(\epsilon = 0)$ is a constant implying that for long imaginary times on-site imaginary times Green's function decays as $\overline{G}(r = 0, \tau \to \infty) \sim \rho_1(0)/\tau$, and finally:

$$\rho_1(\epsilon = 0) \sim \xi^{2-d-\eta}. \tag{I.10}$$

Similarly, at the critical point the single-particle density of states follows the scaling [6]:

$$\rho_1(\epsilon) \sim \epsilon^{-(2-d-\eta)/z}. \tag{I.11}$$

Moreover, in the Superfluid phase the long-time behaviour of the imaginary time on-site Green's function reads $\overline{G}(r = 0, \tau \to \infty) = M^2$, where $M = \langle\Phi\rangle$ is the ground-state expectation value of the order parameter (which scales as $M \sim \delta^\beta$). This can be shown to bring about that in the Superfluid phase the single-particle density of states has a zero-energy contribution [6]:

$$\rho_1(\epsilon) \sim M^2 \delta(\epsilon). \tag{I.12}$$

Finally, combining eqs. I.10, I.11 and I.12, one can state on physical grounds that starting from the BG phase, $\rho_1(0)$ grows as the transition is approached owing to precursor superfluid fluctuations and diverges at the critical point to finally satisfy the δ-peak behaviour in the SF phase. This constraints the power in eq. I.11 to be negative and finally:

$$\eta \leq 2 - d. \tag{I.13}$$

2.3.2 Dynamical exponent z

Concerning the dynamical exponent, the original work by Fisher finds an exact equality based on the free energy excess by applying a twist to the boundary conditions in both the real space and imaginary time directions. We will present their arguments following the reformulation by Weichman and Mukhopadhyay [176]. Upon a twist on the boundary conditions in the real space direction, the free energy density is changed as:

$$\Delta f_{\vec{x}} = \frac{\Upsilon}{2\beta V} \int_0^\beta d\tau \int d^d x |\nabla \phi(\vec{x}, \tau)|^2 \tag{I.14}$$

defining the helicity modulus Υ (proportional to the superfluid density [177]), where V is the volume in d dimensions, β is the inverse temperature and ϕ is the *phase* of the order parameter. Since the gradient of ϕ is an inverse length, it should then scale as the inverse correlation length, *i.e.* as $\xi^{-1} \sim \delta^\nu$. The quantum hyperscaling relation (I.3) (where d is replaced by $d+z$) implies [6] that by definition, the diverging part of the free energy density f_s scales as $f_s \sim \delta^{\nu(d+z)}$. Hence, $\Delta f_{\vec{x}}$ has to follow the same scaling law and the helicity modulus forcefully, in order for this scaling to be fulfilled, scales as:

$$\Upsilon \sim \delta^{(d+z)\nu - 2\nu} = \delta^{\nu(d+z-2)}. \tag{I.15}$$

Similarly, the compressibility $\kappa = -\frac{\partial^2 f}{\partial \mu^2}$ quantifies the response to a change in the chemical potential μ. The Josephson relation connects the changes in chemical potential to the imaginary time derivative of the order parameter [6], so the compressibility κ can be understood as the helicity modulus in the imaginary time direction and will be related to the change in free energy density along this direction by:

$$\Delta f_\tau = \frac{\kappa}{2\beta V} \int_0^\beta d\tau \int d^d x (\partial_\tau \Phi(\vec{x}, \tau))^2. \tag{I.16}$$

Now the time derivative of Φ has the dimensions of an inverse imaginary time and hence should scale as the inverse correlation length on imaginary time, *i.e.* as $\xi_\tau^{-1} \xi^{-z} \sim \delta^{z\nu}$ by the definition of the dynamical exponent z. *If this change in free energy density is included in its singular part*, which scales as $\nu(d+z)$, one immediately recovers, by the exact same arguments as for the helicity modulus, that:

$$\kappa \sim \delta^{(d+z)\nu - 2z\nu} = \delta^{\nu(d-z)}. \tag{I.17}$$

The fact that the both Superfluid and Bose glass phases have finite compressibility leads to [6] the critical point also having a finite compressibility on physical grounds. This means that the scaling exponent for κ in (I.17) is identically vanishing, and finally:

$$z = d. \tag{I.18}$$

Although this predictions were believed to be correct for a long time, with several studies comforting them [6, 157, 178–180] for $d = 1$,2 and 3, there were some studies which found results in violation of the equality (I.18) [160, 181, 182]. This motivated Weichman and Mukhopadhyay [176] to reconsider the above mentioned theoretical arguments. They noted that for a twist in the boundary conditions to generate a change in free energy Δf (associated to a helicity modulus) big enough to produce a non-zero helicity modulus, *i.e.* for Δf to be singular, the twisted boundary conditions needs to break a fundamental symmetry of the model. In this case the twist will create relevant terms (in the sense of the renormalization-group) associated with a new diverging scaling variable in the singular part of the free energy density which dominates all the other contributions to Δf. However, if no symmetry is broken there is no new diverging scaling variable and the only effect of the twist will be shifting the already present parameters. The associated helicity modulus is not singular and will be therefore dominated by the analytic part of the free energy density, the singular part giving a contribution which vanishes at the critical point.

Following this analysis, the twist to the boundary conditions in real space breaks the translational symmetry (which is restored in average for a disordered system) and the scaling for the helicity modulus (I.15) is valid. Nevertheless, in the case of a twist to the imaginary time boundary conditions, the presence of a non-vanishing chemical potential already breaks the time reversal symmetry and the twist does not break any symmetry. This means that the scaling law for the associated helicity modulus, *i.e.* the compressibility κ in eq. (I.17) does not hold and the singular part of the free energy density gives a vanishing contribution to κ at criticality. This implies that the exponent in (I.17) is positive and the equality $z = d$ turns into the inequality

$$z < d, \tag{I.19}$$

in agreement with the 2D results of Refs. [160, 181, 182].

2.4 The nature of the Bose glass phase and physical scenario for the transition

In section 2.2, we presented the theorem of inclusions [166] which applies to the Superfluid - Bose glass transition for generic dimension d. It establishes the absence of a direct Superfluid - Mott Insulator transition in presence of an arbitrary bounded disorder. It states that near the transition in one phase there are always arbitrarily large, though exponentially rare, regions of the competing phase. Such a description of the critical region of the transition naturally gives rise to a description of the Bose glass phase as consisting in disconnected superfluid clusters in an insulating background. The superfluid clusters confer the Bose glass its compressible nature and the lack of global phase coherence between the clusters explains the insulating behaviour.

Furthermore, the transition to the superfluid regime is described often as a percolation transition where the onset of superfluidity at criticality is given by the appearance of a percolating superfluid cluster allowing for macroscopic phase coherence and superfluid transport properties [183]. Such a description has been used in several theoretical [171, 184–187] and experimental [83, 91, 188] studies which find that superfluidity disappears exactly at the percolation threshold. Other studies have put forward a quantum percolation scenario where even when no percolating superfluid cluster is present in the system, quantum tunnelling between disconnected clusters allows for an effective density to be above the threshold and percolate through the system [189–193].

The experimental analysis of Krinner *et al.* [83] in a system of ultracold unitary Fermi gas of ^{6}Li confined along one direction at the middle of the cloud to form a quasi-2D channel linking two particle reservoirs (the channel length is small compared to the cloud which keeps the chemical potential fixed). They introduce disorder by using speckle potentials with average disorder strength $\bar{V}$ and a correlation energy $E_\sigma = \hbar^2/m\sigma^2$, where σ is the disorder correlation length. The experimental values of the parameters are such that there is no Anderson localization of individual atoms at weak disorder and the binding energy of pairs $E_b = 2.4E_\sigma$ so that pairing is affected by disorder. This is to check whether a bosonic or fermioninc mechanism of destruction of superfluidity is in action.

They measure the ratio of absolute resistances $r = R_{\mathrm{SIF}}/R_{\mathrm{WIF}}$, of the strongly interacting (where pairing is important) and weakly interacting (no pairing) Fermi gases in the exact same setup and realization of disorder. This quantity measures the effect of pairing and hence of superfluidity as compared to the ideal Fermi gas. They report, as shown in figure I.7, that for the lowest disordered the absolute resistance of the paired gas R_{SIF} is unmeasurably low, confirming the superfluid state. Upon increasing disorder they see that r rapidly grows until $\bar{V}/\mu \sim 0.7$. Such a fast increase is incompatible with simple diffusion and indicates a superfluid flow [62, 82]. Cranking up disorder even more induces a more slow increase of r and it seems to saturate to a value very close to one. This indicates that in the strongly disordered regime transport is dominated by single atom physics and superfluidity has been destroyed [62, 82]. The offset of superfluidity, corresponding to the change in behaviour in r, happens very close to the theoretical percolation threshold for the potential felt by the tightly bound point-like pairs $\bar{V}_{perc} = 0.95\mu$ [54]. These observations lead to a picture where a percolation process drives the localizaion of pairs, destroying superfluidity before disorder unbinds the pairs. The in-situ density profiles show fragmentation at exactly the same disorder strength, *i.e.* at the percolation threshold further confirming this picture for the transition [83].

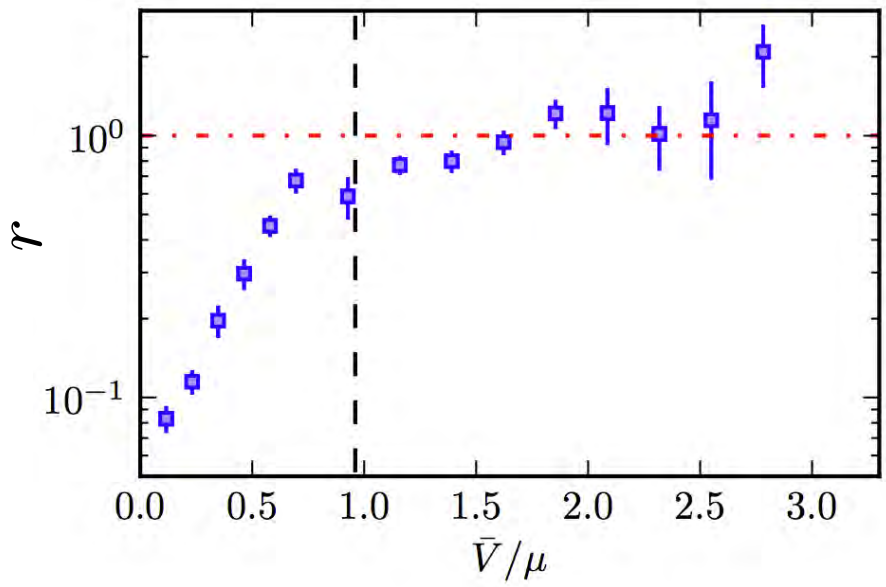

Figure I.7: *Evolution of the ratio of absolute resistances of the strongly and weakly interacting Fermi gas* $r = R_{SIF}/R_{WIF}$ *with disorder strength in units of the chemical potential* $\bar{V}/\mu$*. The dashed-dotted red line shows that* $r \approx 1$ *in the strongly disordered regime* $\bar{V} > \mu$*. The dashed black line shows the theoretical percolation threshold for the potential felt by the tightly bound point-like pairs* $\bar{V}_{perc} = 0.95\mu$*. Taken from Ref. [83].*

2.5 Order parameter distribution in disordered superconductors

While the order-parameter for the Superfluid - Insulator transition (SIT) and the critical exponents governing it have been extensively studied, the local order-parameter distribution (OPD) is another important and very interesting feature of the SIT having received much less attention. On the theoretical side, the SIT of disordered superconducting films has been predicted to present glassy behaviour of the superconducting state close to the SIT [194, 195] by the cavity Mean-Field approach. The emergence of a universal power-law decay of the probability distribution of the local order-parameter is hence brought about by the glassy physics. However, these results on the infinite-dimensionnal Cayley tree may not translate to finite dimensions. On the experimental side, Scanning Tunneling Spectroscopy (STS) is a technique allowing for the measurement of the local density of states at atomic-scale resolutions [196, 197]. It has recently been used to scan the local order-parameter in homogeneously disordered supreconductors [28, 198–200] giving acces to its distribution, but no quantitative connection between theory and experiment was found at that point, despite some efforts [198, 201].

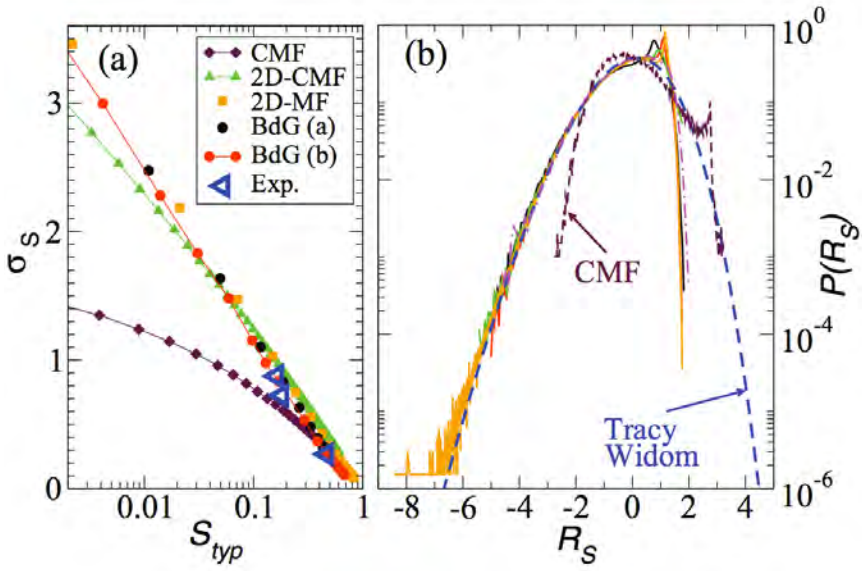

Figure I.8: *Panel a: Evolution of the typical local order-parameter* S_{typ} *and of the distribution width* σ_S *with increasing disorder (or decreasing* S_{typ}*) obtained by 2D cavity Mean-Field, 2D Mean-Field and cavity Mean-Field on the bosonic model and by two types of Bogolyubov-de Gennes theory for the fermionic model. For comparison, the experimental points of the three NbN films of figure I.9 are shown as blue left triangles. Panel b: Distribution of the rescaled variable* R_S *of equation* (I.20) *obtained by the same methods. A perfect collapse of the data for all 2D models is found and the universal distribution is very well fitted by a Tracy-Widom distribution* $TW(-R_S)$ *(blue dashed line). Taken from Ref. [30].*

A breakthrough came with the work of Lemarié *et al.* [30], who investigate theoretically the 2D SIT in both its fermionic and bosonic scenarios by prototype models and compare their results to STS mesarements on three disordered samples of NiN films. The fermionic model is studied using the Bogolyubov - de Gennes (BDG) Mean-Field theory [202–204] which does *not* describe the SIT but already captures several features of strongly disordered superconductors [203] The bosonic model is studied by the 2D cavity Mean-Field approach [205]. The local order-parameter for the fermionic model in BDG theory is connected to the local pairing amplitude Δ_i while in the 2D cavity Mean-Field of the bosonic model it is proportional to the local transverse fields B_i of the equivalent XY model [30, 205]. Let us call the normalized local order parameter in both cases S_i. The main result of their work is that in both fermionic and bosonic models the numerically obtained distributions of S_i (*i.e.* the OPD) can be universally rescaled by considering the rescaled variable

$$R_S = \frac{\ln S - \ln S_{\text{typ}}}{\sigma_S}, \tag{I.20}$$

where S is the local order-parameter, $S_{\text{typ}} = \exp(\overline{\ln S})$ is the typical local order-parameter with $\overline{S}$ denoting the average of S, and $\sigma_S^2 = \overline{\ln^2 S} - \overline{\ln S}^2$ is the variance of $\ln S$ which characterizes the width of the distribution of S. The distributions of this new variable collapse into a universal form describing both the fermionic and the bosonic 2D results as shown in panel b of figure I.8. The universal law is very well fitted by a Tracy-Widom distribution [206] with opposite asymmetry, *i.e.* TW($-R_S$) [30] as evidenced by the blue dashed curve. The fact that the simulations were carried out for a low value of the pairing interaction in the fermionic model and that the fermionic data collapses onto the same behaviour as the bosonic one supports the bosonic scenario of the SIT for which Cooper pairs get localized at the SIT and not destroyed before that and electrons get localized afterwards.

Experimental STS measurements at 500 mK on three different different disordered NbN films of thickness $\sim$ 50nm with critical temperatures $T_c \sim$ 1.65, 2.9 and 6.5 K are also performed. For these systems, the measured local order parameter is the average height of the coherence peaks at positive and negative bias over the normal state conductance, denoted by h_i [30]. The corresponding normalized experimental local order-parameter is

$$S_i^{\text{exp}} \equiv \frac{h_i}{\text{Max}[h]}, \tag{I.21}$$

and the rescaled variable is defined as in equation (I.20).

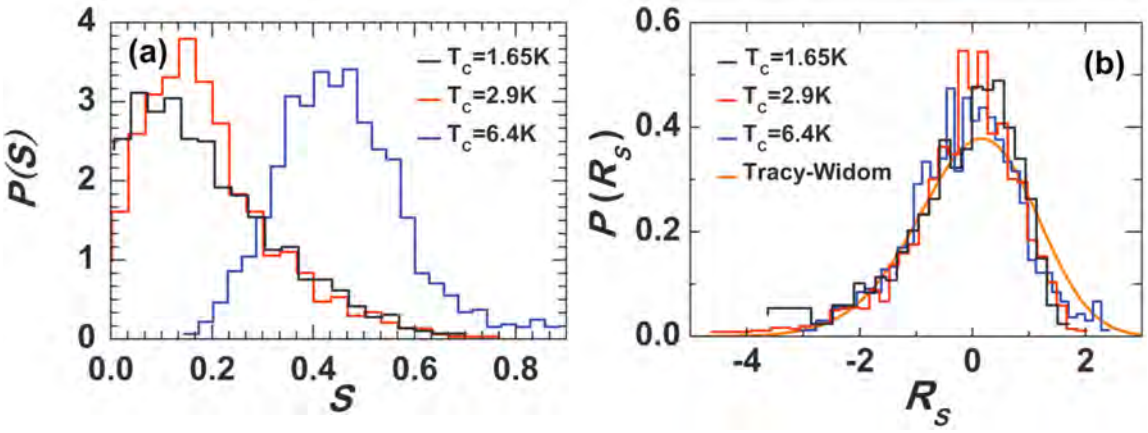

Figure I.9: *Panel a: Distribution of the normalized local order-parameter of three disordered NbN films with critical temperatures $T_c \sim$1.65, 2.9 and 6.5 K. Panel b: The same data for the NbN films plotted in terms of the rescale variable R_S* (I.20)*. A very convincing collapse of the data onto the Tracy-Widom distribution with opposite asymmetry (orange curve) is found. Taken from Ref. [30].*

Panel (a) of figure I.9 shows the distributions of the normalized local order-parameter $P(S)$ for the three disordered NbN films. As expected, the weight of $S \approx 0$ increases with increasing disorder as T_c is smaller [199]. The distributions of the rescaled variables $P(R_S)$ are plotted in panel (b) of figure I.9. They all collapse into a single curve that is very well fitted by the same opposite-asymmetry Tracy-Widom distribution as the numerical data, as shown by the orange curve. This proves that such a rescaling of the (OPD) describes both the experimental and the theoretical data. The universal distribution has relevance in the insulating side of the transition as well, as discussed in Refs. [205, 207].

3 Objectives of this work

This thesis focuses on the Superfluid - Bose glass transition in two dimensions trying to answer some of the open questions raised in this introductory chapter. We will concentrate our efforts on the transition for hard-core bosons in 2D, *i.e.* the Bose-Hubbard model in the limit of diverging repulsive interactions $U \to \infty$. Three different theoretical approaches will be used, namely a classical self-consistent Mean-Field approach, a semi-classical approach where the classical solution is used as a starting point to include quantum fluctuations in the form of non-interacting spin-waves and finally the use of extensive Quantum Monte Carlo simulations using the Stochastic Series expansion method. Each method has its degree of approximation and presents some advantages compared to one another, allowing for a comprehensive study of the properties of the Superfluid - Bose glass transition in 2D.

Chapter II

Mean-Field theory of the SF-BG transition

Contents

This chapter presents a purely classical approach to the "dirty-boson" problem in two dimensions on the square lattice. Although some early seminal studies by Ma *et al.* showed that there is no destruction of long range order, *i.e.* no phase transition to an insulting state at the Mean-Field level [8, 9], this study enables us to test our method for calculating the classical quantities of interest, namely the superfluid and the condensate densities, by comparing our findings to known results. In addition, we present a new numerical way to compute the classical superfluid stiffness as a random resistor network calculation. This is a very important step specially because the semi-classical approach developed in chapter III uses these Mean-Field results as a starting point. The Mean-Field theory for the disordered system developed in this chapter goes beyond the first "naive" one consisting in extrapolating the disorder-free Mean-Field solution to the disordered case and treats the problem self-consistently. There are multiple ways to solve the resulting problem. We will use two distinct ones to treat first, the Heisenberg model in the case of random couplings and in presence of site dilution. The equivalence between the two used methods, namely a first one where spin operators are simply viewed as 3D classical vectors $\vec{S}$ and a second one where spins are treated as two level systems (quantum spins) but a Mean-Field decoupling is introduced and an iterative solution is found, will be proven. Then the actual 2D hard-core boson problem will be tackled with with random on-site chemical potentials taken from three different distributions, namely a bimodal disorder distribution, a uniform disorder distribution centered around zero and a uniform distribution entered around 0 but with a zero weight in 0,*i.e.* a zero probability to find a vanishing local chemical potential, modelling disorder in the system. The results for the superfluid stiffness and the BEC density are presented in each case. Finally, a brief presentation on another more sophisticated Mean-Field method possible for the treatment of the "dirty-boson" problem, the cavity Mean-Field method, will be given despite its not being used in this Ph. D work.

1 Preliminary Studies

This first section presents the calculations of the superfluid stiffness with our two Mean-Field approaches in the case of the two-dimensional Heisenberg model which has been extensively studied both in the clean [208–215] and the disordered [216, 217] cases for its connection to cuprates and high-T_c superconductivity [212] and for which results are known. Two different types of randomness are studied in order to compare our classical results to the known studies using Quantum Monte Carlo simulations. The motivations behind this study are two-fold: on the one hand, the comparison of our findings with known results in an ideal test for our method. On the other hand, the computation of the *classical* superfluid stiffness ρ_{sf} which has not been done before.

Bond randomness is first studied and then site dilution, linked to the percolation problem, is investigated. In the case of bond disorder with singular distribution exact

QMC results by Laflorencie *et al.* show that there is no destruction of the long range order [217] and the stiffness is exponentially suppressed by the bond randomness. In the case of site dilution exact QMC results by Sandvik prove that the superfluid stiffness vanishes exactly at the percolation threshold in the thermodynamic limit with the classical percolation exponents governing the transition [216], though this has been greatly debated [218, 219]. Now, we provide the first Mean-Field calculation of the superfluid stiffness.

1.1 Heisenberg model with random exchange couplings

In this section we study the antiferromagnetic Heisenberg model with random positive couplings on a square lattice of size $N = L \times L$, defined by the Hamiltonian:

$$H_r = \sum_{\langle i,j \rangle} J_{ij} \hat{S}_i \hat{S}_j \tag{II.1}$$

where $\langle i, j \rangle$ denotes a couple of nearest-neighbour sites and the couplings J_{ij} are chosen randomly from the singular distribution:

$$P(J) = \frac{\delta^{-1}}{J^{(1-\frac{1}{\delta})}} \theta(J)\theta(1-J) \tag{II.2}$$

with $\theta(J)$ is the Heaviside distribution and δ the disorder parameter.

The appropriate way to compute the superfluid stiffness is by calculating the helicity modulus in the presence of a twist to the boundary conditions [177] along the x axis. It is the second derivative of the ground-state energy with respect to the twist Φ in the boundary conditions:

$$\rho_{\text{sf}} = \frac{3}{2} \frac{\partial^2 E_0(\Phi)}{\partial \Phi^2}\bigg|_{\Phi=0}. \tag{II.3}$$

This derivative is computed numerically using a small angle twist Φ and hence:

$$\rho_{\text{sf}} = 3\frac{E_0(\Phi) - E_0(\Phi = 0)}{\Phi^2} = 3\frac{\Delta E_0(\Phi)}{\Phi^2}. \tag{II.4}$$

The inhomogeneity makes the problem quite difficult since the global twist angle Φ will be distributed inequally along the disordered bonds, unlike the clean case for which each of the L bonds along the twisted direction is twisted by an angle Φ/L. Let us introduce now the two Mean-field methods used to solve this problem.

1.1.1 Spin operators as classical vectors

This method consists in replacing the spin-$\frac{1}{2}$ operators $\hat{S}$ by classical 3D vectors:

$$\vec{S}_i = \frac{1}{2} \begin{pmatrix} \sin\theta_i \cos\varphi_i \\ \sin\theta_i \sin\varphi_i \\ \cos\theta_i \end{pmatrix}. \tag{II.5}$$

Since the twist is applied on the transverse direction to the quantization axis z, the energy difference does not involve the z component and one can safely neglect them for the computation of the superfluid stiffness. The next step is noting that there is rotational invariance along the z axis and in the case of no twist, one can fix all the angles $\varphi_i = 0$. The initial antiferromagnetic problem $J_{ij} > 0$ can be mapped to a ferromagnetic one $J_{ij} < 0$ by a rotating by an angle of π every other spin. We shall now study this case. The Hamiltonian (II.1) is then simply written:

$$H_r(\Phi = 0) = -\sum_{\langle i,j \rangle} J_{ij} S_i^x S_j^x = -\sum_{\langle i,j \rangle} \frac{J_{ij}}{4} \sin\theta_i \sin\theta_j, \tag{II.6}$$

it immediately follows that $\theta_i = \frac{\pi}{2}$ minimizes the Hamiltonian (II.6) and the Mean-Field ground-state energy in the case of periodic boundary conditions is given by:

$$E_0(\Phi = 0) = -\sum_{\langle i,j \rangle} \frac{J_{ij}}{4}. \tag{II.7}$$

Let us note at this point that If the minimization of this classical energy in terms of the angles θ_i is not trivial (as will be the case for the hard-core bosons model considered in section 2) it has to be computed numerically. We can do so by means of the Newton-Raphson method using the mnewt subroutine of Ref. [220].

In the presence of a twist to the boundary conditions, the rotation invariance with respect to the axis z is broken and $\varphi_i \neq 0$. The Hamiltonian (II.1) becomes in this case:

$$H_r(\Phi) = -\sum_{\langle i,j \rangle} J_{ij}(S_i^x S_j^x + S_i^y S_j^y) = -\sum_{\langle i,j \rangle} \frac{J_{ij}}{4} \sin\theta_i \sin\theta_j \cos(\varphi_i - \varphi_j), \tag{II.8}$$

In order to compute superfluid stiffness, we write the energy difference induced by the twist Φ:

$$\Delta E_0(\Phi) = E_0(\Phi) - E_0(\Phi = 0) = -\sum_{\langle i,j \rangle} \frac{J_{ij}}{4} \sin\theta_i \sin\theta_j (\cos(\varphi_i - \varphi_j) - 1), \tag{II.9}$$

which in the limit of vanishing twist is approximated by:

$$\Delta E_0(\Phi) \approx \sum_{\langle i,j \rangle} \frac{J_{ij}}{8} \sin\theta_i \sin\theta_j (\varphi_i - \varphi_j)^2. \tag{II.10}$$

This energy difference has to be minimal in the ground-state. Paramekanti, Trivedi and Randeria [221] showed that the problem of minimizing the energy cost of applying a twist to the boundaries of the system with disordered links is analogous to calculating the energy dissipated by Joules effect by a network of random ohmic

conductors of resistance $R_{ij} = \frac{1}{\sin\theta_i \sin\theta_j}$. In this picture, the global twist Φ corresponds to the potential difference between the two edges of the system. The global superfluid stiffness is then the equivalent network conductance. The global twist being very small, it is natural to assume that the angles $\{\varphi_i\}$ and their differences are also very small, and applying such a twist does not change the angles θ_i to first approximation.

Minimizing with respect to the set of angles $\{\varphi_i\}$ (*i.e.* allowing for phase relaxation) yields the set of N coupled equations:

$$\forall i,\ \sum_{\langle j\rangle_i} J_{ij} \sin\theta_i \sin\theta_j (\varphi_i - \varphi_j) = 0, \tag{II.11}$$

where the sum runs over all sites j that are nearest-neighbours with i. These equations are then solved by calculating the LU decomposition of the corresponding matrix and hence inverting the system. This is done with the help of subroutines taken from Ref. [220] and we get the set of angles $\{\varphi_i\}$. Now we can compute $\Delta E_0(\Phi)$ and extract the superfluid stiffness by virtue of equation (II.4).

1.1.2 Iterative Mean-Field

In this section we will introduce the iterative Mean-Field solution for the Heisenberg model with random couplings (II.1). When no twist is present, the Mean-Field solution given by equation (II.7) still holds and will be used to compute the energy cost of applying the global twist to the boundary conditions, which is equivalent to having complex couplings along the twisted direction keeping periodic boundary conditions (*cf.* section 2 of appendix B). We will hence work with the Hamiltonian:

$$\begin{aligned} H_{r,2} = &- \sum_i J_{ii+\hat{y}} (S_i^x S_{i+\hat{y}}^x + S_{i+\hat{y}}^y S_i^y) - \sum_i J_{ii+\hat{x}} \cos(\frac{\Phi}{L}) (S_i^x S_{i+\hat{x}}^x + S_i^y S_{i+\hat{x}}^y) \\ &- \sum_i J_{ii+\hat{x}} \sin(\frac{\Phi}{L}) (S_i^y S_{i+\hat{x}}^x - S_i^x S_{i+\hat{x}}^y) \end{aligned} \tag{II.12}$$

To calculate the Mean-Field energy of the twisted ground-state, the starting point of this method is to perform the usual Mean-Field decoupling for the operators:

$$S_i^{x/y} S_j^{x/y} = S_i^{x/y} \langle S_j^{x/y}\rangle + \langle S_i^{x/y}\rangle S_j^{x/y} - \langle S_i^{x/y}\rangle \langle S_j^{x/y}\rangle \tag{II.13}$$

This method treats the spin operators as two level systems (*cf.* appendix A). Applying this decoupling one gets after a few steps (*cf.* appendix A):

$$\begin{aligned} H_{r,2} = &\sum_i h_i \\ &+ \sum_i \left\{ \langle S_i^x\rangle \left[J_{i+\hat{y}} \langle S_{i+\hat{y}}^x\rangle + J_{i+\hat{x}} \cos(\frac{\Phi}{L}) \langle S_{i+\hat{x}}^x\rangle - J_{i+\hat{x}} \sin(\frac{\Phi}{L}) \langle S_{i+\hat{x}}^y\rangle \right] \right. \\ &\left. + \langle S_i^y\rangle \left[J_{i+\hat{y}} \langle S_{i+\hat{y}}^y\rangle + J_{i+\hat{x}} \cos(\frac{\Phi}{L}) \langle S_{i+\hat{x}}^y\rangle + J_{i+\hat{x}} \sin(\frac{\Phi}{L}) \langle S_{i+\hat{x}}^x\rangle \right] \right\} \end{aligned} \tag{II.14}$$

where we have defined:

$$\forall i, h_i = -B_i^x S_i^x - B_i^y S_i^y \tag{II.15}$$

and

$$\begin{cases} B_i^x = \Big[J_{ii+\hat{y}} \langle S_{i+\hat{y}}^x \rangle + J_{ii-\hat{y}} \langle S_{i-\hat{y}}^x \rangle + \cos(\frac{\Phi}{L}) (J_{ii+\hat{x}} \langle S_{i+\hat{x}}^x \rangle + J_{ii-\hat{x}} \langle S_{i-\hat{x}}^x \rangle) \\ \qquad + \sin(\frac{\Phi}{L}) (J_{ii-\hat{x}} \langle S_{i-\hat{x}}^y \rangle - J_{ii+\hat{x}} \langle S_{i+\hat{x}}^y \rangle) \Big] \\ B_i^y = \Big[J_{ii+\hat{y}} \langle S_{i+\hat{y}}^y \rangle + J_{ii-\hat{y}} \langle S_{i-\hat{y}}^y \rangle + \cos(\frac{\Phi}{L}) (J_{ii+\hat{x}} \langle S_{i+\hat{x}}^y \rangle + J_{ii-\hat{x}} \langle S_{i-\hat{x}}^y \rangle) \\ \qquad + \sin(\frac{\Phi}{L}) (J_{ii+\hat{x}} \langle S_{i+\hat{x}}^x \rangle - J_{ii-\hat{x}} \langle S_{i-\hat{x}}^y \rangle) \Big] . \end{cases} \tag{II.16}$$

After a few steps (*cf.* appendix A) we get the ground-state Mean-Field expectation value:

$$\begin{aligned} \langle H_{r,2} \rangle = & - \sum_i \frac{\sqrt{B_i^{x2} + B_i^{y2}}}{2} + \sum_i \Bigg\{ \frac{B_i^x}{4\sqrt{B_i^{x2} + B_i^{y2}}} \Bigg[\frac{J_{ii+\hat{y}} B_{i+\hat{y}}^x}{\sqrt{{B_{i+\hat{y}}^x}^2 + {B_{i+\hat{y}}^y}^2}} \\ & + \cos(\frac{\Phi}{L}) \frac{J_{ii+\hat{x}} B_{i+\hat{x}}^x}{\sqrt{{B_{i+\hat{x}}^x}^2 + {B_{i+\hat{x}}^y}^2}} - \sin(\frac{\Phi}{L}) \frac{J_{ii+\hat{x}} B_{i+\hat{x}}^y}{\sqrt{{B_{i+\hat{x}}^x}^2 + {B_{i+\hat{x}}^y}^2}} \Bigg] \\ & + \frac{B_i^y}{4\sqrt{B_i^{x2} + B_i^{y2}}} \Bigg[\frac{J_{ii+\hat{y}} B_{i+\hat{y}}^y}{\sqrt{{B_{i+\hat{y}}^x}^2 + {B_{i+\hat{y}}^y}^2}} + \cos(\frac{\Phi}{L}) \frac{J_{ii+\hat{x}} B_{i+\hat{x}}^y}{\sqrt{{B_{i+\hat{x}}^x}^2 + {B_{i+\hat{x}}^y}^2}} \\ & + \sin(\frac{\Phi}{L}) \frac{J_{ii+\hat{x}} B_{i+\hat{x}}^x}{\sqrt{{B_{i+\hat{x}}^x}^2 + {B_{i+\hat{x}}^y}^2}} \Bigg] \Bigg\} , \end{aligned} \tag{II.17}$$

and the self-consistency equations for the $B_i^{x/y}$:

$$
\begin{cases}
B_i^x = \dfrac{J_{ii+\hat{y}} B^x_{i+\hat{y}}}{2\sqrt{{B^x_{i+\hat{y}}}^2 + {B^y_{i+\hat{y}}}^2}} + \dfrac{J_{ii-\hat{y}} B^x_{i-\hat{y}}}{2\sqrt{{B^x_{i-\hat{y}}}^2 + {B^y_{i-\hat{y}}}^2}} \\
\quad + \cos(\dfrac{\Phi}{L}) \left(\dfrac{J_{ii+\hat{x}} B^x_{i+\hat{x}}}{2\sqrt{{B^x_{i+\hat{x}}}^2 + {B^y_{i+\hat{x}}}^2}} + \dfrac{J_{ii-\hat{x}} B^x_{i-\hat{x}}}{2\sqrt{{B^x_{i-\hat{x}}}^2 + {B^y_{i-\hat{x}}}^2}} \right) \\
\quad + \sin(\dfrac{\Phi}{L}) \left(\dfrac{J_{ii-\hat{x}} B^y_{i-\hat{x}}}{2\sqrt{{B^x_{i-\hat{x}}}^2 + {B^y_{i-\hat{x}}}^2}} - \dfrac{J_{ii+\hat{x}} B^y_{i+\hat{x}}}{2\sqrt{{B^x_{i+\hat{x}}}^2 + {B^y_{i+\hat{x}}}^2}} \right) \\
B_i^y = \dfrac{J_{ii+\hat{y}} B^y_{i+\hat{y}}}{2\sqrt{{B^x_{i+\hat{y}}}^2 + {B^y_{i+\hat{y}}}^2}} + \dfrac{J_{ii-\hat{y}} B^y_{i-\hat{y}}}{2\sqrt{{B^x_{i-\hat{y}}}^2 + {B^y_{i-\hat{y}}}^2}} \\
\quad + \cos(\dfrac{\Phi}{L}) \left(\dfrac{J_{ii+\hat{x}} B^y_{i+\hat{x}}}{2\sqrt{{B^x_{i+\hat{x}}}^2 + {B^y_{i+\hat{x}}}^2}} + \dfrac{J_{ii-\hat{x}} B^y_{i-\hat{x}}}{2\sqrt{{B^x_{i-\hat{x}}}^2 + {B^y_{i-\hat{x}}}^2}} \right) \\
\quad + \sin(\dfrac{\Phi}{L}) \left(\dfrac{J_{ii+\hat{x}} B^x_{i+\hat{x}}}{2\sqrt{{B^x_{i+\hat{x}}}^2 + {B^y_{i+\hat{x}}}^2}} - \dfrac{J_{ii-\hat{x}} B^x_{i-\hat{x}}}{2\sqrt{{B^x_{i-\hat{x}}}^2 + {B^y_{i-\hat{x}}}^2}} \right)
\end{cases}
\tag{II.18}
$$

The self-consistency equations (II.18) can be solved iteratively to get the ground-state values of the fields $B_i^{x/y}$, plug them into the expression for the ground-state energy in the presence of the twist (II.17) and compute the energy cost of applying the twist as well as the superfluid stiffness using equations (II.7) and (II.4). Note that this explicitly allows for phase relaxation, a key ingredient of the calculation.

1.1.3 Results

Let us now present the results obtained for the superfluid stiffness of the Heisenberg model with random couplings taken from the distribution (II.2) using the direct solution of the system of N-coupled equations for system sizes ranging from $L = 10$ to $L = 32$, and the iterative Mean-Field solution for system sizes ranging from $L = 24$ to $L = 128$. It is worth stressing that the maximal system size the method of considering spins as classical vectors can attain is $L = 32$ since it involves the inversion of a $N \times N$ matrix. On the other hand, the iterative solution can reach much bigger sizes and is much more efficient since it only involves iteratively solving the self-consistency equations (II.18) which is much less costly in computational resources. We deliberately chose to use both methods for the intermediate sizes $L = 24$ and $L = 32$ as a way to verify that both methods are equivalent, which is indeed the case as can be seen in figure II.1, where the curves for these two sizes from the two different methods are identical, numerically confirming their equivalency which is proven in section 1 of appendix B . Figure II.1 shows the evolution of the superfluid stiffness, obtained by averaging over 2000 disorder realizations for every system size, renormalized by its value in the clean case, as a function of increasing disorder strength δ. The superfluid stiffness is exponentially suppressed and the data seem

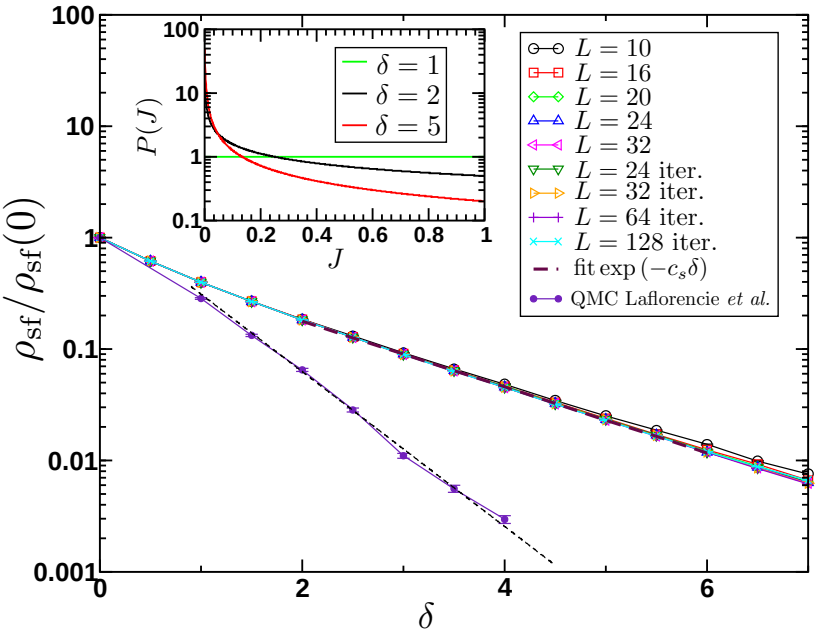

Figure II.1: *Evolution of the superfluid stiffness of the Heisenberg model with random exchange couplings* (II.1) *renormalized by its disorder-free value with disorder strength* δ *as defined in eq. II.2. For the smallest system sizes the direct solving method was used* ($L = 10 \ldots 20$)*. For the biggest sizes the iterative method was used* ($L = 64 \ldots 128$) *and for comparison the sizes* $L = 24$ *and* $L = 32$ *were solved using both methods with identical results. The stiffness decreases exponentially as shown by the fit (thick dashed line) to a form* $\exp(-c_s\delta)$ *with* $c_s = 0.680(5)$*. The results are in qualitative agreement with the QMC results by Laflorencie et al. in Ref. [217] which follows a similar form but with coefficient* $c_s^{QMC} = 1.60(2)$ *as illustrated by the thin black dashed line. The inset shows the distribution of the random bonds* J (II.2) *for* $\delta = 2$ *and* $\delta = 5$*.*

converged in size for $L > 20$. The data for $\delta > 2$ is very well fitted by an exponential decay of the form $\rho_{\rm sf} \sim \exp(-c_s\delta)$ with $c_s = 0.680(5)$ which signifies that there is no critical point for this model, as the stiffness will only vanish in the limit of infinite disorder $\delta \to \infty$.

Exact Quantum Monte Carlo simulations on the same model by Laflorencie *et al.* [217], show the same exponential suppression of the superfluid stiffness with a decay rate of $c_s^{\rm QMC} = 1.60(2)$, as shown in figure II.1 by the thin black dashed line. As expected, the Mean-Field treatments overestimate the XY order as the ignored quantum fluctuations are known to destroy order. Our methods for calculating the classical superfluid stiffness gives good qualitative and quantitative results and can hence be reliably exploited for the purpose of the studies carried out in this thesis.

1.2 Percolation and dilution in the Heisenberg model

We now focus our attention on the problem of site dilution in the Heisenberg model (II.1). As noted in the introductory chapter, a percolation scenario for the Superfluid - Bose glass transition has been put forward by several authors. This motivated us to study the classical percolation problem associated to the model (II.1). This problem was studied very precisely by Quantum Monte Carlo simulations by Sandvik [216], who found that the quantum system is driven to an insulating state at the percolation threshold $x^* = 0.4072538$ [222, 223], with the critical exponents of the classical percolation problem. Let us now solve this problem classically.

The two Mean-Field methods presented in sections 1.1.1 and 1.1.2 apply formally in exactly the same way for this case, we just have to note that all bonds have the same strength except for the 4 bonds linking a site that has been taken away from the lattice to its neighbours, which are 0. We employ the iterative Mean-Field resolution for system sizes up to $L = 128$. Averages over 1000 disorder realizations were performed for system size $L = 24$, down to 400 disordered samples were used for $L = 128$. We plot the superfluid stiffness rescaled by its disorder-free value in figure II.2 in order to compare our classical results (for which in the clean case $\rho_{\rm sf} = 0.25$) and the QMC results by Sandvik (for the quantum clean case $\rho_{\rm sf} \approx 0.18$). We can see the same behavior in both cases, with a linear decrease of the superfluid stiffness for small dilutions, and an average stiffness that vanishes exactly at the percolation threshold (vertical dashed line) at the thermodynamic limit. Some small finite-size effects are present but the vanishing at the percolation threshold is found beyond any doubt. The classical and quantum systems loose superfluidity qualitatively and almost quantitatively in the same way. There is then a Superfluid - Insulator transition for the Heisenberg model with site dilution driven by geometric effectsfor both the quantum and classical cases [216].

The classical diluted Heisenberg model was studied by Harris *et al.* and they found that its stiffness scales in the same way as the conductivity of a random resistor network [224]. Furthermore, the scaling exponent t should be the one of the percolation [224]. Hence near the percolation threshold [216, 222, 224–228],

$$\rho_{\rm sf}(x^* - x) \sim (x^* - x)^t. \tag{II.19}$$

The conductivity exponent for percolation is estimated to $t = 1.310(1)$ [228]. In order to check if our data is consistent with such a scaling, and whether the analogy to the random resistor network holds, we plot the average stiffness renormalized by its disorder-free value as a function of the distance to the percolation threshold $x^* - x$) in log-log scale. This is shown in the inset of figure II.2 along with the scaling form (II.19) (dashed-dotted black line) using the estimate of Ref. [228]. There are some finite-size effects but as L grows the data comes closer to the predicted scaling suggesting that it holds in the thermodynamic limit. However, the diluted quantum

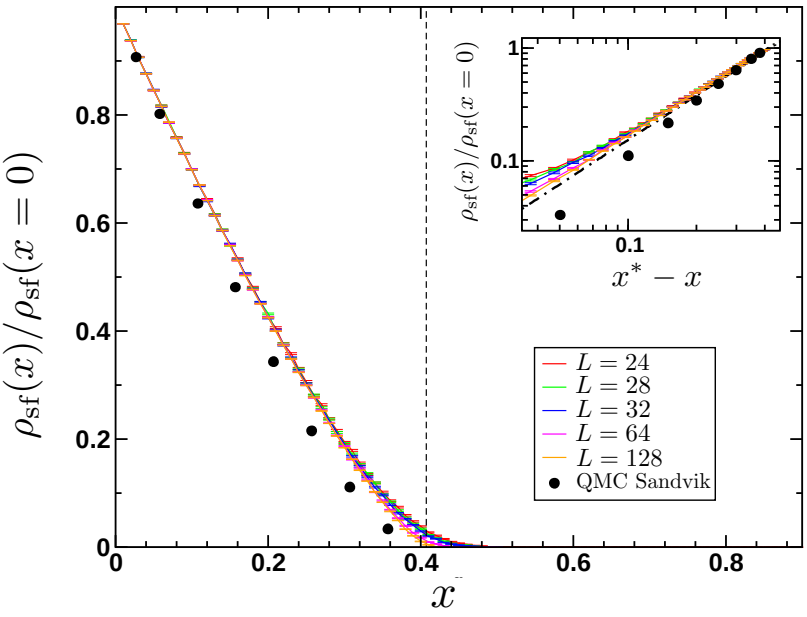

Figure II.2: *Evolution of the superfluid stiffness of the Heisenberg model with site dilution with the dilution factor x, using the iterative method. The stiffness decreases linearly for small dilution factors and vanishes at exactly the percolation $x = x^*$ (indicated by the vertical dashed line). The black dots are the exact QMC results by Sandvik taken from Ref. [216]. Inset: Log-log representation of the same stiffness data near the percolation threshold. The X axis has been rescaled to $x^* - x$. The dashed-dotted line gives the scaling behaviour of the conductivity of a 2D percolating resistor network near the percolation threshold $\rho_{sf} \sim (x^* - x)^t$ with $t = 1.310(1)$. The data at the thermodynamic limit should be in good agreement with such a scaling.*

Heisenberg model results by Sandvik extrapolated to the thermodynamic limit taken from Ref. [216] do not scale as predicted and the analogy to the resistor network breaks down as was already found in Ref. [216].

2 Hard-core bosons on the 2D square lattice

In this section we turn to the model of hard-core bosons on a square lattice of size $N = L \times L$, which represents the limit of infinite on-site repulsion of the Bose-Hubbard model. This model has been shown to have a superfluid-insulator transition by Quantum Monte Carlo studies [179]. The main goal of this section is to see if our Mean-Field resolution can capture the Bose glass physics with two different distributions of disorder, namely a box distribution and a bimodal distribution. This model is governed by the Hamiltonian:

$$H = -t \sum_{\langle i,j \rangle} \left(b_i^\dagger b_j + b_j^\dagger b_i \right) - \sum_i \mu_i n_i \tag{II.20}$$

where $\sum_{\langle i,j \rangle}$ denotes the sum over all nearest neighbour pairs, t is the hopping amplitude between neighbouring sites, μ_i is the chemical potential on the site i, $b_i^\dagger$ and b_i are, respectively, the bosonic creation and annihilation operators on the i^{th} site and $n_i = b_i^\dagger b_i$ is the number operator, which follows the hard-core constraint $n_i = 0$ or 1. The chemical potentials μ_i are quenched random variables taken from a given distribution.

Since the hard-core nature of the bosons constraints the number of bosons per site to either 0 or 1, this Hamiltonian can be mapped to a spin-$\frac{1}{2}$ Hamiltonian, which also has only two possible states per site, by the Matsubara-Matsuda transformation [229]:

$$\begin{cases} S_i^+ = b_i^\dagger \\ S_i^- = b_i \\ S_i^z = n_i - \dfrac{1}{2}, \end{cases} \tag{II.21}$$

which yields the XY Hamiltonian:

$$H_{XY} = -\frac{1}{2} \sum_i \mu_i - 2t \sum_{\langle i,j \rangle} (S_i^x S_j^x + S_j^y S_i^y) - \sum_i \mu_i S_i^z. \tag{II.22}$$

This will be the starting point for all our calculations. The order parameter in the spin language is the XY magnetization m_{XY} which is linked to the bosonic order parameter, the Bose-Einstein condensate density by $\rho_0 = m_{XY}^2$. The presence of the coherent Bose-Einstein condensate is translated to the spin language by spontaneous long-range order in the XY plane.

2.1 Bimodal on-site disordered XY model

The Hamiltonian (II.22) can be solved at the Mean-Field level by the same methods introduced in sections 1.1.1 and 1.1.2, but the equations have to be rewritten. Treating the spin operators as classical vectors again (see equation (II.5)), we get the classical Hamiltonian for the non twisted case (*i.e.* the spins lie on the XZ plain):

$$H_{\text{class}} = -\frac{1}{2} \sum_i \mu_i - \frac{t}{2} \sum_{\langle i,j \rangle} \sin\theta_i \sin\theta_j - \sum_i \frac{\mu_i}{2} \cos\theta_i. \tag{II.23}$$

The minimization of this energy with respect to the set of angles $\{\theta_i\}$ yields the set of N equations:

$$-t\cos\theta_i\sum_{\langle j\rangle_i}\sin\theta_j+\mu_i\sin\theta_i=0. \tag{II.24}$$

with $\sum_{\langle j\rangle_i}$ the sum over all sites j nearest-neighbours of site i. The solution is given straightforwardly in the case of the bimodal distributed disorder, for which $\mu_i=\epsilon_i W$ with $\epsilon_i=\pm1$ with probability $\frac{1}{2}$, by:

$$\forall i,\begin{cases}\cos\theta_i=\dfrac{\mu_i}{4t}=\dfrac{\epsilon_i W}{4t}\\ \sin\theta_i=\sqrt{1-\dfrac{W^2}{16t^2}}\end{cases}, \tag{II.25}$$

if $W<4t$. At this level of approximation, for the bimodal disorder distribution, the system is divided in two disorder-free randomly spaced sub-lattices, one with $\mu_i=W$ for all its sites and the other with $\mu_i=-W$. This can be seen in equation (II.25), where the $\sin\theta_i$ do not depend on the index i. Hence, the solution is exactly the same that the one of the disorder-free case [230]. Applying a twist to the boundary conditions in order to calculate the superfluid density, is exactly the same as described in section 1.1.1 with the only difference of a missing factor 3 here because of the U(1) symmetry of the problem.The calculation steps are similar and we end up with the energy in the presence of a twist:

$$H_{\text{class}}(\Phi)=-\frac{1}{2}\sum_i\mu_i-\frac{t}{2}\sum_{\langle i,j\rangle}\sin\theta_i\sin\theta_j\cos(\varphi_i-\varphi_j)-\sum_i\frac{\mu_i}{2}\cos\theta_i, \tag{II.26}$$

and the energy cost of the *small* twist Φ (*i.e.* the differences $\varphi_i-\varphi_j$ are small too):

$$\Delta E(\Phi)\approx\frac{t}{4}\sum_{\langle i,j\rangle}\sin\theta_i\sin\theta_j(\varphi_i-\varphi_j)^2 \tag{II.27}$$

and the set of N coupled equations:

$$\forall i,\ t\sum_{\langle j\rangle_i}\sin\theta_i\sin\theta_j(\varphi_i-\varphi_j)=0. \tag{II.28}$$

We solve this as for the Heisenberg model and obtain the superfluid density.

The Bose-Einstein condensate fraction then reads:

$$\rho_0=\frac{1}{N}\langle b^\dagger_{k=0}b_{k=0}\rangle=\frac{1}{N^2}\sum_{i,j}b_i^\dagger b_j=\frac{1}{4N^2}\sum_{i,j}\sin\theta_i\sin\theta_j=\frac{1}{4}\left(1-\frac{W^2}{16t^2}\right). \tag{II.29}$$

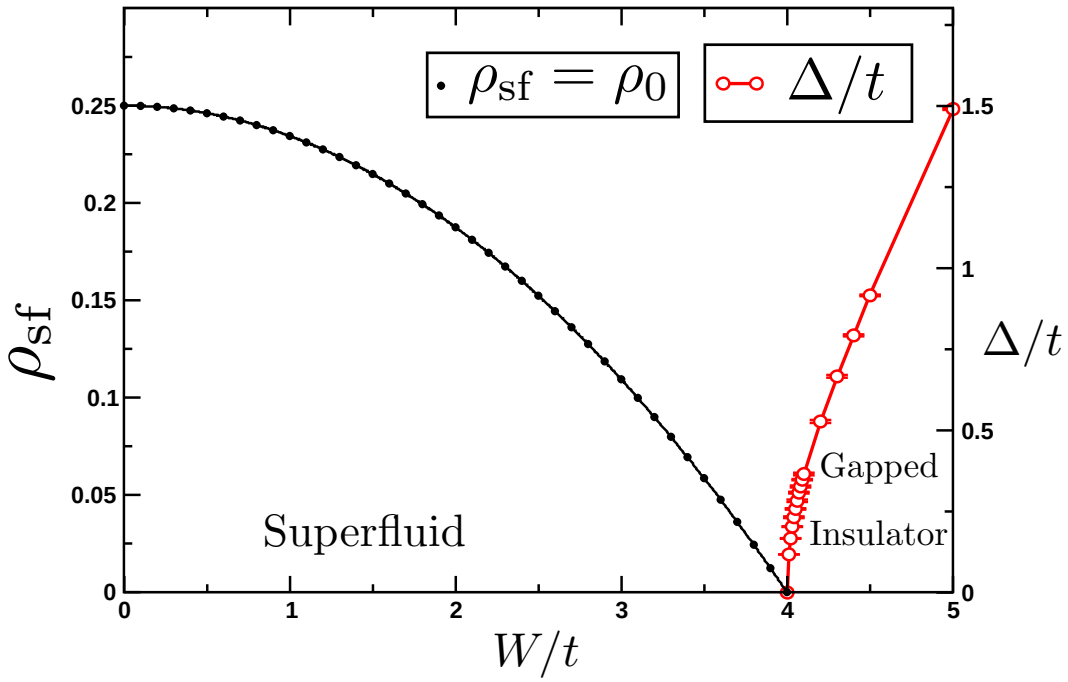

Figure II.3: *Evolution of superfluid and Bose condensed densities vs. disorder strength W/t for a bimodal disorder on the chemical potential μ. There are no finite size effects so only one size is shown. The superfluid and condensate densities are equal and both decrease from their disorder-free value of* 0.25 *and vanish at a disorder strength equal to the band-width $W/t = 4$. A gapped insulator is present for higher disorder strengths.*

The superfluid and BEC densities turn out to be equal at this level of approximation as can be seen in figure II.3. They decrease from 0.25 in the clean case $W = 0$ and vanish exactly at the band edge $W = 4t$. For stronger values of disorder the system is in a disordered insulating state with $\cos\theta_i = \pm 1$ and the spins completely polarized along the z axis. These results are shown in figure II.3, where the two phases present in the phase diagram are visible: the superfluid and the disordered gapped insulator. It is worth noting that no finite-size effects are present at this level of approximation, so only one system size is shown. This is a direct consequence of the fact that there is an analytical solution (*cf.* equation (II.29)). Figure II.3 also shows the gap Δ in units of t which is actually calculated at the linear spin wave level, beyond the scope of the treatment discussed here. We decided to show it to stress the fact that the high disorder phase is indeed a gapped insulator. Nevertheless, it is important to say that this level of approximation does not capture the Bose glass physics.

2.2 Iterative Mean-Field method: box disorder

2.2.1 Computation the superfluid density

When considering the uniform disorder distribution $\mu_i \in [-W; W]$, there is no analytical solution like for the bimodal distribution. The minimization of the classical energy has to be done numerically. In the absence of a twist to the boundary conditions, the classical energy (II.23) can be minimized using a Newton-Raphson algorithm [220] in order to get the $\{\theta_i\}$ angles by iteratively solving the set of N equations given by minimizing the energy with respect to each angle θ_i, starting from the naive solution given by equation (II.25), until the zeros are found.

However, the most efficient way to compute the ground-state energy is applying the iterative Mean-Field solution described in section 1.1.2. In this case, for the model (II.22) under consideration with periodic boundary conditions and no twist, the self-consistency equations read (*cf.* section 1.1 of appendix A)

$$B_i = t \sum_{\langle j \rangle_i} \frac{B_j}{\sqrt{\mu_j^2 + B_j^2}}, \tag{II.30}$$

and the ground-state energy:

$$\langle H(\phi = 0) \rangle = -\sum_i \frac{\sqrt{\mu_i^2 + B_i^2}}{2} + \frac{t}{2} \sum_{\langle i,j \rangle} \frac{B_i B_j}{\sqrt{(\mu_i^2 + B_i^2)(\mu_j^2 + B_j^2)}}. \tag{II.31}$$

Applying a twist Φ to the boundary conditions is the analog of applying a magnetic field along the same direction to the charged hard-core bosons, rendering the hoppings along said direction complex and keeping periodic boundary conditions (*cf.* section 1 of appendix B). The corresponding Hamiltonian is:

$$\begin{aligned} H = & -\textstyle\sum_i \frac{\mu_i}{2} - \sum_i \mu_i S_i^z - 2t \sum_i (S_i^x S_{i+\hat{y}}^x + S_{i+\hat{y}}^y S_i^y) \\ & -2t \cos(\tfrac{\Phi}{L}) \textstyle\sum_i (S_i^x S_{i+\hat{x}}^x + S_i^y S_{i+\hat{x}}^y) - 2t \sin(\tfrac{\Phi}{L}) \sum_i (S_i^y S_{i+\hat{x}}^x - S_i^x S_{i+\hat{x}}^y). \end{aligned} \tag{II.32}$$

Following the same calculation steps for the iterative Mean-Field solution applied to this Hamiltonian yields the self-consistency equations (*cf.* section 1.3 appendix A):

$$\begin{cases} B_i^x = t\left[\dfrac{B_{i+\hat{y}}^x}{\sqrt{\mu_{i+\hat{y}}^2 + {B_{i+\hat{y}}^x}^2 + {B_{i+\hat{y}}^y}^2}} + \dfrac{B_{i-\hat{y}}^x}{\sqrt{\mu_{i-\hat{y}}^2 + {B_{i-\hat{y}}^x}^2 + {B_{i-\hat{y}}^y}^2}}\right. \\ \quad + \cos(\dfrac{\Phi}{L})\left(\dfrac{B_{i+\hat{x}}^x}{\sqrt{\mu_{i+\hat{x}}^2 + {B_{i+\hat{x}}^x}^2 + {B_{i+\hat{x}}^y}^2}} + \dfrac{B_{i-\hat{x}}^x}{\sqrt{\mu_{i-\hat{x}}^2 + {B_{i-\hat{x}}^x}^2 + {B_{i-\hat{x}}^y}^2}}\right) \\ \quad \left. + \sin(\dfrac{\Phi}{L})\left(\dfrac{B_{i-\hat{x}}^y}{\sqrt{\mu_{i-\hat{x}}^2 + {B_{i-\hat{x}}^x}^2 + {B_{i-\hat{x}}^y}^2}} - \dfrac{B_{i+\hat{x}}^y}{\sqrt{\mu_{i+\hat{x}}^2 + {B_{i+\hat{x}}^x}^2 + {B_{i+\hat{x}}^y}^2}}\right)\right] \\ B_i^y = t\left[\dfrac{B_{i+\hat{y}}^y}{\sqrt{\mu_{i+\hat{y}}^2 + {B_{i+\hat{y}}^x}^2 + {B_{i+\hat{y}}^y}^2}} + \dfrac{B_{i-\hat{y}}^y}{\sqrt{\mu_{i-\hat{y}}^2 + {B_{i-\hat{y}}^x}^2 + {B_{i-\hat{y}}^y}^2}}\right. \\ \quad + \cos(\dfrac{\Phi}{L})\left(\dfrac{B_{i+\hat{x}}^y}{\sqrt{\mu_{i+\hat{x}}^2 + {B_{i+\hat{x}}^x}^2 + {B_{i+\hat{x}}^y}^2}} + \dfrac{B_{i-\hat{x}}^y}{\sqrt{\mu_{i-\hat{x}}^2 + {B_{i-\hat{x}}^x}^2 + {B_{i-\hat{x}}^y}^2}}\right) \\ \quad \left. + \sin(\dfrac{\Phi}{L})\left(\dfrac{B_{i+\hat{x}}^x}{\sqrt{\mu_{i+\hat{x}}^2 + {B_{i+\hat{x}}^x}^2 + {B_{i+\hat{x}}^y}^2}} - \dfrac{B_{i-\hat{x}}^x}{\sqrt{\mu_{i-\hat{x}}^2 + {B_{i-\hat{x}}^x}^2 + {B_{i-\hat{x}}^y}^2}}\right)\right] \end{cases} \tag{II.33}$$

and a ground-state expectation value of the energy:

$$\begin{aligned} \langle H(\Phi)\rangle = \quad & -\textstyle\sum_i \frac{\sqrt{\mu_i^2 + {B_i^x}^2 + {B_i^y}^2}}{2} + \frac{t}{2}\sum_i \left\{ \frac{B_i^x}{\sqrt{\mu_i^2 + {B_i^x}^2 + {B_i^y}^2}} \left[\frac{B_{i+\hat{y}}^x}{\sqrt{\mu_{i+\hat{y}}^2 + {B_{i+\hat{y}}^x}^2 + {B_{i+\hat{y}}^y}^2}} \right.\right. \\ & \left. + \cos(\tfrac{\Phi}{L}) \frac{B_{i+\hat{x}}^x}{\sqrt{\mu_{i+\hat{x}}^2 + {B_{i+\hat{x}}^x}^2 + {B_{i+\hat{x}}^y}^2}} - \sin(\tfrac{\Phi}{L}) \frac{B_{i+\hat{x}}^y}{\sqrt{\mu_{i+\hat{x}}^2 + {B_{i+\hat{x}}^x}^2 + {B_{i+\hat{x}}^y}^2}} \right] \\ & + \frac{B_i^y}{\sqrt{\mu_i^2 + {B_i^x}^2 + {B_i^y}^2}} \left[\frac{B_{i+\hat{y}}^y}{\sqrt{\mu_{i+\hat{y}}^2 + {B_{i+\hat{y}}^x}^2 + {B_{i+\hat{y}}^y}^2}} + \cos(\tfrac{\Phi}{L}) \frac{B_{i+\hat{x}}^y}{\sqrt{\mu_{i+\hat{x}}^2 + {B_{i+\hat{x}}^x}^2 + {B_{i+\hat{x}}^y}^2}} \right. \\ & \left.\left. + \sin(\tfrac{\Phi}{L}) \frac{B_{i+\hat{x}}^x}{\sqrt{\mu_{i+\hat{x}}^2 + {B_{i+\hat{x}}^x}^2 + {B_{i+\hat{x}}^y}^2}} \right] \right\}. \end{aligned} \tag{II.34}$$

Putting together equations (II.34) (II.31) and (II.4) we can now compute the superfluid density.

2.2.2 Global thermodynamic quantities - Absence of transition

The equivalency between the two Mean-Field approaches is treated in detail in section 1 of appendix B. One of its results is that the expectation value of S_i^x when no twist is applied is given by:

$$\langle S_i^x \rangle = \frac{B_i}{2\sqrt{\mu_i^2 + B_i^2}} = \frac{1}{2}\sin\theta_i. \tag{II.35}$$

We can use this relation between the classical angles $\{\theta_i\}$ and the iterative fields B_i to write the Bose-Einstein condensate density in terms of the iterative fields:

$$\rho_0 = \frac{1}{4N^2}\sum_{i,j}\sin\theta_i\sin\theta_j = \frac{1}{4N^2}\sum_{i,j}\frac{B_iB_j}{\sqrt{\mu_i^2+B_i^2}\sqrt{\mu_j^2+B_j^2}}. \tag{II.36}$$

We can now compute both the superfluid and BEC densities as a function of the disorder strength, averaging over several hundreds of disorder realizations for each disorder strength. The results are shown in figure II.4 for system sizes ranging from $L = 8$ to $L = 36$. When no disorder is present both densities are equal to 0.25. However, upon including disorder, the superfluid density becomes smaller than the BEC density, $\rho_{\rm sf} < \rho_0$ even at the Mean-Field level. This shows the different nature of these two quantities: while the BEC is a static property of the system, the superfluid fraction is a response to an external perturbation (the twist Φ) therefore a dynamic property of the system. The fact that such a distinction is found at the Mean-Field level is a consequence of the phase relaxation.

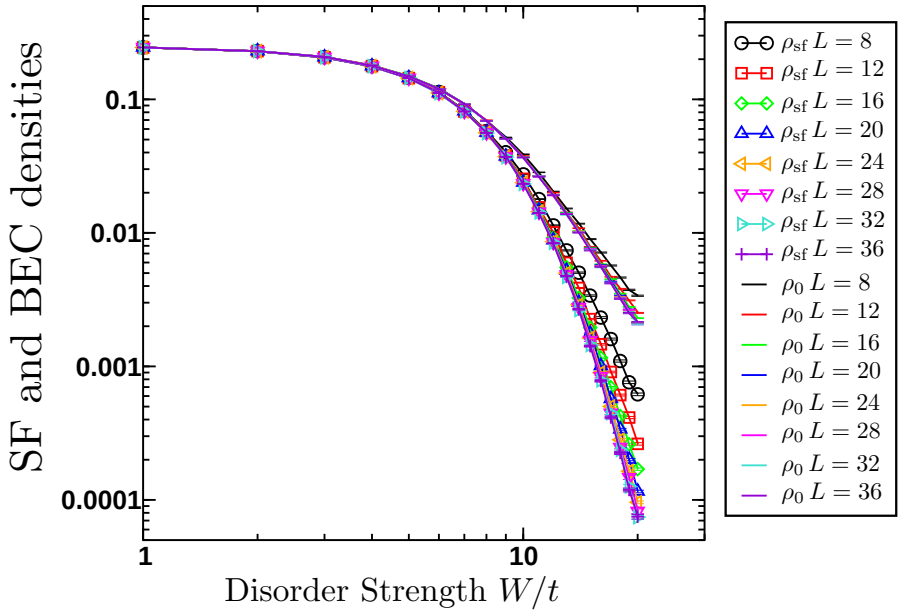

Figure II.4: *Evolution of superfluid (ρ_{sf}) and Bose condensed (ρ_0) densities vs. disorder strength in units of the hopping parameter W/t for the uniform disorder distribution $\mu_i \in [-W;W]$. Even at the MF level the two densities are different: $\rho_{sf} < \rho_0$. Both densities show a linear dependence on disorder in either log-log or log-normal (not shown) scales: the data is compatible with both an exponential and a power-law decrease. Hence, both quantities only vanish in the limit of infinite disorder $W \to \infty$ indicating no transition to a Bose glass phase at this level of approximation.*

Furthermore, the data for both quantities can be fitted equally well by exponential or power-law decays, in the considered parameter range. Even though we cannot exactly determine the form in which superfluidity and BEC are suppressed by disorder in this MF level, it is clear that both densities will only vanish in the limit of infinite disorder strength $W \to \infty$ indicating that the Bose glass physics cannot be captured by such a Mean-Field treatment: therefore, we conclude that quantum fluctuations are a key ingredient for the Superfluid - Bose glass transition to occur. This result is in agreement with the prediction by Ma *et al.* [9]. However, the fact that the superfluid stiffness vanishes in the case of the bimodal disorder only when the system is trivially in its insulating state, *i.e.* when all sites have chemical potentials lying outside the band ($W > 4t$), disagrees with their conclusion that the important feature for the MF stiffness to vanish at a finite disorder strength (*i.e.* for Mean-Field theory not to break-down) is that the disorder distribution has a zero weight at 0, $P(0) = 0$. The bimodal distribution being the most extreme case of such a distribution, their argument seems to fail. We will further explore this in section 2.3.

2.2.3 Current distributions

Even though there is no transition to an insulating state at the Mean-Field level, we explore the classical transport properties in order to extract the most information as possible. We therefore compute the classical currents induced by applying a twist Φ to the boundary conditions, or equivalently by applying a fraction of the twist Φ/L on each of the L bonds along the direction and allowing for phase relaxation. The hopping parameter along those bonds bond undergoes the transformation $t \mapsto te^{\pm\frac{\Phi}{L}}$ and the corresponding Hamiltonian is the one given in equation (II.32). Therefore, there are two types of currents: the ones in the X direction (with complex hopping) and the ones along the Y direction (with real hopping).

Along the Y direction the transverse current operator is defined by:

$$J^y_{i\to i+\hat{y}} = -\imath\langle b_i b^\dagger_{i+\hat{y}} - b^\dagger_i b_{i+\hat{y}}\rangle = -\imath\langle S^-_i S^+_{i+\hat{y}} - S^+_i S^-_{i+\hat{y}}\rangle = 2(S^x_i S^y_{i+\hat{y}} - S^y_i S^x_{i+\hat{y}}) \quad \text{(II.37)}$$

which finally yields:

$$J^y_{i\to i+\hat{y}} = \frac{1}{2}\sin\theta_i \sin\theta_{i+\hat{y}} \sin(\varphi_{i+\hat{y}} - \varphi_i). \quad \text{(II.38)}$$

Along the X direction, the current is:

$$\begin{aligned} J^x_{i\to i+\hat{x}} =& -\imath\langle e^{\imath\frac{\Phi}{L}} b_i b^\dagger_{i+\hat{x}} - e^{-\imath\frac{\Phi}{L}} b^\dagger_i b_{i+\hat{x}}\rangle = -\imath\langle e^{\imath\frac{\Phi}{L}} S^-_i S^+_{i+\hat{x}} - e^{-\imath\frac{\Phi}{L}} S^+_i S^-_{i+\hat{x}}\rangle \\ J^x_{i\to i+\hat{x}} =& 2\sin(\frac{\Phi}{L})(S^x_i S^x_{i+\hat{x}} + S^y_i S^y_{i+\hat{x}}) + 2\cos(\frac{\Phi}{L})(S^x_i S^y_{i+\hat{x}} - S^y_i S^x_{i+\hat{x}}) \end{aligned} \quad \text{(II.39)}$$

and finally:

$$J^x_{i\to i+\hat{x}} = \frac{1}{2}\sin(\frac{\Phi}{L})\langle \sin\theta_i \sin\theta_{i+\hat{x}} \cos(\varphi_{i+\hat{x}} - \varphi_i)\rangle + \frac{1}{2}\cos(\frac{\Phi}{L})\langle \sin\theta_i \sin\theta_{i+\hat{x}} \sin(\varphi_{i+\hat{x}} - \varphi_i)\rangle. \quad \text{(II.40)}$$

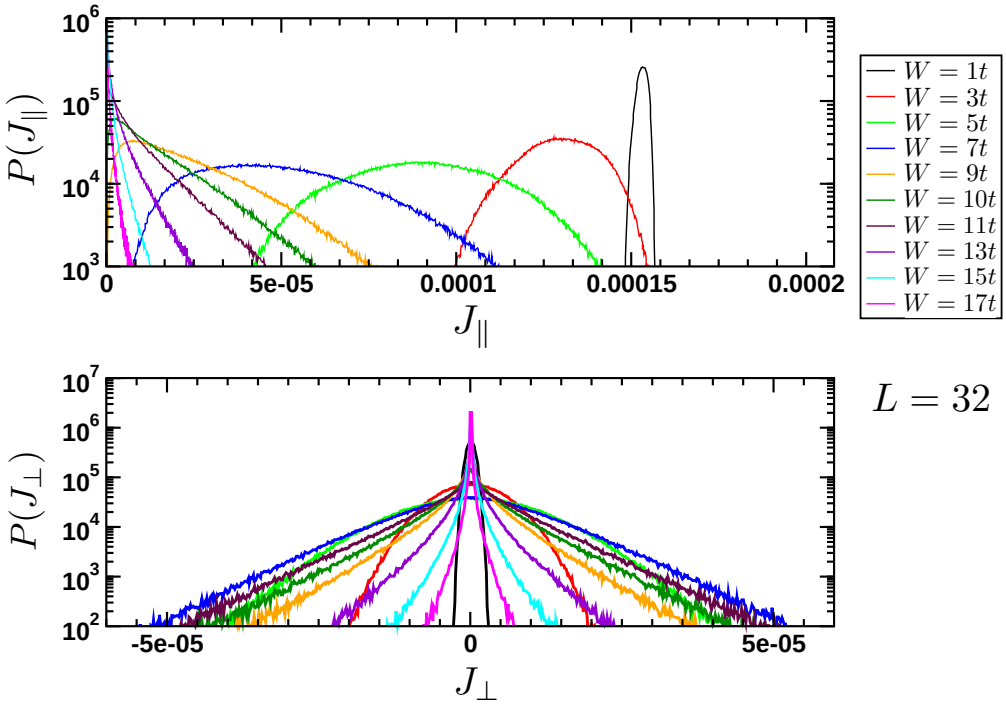

Figure II.5: *Distribution of the longitudinal ($J_\parallel$) and transverse ($J_\perp$) currents for a system of size $L = 32$ and different disorder strengths W in the case of a uniform disorder distribution $[-W; W]$. The longitudinal currents are smaller for growing disorder strengths. At low disorder, the transport is mainly longitudinal while at strong disorder ($W \geq 10t$) it becomes isotropic with longitudinal and transverse currents of the same order of magnitude both presenting distributions with exponential tails, a classical manifestation of the underlying Bose glass physics (see text) .*

One should notice that for the current $J^x_{i\to i-\hat{x}}$ the circulation of the magnetic field is then negative and one should do the replacement $\Phi \mapsto -\Phi$, recovering the fact that $J^{x/y}_{i\to i+\hat{x}} = -J^{x/y}_{i+\hat{x}\to i}$.

The distributions of the longitudinal $J_\parallel$ and transverse $J_\perp$ currents obtained for 800 disordered samples of a system of size $N = 32\times 32$ at different disorder strengths are plotted in log-normal scale in figure II.5. For small disorders, the transport is mainly longitudinal with $J_\parallel$ larger than $J_\perp$ by nearly two orders of magnitude. Cranking the disorder strength gradually reduces $J_\parallel$ and increases $J_\perp$. Finally, for $W \geq 10t$ both current distributions are of the same order of magnitude and develop exponential tails as demonstrated by the straight line tails in the log-normal scale. The transport at strong disorders becomes exponentially suppressed and isotropic, which we interpret as a classical precursor of the glassy physics even when no transition is found at the Mean-Field level.

In order to show this effect in a more quantitative way, we compute the disorder averaged local currents as a function of disorder strength, renormalized by the clean case local current $J_{\text{clean}} = \frac{1}{2}\overline{\rho_{\text{sf}}}\frac{\Phi}{L}$, where $\overline{\rho_{\text{sf}}}$ is the average value of the superfluid stiffness at the given disorder strength. The results are illustrated in the top panel of figure II.6. For low disorders, the mean longitudinal current $\langle J_{\parallel}\rangle$ is two orders of magnitude larger than the mean transverse current $\langle J_{\perp}\rangle$. Cranking up the disorder strength reduces the longitudinal mean value and increases the transverse ones. Further increasing the disorder strength reduces both mean values which become of the same order of magnitude for strong disorders $W \geq 10t$.

We have represented in the bottom panel of figure II.6 the standard deviation of the currents divided by their mean value as a function of disorder strength. Although at low disorders the relative spread of the longitudinal currents is almost zero it in-

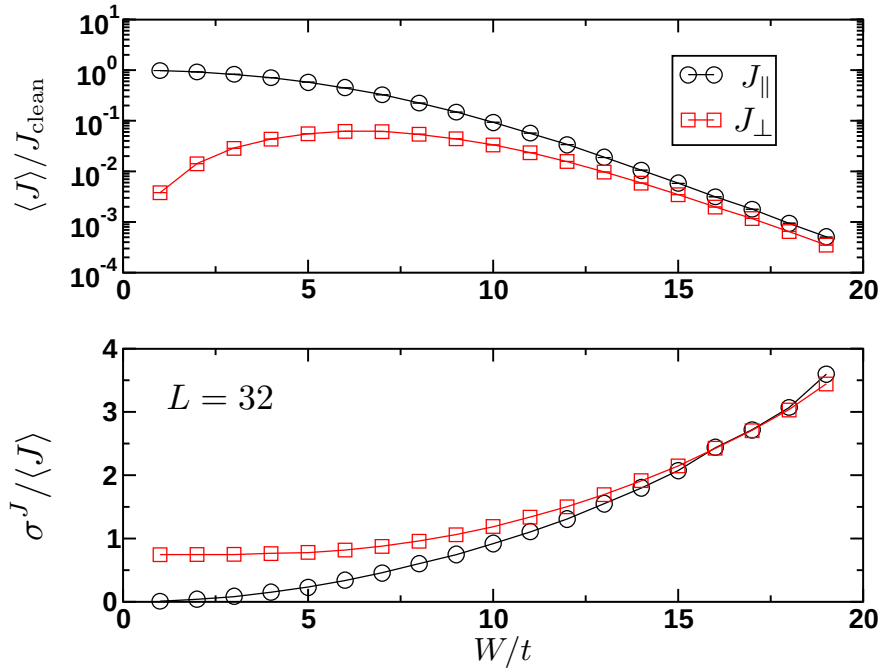

Figure II.6: *Top: Disorder averaged longitudinal ($J_{\parallel}$) and transverse ($J_{\perp}$) currents for a system of size $L = 32$ vs. disorder strength W/t in the case of a uniform disorder distribution $[-W;W]$, renormalized by the clean value of the current $\bar{J}_{clean} = \frac{1}{2}\bar{\rho}_{sf}\frac{\Phi}{L}$. At low disorder, the longitudinal transport is several orders of magnitude more important than transverse transport while at strong disorder ($W \geq 10t$) longitudinal and transverse currents are of the same order of magnitude. Error bars are smaller than the symbols. Bottom: Standard deviation of longitudinal and transverse currents σ^J divided by their mean value $\langle J\rangle$ as a function of disorder. The transverse currents have a wider relative spread at low disorders but it becomes equivalent to the longitudinal current spread at strong disorders $W > 10t$.*

creases with disorder strength becoming equivalent to that of the transverse currents at strong disorders. Indeed, the transverse currents have a finite relative spread at low disorders which grows monotonically with disorder strength but at a smaller pace than the longitudinal disorders. Summing up, figure II.6 shows quantitatively that at strong disorders $W > 10t$, the classical transport is isotropic despite the fact that the cause of transport (the twist Φ or equivalently the gauge field flux Φ/L) is along one direction only. Accompanied by the fact that the currents are exponentially suppressed at those high disorders, we recover the transport properties of the glassy insulating phase at strong disorders even when no phase transition is observed at the Mean-Field level. The change of behaviour seems to happen at a disorder strength close to $W = 10t$. Indeed, the disorder strength $W \approx 10t$ is the critical threshold for the Superfluid - Bose glass transition for this model given both by the linear spin wave approach developed in chapter III (*cf.* figure III.4) and the Quantum Monte Carlo simulations of chapter IV (*cf.* table IV.2), which further justifies our interpretation of these features being a classical precursor of the underlying Bose glass physics.

2.3 Iterative Mean-Field method: disorder distribution with $P(0) = 0$

A seminal work by Ma, Halperin and Lee back in 1986 [9] showed that the Mean-Field theory breaks down for the Superfluid - Insulator transition since it results in a superfluid density that only vanishes for infinitely large disorder, when considering the box distribution, while experiments on superfluid Helium 4 adsorbed on porous media showed otherwise [7]. They claimed that the key ingredient for such a breakdown is the fact that the disorder distribution has a non-zero weight at 0, meaning that there are always almost disorder-free sites which can be tilted in the XY plane with little energy cost, *i.e.* it is energetically favourable for coherence (or XY order) to be established at these sites which then act as nucleation centers for macroscopic coherence (long-range XY order). Our results for both the bimodal and the box distribution are in full agreement with such a scenario (*cf.* figures II.3 and II.4 sections 2.1 and 2.2) since for the bimodal disorder, with $P(0) = 0$, the system is in an insulating state as soon as the disorder bound lies outside the band-width ($W > 4t$) and for the box disorder (with $P(0) \neq 0$) the superfluid density and the BEC density (*i.e.* the XY order parameter) only vanish for infinite disorder.

In order to check if the $P(0) \neq 0$ condition holds in other cases, we study the case of a uniform disorder distribution with zero weight around zero, *i.e.* a uniform distribution for values in $[-W; -\alpha]$ and $[\alpha; W]$. This can be done with the same expressions as for the box distribution for the consistency equations (II.33) and the ground-state energy both with and without the twist (*cf.* section 2.2). The distribution is still symmetric with respect to 0, meaning that we are still studying the physics at half-filling. The results for the superfluid and BEC densities as a

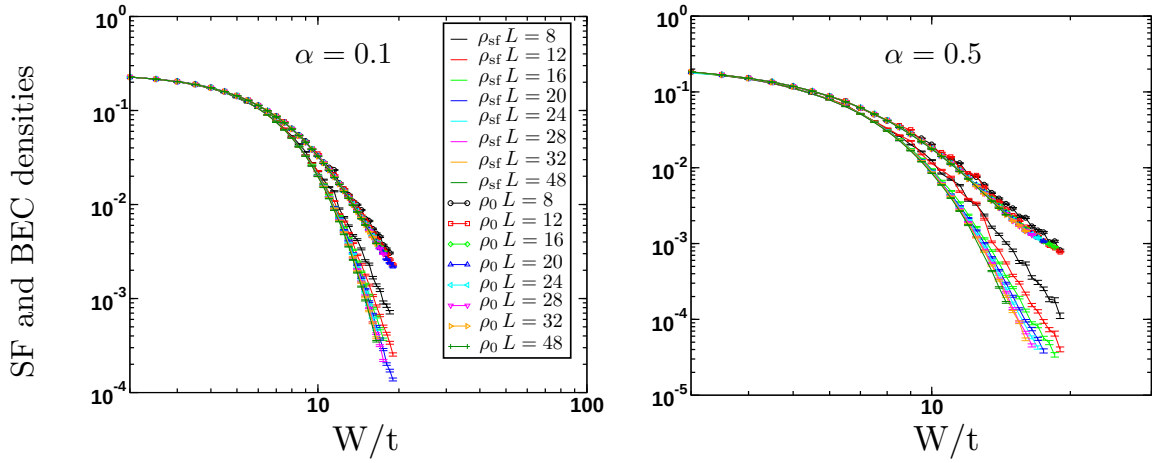

Figure II.7: *Evolution of the Bose-Einstein condensate and superfluid densities as a function of disorder for the uniform disorder distribution in* $[-W;-\alpha]\bigcup[\alpha;W]$ *for two different values of* $\alpha = 0.1$ *and 0.5, and system sizes ranging from* $L = 8$ *to* $L = 48$*. Disorder averages were performed over 3000 for the smallest sizes and 700 samples for* $L = 48$*. For both values of* α *the behaviour is very similar to that of the box disorder* $\alpha = 0$*:* $\rho_{sf} < \rho_0$ *and both quantities drop with disorder strength* W *as either a power-law or an exponential form. There is no critical disorder strength.*

function of the disorder bound W for three values of $\alpha = 0.1$, 0.5 are shown in figure II.7, for system sizes up to $N = 48 \times 48$. Disorder averages were performed over 3000 samples for $L = 8$ down to 700 samples for $L = 48$. For both values of α the behavior is very similar to the one of the box disordered case with no hole. Indeed, we find again that even at the Mean-Field level $\rho_{\rm sf} < \rho_0$. Once again, the data is well fitted either by a power-law or an exponential form, indicating that the XY order will only vanish in the limit of infinite disorder strength $W \to \infty$.

As a conclusion, the energetic argument by Ma *et al.* seems to be valid also for disorder distributions with $P(0) = 0$. In other words, it is still energetically favourable to tilt a site which has small local filed (or chemical potential) onto the XY plane and it being a nucleation center for long-range order if the disorder distribution allows for such small local fields. It would be very interesting, nonetheless, to carry out a more thorough study of the effect of the α parameter to see if this effect remains for all values of α inside the band-width. We can already predict that if α is larger than the the band-width the scenario will be identical to the bimodal disorder case studied in section 2.1 for which there is a disordered insulating phase in competition with the superfluid phase.

3 Alternative Mean-Field approach: The cavity mean-field

We have presented in the previous sections of this chapter the results of two different fairly simple Mean-Field methods which do not capture the phase transition from the Superfluid to the Bose glass although they do provide some interesting information concerning the transport properties. However, more sophisticated Mean-Field approaches exist. One example is the cavity Mean-Field approach. First developed to study classical frustrated spin systems, *i.e.* spin glasses [231], it is a Mean-Filed theory that solved the fully connected Sherrington-Kirkpatrick model of spin glasses [232] in a much more transparent way than the previously found Replica Symmetry Breaking ansatz in the replica approach by Parisi [233–235]. It uses a probabilistic approach based on three assumptions: ultrametricity [236], the existence of many pure states [237, 238] and the exponential distribution of their free energies [239].

This method can be extended to the quantum cavity-method and be used in the context of quantum phase transitions in quantum disordered systems [194, 195]. In the following we will briefly present this method treated in detail in Ref. [240]. To make things more concrete, let us consider the random transverse-field ferromagnet described by the Hamiltonian on the Bethe lattice with connectivity $z = K + 1$, at an inverse temperature β:

$$H_{RTFIM} = -\sum_i \xi_i \sigma_i^z - \sum_{(ij)} J_{ij} \sigma_i^x \sigma_j^x \tag{II.41}$$

where $\sigma^{x/z}$ are the Pauli matrices, the second sum runs over all bonds (ij), and J_{ij} is the couplings on bond $()ij$. Using the Suzuki-Trotter representation with M imaginary time steps we can describe the system by the classical time trajectory of each spin.

The resolution in the Replica Symmetric case for this problem is exactly the same as for the classical method with the only difference of treating spin trajectories instead of Ising spins [240, 241]. The natural order parameter for this problem is a distribution of distributions, a very complicated object, and this resolution is too numerically costly.

At this point, the necessity of developing an approximate version of this exact mapping becomes evident. One possible approximation, called the projected cavity mapping, can be thought of as studying the properties of a spin 0 in the Bethe lattice where one of its neighbours has been deleted from the graph. Under a few assumptions, the local Hamiltonian describing the system of spin 0 and its K neighbours

is [240]:

$$H_0 = -\xi_0\sigma_0^z - \sum_{i=1}^{K}\left(\xi_i\sigma_i^z + B_i\sigma_i^x + J_{0i}\sigma_0^x\sigma_i^x\right). \tag{II.42}$$

where B_i is a variable that parametrizes the problem. This $2^{K+1}\times 2^{K+1}$ Hamiltonian can be diagonalized so as to compute the magnetisation of spin 0. This projected cavity mapping uses a single number B_i to describe the trajectory distribution and gives a self-consistent equation for the distribution of the B_i.

However, this resolution is also very costly numerically for it involves diagonalizing a $2^{K+1}\times 2^{K+1}$ matrix at each iteration step. One further approximation allowing to obtain an explicit mapping [194, 195] similar to that of the classical problem [231], is a Mean-Field approximation to compute the magnetisation m_0 from the cavity Hamiltonian (II.42). This is the cavity mean-field approximation consisting in writing the cavity Hamiltonian acting on spin 0 by

$$H_0^{\text{cav}-MF} = -\xi_0\sigma_0^z - \sigma_0^x\sum_{i=1}^{K} J_{0i}\langle\sigma_i^x\rangle. \tag{II.43}$$

And a recursion relation between the B_i field follows:

$$B_0 = \sum_{i=1}^{K} J_{0i}\frac{B_i}{\sqrt{\xi_i^2+B_i^2}}\tanh\left(\beta\sqrt{\xi_i^2+B_i^2}\right) \tag{II.44}$$

Finally, a self-consistent equation for the distribution of the B fields $P(B)$ is obtained. By solving it one has access to the order parameter for the quantum phase transition from a ferromagnetic to a paramagnetic phase [240] since in the paramagnetic phase $P(B) = \delta(B)$ and the distribution is non trivial in the ferromagnetic phase.

It is capital to notice that the cavity mean-field approach does not neglect quantum fluctuations. Therefore, an adapted version of this method to the two-dimensional case [205] of the square lattice with the same Hamiltonian enabled Lemarié *et al.* to study a Superfluid - Insulator transition and find a transition even at the Mean-Field level [30], as discussed in section 2.5 of chapter I.

To conclude, the cavity Mean-Field is a much more sophisticated and powerful method than the Mean-Field approaches used in this chapter. However, since quantum fluctuations are already present in its framework, including them by linear spin-wave theory (LSWT) is unnecessary. On the contrary, the simpler Mean-Field approaches previously developed in this chapter, which neglect quantum fluctuations, are perfectly suited for the LSWT formalism as will be shown in the next chapter.

Chapter III

Beyond Mean-Field: Semi-classical approach

Contents

In this chapter, we will present a semi-classical approach to the Superfluid - Bose glass transition for hard-core bosons in the presence of disorder on the two-dimensional square lattice. Starting from the classical Mean-Field results presented in chapter II, we will add the quantum fluctuations that were completely neglected at the Mean-Field level by means of Linear Spin-Wave Theory (LSWT) in real space. This theory is exact in the limit of infinite spin value $S \to \infty$ and it has proven very useful in the studies of diluted quantum Heisenberg antiferromagnets in different geometries such as diluted two-dimensional lattices [242, 243], the Penrose tiling [244] and two dimensional quasi-crystals [245]. It has also been used with great success in the study of hard-core bosons in two dimensions in the disorder-free case [230, 246] even if the corresponding spin XXZ problem obtained via the Matsubara-Matsuda transformation [229] (*cf.* equation (II.21) in section 2 of chapter II) gives spins with $S = \frac{1}{2}$, in the opposite limit were the theory is justified. In spite of this, Linear Spin-Wave theory for hard-core bosons in the clean case actually gives results in qualitative *and* quantitative agreement with exact QMC simulations [246] which motivates us to use it in the disordered case as well.

We will see that contrary to the Mean-Field classical techniques used in the previous chapter, this semi-classical approach does find a transition from the Superfluid state at low disorder to a Bose glass phase at strong disorder with a finite value of the critical disorder for both bimodal and box disorder distributions. We will see that the critical disorder strength in the case of a box distributed disorder is in remarkable good agreement with the critical values given by both the 2D cavity Mean-Field method [30] and exact the QMC simulations presented in chapter IV [247]. Secondly, the values of the critical exponents are then estimated at the spin-wave level, first in a simple fashion and then in a more detailed way by means of a bootstrap analysis. Finally, the properties of spin-wave excitations and finite frequency physics are explored. The presence of a mobility-edge above which excitations are localized is discussed for our non-interacting spin-wave bosonic excitations.

1 Linear spin-wave theory in real space

This section introduces the main concepts of Linear Spin-Wave Theory (LSWT) written for our hard-core bosons model in its equivalent spin-$\frac{1}{2}$ XXZ model (II.22) representation. This theory includes quantum fluctuations on top of a purely classical resolution and gives corrections to the different observables to $1/S$ order. Furthermore, it gives access to eigenvalues and eigenvectors of the Hamiltonian under consideration, enabling one to study the excitation properties as well as ground-state properties of the system. The usual steps of the LSWT calculation are the following:

1. Consider the spin operators as 3D classical vectors $\vec{S}_i$.

2. Perform a (local) rotation of the axis in order to align the spins with the quantification axis.

3. Apply the Holstein-Primakoff (HP) transformation, in its linearized version, to describe the bosonic spin-waves.

4. The terms linear in HP bosons vanish giving the exact same equations that those for the minimization of the classical MF energy.

5. Keep only the quadratic terms in HP bosons to be at the level of approximation of non-interacting HP bosons.

6. Diagonalize the resulting Hamiltonian.

7. Compute the $1/S$-corrected expectation values of physical observables.

In the following we will apply these steps to our model for the Superfluid - Bose glass transition of hard-core bosons in the 2D square lattice of size $N = L \times L$.

1.1 Linear Spin-Wave Theory for Hard-core bosons

We start from the spin-$\frac{1}{2}$ XXZ Hamiltonian (II.22) and apply the steps described above. When periodic boundary conditions are taken, we can write the spin operators in the MF approximation as classical 3D vectors of the form (II.5) with all spins in the XZ plane due to rotational invariance around the z-axis (*i.e.* $\varphi = 0$). Applying a local rotation so as to align each spin with the quantization axis we obtain the relation between the spins in the new rotated frame $\vec{S}_i'$ and the old frame spins $\vec{S}_i$:

$$\begin{cases} S_i^x = \cos\theta_i S_i'^x + \sin\theta_i S_i'^z \\ S_i^y = S_i'^y \\ S_i^z = -\sin\theta_i S_i'^x + \cos\theta_i S_i'^z. \end{cases} \tag{III.1}$$

Inserting this into the Hamiltonian (II.22) yields:

$$\begin{aligned} H = &-\sum_i \frac{\mu_i}{2} + \sum_i \mu_i \sin\theta_i S_i'^x - \sum_i \mu_i \cos\theta_i S_i'^z \\ &+ \sum_{\langle i,j\rangle} \Big\{ -2t\cos\theta_i\cos\theta_j S_i'^x S_j'^x - 2t\sin\theta_i\sin\theta_j S_i'^z S_j'^z - 2t S_i'^y S_j'^y \\ &\qquad -2t\cos\theta_i\sin\theta_j S_i'^x S_j'^z - 2t\sin\theta_i\cos\theta_j S_i'^z S_j'^x \Big\}. \end{aligned} \tag{III.2}$$

where $\langle i,j\rangle$ denotes a summation over pairs of nearest-neighbour sites i and j. Next, we have to apply the Holstein-Primakoff transformation [248] for our spins $S = \frac{1}{2}$ in its linearized version so as to include quantum fluctuations around the classical MF solution:

$$\forall i,\ \begin{cases} S_i'^{+} = \sqrt{2S}\left(1 - \dfrac{a_i^\dagger a_i}{2S}\right)^{1/2} a_i \approx a_i \\ S_i'^{-} = \sqrt{2S} a_i^\dagger \left(1 - \dfrac{a_i^\dagger a_i}{2S}\right)^{1/2} \approx a_i^\dagger \\ S_i'^{z} = S - a_i^\dagger a_i = \dfrac{1}{2} - a_i^\dagger a_i \end{cases} \tag{III.3}$$

where the Holstein-Primakoff operators a_i and $a_i^\dagger$ follow bosonic commutation relations. Replacing the spins in the rotated frame by their expressions in terms of Holstein-Primakoff (HP) bosons in the Hamiltonian (III.2) leads, after a few steps where terms of third order and higher in HP bosons have been neglected, to:

$$\begin{aligned} H = &- \sum_i \frac{\mu_i}{2} - \sum_i \frac{\mu_i}{2}\cos\theta_i - \frac{t}{2}\sum_{\langle i,j\rangle} \sin\theta_i \sin\theta_j \\ &+ \sum_i \frac{\mu_i}{2}\cos\theta_i a_i^\dagger a_i + t\sum_{\langle i,j\rangle} \sin\theta_i\sin\theta_j (a_i^\dagger a_i + a_j^\dagger a_j) \\ &+ \sum_{\langle i,j\rangle} \left\{ -\frac{t}{2}(1+\cos\theta_i\cos\theta_j)(a_i^\dagger a_j + a_i a_j^\dagger) + \frac{t}{2}(1-\cos\theta_i\cos\theta_j)(a_i a_j + a_i^\dagger a_j^\dagger) \right\} \\ &+ \sum_i \frac{\mu_i}{2}\sin\theta_i (a_i + a_i^\dagger) - t\sum_{\langle i,j\rangle} \cos\theta_i \sin\theta_j (a_i + a_i^\dagger). \end{aligned} \tag{III.4}$$

The following step is to take out the terms linear in HP bosons which vanish giving the set of N equations:

$$-t\cos\theta_i \sum_{\langle j\rangle_i} \sin\theta_j + \mu_i \sin\theta_i = 0 \tag{III.5}$$

with $\sum_{\langle j\rangle_i}$ the sum over sites j nearest-neighbours of site i. These are the same equations for minimizing the classical mean-field energy (II.24). Finally, the systems Hamiltonian can be written in the form:

$$H = H_{\text{class}} + H^{(2)}$$

where H_{class} is the Mean-Field Hamiltonian (II.23) and $H^{(2)}$ includes only the terms quadratic in the Holstein-Primakoff operators:

$$H_2 = \sum_{\langle i,j\rangle} \{ t_{ij}(a_i a_j^\dagger + a_i^\dagger a_j) + \bar{t}_{ij}(a_i a_j + a_i^\dagger a_j^\dagger)\} - \sum_i \epsilon_i n_i, \tag{III.6}$$

and we have defined the coefficients:

$$\begin{cases} t_{ij} = -\dfrac{t}{2}(1+\cos\theta_i\cos\theta_j) \\ \bar{t}_{ij} = \dfrac{t}{2}(1-\cos\theta_i\cos\theta_j) \\ \epsilon_i = -\mu_i\cos\theta_i - t\sin\theta_i(\sum\limits_{\langle j\rangle_i}\sin\theta_j). \end{cases} \tag{III.7}$$

The classical Hamiltonian H_{class} is independent from HP bosonic operators, hence it is diagonal in the HP basis. However, the quadratic Hamiltonian $H^{(2)}$ has an off-diagonal part depending on the coefficients t_{ij} and $\bar{t}_{ij}$. It is then necessary to diagonalize it in order to obtain the energies and associated eigenvectors of the spin-wave excitations. This next step will be discussed in the next section.

1.2 Real space diagonalization

We are interested in the disordered XXZ Hamiltonian, with disorder in the chemical potential *i.e.* in the local transverse magnetic field for spins with $S = \frac{1}{2}$. The presence of disorder breaks the translational symmetry, therefore taking the Fourier transform to be in the basis of wave-vectors $\vec{k}$ is not a good strategy since the k are not good quantum numbers and the HP Hamiltonian $H^{(2)}$ (III.6) will not be diagonalized after a Bogolyubov transformation from the $\vec{k}$ basis, like in the clean case [230, 246]. Instead, we will have to perform the diagonalization in real space. We will do so by following the real space diagonalization procedure [242–245] now described.

Let X be the *column* vector $X = (a_1, a_2, ..., a_N, a_1^\dagger, ..., a_N^\dagger)$. The HP non-diagonal part of the Hamiltonian $H^{(2)}$ can be written as:

$$H^{(2)} = X^\dagger H_2 X + \sum_i \frac{\epsilon_i}{2} \tag{III.8}$$

Where H_2 is a $2N \times 2N$ sparse matrix with eight non-zero elements per line, directly given by $t_{ij}/2$, $\bar{t}_{ij}/2$ and $\epsilon_i/2$. For each site $i \in [1; N]$ with nearest-neighbour sites j, we have:

$$\begin{aligned} H_2(i,i) = H_2(i+N, i+N) &= -\epsilon_i/2 \\ H_2(i,j) = H_2(j,i) &= t_{ij}/2 \\ H_2(i,j+N) = H_2(j+N,i) &= \bar{t}_{ij}/2 \\ H_2(i+N,j) &= \bar{t}_{ij}/2 \\ H_2(i+N,j+N) &= t_{ij}/2. \end{aligned} \tag{III.9}$$

We now need to diagonalize H_2. The procedure consists in diagonalizing ΛH_2 where Λ is a $2N \times 2N$ diagonal matrix with 1 in the first N elements and -1 in

the last N. Let $\hat{S}$ be the transformation from the $\{a_i\}$ basis to the $\{\alpha_i\}$ basis where both ΛH_2 and H_2 are diagonal. Enforcing bosonic commutation relations for the $\{\alpha_i\}$ yields:

$$\hat{S}\Lambda\hat{S}^\dagger = \Lambda \tag{III.10}$$

Since H_2 is diagonalized by $\hat{S}$, we also have, with Ω a diagonal matrix obtained by diagonalizing ΛH_2 with the subroutine DGEEV of the LAPACK© library [249], that:

$$\hat{S}^\dagger H_2 S = \Omega. \tag{III.11}$$

Combining these relations we finally get:

$$\Lambda H_2 = \hat{S}\Lambda\Omega\hat{S}^{-1}. \tag{III.12}$$

On the other hand, there is also the relation

$$(X')^\dagger\,\Omega(X') = 2\sum_p \Omega_p \alpha_p^\dagger \alpha_p + \sum_p \Omega_p \tag{III.13}$$

where Ω_p are the eigenvalues of H_2, *i.e.* the elements of the diagonal $2N \times 2N$ matrix Ω. It is worth noting that the Ω_p come by pairs such as there are only N different eigenvalues (corresponding to the energies of excitations of the system) and in matrix Ω they are present as $\pm\Omega_p$. In the end, the hamiltonian is:

$$H = H_{\text{class}} + 2\sum_{p=1}^{N} \Omega_p(\alpha_p^\dagger\alpha_p + \frac{1}{2}) + \sum_i \frac{\epsilon_i}{2} \tag{III.14}$$

with only the N positive Ω_p entering the sum.

The ground state expectation value corresponds to the vacuum of Bogoliubov quasi-particles $\langle\alpha_p^\dagger\alpha_p\rangle = 0$:

$$E^{1/S} = E_0 + \sum_p \Omega_p + \sum_i \frac{\epsilon_i}{2} \tag{III.15}$$

which is indeed lower than E_0 (ground-state expectation value of H_{class}) because $\sum_p \Omega_p + \sum_i \epsilon_i/2 < 0$, which we have checked numerically in every simulation here forth presented. This is the linear spin wave ground-state energy with corrections to order $1/S$.

2 Derivation of observables

Now that the principles of LSWT have been exposed and the way to compute the corrected ground-state energy is obtained, we have to concentrate in deriving the estimates of other physical observables of interest in the LSWT framework. We will focus on the order parameter for the Superfluid - Bose glass transition, the BEC density ρ_0 and the superfluid density ρ_{sf} corrected to order $1/S$.

2.1 Superfluid density

The way to compute the superfluid density was already discussed in section 1 of chapter II. In a nutshell, the superfluid density is proportional to the helicity modulus Υ_{sf} of the system when a twist Φ is applied to the periodic boundary conditions [177], in our case:

$$\rho_{\text{sf}} = \frac{m^*}{\hbar}\Upsilon_{\text{sf}} = \frac{1}{2t}\Upsilon_{\text{sf}} = \frac{1}{2t}\frac{\partial^2 E(\Phi)}{\partial \Phi^2} = \frac{1}{t}\frac{E(\Phi) - E(\Phi = 0)}{\Phi^2}. \tag{III.16}$$

Notice the absence of the factor 3 in this U(1) symmetric case with respect to the Heisenberg case, which is SU(2) symmetric, given in equation (II.4). We have once again replaced the derivative by a numerical derivative taking advantage of the fact that $\partial E(\Phi)/\partial\Phi = 0$. The numerical derivative is then computed using a small value of the twist $\Phi = 10^{-2}$. Such a definition works both in the classical case, where we use the classical ground-state expectation values with and without a twist, and in the LSWT case: we just need to take the $1/S$ corrected energies with and without the twist. In the absence of a twist the $1/S$ corrected ground-state energy was already derived in equation (III.15). We now need to compute the corrected energy in the presence of the twist using the steps described in section 1. In this case the rotation in order to align the classical spins (II.5) with the quantization axis is:

$$\begin{cases} S_i^x = \cos\theta_i \cos\varphi_i S_i'^x - \sin\varphi_i S_i'^y + \sin\theta_i \cos\varphi_i S_i'^z \\ S_i^y = \cos\theta_i \sin\varphi_i S_i'^x + \cos\varphi_i S_i'^y + \sin\theta_i \sin\varphi_i S_i'^z \\ S_i^z = -\sin\theta_i S_i'^x + \cos\theta_i S_i'^z \end{cases} \tag{III.17}$$

Plugging these expressions in the Hamiltonian in the presence of a the twist Φ (II.26) leads to:

$$\begin{aligned} H(\Phi) = &-\sum_i \frac{\mu_i}{2} + \sum_i \mu_i \sin\theta_i S_i'^x - \sum_i \mu_i \cos\theta_i S_i'^z \\ &+ \sum_{\langle i,j\rangle} \Big\{ -2t\cos\theta_i\cos\theta_j\cos(\varphi_i-\varphi_j) S_i'^x S_j'^x - 2t\cos(\varphi_i-\varphi_j) S_i'^y S_j'^y \\ &- 2t\sin\theta_i\sin\theta_j\cos(\varphi_i-\varphi_j) S_i'^z S_j'^z - 2t\sin\theta_i\sin(\varphi_i-\varphi_j) S_i'^z S_j'^y \\ &- 2t\cos\theta_i\sin(\varphi_i-\varphi_j) S_i'^x S_j'^y + 2t\cos\theta_j\sin(\varphi_i-\varphi_j) S_i'^y S_j'^x \\ &+ 2t\sin\theta_j\sin(\varphi_i-\varphi_j) S_i'^y S_j'^z - 2t\cos\theta_i\sin\theta_j\cos(\varphi_i-\varphi_j) S_i'^x S_j'^z \\ &-2t\sin\theta_i\cos\theta_j\cos(\varphi_i-\varphi_j) S_i'^z S_j'^x \Big\}. \end{aligned} \tag{III.18}$$

In the previous equation, the twist angle Φ does not appear explicitly, but is implicitly present since for a site on the right boundary (*i.e.* on the Lth column) i_L, its right neighbour is the virtual site i_{L+1} which has $\varphi_{i_{L+1}} = \varphi_{i_1} + \Phi$, where site i_1 is the site on the left boundary of the system in the same line as site i_L. Therefore,

$\varphi_L - \varphi_{i_{L+1}} = \varphi_L - \varphi_1 - \Phi$ due to the twisted boundary conditions. Similarly, for a site on the left boundary (*i.e.* on the first column) its left neighbour is the virtual site i_0 that has $\varphi_{i_0} = \varphi_{i_L} - \Phi$, and hence $\varphi_{i_1} - \varphi_{i_0} = \varphi_{i_1} - \varphi_{i_L} + \Phi$.

As usual, we apply the Holstein-Primakoff transformation (III.3), the linear terms in the Holstein-Primakoff bosonic operators vanish and we get the twisted boundary conditions Hamiltonian:

$$H = H_{\text{class}}(\Phi) + \sum_{\langle i,j \rangle} \{t_{ij}(\Phi)(a_i a_j^\dagger + h.c.) + \bar{t}_{ij}(\Phi)(a_i a_j + h.c.)\} - \sum_i \epsilon_i(\Phi) n_i \quad \text{(III.19)}$$

where $H_{\text{class}}(\Phi)$ is the classical Hamiltonian in the presence of a twist (II.26).

This is formally the same as the non-twisted spin-wave Hamiltonian (III.6) but with different coefficients implicitly depending on the global twist angle Φ as is the case for the Hamiltonian (III.18):

$$\begin{cases} t_{ij}(\Phi) = -\dfrac{t}{2}\cos(\varphi_i - \varphi_j)(1 + \cos\theta_i \cos\theta_j) + \\ \bar{t}_{ij}(\Phi) = \dfrac{t}{2}\cos(\varphi_i - \varphi_j)(1 - \cos\theta_i \cos\theta_j) \\ \epsilon_i(\Phi) = -\mu_i \cos\theta_i - t \sin\theta_i (\sum\limits_{\langle j \rangle_i} \sin\theta_j \cos(\varphi_i - \varphi_j)). \end{cases} \quad \text{(III.20)}$$

One should notice that putting $\Phi = 0$ in these expressions (*i.e.* $\forall i,\ \varphi_i = 0$) we get back the same coefficients that for the periodic boundary conditions case (III.7). Since it is formally the same, the same real space diagonalization scheme of section 1.2 can be applied and finally we get:

$$E^{1/S}(\Phi) = E_0(\Phi) + \sum_p \Omega_p(\Phi) + \sum_i \frac{\epsilon_i(\Phi)}{2}. \quad \text{(III.21)}$$

Finally we can compute the superfluid density corrected to order $1/S$ using equations (III.16), (III.15) and (III.21):

$$\rho_{sf}^{1/S} = \rho_{sf}^0 + \frac{1}{\Phi^2}\sum_p (\Omega_p(\Phi) - \Omega_p(\Phi = 0)) + \frac{1}{\Phi^2}\sum_i \frac{\epsilon_i(\Phi) - \epsilon_i(\Phi = 0)}{2}. \quad \text{(III.22)}$$

with ρ_{sf}^0 the classical Mean-field value of the stiffness (*i.e.* the stiffness computed with corrections to "0^{th}" order).

2.2 Bose-Einstein condensate density

The true order parameter for the transition is the XY order parameter in spin language or, equivalently, the Bose-Einstein condensate density. The appropriate

way to compute the $1/S$ corrections to such observables was introduced by Coletta *et al.* [246]. Basically, one can either evaluate the expectation value of the BEC density in the $1/S$-corrected ground-state wave-function which is very difficult to compute in our disordered case, or one can add a small symmetry-breaking term to the Hamiltonian which couples to the XY order parameter and compute the $1/S$-corrected energy in the presence of the field and take the derivative with respect to the field in the limit where it vanishes.

For the condensate density, one needs to add the symmetry breaking term coupled to the XY order which, when periodic boundary conditions are taken ($S_i^y = 0$), it takes the simple form $-\Gamma \sum_i S_i^x$. This gives the Hamiltonian:

$$H = -\frac{1}{2}\sum_i \mu_i - 2t \sum_{\langle i,j \rangle} S_i^x S_j^x - \sum_i \mu_i S_i^z - \Gamma \sum_i S_i^x \tag{III.23}$$

and hence:

$$m_{xy} = \frac{1}{N}\sum_i \langle S_i^x \rangle = -\frac{1}{N}\frac{\partial \langle H \rangle}{\partial \Gamma}\bigg|_{\Gamma=0} = -\frac{\langle H(\Gamma) \rangle - \langle H(\Gamma = 0) \rangle}{N\Gamma}. \tag{III.24}$$

Applying the steps of LSWT described in section 1, we can compute the $1/S$-corrected ground-state energy in the presence of the small field Γ. The calculation is very similar to the ones discussed before for the superfluid density in the presence of a twist. The final result takes the similar form:

$$H = H_{\text{class}}(\Gamma) + \sum_{\langle i,j \rangle} \{t_{ij}(\Gamma)(a_i a_j^\dagger + h.c.) + \bar{t}_{ij}(\Gamma)(a_i a_j + h.c.)\} - \sum_i \epsilon_i(\Gamma) \tag{III.25}$$

were we have defined the coefficients:

$$\begin{cases} t_{ij}(\Gamma) = -\dfrac{t}{2}(1 + \cos\theta_i \cos\theta_j) \\ \bar{t}_{ij}(\Gamma) = \dfrac{t}{2}(1 - \cos\theta_i \cos\theta_j) \\ \epsilon_i(\Gamma) = -\mu_i \cos\theta_i - t \sin\theta_i (\sum\limits_{\langle j \rangle_i} \sin\theta_j) - \Gamma \sin\theta_i. \end{cases} \tag{III.26}$$

Once again, $H_{\text{class}}(\Gamma)$ is the classical Mean-Field Hamiltonian in the presence of the field Γ which can be minimzed with any of the two methods described in section 1 of chapter II so as to obtain its ground-state expectation value $E_0(\Gamma)$. The total Hamiltonian (III.25) is formally the same as in the previous cases and can be diagonalized with the real space diagonalization method described in section 1.2, which yields:

$$E^{1/S}(\Gamma) = E_0(\Gamma) + \sum_p \Omega_p(\Gamma) + \sum_i \frac{\epsilon_i(\Gamma)}{2}. \tag{III.27}$$

The spin-wave corrected m_{xy} can now be computed using equations (III.15) and (III.27):

$$\begin{aligned} m_{xy}^{(1/S)} =& m_{xy}^{(0)} + \frac{1}{N\Gamma}\sum_p(\Omega_p(\Gamma) - \Omega_p(\Gamma=0)) + \frac{1}{N\Gamma}\sum_i \frac{\epsilon_i(\Gamma) - \epsilon_i(\Gamma=0)}{2} \\ =& m_{xy}^{(0)} + \delta m_{xy}^{(1/S)}. \end{aligned} \tag{III.28}$$

The corrected condensed density to order $1/S$ is then:

$$\rho_0^{(1/S)} = (\lim_{L\to\infty} m_{xy}^{1/S})^2. \tag{III.29}$$

One should be careful when taking the square of $\langle m_{xy}\rangle^{1/S}$ since this brings about the inclusion of correction terms of order higher than $1/S$. Indeed, taking the square means we are including a term $\left(\delta m_{xy}^{(1/S)}\right)^2$ which is actually of order $1/S^2$. We are thus over-estimating the corrected BEC density by doing so. Therefore, the numerical values of the condensate density are not correct to order $1/S$ but we are properly estimating the true order parameter for XY order, and the transverse magnetization $m_{xy}^{(1/S)}$ and ρ_0 defined as in equation (III.29) vanish at the same point.

3 Ground-state critical properties

Now that the generalities of the LSWT and how to compute the expectation values to order $1/S$ in its framework have been presented, we focus on the results obtained for the two disorder distributions treated in with Mean-Field theory in chapter II, namely the bimodal distribution and the box distribution. We will see that quantum fluctuations are indeed able to capture the Bose glass physics of the problem in both cases.

3.1 Bimodal disorder

We have applied the LSWT scheme and computed the $1/S$-corrected superfluid and Bose condensed densities for systems of sizes ranging from $N = 8\times 8$ to $N = 32\times 32$ and performed averages over several hundreds of disordered samples for each system size and disorder strength W, in the case of a bimodal disorder distribution of the on-site chemical potential $\mu_i = \epsilon_i W$ with $\epsilon_i = \pm 1$ with probability $1/2$. For this case, the Holstein-Primakoff Hamiltonian describing the spin-wave quantum fluctuations (III.6) takes the simplified form:

$$H_2 = -\frac{1}{2}\sum_{\langle ij\rangle}\Big[(t_{ij}a_i^\dagger a_j^\dagger + \bar{t}_{ij}a_i^\dagger a_j^\dagger) + \text{h.c.}\Big] + \nu\sum_i n_i, \tag{III.30}$$

with the coefficients

$$\begin{cases} t_{ij} = t[1+\epsilon_i\epsilon_j(\bar{\nu}/4t)^2] \\ \bar{t}_{ij} = t[\epsilon_i\epsilon_j(\bar{\nu}/4t)^2 - 1] \\ \nu = \max(W, 4t) \\ \bar{\nu} = \min(W, 4t). \end{cases} \tag{III.31}$$

The diagonalization of this Hamiltonian yields:

$$H_2 = 2\sum_{p=1}^{N}\Big[\Omega_p(\alpha_p^\dagger\alpha_p + \frac{1}{2}) - \frac{\nu}{4}\Big]. \tag{III.32}$$

The ground-state energy corrected to order $1/S$ corresponds by the vacuum of Bogolyubov quasi-particles $\langle\alpha_p^\dagger\alpha_p\rangle = 0$ and hence:

$$E^{(1/S)} = E^0 + \sum_p \Omega_p - \frac{N\nu}{2}. \tag{III.33}$$

The extrapolations to the thermodynamic limit $L \to \infty$ of the spin-wave corrected superfluid (blue squares) and Bose condensed (green diamonds) densities are plotted against disorder strength in figure III.1 along with their Mean-Field (MF) estimates obtained in chapter II (black small circles) and the spin-wave gap in the spectrum (red circles). The Bose-Einstein condensate is depleted by quantum fluctuations with respect to its MF value by a factor surrounding 25% in the clean case $W = 0$, in agreement with previous estimations [230, 246]. The addition of disorder further reduces the BEC density which vanishes at a disorder strength $W_0 < 4t$ which will be carefully determined further along. The superfluid density is enhanced by quantum fluctuations at weak disorder and our numerical estimate for the clean case is in agreement with the analytical previous results [230, 246]. It is monotonically reduced by disorder and vanishes at a disorder strength $W_{\rm sf} < 4t$. The spin-wave gap Δ is exactly zero for all disorder strengths inside the band-width $W < 4t$ and opens up exactly at $W = 4t$. This means that a gapless (compressible) insulating phase intervenes between the superfluid and the insulating phases for disorder strengths $W_{\rm sf} < W < 4t$, *i.e.* a Bose glass phase is stabilized by quantum fluctuations at order $1/S$. The spin-wave gap will be studied in more detail in section 5.1.

Let us now determine the vanishing points of the spin-wave corrected superfluid and BEC densities. In order to do so, we first use the finite-size scaling theory described in the chapter I section 2.3.2. This is illustrated in figure III.2 where we have plotted in panel (a) the crossing of the disorder averaged corrected superfluid density curves as a function of disorder strength for different system sizes when they are multiplied by L^z with z the dynamical exponent. The best crossings are obtained for $z = 2.0(1)$ in agreement with the equality $z = d$ [6]. Panel (b) of figure III.2 shows

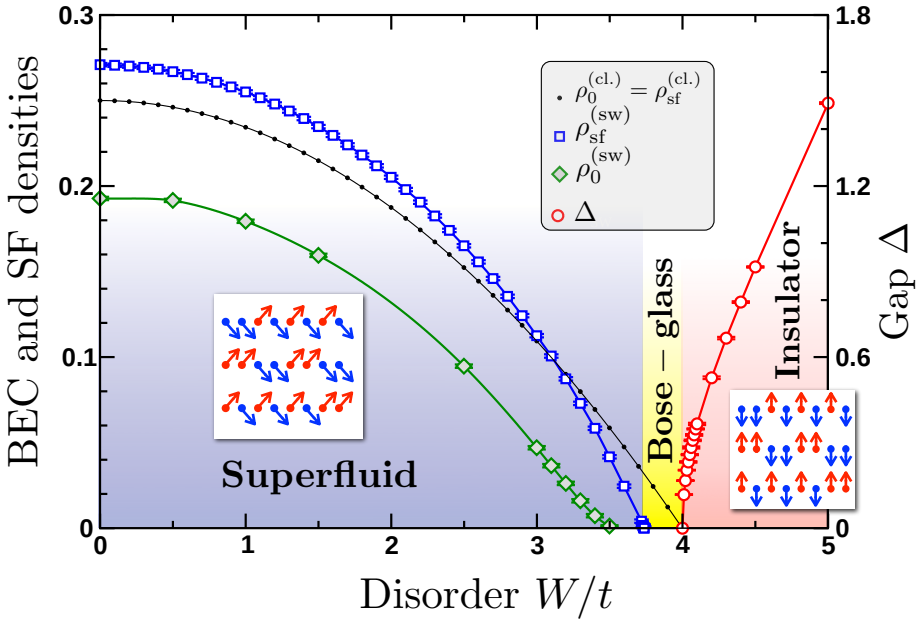

Figure III.1: *Evolution of the thermodynamic limit extrapolations of the Superfluid stiffness ρ_{sf}, Bose-Einstein condensate density ρ_0 and the gap of the excitation spectrum Δ with disorder strength W/t. The classical densities (•) are equal and vanish at the edge of the band-width $W = 4t$. The spin-wave corrected quantities $\rho_{sf}^{(sw)}$ (□) and $\rho_0^{(sw)}$ (◇) vanish at different points $W_0 < W_{sf} < 4t$, leaving a finite window for an intervening gapless Bose glass before the gapped insulator present for $W > 4t$. Insets show superfluid and insulating phases in the pseudo-spin representation. Disorder average was performed over several hundreds of disordered samples. The green line is a guide to the eyes.*

the disorder averaged spin-wave estimate of the transverse magnetization $m_{xy} = \langle S^x \rangle$ plotted against the inverse system size $1/N$ for different disorder strengths. When the quantum corrections become bigger than the classical value yielding a negative magnetization we interpret this as a vanishing real magnetization. The extrapolation to the thermodynamic limit $N \to \infty$ becomes negative for a value of disorder strength $W_0/t = 3.55(5)$, hence XY order disappears at this disorder strength.

At the $1/S$ level, we find a small window of disorder strengths $W_0 < W < W_{sf}$ for which a condensate-free superfluid phase is stable. Although such a phase has been shown to be possible in frustrated systems like $BaCuSi_2O_6$ [250–252], it is relevant to ask whether this window survives upon the inclusion of higher order quantum fluctuations. Anyhow, there is a small finite window of disorder $W_{sf} < W < 4t$ where both densities vanish and the system is compressible, *i.e.* the system is in the Bose glass phase. The inclusion of quantum fluctuations allows for the capture of the Bose glass physics that the Mean-Field treatment failed to capture.

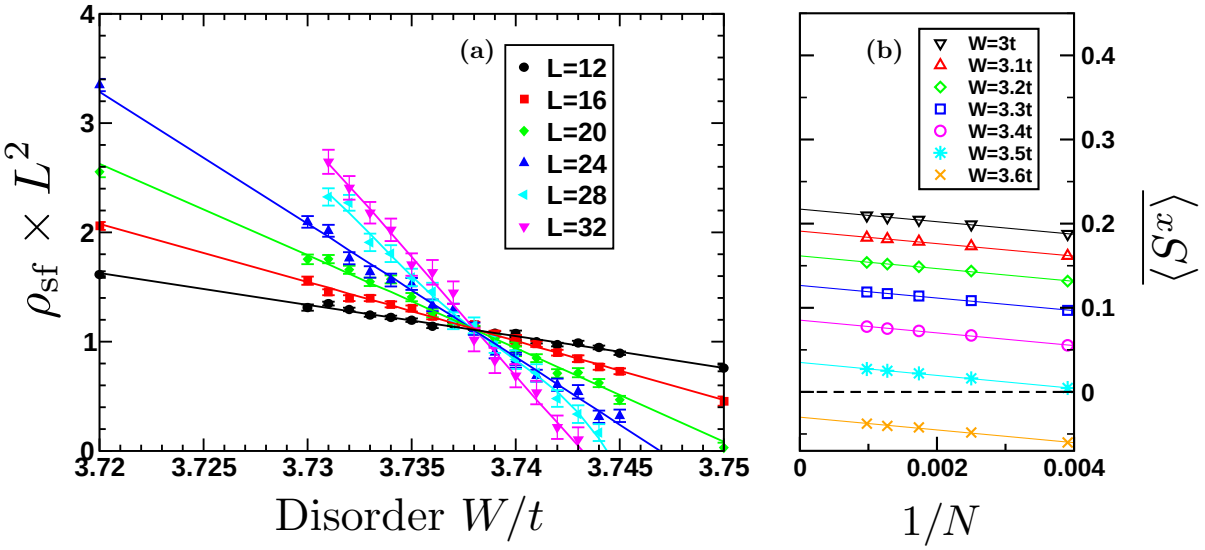

Figure III.2: *Panel a: Crossing of the curves of* $\rho_{sf} \times L^z$ *for system sizes* $L = 12$ *to* $L = 32$. *The dynamical exponent used to find a very good crossing is* $z = 2.0(1)$ *and the crossing point is estimated to* $W_{sf}/t = 3.738(1)$. *Full lines are polynomial fits of degree 2. Panel b: Finite-size scaling of the spin-wave transverse magnetization* $m_{xy} = \overline{\langle S^x \rangle}$ *for different disorder strengths. Negative infinite size extrapolations are interpreted as zero. The XY order parameter vanishes at a disorder strength* $W_0/t = 3.55(5)$.

3.2 Box distributed disorder

We now present in this section the results obtained by applying the LSWT to the system with box distributed disorder on the chemical potential $\mu_i \in [-W; W]$. Unlike the case of the bimodal disorder distribution, in this case no simplification or analytical solution are available. Therefore the relevant equations are exactly those presented in section 1. However, as discussed in section 2.2.1, it is convenient to treat the computation of the superfluid density not by applying a global twist Φ to the boundary conditions but equivalently keeping periodic boundary conditions and having a complex hopping along the direction the twist would have been applied. The starting point for the LSWT is taken to be the Hamiltonian (II.32). The computation steps of LSWT already described lead to the Hamiltonian:

$$H = H_{\text{class}}(\Phi) - \sum_i \epsilon_i(\Phi) n_i + \sum_i \{(t_{ii+\hat{y}}(\Phi) a_i^\dagger a_{i+\hat{y}} + h.c.) + (\bar{t}_{ii+\hat{y}}(\Phi) a_i a_j + h.c.)\} + \sum_i \{(t_{ii+\hat{x}}(\Phi) a_i^\dagger a_{i+\hat{x}} + h.c.) + (\bar{t}_{ii+\hat{x}}(\Phi) a_i a_{i+\hat{x}} + h.c.)\} \tag{III.34}$$

where $H_{\text{class}}(\Phi)$ is the classical ground-state expectation value of the energy in the presence of the complex hoppings (II.34) and we have defined the *complex* coefficients:

$$\begin{cases} t_{ii+\hat{y}}(\Phi) = -\frac{t}{2}\left[\cos(\varphi_i-\varphi_{i+\hat{y}})(1+\cos\theta_i\cos\theta_{i+\hat{y}})+i\sin(\varphi_i-\varphi_{i+\hat{y}})(\cos\theta_i+\cos\theta_{i+\hat{y}})\right] \\ t_{ii-\hat{y}}(\Phi) = -\frac{t}{2}\left[\cos(\varphi_{i-\hat{y}}-\varphi_i)(1+\cos\theta_i\cos\theta_{i-\hat{y}})-i\sin(\varphi_{i-\hat{y}}-\varphi_i)(\cos\theta_i+\cos\theta_{i-\hat{y}})\right] \\ \bar{t}_{ii+\hat{y}}(\Phi) = \frac{t}{2}\left[\cos(\varphi_i-\varphi_{i+\hat{y}})(1-\cos\theta_i\cos\theta_{i+\hat{y}})+i\sin(\varphi_i-\varphi_{i+\hat{y}})(\cos\theta_i-\cos\theta_{i+\hat{y}})\right] \\ \bar{t}_{ii-\hat{y}}(\Phi) = \frac{t}{2}\left[\cos(\varphi_{i-\hat{y}}-\varphi_i)(1-\cos\theta_i\cos\theta_{i-\hat{y}})+i\sin(\varphi_{i-\hat{y}}-\varphi_i)(\cos\theta_{i-\hat{y}}-\cos\theta_i)\right] \\ \epsilon_i(\Phi) = -\mu_i\cos\theta_i - t\sin\theta_i\left(\sum_{\langle j\rangle y}\sin\theta_j\cos(\varphi_i-\varphi_j)+\right. \\ \qquad\left.\sin\theta_{i+\hat{x}}\cos(\frac{\Phi}{L}-(\varphi_i-\varphi_{i+\hat{x}}))+\sin\theta_{i-\hat{x}}\cos(\frac{\Phi}{L}-(\varphi_{i-\hat{x}}-\varphi_i))\right), \end{cases} \tag{III.35}$$

and:

$$\begin{cases} t_{ii+\hat{x}}(\Phi) = -\frac{t}{2}\left[\cos(\frac{\Phi}{L}-(\varphi_i-\varphi_{i+\hat{x}}))(1+\cos\theta_i\cos\theta_{i+\hat{x}})\right. \\ \qquad\left.-i\sin(\frac{\Phi}{L}-(\varphi_i-\varphi_{i+\hat{x}}))(\cos\theta_i+\cos\theta_{i+\hat{x}})\right] \\ t_{ii-\hat{x}}(\Phi) = -\frac{t}{2}\left[\cos(\frac{\Phi}{L}-(\varphi_{i-\hat{x}}-\varphi_i))(1+\cos\theta_i\cos\theta_{i-\hat{x}})\right. \\ \qquad\left.+i\sin(\frac{\Phi}{L}-(\varphi_{i-\hat{x}}-\varphi_i))(\cos\theta_i+\cos\theta_{i-\hat{x}})\right] \\ \bar{t}_{ii+\hat{x}}(\Phi) = \frac{t}{2}\left[\cos(\frac{\Phi}{L}-(\varphi_i-\varphi_{i+\hat{x}}))(1-\cos\theta_i\cos\theta_{i+\hat{x}})\right. \\ \qquad\left.-i\sin(\frac{\Phi}{L}-(\varphi_i-\varphi_{i+\hat{x}}))(\cos\theta_i-\cos\theta_{i+\hat{x}})\right] \\ \bar{t}_{ii-\hat{x}}(\Phi) = \frac{t}{2}\left[\cos(\frac{\Phi}{L}-(\varphi_{i-\hat{x}}-\varphi_i))(1-\cos\theta_i\cos\theta_{i-\hat{x}})\right. \\ \qquad\left.-i\sin(\frac{\Phi}{L}-(\varphi_{i-\hat{x}}-\varphi_i))(\cos\theta_{i-\hat{x}}-\cos\theta_i)\right]. \end{cases} \tag{III.36}$$

This *complex* Hamiltonian is formally the same as all the Holstein-Primakoff Hamiltonians encountered in this thesis work. It can be numerically diagonalized by the same procedure described in section 1.2 with similar results, with the only difference that since it has complex coefficients we have to use the subroutine ZGEEV of the Lapack© library [249].

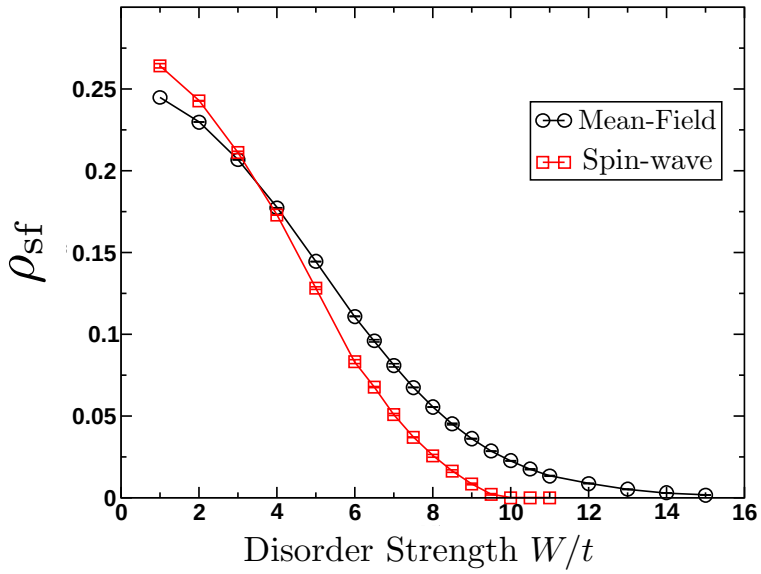

Figure III.3: *Evolution of the superfluid density ρ_{sf} extrapolated to the thermodynamic limit $N \to \infty$ against disorder strength for the box disorder distribution $\mu_i \in [-W;W]$. The black circles are the Mean-Field classical results which only vanish in the limit of infinite disorder $W \to \infty$. The red squares are the spin-wave corrected estimates to order $1/S$ which vanish for a finite critical disorder strength $W_c \approx 10t$.*

We performed simulations for square lattices of sizes ranging from $N = 8 \times 8$ to $N = 64 \times 64$ and several hundreds of disordered samples were used for disorder averaging. The results extrapolated to the thermodynamic limit $N \to \infty$ obtained by Mean-Field theory along with the $1/S$ corrected ones are shown in figure III.3. While the MF result (black circles) only vanishes for infinite disorder strength $W \to \infty$ (*cf.* figure II.4 in section 2.2.2 of chapter II) the spin-wave corrected to order $1/S$ stiffness (red squares) is enhanced with respect to the classical value at low disorders. Quantum fluctuations and disorder start to cooperate reducing the superfluid density which vanishes at a finite critical disorder strength $W_c \approx 10t$. The $1/S$-corrected superfluid density remains zero for all higher disorder strengths $W > W_c$, indicating the presence of a Bose glass phase at high disorders.

We determine more precisely the value of the critical disorder W_c by performing further simulations at disorder values very close to $W = 10t$ by steps of $0.05t$. The results are illustrated in panel *a*) of figure III.4 as the value of the spin-wave corrected stiffness $\rho_{\rm sf}$ *vs.* inverse linear system size $1/L$ for the various disorder strengths in log-log scale. For the range of system sizes considered (again up to $L = 64$ for disorders closest to $W = 10t$ and up to $L = 48$ for the others) the data for $W = 10t$ are well described by a power-law fit of the form $\rho_{\rm sf} \sim L^{-z}$ (following the finite-size scaling at criticality described in section 2.3.2 of the chapter I) with a dynamical exponent

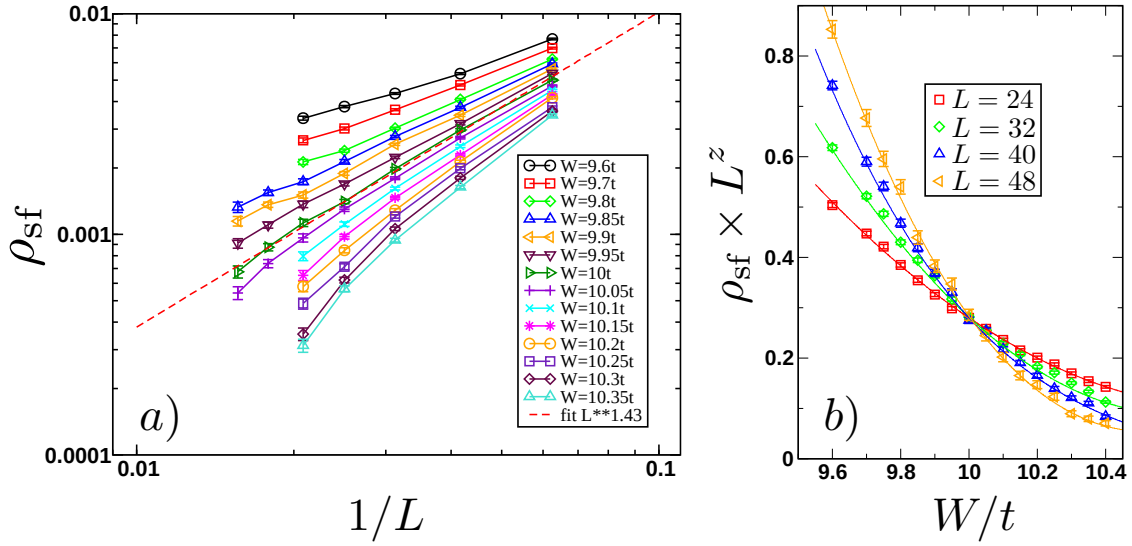

Figure III.4: *Panel a: Spin-wave corrected superfluid density ρ_{sf} vs. inverse system size for different disorder strengths. The red dashed line is a power-law fit to the form $\rho_{sf} \sim L^{-z}$ with $z = 1.43$ describing the data at $W = 10t$. Data for other disorder strengths seem to follow a similar scaling for small system sizes but clearly deviate from it as bigger sizes are included, except for $W/t = 9.95$ and $W/t = 10.05$. Panel b: Crossing of the curves of $\rho_{sf} \times L^z$ for system sizes from $L = 24$ to $L = 48$. The dynamical exponent used to find a very good crossing is $z = 1.43(1)$ and the crossing point is estimated to $W_c/t = 10.00(5)$. Full lines are polynomial fits of third degree.*

$z = 1.43(1)$, while the curves for $W = 9.95t$ and $W = 10.05t$ seem to deviate at large sizes from the power-law behaviour. Testing this value of the dynamical exponent by plotting the curves of $\rho_{\rm sf} \times L^z$ using $z = 1.43$ again disorder strength for $L = 24$, 32, 40 and 48 in panel *b*) of figure III.4 yields a pretty convincing crossing at $W = 10t$ thus confirming the estimate for the dynamical exponent. Summing up, we find for the box distributed disorder that a Bose glass phase is stabilised by the quantum corrections to order $1/S$. The phase transition takes place at a critical disorder of $W_c/t = 10.00(5)$ and a dynamical exponent $z = 1.43(1)$ governs it.

As a matter of fact, the estimated critical disorder at the spin-wave level is in fair numerical agreement with the corresponding value found by QMC simulations in chapter IV, for which $W_c^{\rm QMC}/t \approx 4.8/0.5 = 9.6$, and the result obtained by the 2D cavity Mean-Field by Lemarié *et al.* [30] $g_c \approx 0.22$ which corresponds to $W_c/t = 2/g_c \approx 9.1$. The found estimate for the dynamical exponent is in flagrant disagreement with both the estimate for the bimodal case and the equality $z = d = 2$ by Fisher *et al.* [6] as well as with the estimate from our QMC simulations $z^{\rm QMC} = 1.85(15)$.

It is worth mentioning that we did not compute the corrections to order $1/S$ of the Bose-Einstein condensate fraction and instead decided to leave that study be carried out by exact state-of-the art Quantum Monte Carlo simulations of the same model which will be presented in chapter IV, which will also serve to confront the estimate for z.

4 Detailed finite-size scaling analysis

The previous section showed that the inclusion of quantum fluctuations above the Mean-Field solution allows us to study the Superfluid - Bose glass quantum phase transition for 2D hard-core bosons. We extracted some estimates for the dynamical exponent as well as for the critical threshold. However, using a much more careful finite-size scaling analysis of the available data we can obtain estimates and proper uncertainties not only for the same critical parameters but also for the correlation length exponent ν. We will use the finite-size scaling theory developed in section 2.3 of chapter I and we remind here only the main results.

In the vicinity of the 2D quantum critical point, the finite-size scaling of the SF density is:

$$\rho_{\rm sf}(L) = L^{-z}\, \mathcal{G}_{\rm sf}[L^{1/\nu}(W - W_c)], \tag{III.37}$$

where z is the dynamical critical exponent, ν the correlation length exponent, W_c the critical disorder, and $\mathcal{G}_{\rm sf}$ a universal function. We will use this scaling form in the analysis scheme described in detail in section 3.1 of chapter IV so as to extract estimates of the three critical parameters available to us, namely the critical disorder W_c, the correlation length exponent ν and the dynamical exponent z.

One should already notice that there is no strong argument for the estimates obtained at the level of approximation of LSWT to be the ones describing the real Superfluid - Bose glass transition. Indeed, the spin-waves are only controlled on the ordered side of the transition and when quantum fluctuations become equal to the classical order-parameter is when we consider the ordered phase to be destabilized. The spin-wave corrected superfluid density thus vanishes in an uncontrolled fashion, making the critical exponents uncontrolled as well. We will however, for the sake of completeness, carry out this study.

4.1 Bimodal disorder

In the case of the bimodal distribution, we found that the spin-wave corrected superfluid density vanishes at a disorder strength $W_{\rm sf}/t = 3.738(1)$. We will only perform the scaling analysis on the superfluid stiffness since, as discussed in section 3.1, the spin-wave corrected Bose-Einstein condensate fraction is overestimated in our calculation. We performed fits of the superfluid density data near $W_{\rm sf}$ shown

in panel (a) of figure III.2 to the scaling form (III.37), the scaling function $\mathcal{G}_{\rm sf}$ is approximated by a third degree polynomial. Since the spin-wave data is well controlled only on the ordered side of the transition, we will perform the fits in windows of disorder strength $[3.73; W_{\rm max}]$ including the system sizes in $[L_{\rm min}; 32]$, and vary $W_{\rm max}$ and $L_{\rm min}$. The quality of the fit is estimated by the probability (IV.41) which is explained in detail in section 3.1.1 of chapter IV and Ref. [253]. We also estimate the error on the fit estimates by gaussian resampling of the data and a bootstrap analysis with 500 bootstrap samples.

	Q ($\times 100$)						
$L_{\rm min} \setminus W_{\rm max}$	3.735	3.736	3.737	3.738	3.739	3.74	3.741
12	12.93	17.46	18.97	30.22	41.04	42.45	41.74
16	23.78	21.43	24.57	37.73	45.34	50.84	51.73

Table III.1: *Quality of the fits Q, as defined in equation* (IV.41)*, of the critical parameters from the spin-wave corrected superfluid density for the bimodal disorder distribution corresponding to the parameters shown in figure III.5, for different windows of disorder* $[3.73; W_{max}]$ *and of system size* $[L_{\rm min}; 32]$.

The results for W_c, z and ν for different $W_{\rm max}$ and $L_{\rm min} = 12$ and 16 are shown in figure III.5. The corresponding qualities of fit are listed in table III.1. We can see that the qualities are systematically higher for the largest $W_{\rm max}$. This comes from the fact that including more data points further constrains the fit which become more stable, as is also confirmed by the fact that the bootstrap obtained error-bars decrease with increasing $W_{\rm max}$ for all the parameters, as shown in figure III.5. The estimates of the critical disorder strength seem to converge towards the same value as determined in section 3.1, $W_c/t = W_{\rm sf}/t = 3.738(2)$ (indicated by the black dashed line). The estimates for the dynamical exponent are also consistent with $z = 2.0(2)$ (black dashed line) in agreement with the equality $z = d$ as was determined in section 3.1.

Concerning the correlation length exponent ν, the best estimate we can extract is $\nu = 0.5(2)$ which clearly violates the Harris criterion $\nu \geq 2/d = 1$ [173–175]. The spin-wave corrected superfluid density data having quite large error bars, the fits are not constrained enough. This added to the aforementioned possibility uncontrolled vanishing of the superfluid density may explain this. Future Quantum Monte Carlo simulations of this model will allow to clarify this issue, as well as corroborating the estimates for the critical disorder strength and the dynamical exponent.

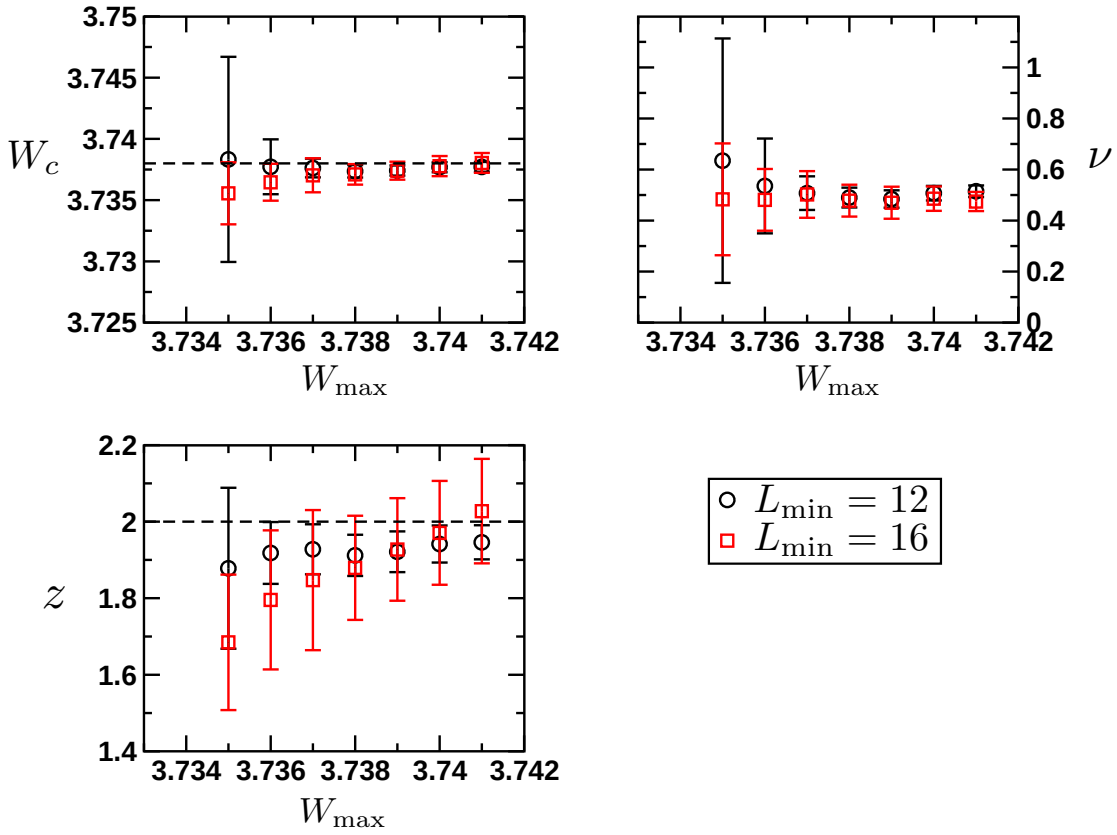

Figure III.5: *Bootstrap estimates of the critical exponents for different windows of disorder* $[3.73; W_{max}]$ *and system size* $[L_{\min}; 32]$ *with* $L_{\min} = 12$ *and 16. The black dashed lines represent the estimates obtained in section 3.1,* $z = 2.0(1)$ *and* $W_c/t = 3.738(1)$*. The new estimates are in good agreement with these previous estimates. The correlation length exponent* ν *estimate converges to* $0.50(5)$ *in clear violation of the Harris criterion.*

4.2 Box disorder

Let us now use the same procedure used in the previous section to extract the ground-state critical parameters from the spin-wave corrected superfluid density data for the problem with the uniform disorder distribution. We focus on the data close to the critical disorder found in section 3.2 and shown in panel (b) of figure III.4. We once again approximate the scaling function of the scaling form (III.37) $\mathcal{G}_{\text{sf}}$ by a third degree polynomial. The error-bars on the estimates are obtained by a bootstrap analysis with gaussian resampling of the data. 500 bootstrap samples were used.

The results of the fits performed over the windows of disorder $[9.6; W_{\max}]$ and included system sizes L in $[L_{\min}; 48]$ are shown in figure III.6 and the corresponding qualities of fit Q are listed in table III.2. The first remark one can make is that,

given that the included system sizes are only 4 (for $L_{\min} = 24$) or 5 (for $L_{\min} = 16$), *i.e.* one less than for the bimodal distribution of disorder, and the error-bars are quite large, the fits are not constrained enough and in particular for $L_{\min} = 24$ and $W_{\max} < 10$ they do not converge. In addition, when they do converge, the qualities of the fit are always big even for fits yielding unphysical results. This leads us to disregard the results for $L_{\min} = 24$, which we show here for the sake of completeness.

The estimate for the critical disorder seems to converge towards $W_c = 9.89(1)t$ in surprisingly good agreement with our QMC estimate $W_c^{\mathrm{QMC}}/t = 9.6(1)$ (*cf.* chapter IV), but disagrees with our previous spin-wave estimate of section 3.2 $W_c/t = 10.05t$. The correlation length exponent is estimated to $\nu = 1.07(3)$, satisfying the Harris criterion.

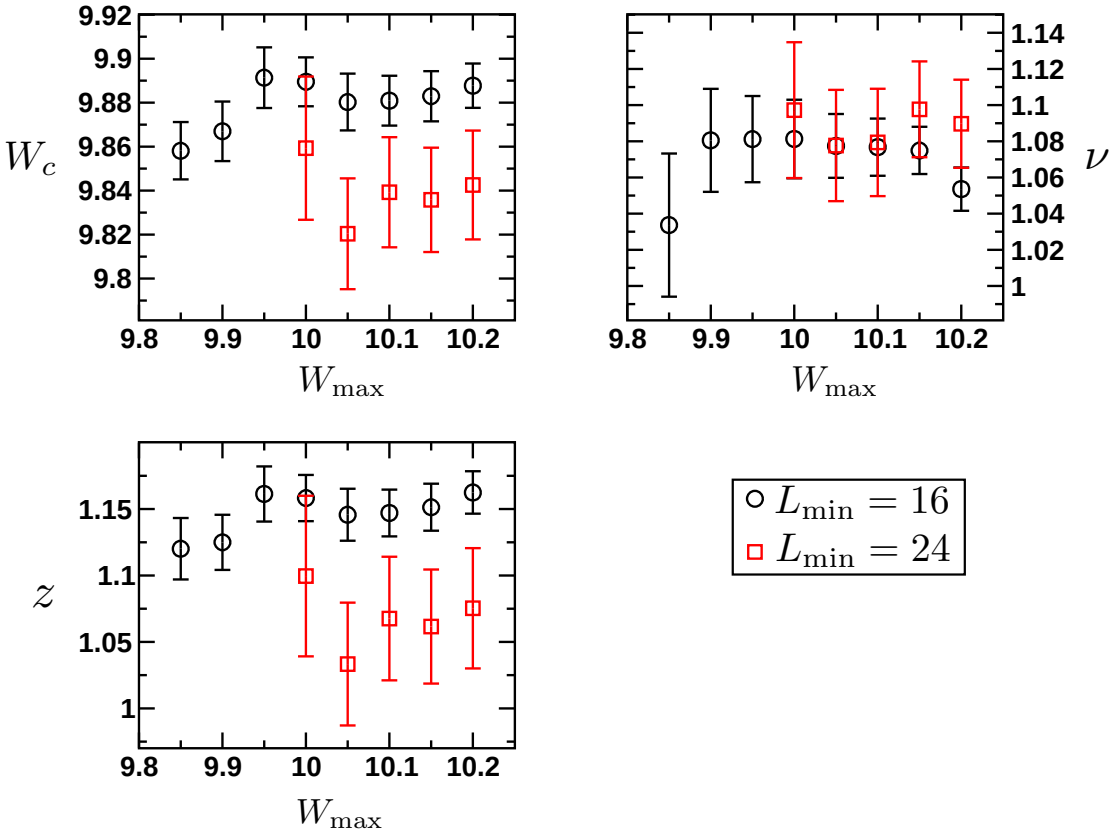

Figure III.6: *Bootstrap estimates of the critical exponents for different windows of disorder* $[3.73; W_{max}]$ *and system size* $[L_{\min}; 32]$ *with* $L_{\min} = 16$ *and 24. The black dashed lines represent the estimates obtained in section 3.1,* $z = 2.0(1)$ *and* $W_c/t = 3.738(1)$. *The new estimates are in good agreement with these previous estimates. The correlation length exponent* ν *estimate converges to* $0.50(5)$ *in clear violation of the Harris criterion.*

	Q ($\times 100$)							
$L_{\min} \setminus W_{\max}$	9.85	9.9	9.95	10	10.05	10.1	10.15	10.2
16	74.1	44.39	46.7	60.4	66.14	81.74	79.47	63.11
24				30	40.43	56.1	57.48	70.18

Table III.2: *Quality of the fits Q, as defined in equation* (IV.41)*, of the critical parameters from the spin-wave corrected superfluid density for the box disorder distribution corresponding to the parameters shown in figure III.6, for different windows of disorder* $[9.6; W_{max}]$ *and of system size* $[L_{\min}; 48]$.

The case of the dynamical exponent is more delicate. The estimate seems to converge towards $z = 1.14(4)$ which is very far from the equality $z = d$ on the one hand, and from our previous spin-wave estimate $z = 1.43(1)$ in section 3.2 (*cf.* figure III.4) on the other hand.

It becomes clear at this point that the determination of the ground-state critical parameters needs the use of QMC simulations so as to properly constrain the fits. This is what will be discussed in chapter IV in the case of the box disorder distribution.

5 Excitation properties

Ground-state properties are important but it is also of great interest to explore the properties of the excitations above the ground-state since they are intimately related to transport properties. Linear Spin-Wave theory allows for the computation of some of these since the subroutines used in the diagonalization of the full Hamiltonian describing the Holstein-Primakoff bosons gives access to the corresponding eigenfunctions as well. In this respect, LSWT presents a distinct advantage to Quantum Monte Carlo simulations which give essentially exact results for static quantities but are much less efficient for dynamical and excitation properties. Therefore, we now study the properties of the spin-wave one-particle excitation spectrum starting with the energy gap between the ground-state and the first excited state. Then we will focus our attention on the full spectrum and its localization properties in the case of a bimodal distribution.

5.1 Spin-wave gap: First excited state

The energy gap between the ground-state and the first excited state is directly linked to the compressibility of the system: if the system at the thermodynamic limit has a gap in its excitation spectrum, it is in an incompressible phase while a vanishing gap is indicative of a compressible phase. The energy gap extrapolated

to the thermodynamic limit was presented in the case of a bimodal distribution of disorder in figures II.3 and III.1. We see that the state remains gapless as long as the disorder bound W is in the band-width $W < 4t$. Let us first study the finite-size gap in the gapless phases and turn our attention to the gapped phase in a second time.

5.1.1 Finite-size gap in the gapless phases

The way the finite size gap vanishes approaching the thermodynamic limit gives access to the sound velocity of the one-particle spin-wave excitations so we plot in panel a of figure III.7 the value of the finite-size spin-wave gap in units of the hopping parameter $\Delta_{\rm SW}(L)/t$ against the inverse linear system size $1/L$ for different disorder strengths inside the band $W < 4t$. $\Delta_{\rm SW}(L)/t$ tends to zero for increasing system sizes, as expected for the compressible phases present in this disorder range (*i.e.* the superfluid and the Bose glass). Quadratic polynomial fits in the inverse system size of the form $\Delta_{\rm SW}(L)/t = 2\pi v/L + b/L^2$ are shown in full straight lines. The Extracted sound velocity v renormalized by its clean case value $v_0 = 2t$ [246] is plotted against disorder strength along with its estimate obtained using the hydrodynamic relation

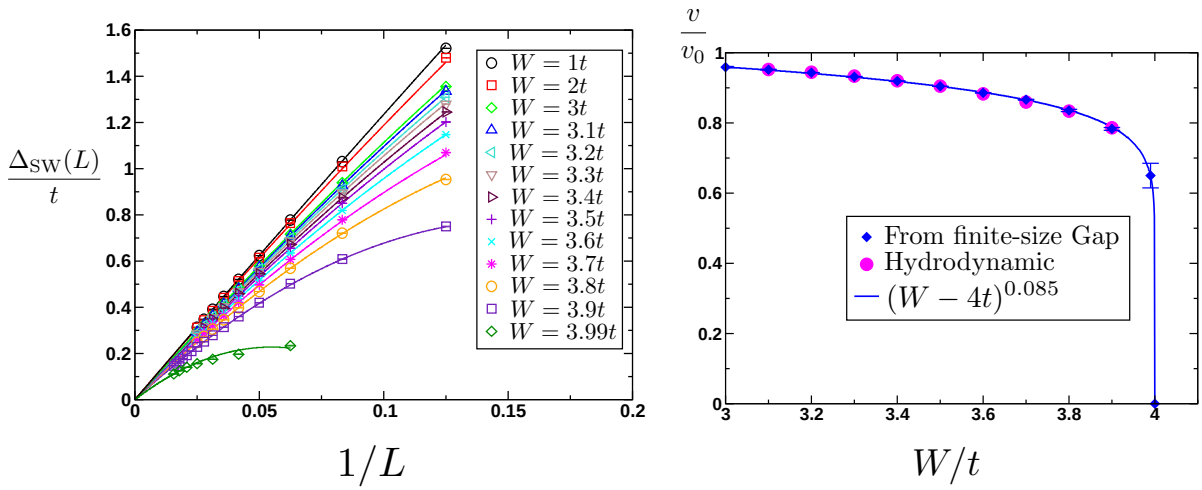

Figure III.7: *Left panel: Spin-wave gap as a function of inverse system size for different disorder strengths in the compressible regime $W < 4t$. Full straight lines are fits to the form $\Delta_{SW}(L)/t = 2\pi v/L + b/L^2$. Right panel: The spin-wave sound velocity v extracted from the fit of the spin-wave gap and renormalized by its value in the disorder-free case $v_0 = 2t$ plotted against disorder strength. Even inside the Bose glass phase $W > W_{sf}$ the sound-velocity is very little affected by disorder. The value of sound velocity obtained with the hydrodynamic relation* (III.38) *is in excellent agreement with the estimate from finite-size gap. The straight blue line is a fit to the power-law $(4t - W)^{0.085}$.*

$$v = \sqrt{\frac{\Upsilon_{\rm sf}}{\kappa}} = \sqrt{\frac{2t\rho_{\rm sf}}{\kappa}}, \tag{III.38}$$

with $\Upsilon_{\rm sf}$ the *classical* Mean-Field superfluid helicity modulus and κ the classical compressibility. Both estimates are in remarkable good agreement and are not very much affected by disorder. Indeed, even inside the Bose glass phase $W > W_{\rm sf}$ and very close to the insulating phase ($W = 3.99t$) the sound velocity has only decreased by some 40% with respect to the clean value v_0, indicating that the first excited state remains delocalized (phonon-like) throughout the entire superfluid and Bose glass phases. This is in agreement with recent studies of Anderson localization of phonons in disordered solids by Monthus and Garel [254] and Amir *et al.* [255].

We can actually fit the behaviour of v/v_0 near its vanishing point $W = 4t$ by a power-law $v/v_0 \sim (4t - W)^{0.085}$, *i.e.* the sound velocity has an extremely slow evolution towards zero as $W \to 4t$. A scenario where the sound velocity jumps from a finite the large value for $W = 3.99t$ to 0 at $W = 4t$ is not in agreement with the data since the power-law fit is very good. Nevertheless, the very low exponent of 0.085 does not rule out possible logarithmic corrections.

5.1.2 Finite-size gap in the Gapped insulator

Let us now focus on the gap in the spectrum on the classical gapped insulator side of the phase diagram. The spin-wave gap extrapolated to the thermodynamic limit shown in figure II.3 opens when the disorder bound is exactly equal to the band edge $W = 4t$. Furthermore, it is known to open up linearly with the chemical potential μ in the classical insulating phase for the disorder-free case, which translates in our disordered case to:

$$\Delta_{\rm clean} = W - 4t. \tag{III.39}$$

Figure III.8 shows the spin-wave gap extrapolated to the thermodynamic limit $\Delta_{\rm SW}$ plotted against disorder strength inside the insulating regime $W > 4t$ in log-log scale. The red circles are the spin-wave gap data which are very well described by a power-law with exponent very close to 1/2 in the vicinity of the critical point $W = 4t$. Hence, the spin-wave gap opens as the square of the distance to the critical point $\sqrt{W - 4t}$, a faster growth than for the clean case (III.39). In addition, there is a transient behaviour at intermediate disorder strengths $4.5 < W < 5$ for which the spin-wave gap deviates from its square root dependance near its opening point. Interestingly enough, $\Delta_{\rm SW}$ adopts the linear behaviour of the clean case for very strong disorders.

It is possible that the square-root behaviour is a finite-size effect since one expects rather that the average gap opens in the same way as the clean case following equation (III.39). This is due to the fact that in the thermodynamic limit, there are arbitrarily large clusters (though exponentially rare) that look like the clean system

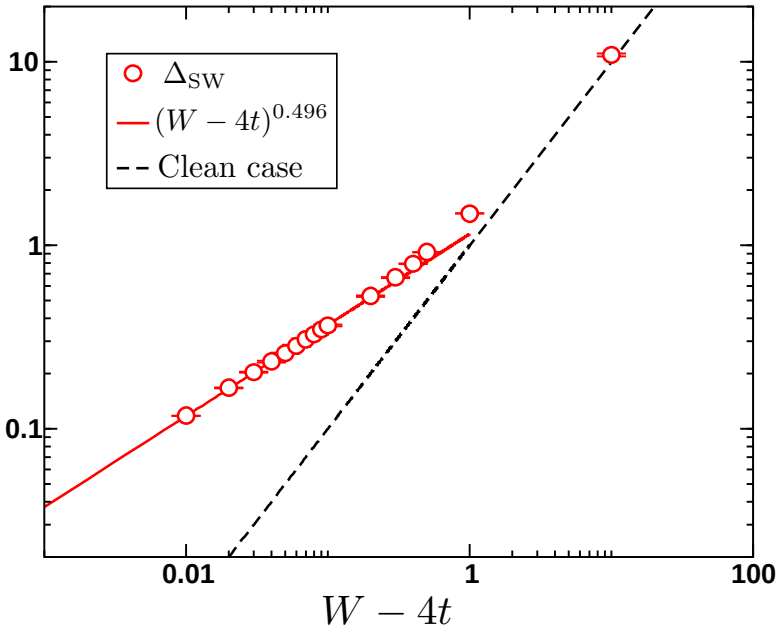

Figure III.8: *Evolution of the spin-wave gap extrapolated to the thermodynamic limit* $\Delta_{\rm SW}(L\to\infty)=\Delta_{\rm SW}$ *(red circles) with disorder strength inside the gapped disordered insulator* $W>4t$ *in logarithmic scale. The straight red line is a fit of the data close to* $W=4t$ *to a power law* $(W-4t)^{0.496}$ *with an exponent* $0.496\approx 0.5$*. The black dashed line is the result in the clean case* $\Delta_{\rm clean}$ *given by equation* (III.39) *which seems to describe the data at strong disorders.*

with all its sites having chemical potentials equal to W (or equivalently to $-W$). The energy cost of creating an excitation (spin-flip) in the system is that of creating it in this cluster hence, that of the clean case, *i.e.* it is equal to W. From percolation theory, we know that beyond the percolation threshold (like in our case since we have 50% of sites with $\mu_i=W$ and 50% with $\mu_i=-W$) the number of such clusters with s sites inside a system of total size N scales as $N_{\rm clusters}(s)\sim Ne^{-b\sqrt{s}}$ with b a constant [222]. Since the biggest gain in energy by delocalizing the spin-flip inside such a cluster is obviously obtained in the largest cluster, this is where the excitation will take place. There is only one largest cluster $N_{\rm cluster}(s_{\rm max})=1$ which yields

$$Ne^{-b\sqrt{s_{\rm max}}}=1 \quad \Rightarrow s_{\rm max}\sim(\ln N)^2. \tag{III.40}$$

The gap in the largest (clean-like) cluster is given by

$$\Delta=W-2t\left(\cos\left(\frac{2\pi}{\sqrt{s^x_{\rm max}}}\right)+\cos\left(\frac{2\pi}{\sqrt{s^y_{\rm max}}}\right)\right)\approx W-4t\left(1-\frac{\pi^2}{s^x_{\rm max}}-\frac{\pi^2}{s^y_{\rm max}}\right), \tag{III.41}$$

and finally, since the linear sizes of the cluster in both directions scale in the same

way with N according to (III.40):

$$\Delta - (W - 4t) \sim \frac{1}{s_{\max}} \sim \frac{1}{\ln^2 N} \tag{III.42}$$

which very slowly tends to zero in the infinite size limit and hence, the gap of the infinite size system should also follow equation (III.39).

5.2 Study of the excitation spectrum

We present in this section the study of the full spin-wave excitation spectrum and in particular its localization properties. This is relevant for understanding the transport properties of the system as has been demonstrated in the case of Anderson localization [3, 5]. Indeed, a fully localized spectrum is tantamount to an insulating phase. By studying the spectrum given by Linear Spin-Wave theory, we are investigating the one-particle non-interacting excitation properties of the system.

Following the work of Monthus and Garel with Anderson localization of phonons [254], as well as the work of the Castellani group in Rome [256], we carry out this study by computing the Inverse Participation Ratios (IPR) at a given energy or frequency Ω. The energy dependent IPRs are defined for a normalized state $|p\rangle = \sum_i a_i^p |i\rangle$ as

$$\mathrm{IPR}_p = \sum_{i=1}^{N} |a_i^p|^4. \tag{III.43}$$

They are very well suited to study the localization of the excited states since they behave as for the Anderson localization transition [4, 254]:

$$\begin{cases} \mathrm{IPR} \sim \dfrac{1}{N}, & \text{if the state is delocalized} \\ \mathrm{IPR} \sim \dfrac{1}{L^{D_2}}, & \text{at the localization-delocalization transition} \\ \mathrm{IPR} \sim \dfrac{1}{\xi^2}, & \text{if the state is localized with a localization length } \xi \end{cases} \tag{III.44}$$

which defines the multifractal exponent D_2 and the localization length ξ of a localized state. Given the fact that the spin-wave excitation spectra are discrete for finite-size systems, and especially so at low energies, and that for each disordered sample with the same disorder strength W/t the numerically determined excitation energies are close to one another but not identical, the strategy we chose to study the energy dependent IPRs at a given frequency Ω is to take the IPRs as averages over all disorder realizations at a given disorder bound W/t over a finite slice of frequencies centered around Ω such that

$$\mathrm{IPR}(\Omega) = \frac{\sum_p \Theta(\Omega_p, \Omega \pm \delta\Omega)\mathrm{IPR}_p}{\sum_p \Theta(\Omega_p, \Omega \pm \delta\Omega)}, \tag{III.45}$$

where $\Theta(\Omega_p, \Omega \pm \delta\Omega) = 1$ if $\Omega - \delta\Omega \leq \Omega_p \leq \Omega + \delta\Omega$, and 0 otherwise. In the following, we will always use $\delta\Omega/v_0 = 1/20$ steps in frequency.

5.2.1 Localization properties of excitations in the superfluid phase

In order to illustrate the IPRs' behaviour of equation (III.44), we plot in figure III.9 the averaged IPR multiplied by system size N plotted against system size for three different disorder strengths: $W = t$ inside the weakly disordered SF phase, $W = 3.4t$ in the strongly disordered SF phase and $W = 3.9t$ inside the BG phase. Completely localized states have an IPR$\times N$ which scales with N (red dashed line) whereas delocalized states have an IPR$\times N$ which scales independently on N. The scaling at the localization-delocalization transition is given by the full black line using the value for the multifractal exponent D_2 determined further along this section. For low disorders $W = t$ (and this is the case for all $W < 2t$) all excited states appear extended. Much richer finite frequency physics emerge in the strongly disordered superfluid phase as can be seen in panel b of figure III.9. Indeed, for $W = 3.4t$ the low energy excitations are delocalized but there is a finite mobility edge Ω_c above which the excitations are localized. The situation inside the Bose glass phase is very similar but with a much smaller mobility-edge since almost all excited states seem to be localized. It is worth mentioning that the ground-state Ω_0 represented by black full circles is completely delocalized throughout the compressible phases with an $\mathrm{IPR}_0 = 1/N$.

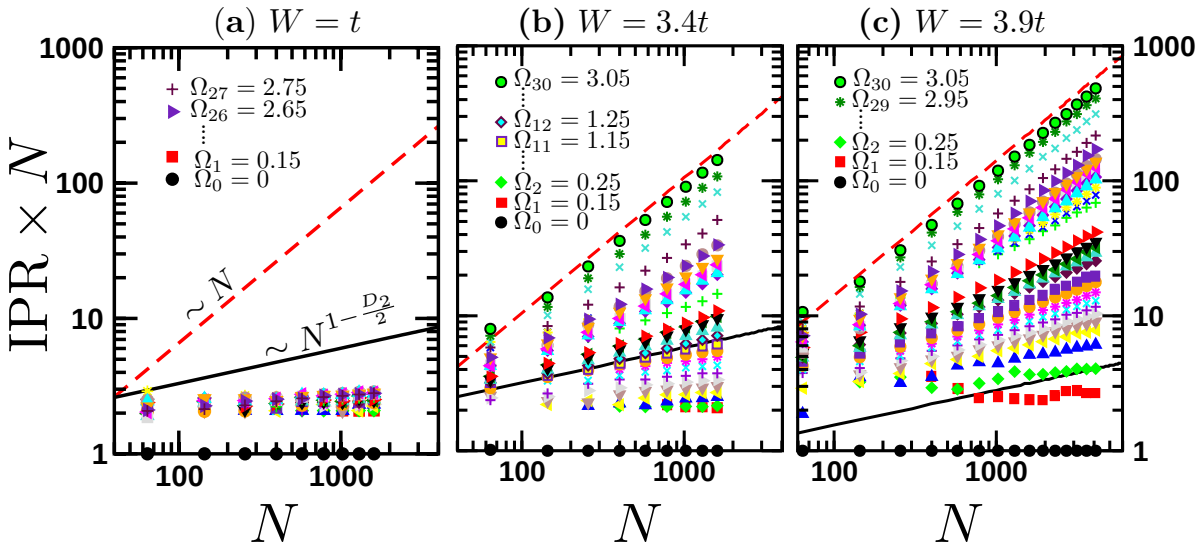

Figure III.9: *Evolution with system size of the averaged Inverse Participation Ratios multiplied by system size N for the N excitation energies at different disorder strengths $W = t$ and $W = 3.4t$ in the superfluid phase, and $W = 3.9t$ in the Bose glass phase. Completely delocalised states have an* IPR$\times$N *which scales as N (dashed red line) and the expected behaviour at the localization-delocalization transition is indicated by the full black line with $D_2 = 1.48$ (see text).*

Let us now determine the single-particle mobility edge Ω_c and the multifractal exponent D_2. According to equation (III.44), at Ω_c, the IPRs *vs.* Ω curves for different system sizes multiplied by L^{D_2} should intersect in a single point. This is illustrated in figure III.10 where a very good crossing of such curves for a disorder strength of $W = 3.4t$ is found using the value for the multifractal exponent $D_2 = 1.48 < 2$, yielding a mobility edge at this disorder strength $\Omega_c/v_0 \approx 1.15$ (*cf.* also panel b in figure III.9). In order to check whether this value of the multifractal exponent $D_2 = 1.48$ is not dependent on the value of disorder strength W/t we plot the crossings of the same curves using this value of D_2 for two other disorder strengths $W = 3.1t$ and $W = 3.6t$ inside the superfluid phase in figure III.11. Convincing crossings are found at a mobility edge that decreases with increasing disorder strength. There is, however, a small drift in the crossing point which gives rise to an uncertainty in the determination of Ω_c. We can still conclude that the value for the multifractal exponent of D_2 is consistent and independent on disorder strength inside the Superfluid phase.

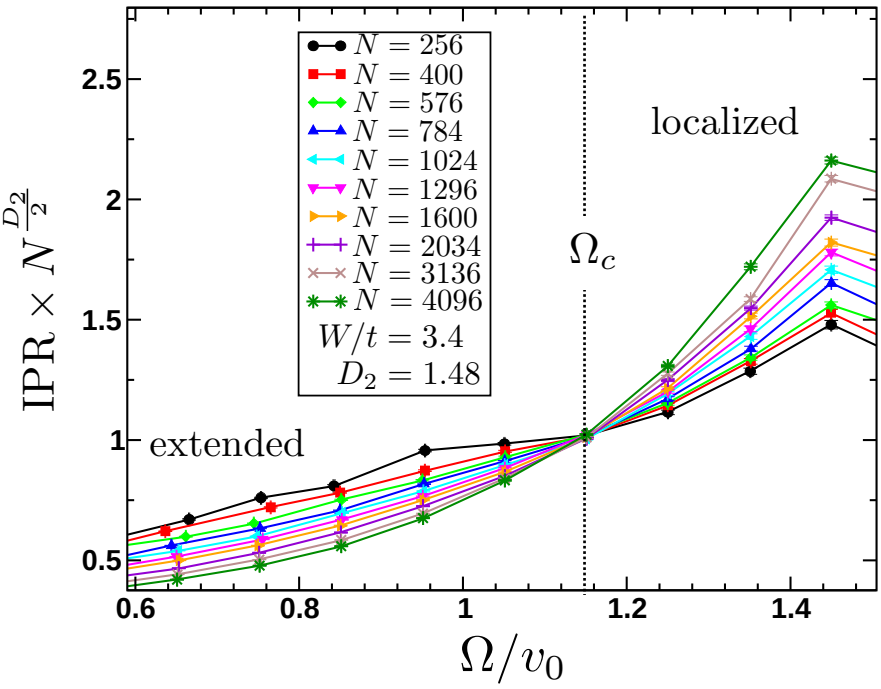

Figure III.10: *Crossings of the Inverse Participation Ratio curves for different system sizes* $L = 16, \ldots, 64$ *multiplied by* L^{D_2} *with a multifractal exponent* $D_2 = 1.48$ *at a disorder strength* $W = 3.4t$ *inside the superfluid phase. A pretty convincing crossing at a finite frequency* $\Omega_c/v_0 \approx 1.15$ *separating low energy delocalized states for* $\Omega < \Omega_c$ *and high energy localized states for* $\Omega > \Omega_c$ *is found. Error bars are shown but are of size comparable to that of the symbols.*

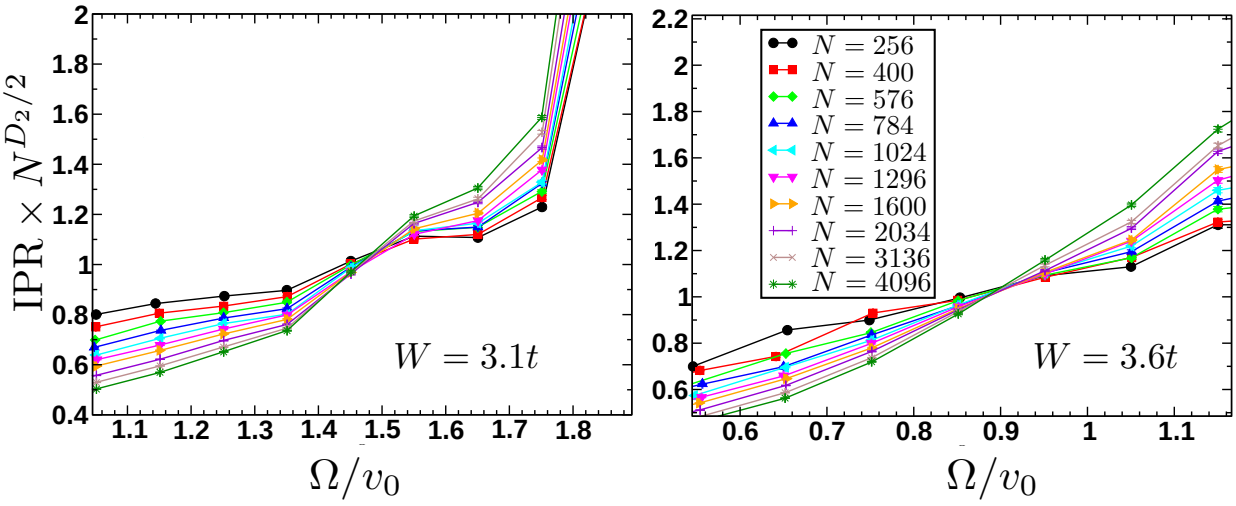

Figure III.11: *Crossings of the Inverse Participation Ratio curves for different system sizes* $L = 16, \ldots, 64$ *multiplied by the* L^{D_2} *with a multifractal exponent* $D_2 = 1.48$ *at disorder strengths* $W = 3.1t$ *(left) and* $W = 3.6t$ *(right) inside the superfluid phase. Error bars are shown but are of size comparable to that of the symbols. Good crossings are found in both cases although a small drift is present, particularly at the strongest disorder, which yields an uncertainty in the determination of the mobility edge* Ω_c*:* $\Omega_c(W = 3.1t)/v_0 \simeq 1.5$ *and* $\Omega_c(W = 3.6t)/v_0 \simeq 0.9$.

5.2.2 Localization properties of excitations inside the Bose glass phase

Moving on to the Bose glass phase, we could already see in the left panel of figure III.7 that in this regime finite-size effects become stronger and stronger approaching $W = 4t$. This is also the case for the study of the IPRs in this regime. Figure III.12 shows the curves for IPR$\times N^{D_2/2}$ for system sizes ranging from $N = 256$ to $N = 4096$ plotted against the energy Ω/v_0 at disorder strength $W = 3.9t$ inside the Bose glass phase, using once again the same estimate for the multifractal exponent $D_2 = 1.48$. The crossing point displays a very important drift towards smaller frequencies as the system size increases. This suggests that the mobility edge inside the Bose glass is indeed vanishing.

One way to quantify this is to compute the successive crossing points $\Omega^\star$ for each successive couple of system sizes L_1 and L_2 and monitor its evolution when increasing the considered systems. In order to do so we define the crossing points $\Omega^\star(L^\star)$ at system size $L^\star = (L_1 + L_2)/2$ and plot it against $1/L^\star$ as shown in the inset of figure III.12. The crossing points are less and less well defined as the curves for different (big) sizes overlap and therefore big error bars on $\Omega^\star$ can be seen. Nevertheless, a general trend of $\Omega^\star$ going to zero as $L^\star$ tends to infinity can be extracted, as emphasized by the dashed red line. This strongly suggests that the mobility edge Ω_c vanishes for $W = 3.9t$ and the only extended state is the ground-

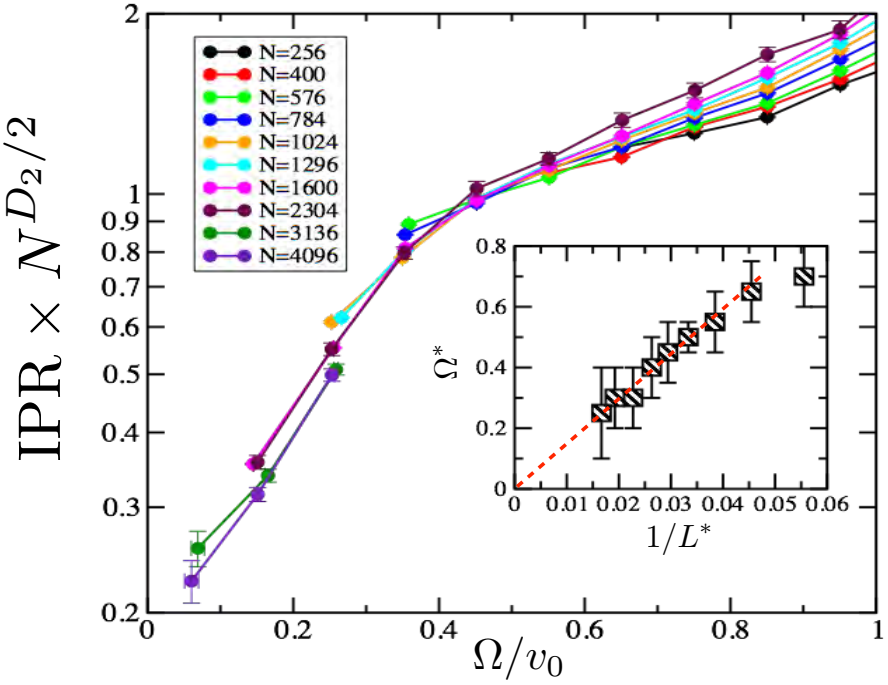

Figure III.12: *Crossings of the Inverse Participation Ratio curves for different system sizes* $L = 16, \ldots, 64$ *multiplied by the* L^{D_2} *with a multifractal exponent* $D_2 = 1.48$ *at a disorder strength of* $W = 3.9t$ *inside the Bose glass phase. A big drift in the crossing points is present. The inset shows the successive* Ω^* *crossing points for a couple of adjacent system sizes* L_1 *and* L_2 *as a function of the inverse of* $L^* = (L_1 + L_2)/2$. Ω^* *drops to zero as* L^* *tends to infinity signalling a vanishing mobility edge* $\Omega_c = 0$.

state (*cf.* panel c of figure III.9). For $W = 3.8t$, we have checked that although the dropping to zero of the crossing points $\Omega^\star$ is less clear, it is still compatible with our data.

5.2.3 Resulting phase diagram and discussion

Let us now summarize the results presented in the two previous sections. We have performed the determination of the mobility edge using the crossing of the IPR$\times N^{D_2/2}$ curves with the same multifractal exponent $D_2 = 1.48$ for all our values of disorder $3t < W < 4t$. The results are represented in the energy *vs.* disorder phase diagram plotted in figure III.13. We can see how the mobility edge Ω_c (yellow diamonds) separating extended states at $\Omega < \Omega_c$ from localized states at $\Omega > \Omega_c$ has finite, quite large values in the Superfluid phase and continuously drops down as the Bose glass phase is approached, the localization-delocalization transition boundary (shaded area) has large error bars. The mobility edge presumably vanishes at the Superfluid - Bose glass transition evidenced by the blue asterisk in the phase dia-

gram III.13. All states except the ground-state are localized inside the Bose glass in contrast with the findings by Feigel'man, Ioffe and Mézard on the one hand [194, 195] and by Markus Müller on the other hand [257]. Inside the gapped insulator ($W > 4t$) there are no states below the gap Δ (red circles) and all states are localized above it.

However, these results need to be taken with a pinch of salt. As a matter of fact, Gabriel Lemarié has recently studied the spin-wave excitation spectrum of exactly the same model on the 2D square lattice using a transfer matrix approach allowing him to reach much bigger system sizes [258], and though he has not reached a firm conclusion yet, his results indicate that the mobility edge may vanish *also* inside the Superfluid phase. The localization length being exponentially large might explain why when only the small sizes are used the states appear delocalized. In addition, all states remain localized in the Bose glass phase, in agreement with our conclusions.

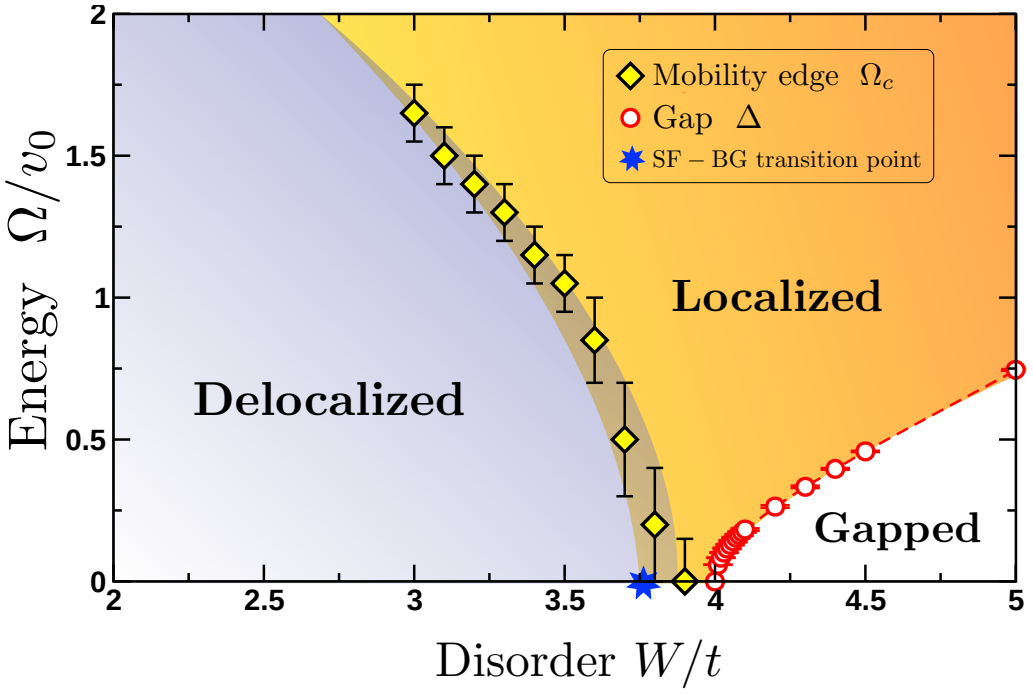

Figure III.13: *Spin-wave excitation energy rescaled by $v_0 = 2t$ plotted against disorder stength W/t. The excited states are delocalized below the mobility edge Ω_c (yellow diamonds) and localized above it. Ω_c, which determines the boundary of localized and delocalized states (shaded area) with quite large error bars close to the superfluid - Bose glass transition (blue asterisk), is expected to vanish at the SF-BG transition point $W_{sf}/t = 3.738(1)$ and all states are localized in the BG phase. The gapped insulator presents no states below the gap Δ (red circles) and only localized states above it.*

This emerging scenario is consistent with Anderson localization of non-interacting electrons in two dimensions [4, 259] and of 2D phonons [254, 259]. Our spin-wave excitations are non-interacting Holstein-Primakoff bosons but have a linear dispersion at small energies in the clean system [230, 246], like phonons but contrary to the quadratic dispersion at low energies for clean non-interacting electrons. Note however that above the Bose-condensed ground-state (present for $W < W_c$) we expect an Anderson tower of states [260, 261] that is not captured by our SW analysis since the continuous U(1) symmetry is already broken on our finite systems. That may be a crucial ingredient to include in the analysis of the localization properties of the excitations above the Bose-condensed ground-state, which is beyond the present scope.

Chapter IV

Quantum Monte Carlo study

Contents

This chapter presents the study of various aspects of the quantum phase transition from the Superfluid to the Bose glass phases by Quantum Monte Carlo simulations using the so-called *Stochastic Series Expansion* (SSE). This method, developed by Anders Sandvik during the decade of 1990s and the early 2000s, has the advantage of being applicable to any Hamiltonian on a lattice as long as there is no sign problem, or it is weak; unlike some of the other Quantum Monte Carlo algorithms that exist like the *world line* loop algorithm which was specially conceived for the Heisenberg Hamiltonian. Furthermore, the SSE algorithm out-performs the *world line* loop algorithm which suffers from critical slowdown [262].

The SSE method is based on the expansion of the partition function in powers of the inverse temperature β and is intrinsically free of projection or discretisation errors (like Trotter errors). In this approach, two kinds of movements in the configuration space are allowed: the *local* or *diagonal update* [215, 263, 264], and the *loop operator update* [262, 265] which performs non-local movements. This chapter aims at giving a brief presentation of the SSE method applied to the 2D hard-core bosons with on-site disorder Hamiltonian, in order to investigate the Superfluid - Bose glass transition in two dimensions. For a more detailed and thorough understanding of the SSE with directed loops algorithm, we refer the interested reader to the original work on this method [215, 262–266] as well as references [267–269], from which we took great inspiration. We will first describe the algorithm and the possible movements in the configuration space with particular emphasis on the non-local movements. Secondly, we will show how to measure physical observables, both diagonal and off-diagonal, within this framework. Then, we will explain some special cautions and considerations to properly simulate this quantum disordered problem, like the β-doubling scheme to access equilibrated samples and reliable measurements, among others. The last three parts of this chapter will address the new results obtained for the SF - BG transition in two dimensions: *i*) the critical point at which the transition takes place and the critical exponents governing the transition for both average and typical quantities, which have been greatly debated [6, 157, 160, 176, 178–182, 270, 271] *ii*) The distributions of the logarithm of the stiffness $\ln(\rho_{\mathrm{sf}})$ across the phase transition which yields a self-averaging superfluid phase and a non self-averaging Bose glass phase, in agreement with recent results [272]. *iii*) The study of the microscopic features of the BG phase such as the local density indicating a lack of a percolation scenario at the transition in contradiction with a number of discussions [187, 188].

1 Quantum Monte Carlo SSE with Directed Loops

We are going to apply an exact quantum mechanical approach to treat the two dimensional hard-core bosons problem with on-site disorder on the chemical potential on the square $L \times L = N$ sites lattice. Let us first describe the Hamiltonian we are interested in. The original bosonic Hamiltonian is:

$$\mathcal{H} = -t \sum_{\langle ij \rangle} \left(b_i^\dagger b_j + b_j^\dagger b_i \right) - \sum_i \mu_i b_i^\dagger b_i, \tag{IV.1}$$

where hopping between nearest neighbours is fixed to $t = 1/2$, and the random chemical potential μ_i is drawn from a uniform distribution $[-W, W]$, *i.e.* half-filling is statistically achieved, on average [164]. It can be mapped, as seen before (cf. section 2 of chapter II) to a spin-$\frac{1}{2}$ XY Hamiltonian with transverse magnetic field along the z-axis (*cf.* (II.22)). It can be re-written as the sum of diagonal and off-diagonal terms:

$$H_{XY} = -t \sum_{b=1}^{N_b} [H_{1,b} - H_{2,b}] - N_b \epsilon, \tag{IV.2}$$

where b defines the bond connecting the pair of interacting spins $(i(b), j(b))$, $N_b = 2N$ is the number of bonds and ϵ is a constant added to the diagonal term of the original Hamiltonian. This constant shifts the zero energy so as to make all matrix elements positive or vanishing. This is necessary for the stochasticity (ergodicity) of the random walk in the configuration space to be fulfilled, and hence for a reliable evaluation of physical quantities. Its effect will be studied further along the chapter in section 2.1.

The diagonal part of (IV.2) reads:

$$H_{1,b} = \epsilon + h_b (S^z_{i(b)} + S^z_{j(b)}), \tag{IV.3}$$

where h_b is the magnetic filed defined on bond b. The off-diagonal part is given by:

$$H_{2,b} = \frac{1}{2} \left[S^+_{i(b)} S^-_{(j(b))} + S^-_{i(b)} S^+_{(j(b))} \right]. \tag{IV.4}$$

Now that we have defined the Hamiltonian to be treated for the rest of the chapter, we will describe the method used in this quantum mechanical approach: the Quantum Monte Carlo Stochastic Series Expansion with Directed Loops.

1.1 Stochastic Series Expansion of the partition function

The quantisation axis of this problem is given by the transverse magnetic field along the z-axis, therefore, the Hilbert space of the Hamiltonian (IV.2) has a natural work basis:

$$\{|\alpha\rangle\} = \{|S^z_1, S^z_2, S^z_3, \ldots, S^z_{N-1}, S^z_N\rangle\}. \tag{IV.5}$$

We will work with basis (IV.5) in all of the following calculations and derivations.

1.1.1 Taylor expansion of the partition function

A central quantity in Quantum Monte Carlo simulations is the partition function. From it we can derive other observables, like shown in section 1.3, although it is never itself actually evaluated. The SSE method is based on the Taylor expansion of the exponential in the partition function in powers of the inverse temperature β as:

$$Z = \mathrm{Tr}\left[\exp(-\beta H_{XY})\right] = \sum_{n=0}^{\infty} \frac{(-\beta)^n}{n!} \mathrm{Tr}\left[H_{XY}^n\right]. \tag{IV.6}$$

The powers of the Hamiltonian can be rewritten as all possible products of all the terms in the Hamiltonian (two kinds in our case), every product of n terms is represented by a sequence S_n of n indexes $i_1 \dots i_n$ and each index can be either 1 or 2, meaning it is a diagonal (if the index is 1) or an off-diagonal (if the index is 2) term in the Hamiltonian (IV.2). The partition function is then the sum over n of all possible sequences S_n of size n [263]:

$$Z = \sum_{n=0}^{\infty} \sum_{S_n} \frac{\beta^n}{n!} \mathrm{Tr}\left[\prod_{p=1}^{n} H_{ip}\right]. \tag{IV.7}$$

At this point it is worth noticing that if the trace in (IV.7) can be computed analytically, one can access expectation values of physical observables by performing a Monte Carlo sampling in the space of sequences S_n, which is true for the spin$\frac{1}{2}$ Heisenberg Hamiltonian (this is the Handscomb method [273]). However the SSE method is more general and the evaluation of physical quantities is achieved by using a complete basis of the Hilbert space [263, 264] so that the partition function reads:

$$Z = \sum_{\alpha} \sum_{n=0}^{\infty} \sum_{S_n} \frac{\beta^n}{n!} \langle\alpha| \prod_{p=1}^{n} H_{ip} |\alpha\rangle. \tag{IV.8}$$

Now it becomes clear that a Monte Carlo configuration for a given value of the length n of the sequence S_n is determined by a value of α and a sequence S_n. In addition, the weight of such a configuration is straightforwardly defined by:

$$W(\alpha, S_n) = \frac{\beta^n}{n!} \langle\alpha| \prod_{p=1}^{n} H_{ip} |\alpha\rangle, \tag{IV.9}$$

where the order of the product of H_{ip} is given by the sequence S_n. The ergodicity of the algorithm requires all the weights (IV.9) to be positive, if this is the case, we can perform the stochastic computation of this partition function via the allowed movements in the space $\{\alpha, S_n, n = 0 \dots \infty\}$ verifying the detailed balance on the weights.

In principle, the Taylor expansion in powers of β has to be taken to all powers up to infinity. However, when $n \to \infty$, the length of the sequence S_n goes to infinity as well, meaning that the number of operators in S_n goes to infinity too. This cannot be computed in a real-life computer with finite memory, however, the fact that the simulated system has a finite-size $L \times L = N$ and the temperature is finite brings about that only sequences S_n of finite-size n give significative contributions to the trace in the partition function. Taking this into account, it becomes realistic to impose a maximal value $\mathcal{M}$ of the sequence lengths n. We can then work at fixed sequence length $\mathcal{M}$ knowing that sequences of length $n > \mathcal{M}$ give a negligible contribution to the trace. The way to determine this cut-off dynamically during the thermalisation part of the simulations will be further explained in section 2.2.1. The sequences of lengths $n < \mathcal{M}$ are artificially enlarged to be of length $\mathcal{M}$ by adding $\mathcal{M} - n$ identity operators to it, thus n becomes the number of non-identity operators inside the operator string $S_\mathcal{M}$. There are $C_\mathcal{M}^{\mathcal{M}-n}$ ways to add these identity operators to the sequence, which finally yields for the partition function:

$$Z = \sum_\alpha \sum_{S_\mathcal{M}} \frac{\beta^n (\mathcal{M} - n)!}{\mathcal{M}!} \langle \alpha | \prod_{p=1}^{n} H_{ip} | \alpha \rangle. \tag{IV.10}$$

Let us now look deeper in to the details of the *operator string* $\prod_{p=1}^{n} H_{ip}$ and its representation, before getting to the description of the possible movements allowed in the SSE algorithm.

1.1.2 The operator string representation

In what follows we will use the notations and definitions from Anders Sandvik's original work [263]. The action of the so called *operator string* $\prod_{p=1}^{n} H_{ip}$ on a given initial state of the system $|\alpha\rangle$ can be interpreted as the propagation of this initial state along the operator string itself. We can define a propagated state $|\alpha(l)\rangle$ as the state obtained by the action of the first l operators in the operator string on the initial state $|\alpha(0)\rangle = |\alpha\rangle$ as:

$$|\alpha(l)\rangle = \prod_{p=1}^{l} H_{ip} |\alpha\rangle. \tag{IV.11}$$

The cyclicality of the trace imposes that if the sequence length is $\mathcal{M}$, then $|\alpha(\mathcal{M})\rangle = |\alpha(0)\rangle$. Recursively, we can get every propagated state $|\alpha(l)\rangle$ by applying the l-the operator in the operator string on the previous state $|\alpha(l-1)\rangle$.

There are three types of operators in the operator string $S_\mathcal{M}$, namely the identity operators of type 0, the diagonal operators of type 1 and the off-diagonal operators of type 2. In the base (IV.5) we can then write the operator string as [265]:

$$S_\mathcal{M} = [a_1, b_1], [a_2, b_2], \ldots, [a_l, b_l], \ldots, [a_\mathcal{M}, b_\mathcal{M}], \tag{IV.12}$$

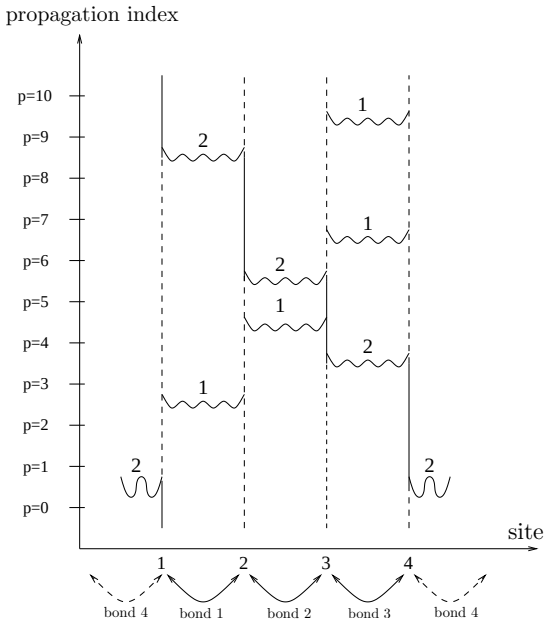

Figure IV.1: *Example of the graphical representation of the string operator $S_{\mathcal{M}=10}$ for a chain of 4 $\frac{1}{2}$-spins. The full (dashed) line represents a spin up (down) and the operator acting at propagation indexx p on a bond is represented by a curly line with the type of the operator on top (see text). The added identity operators are not represented. Taken from reference [267].*

where a_l is the type of the l-th operator in $S_{\mathcal{M}}$ (0, 1 or 2) and b_l is the bond on which it acts ($b_l = 0$ if the operator is of type 0). Within this notation, the string operator can be graphically represented as showed in figure IV.1.

1.2 The SSE with Directed Loops algorithm

The SSE algorithm starts from an initial random state $|\alpha\rangle_i$ and a sequence of length $\mathcal{M}$ with only identity operators in it $S^i_{\mathcal{M}} = [0,0]_1, \ldots, [0,0]_{\mathcal{M}}$. There are two possible movements for the random walk in the configuration space. First, the *diagonal update* which tries with some probability to exchange identity operators with diagonal operators one after the other in the order of propagation along the sequence $S_{\mathcal{M}}$: $[0,0] \leftrightarrow [1,b]$. Secondly, a more complex, non-local *loop operator update* that proposes exchanging diagonal and off-diagonal operators: $[1,b] \leftrightarrow [2,b]$ by constructing a loop of operators [265]. Let us remind the reader that the simulation takes place at a temperature $T = 1/\beta$.

1.2.1 Diagonal update

This simpler of the two movements looks at what type of operator acts on every propagation index p in the sequence $S_{\mathcal{M}}$. If the operator if of type 2 it does nothing at that index of propagation. If the operator is of type 0 (identity operator) it proposes the exchange $[0,0]_p \to [1,b]_p$: a diagonal operator acting on a bond b, randomly chosen among the N_b possible bonds, is put in the sequence at the propagation index p with a given probability which will be specified a little further down. If the encountered operator is of type 1 (diagonal operator), the algorithm proposes to change it by an identity operator $[1,b]_p \to [0,0]_p$.

The probabilities involved in these exchanges have to verify the detailed balance condition. Taking these probabilities to be proportional to the weight of the configuration that results from the exchange ensures that the detailed balance condition is satisfied [265]:

$$\frac{P([0,0]_p \to [1,b]_p)}{P([1,b]_p \to [0,0]_p)} = \frac{N_b W(\alpha, S_{n+1})}{W(\alpha, S_n)}, \tag{IV.13}$$

the N_b factor coming from there being N_b possible bonds on which the diagonal operator that's being included in the sequence can act. The Metropolis probabilities fulfil this condition [263, 274] and we have:

$$P([0,0]_p \to [1,b]_p) = \min\left(1, \frac{N_b \beta \langle \alpha_p | H_{1,b} | \alpha(p) \rangle}{\mathcal{M} - n}\right) \tag{IV.14}$$

and

$$P([1,b]_p \to [0,0]_p) = \min\left(1, \frac{\mathcal{M} - n + 1}{N_b \beta \langle \alpha_p | H_{1,b} | \alpha(p) \rangle}\right). \tag{IV.15}$$

Since at the same time that these diagonal updates are attempted the state of the configuration $|\alpha\rangle$ is updated to $|\alpha(p)\rangle$, we have all the information required to calculate the probabilities (IV.14) and (IV.15) whenever needed.

It is worthwhile noticing that during this update, the number n of non-identity operators in $S_{\mathcal{M}}$ changes. This may cause some problems with the equilibration of the configuration since the infrared cut-off to the expansion $\mathcal{M}$ could be too small and errors to the measurements carried out may emerge. It is then really important to dynamically adjust $\mathcal{M}$ during the thermalization of the configuration as will be discussed in more detail in section 2.2.1.

1.2.2 Loop operator update

We will now describe the more complex movement in configuration space. Why does it have to be more complicated? This is due to the fact that a simple substitution of a diagonal operator by an off-diagonal one will give a configuration non-contributing to the partition function because an off-diagonal element $[2,b]_p$ in $S_{\mathcal{M}}$

will change the propagated state $|\alpha(p)\rangle \neq |\alpha(p-1)\rangle$ (since it involves the spins of bond b being flipped). Then, if only one such a substitution is performed, the condition $|\alpha(\mathcal{M})\rangle = |\alpha(0)\rangle$ will be violated. What's more, since our basis (IV.5) is orthogonal, the associated matrix element $\langle\alpha(p-1)|H_{2,b}|\alpha(p)\rangle$ will vanish and the resulting configuration does not contribute to the trace in the partition function. To overcome this problem, Sandvik devised an efficient non-local loop algorithm, the *loop operator update* [265]. Let us now describe how the loop is constructed.

Since the update only involves non-identity operators, it works at fixed n and we can forget about the identity operators in the sequence $S_{\mathcal{M}}$ and work with the original S_n sequences. Let us now introduce the two-spin states (or reduced states) for a given bond b_p in the propagated state $|\alpha(p)\rangle$:

$$|\alpha_{b_p}(p)\rangle = |S^z_{i(b_p)}(p), S^z_{j(b_p)}(p)\rangle, \tag{IV.16}$$

the weights of equation (IV.9) read, in terms of these new states:

$$W(\alpha, S_n) = \frac{\beta!}{n!}\prod_{p=1}^{n}\langle\alpha_{b_p}(p)|H_{b_p}|\alpha_{b_p}(p-1)\rangle. \tag{IV.17}$$

The only nonzero two-spin matrix elements are:

$$\begin{aligned}
&\langle\downarrow\downarrow|H_b|\downarrow\downarrow\rangle = \epsilon,\\
&\langle\uparrow\uparrow|H_b|\uparrow\uparrow\rangle = 2h_b + \epsilon,\\
&\langle\downarrow\uparrow|H_b|\downarrow\uparrow\rangle = \langle\uparrow\downarrow|H_b|\uparrow\downarrow\rangle = h_b + \epsilon,\\
&\langle\downarrow\uparrow|H_b|\uparrow\downarrow\rangle = \langle\uparrow\downarrow|H_b|\downarrow\uparrow\rangle = 1/2.
\end{aligned} \tag{IV.18}$$

It is easier to continue the discussion in the vertex representation of the configuration space. As a matter of fact, the matrix element product in the weights IV.17 can be represented as a network of n 4-legged vertices, with the two spins $S^z_i(p-1), S^z_j(p-1)$ entering the p-th vertex and $S^z_i(p), S^z_j(p)$ exiting. The allowed vertices are those corresponding to the nonzero matrix elements IV.18. The next step is to create a linked list of the vertices such that for each of the four legs on each vertex there is a spin state and a link to the following or previous (increasing or decreasing direction of the propagation index p) vertex leg at the same site. The exit leg is linked to a leg which is taken as the entrance leg to the next vertex. One must be careful to take into account the periodic boundary condition on the propagated states imposed by the cyclicality of the trace: if the loop goes through the boundary, the state $|\alpha_b(0)\rangle = |\alpha_b(\mathcal{M})\rangle$ will be changed too.

The way an operator loop is constructed is the following, first one of the $4n$ vertex legs is randomly chosen as the initial entrance leg. (growing or decreasing propagation index p) is also randomly chosen. An exit leg on the same vertex has

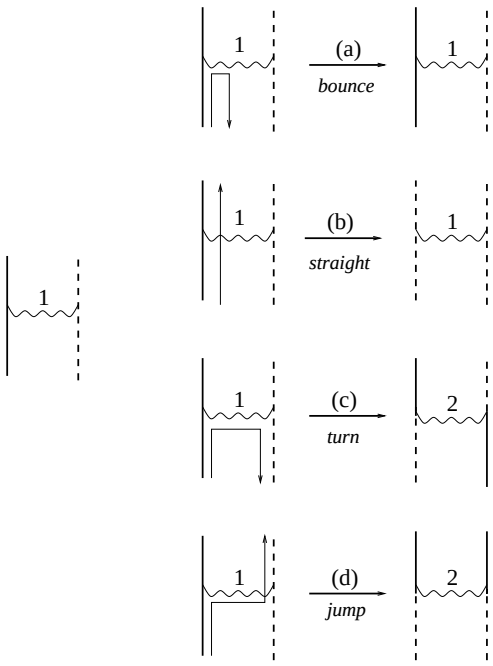

Figure IV.2: *Graphical representation of the four possible movements the loop operator updates can perform for the construction of the loops. The conventions are identical to those in figure IV.1. Taken from reference [267].*

to be chosen according to some probability law: four spins define the considered vertex and an entrance leg was chosen, the probability of going out of the vertex by a given leg (which has a given spin) is proportional to the matrix element in (IV.18) corresponding to the vertex obtained after flipping both the entrance and exit spins. This probability law ensures that only allowed vertices (nonzero matrix element) are generated and that the detailed balance condition is met [265]. This procedure is repeated until the the starting point is reached again, then all the spins that the loop touches are flipped.

We have seen that for a given entrance leg, there are four types of movements the loop can follow, each one corresponding to one of the four vertex legs being the exit one. These movements are represented in the figure IV.2. Let us detail each movement:

- the *bounce* movement: the exit and entrance legs are the same. It is not very useful since it means that the loop being constructed goes back a step and it can be avoided if all nonzero matrix elements are the same (this will depend on the choice of the value of ϵ in our case). Since the two spins to be flipped are actually the same, it is flipped twice which amounts to no flipping at all.

This movement does not exchange the operator type acting on the considered bond b_p.

- the *straight* movement: the exit and the entrance legs are on the same side of the vertex. In this case both the entrance and exit legs correspond to the spin on the same site but at different propagation indexes. Since the action of this movement is on a single site, it involves no exchange of the operator type acting on the considered bond b_p.

- the *turn* movement: the entrance and exit legs are spins on different sites and the construction direction of the loop is changed. Since this movement involves two spins on different sites the change in the vertex corresponds to a change of the type of the operator.

- the *jump* movement: the entrance and exit legs are on different sites (sides of the vertex) but the construction direction of the loop remains the same. As well as the turn movement, the jump movement will change the type of the operator.

If there is only one possible way to construct the loop (*i.e.* only one type of movement has a nonzero probability), we talk about a deterministic loop and no random choice of exit leg is required. The construction of the loop inserts off-diagonal operators coherently and allowed the sampling of both the operator string and the states in the basis (IV.5), hence all the possible values of n, all the possible operator strings $S_{\mathcal{M}}$ and states $|\alpha\rangle$ are accessible to the algorithm: it is an ergodic algorithm.

1.2.3 Summary: a Monte Carlo Step in the SSE method

For the sake of completeness, we describe how the entire first Monte Carlo step unfolds in the SSE framework in the case of a 6 spin-$\frac{1}{2}$ chain. The SSE Monte Carlo step then follows the procedure represented graphically on figure IV.3:

- At first, the spin configuration is chosen randomly and the initial state in this example is $|\alpha(0)\rangle = |\ \downarrow\uparrow\downarrow\downarrow\uparrow\downarrow\rangle$ and the operator string is initialised to length $\mathcal{M} = 4$ with only identity operators in it (empty operator string), $S_{\mathcal{M}=4} = [0,0],[0,0],[0,0],[0,0]$.

- a) The diagonal update is performed: diagonal operators of type 1 are inserted to the operator string. The number of non-identity operators n varies and one should adjust the cut-off limit of the expansion $\mathcal{M}$ as described in section 2.1.

- b) Perform the loop operator update described in section 1.2.2. All the loops are constructed, in this example three loops are constructed. During the construction of each loop, some off-diagonal observables can be measured, as will be described on section 1.3.2. In some cases, a loop can take very long times

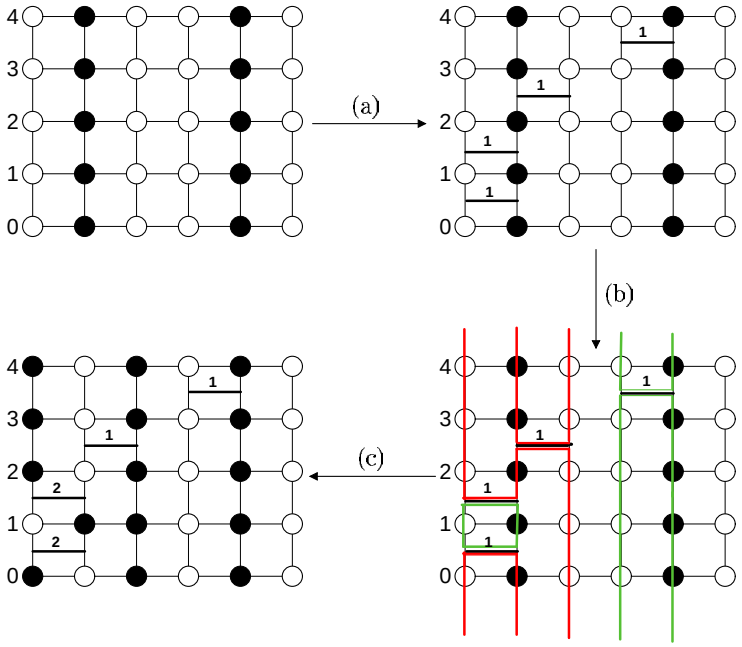

Figure IV.3: *Example of the different stages of a Monte Carlo step on a chain of 6 spins-$\frac{1}{2}$ with periodic boundary conditions. The spin configuration $\uparrow$ is represented by $\bullet$ and $\downarrow$ by $\circ$, hence, the initial state (top-left corner) is $|\alpha(0)\rangle = |\downarrow\uparrow\downarrow\downarrow\uparrow\downarrow\rangle$. See text for details on the different stages a), b) and c). The final configuration (bottom-letf) is $|\alpha\rangle = |\uparrow\downarrow\uparrow\downarrow\uparrow\downarrow\rangle$. Figure taken from reference [268].*

before closing. We impose a maximum loop length such that loops with length exceeding this limit are thrown away and another loop is constructed. You can also fix the number of loops that will be constructed, N_l. For all the simulations used in the results sections 3, 4 and 5 of this manuscript, we used $N_l = 10$.

- c) Flip the loops. In this case, only the red loop is flipped and all the spins touched by the red loop are flipped and all the operators are changed $1 \leftrightarrow 2$. The new configuration is $|\alpha\rangle = |\uparrow\downarrow\uparrow\downarrow\uparrow\downarrow\rangle$ and the operator string has become $S_{(M)=4} = [2,1],[2,1],[1,2],[1,4]$.

- Eventually perform the desired measurements. (Depends on whether it is an equilibration or a measurement step, details on this are given in section 2.2.2).

Now that the SSE algorithm has been explained in detail, let us now describe the different physical measures that it can efficiently perform.

1.3 Measurement of physical observables

Now that we have explained how the SSE algorithm works, we turn our attention to the expectation values of some of the physical observables of interest that can be measured during the SSE simulations. The SSE algorithm aims at good stochastic sampling of the partition function which will allow accessing good expectation values of several physical observables. As a preliminary note, we would like to point out that the identity operators added to the bond operator string are non relevant for the measurements and can be disregarded since they bear no true physical meaning, their roll is to "enlarge" the operator string to size $\mathcal{M}$. There are two kinds of physical observables the SSE mechanism can compute, the diagonal and the off-diagonal observables. We will note the statistical mean over the Monte Carlo configurations of operator $\mathcal{O}$ by $\langle\mathcal{O}\rangle$. In this section, the equivalence between the hard-core bosons and the spins-$\frac{1}{2}$ given by the Matsbura-Matsuda transformation [229] (see eq. (II.21)) becomes apparent since the physical observables measured can be named using either the bosonic or spin vocabularies.

1.3.1 Diagonal observables

The efficient estimators for many static observables in the SSE method were derived by Sandvik *et al.* [275]. Some of these are addressed in this section.

i) Energy and Specific Heat

All operators constituting an elementary interaction of the Hamiltonian $\hat{H}$ can be measured by simply counting how many vertices corresponding to that interaction are present in the operator string $S_{\mathcal{M}}$. By summing over all the elementary interactions of the Hamiltonian, we can access the energy:

$$E = -\frac{\partial \ln Z}{\partial \beta} = -\frac{1}{\beta}\langle n\rangle - N_b\epsilon, \tag{IV.19}$$

where n is the average number of non-identity operators in the operator string $S_{\mathcal{M}}$. The specific heat can be derived from this equality as the fluctuations of n:

$$C_v = \frac{\partial E}{\partial T} = \beta^2\frac{\partial^2 \ln Z}{\partial \beta^2} = \langle n^2\rangle - \langle n\rangle^2 - \langle n\rangle. \tag{IV.20}$$

ii) Density

The density of bosons in the system is linked to the z-component of the spins by the Matsubara-Matsuda transformation (II.21), the expectation value of the bosonic

density is then related to the average magnetization per site:

$$\langle\rho\rangle = \frac{1}{2} + \langle S^z\rangle = \frac{1}{2} + \frac{1}{N}\left\langle \langle\alpha(0)\left|\left(\sum_i^N S_i^z\right)\right|\alpha(0)\rangle \right\rangle, \tag{IV.21}$$

where $\left\langle . \right\rangle$ denotes the average over all Monte Carlo configurations. A related quantity is the local density of bosons:

$$\langle\rho_i\rangle = \frac{1}{2} + \langle S_i^z\rangle = \frac{1}{2} + \left\langle \langle\alpha(0)\left|S_i^z\right|\alpha(0)\rangle \right\rangle, \tag{IV.22}$$

and the total density is given by the average of the local densities: $\langle\rho\rangle = \frac{1}{N}\sum_i^N \langle\rho_i\rangle$.

iii) Compressibility and diagonal susceptibilities

The compressibility of a bosonic system is defined as the second derivative of the energy with respect to the chemical potential $\kappa = -\frac{\partial^2 E}{\partial \mu^2}$. Its equivalent in the spin vocabulary is the uniform static susceptibility $\chi = -\frac{\partial^2 E}{\partial B^2}$, because the equivalent of the external magnetic field B for the spins is the bosonic chemical potential μ. Finally, in the SSE QMC formalism the compressibility reads:

$$\kappa \equiv \chi = \frac{\beta}{N}\left[\left\langle\left(\sum_{i=1}^N S_i^z\right)^2\right\rangle - \left\langle\left(\sum_{i=1}^N S_i^z\right)\right\rangle^2\right]. \tag{IV.23}$$

More generally, the susceptibility between two diagonal operators $\mathcal{O}_1$ and $\mathcal{O}_2$ defined by:

$$\chi_{\mathcal{O}_1\mathcal{O}_2} = \int_0^\beta \langle\mathcal{O}_1(\tau)\mathcal{O}_2(0)\rangle d\tau, \tag{IV.24}$$

is computed in a SSE simulation as:

$$\begin{aligned}\chi_{\mathcal{O}_1\mathcal{O}_2} =& \beta\left\langle \frac{1}{n(n-1)}\left(\sum_{p=0}^{n-1}\mathcal{O}_1(p)\right)\left(\sum_{p=0}^{n-1}\mathcal{O}_2(p)\right)\right. \\ &\left. + \frac{1}{(n+1)^2}\sum_{p=0}^{n}\mathcal{O}_1(p)\mathcal{O}_2(p)\right\rangle,\end{aligned} \tag{IV.25}$$

where we have defined $\mathcal{O}(p) = \langle\alpha(p)|\mathcal{O}|\alpha(p)\rangle$.

iv) Superfluid density

The equivalent of the bosonic superfluid density in the spin language is the spin stiffness, defined as the second derivative of the ground-state energy with respect to a twist Φ in the boundary conditions around one of the axis perpendicular to the

direction of the broken symmetry, which in the thermodynamic limit is the z-axis chosen as the axis of quantisation of the spins.

$$\rho_{\text{sf}} = \left.\frac{\partial^2 E_0(\Phi)}{\partial \Phi^2}\right|_{\Phi=0}. \tag{IV.26}$$

Sandvik derived an efficient estimator for the stiffness, depending only on the ground-state at $\Phi = 0$ [215]. To access it an expansion to second order in Φ of the Hamiltonian in presence of the twist is made:

$$H(\Phi) - H(0) = -\frac{1}{2}\sum_{<i,j>}\left[\Phi^2(S_i^x S_j^x + S_i^y S_j^y) + \imath\Phi(S_i^+ S_j^- - S_i^- S_j^+)\right] \tag{IV.27}$$

The first term is proportional to $H(0)$ and the second term is proportional to the spin current operator:

$$j_s = \frac{\imath}{2}\sum_{<i,j>}(S_i^+ S_j^- - S_i^- S_j^+). \tag{IV.28}$$

It can be shown [215] that if we define the current-current correlation function at Matsubara frequency $\omega_m = 2\pi m T$ by

$$\Lambda_s(\omega_m) = \frac{1}{L^2}\int_0^\beta d\tau \exp^{-\imath\omega_m\tau}\langle j_s(\tau) j_s(0)\rangle, \tag{IV.29}$$

then the stiffness reads [215]

$$\rho_{\text{sf}} = -[\frac{1}{3}E + \Lambda_s(0)], \tag{IV.30}$$

where E is the ground-state energy per spin, given by eq. (IV.19). Finally, the spin stiffness is given by [215]:

$$\rho_{\text{sf}} = \frac{1}{2\beta}\langle w_x^2 + w_y^2\rangle, \tag{IV.31}$$

where we defined the winding number in direction α as:

$$w_\alpha = \frac{N_\alpha^+ - N_\alpha^-}{L}, \tag{IV.32}$$

with N_α^+ and N_α^- respectively the number of operators $S_i^+ S_j^-$ and $S_i^- S_j^+$, with $< i, j >$ a bond in the α direction, that appear in the operator string $S_{\mathcal{M}}$ [215].

1.3.2 Off-diagonal observables

In the original works by Sandvik *et al.* only efficient estimators for static observables were derived in the SSE frame. The system's dynamics were not accessible at the time. Dorneich and Troyer devised an efficient algorithm to calculate a system's dynamic properties by calculating the system's Green's functions within the QMC

SSE formalism [262]. The measurement of such Green's functions requires inserting local changes on world lines, for instance removing a particle at a propagation level p_1 on a world line w_1 and reinserting it at the propagation level p_2 on another world line w_2, while respecting detailed balance during such a process. Furthermore, this process has to sample all distances between world lines (e.g. between sites) $r = w_2 - w_1$ as well as all the distances in propagation direction $\Delta p = p_2 - p_1$. All these requirements are met by the loop update steps which inserts and moves local changes on the vertex network (i.e. in the world line network), hence the Green's functions $G(r, \Delta p)$ can be computed during the construction of the loop update. For the details on this algorithm we refer the interested reader to the original paper by Dorneich and Troyer [262]. Here we will focus on the estimation of the Bose Einstein condensate density, defined as:

$$\langle \rho_0 \rangle = \frac{1}{N} \langle b^\dagger_{\boldsymbol{k}=0} b_{\boldsymbol{k}=0} \rangle = \frac{1}{N^2} \sum_{i,j}^{N} \langle b^\dagger_i b_j \rangle = \frac{1}{N^2} \sum_{i,j}^{N} \langle G^{+-}(i,j) \rangle. \tag{IV.33}$$

with $\langle G^{+-}(i,j) \rangle = \langle b^\dagger_i b_j \rangle$ being the plus-minus Green's functions averaged over all Monte Carlo configurations.

2 Specificities of the SSE simulations for disordered systems

In the previous section, we presented the general features of the Stochastic Series Expansion Quantum Monte Carlo simulations. However, in order to study the Superfluid - Bose glass transition, some subtleties and special considerations have to be taken into account. As a matter of fact, the simulation of quantum disordered systems is very delicate and can suffer from errors coming from different sources like temperature effects as well as statistical Monte Carlo and disorder fluctuations. The issue of computational resources is also very important. The energy shift affects the simulation times and the total computing time can grow very fast with the inverse temperature β, the number of disorder realizations $\mathcal{N}_\mathrm{s}$, the number of measurement Monte Carlo steps N_m and the system size $N = L \times L$ as

$$\tau_\mathrm{cpu} \propto L^2 \times \beta \times N_\mathrm{m} \times \mathcal{N}_\mathrm{s}. \tag{IV.34}$$

This greatly limits the accessible system sizes. In our simulations the biggest available size is $L = 32$. This section addresses how to find the best strategy to optimize the final precision of the results while dealing with finite cpu time and what values have to be used for the parameters β, N_m and $\mathcal{N}_\mathrm{s}$ so as to obtain the most reliable results for the study of the Superfluid - Bose glass transition in 2D.

2.1 Effect of the energy shift

As stated during the presentation of the SSE algorithm in section 1, a way to avoid the dreaded "sign problem" in Quantum Monte Carlo SSE simulations, and hence perform a true ergodic simulation in order to stochastically determine the partition function, is to introduce an energy shift to the diagonal part of the Hamiltonian (see eqs. (IV.2) and (IV.18)).

This shift ensures that all diagonal matrix elements are positive or vanishing. What's more, the shift ϵ has been shown to reduce the probability of a bounce movement happening [266], allowing for longer loops to be formed and we have seen that a bigger value of ϵ helps closing the loops. One might then be tempted to choose a large value of the energy shift ϵ. However, it also appears in the expectation value of the energy as seen in equation (IV.19), hence the average expansion order has a contribution $\epsilon\beta N_b$ which means that the bigger ϵ is, the bigger the average number of non-identity operators in the operator string is and therefore the bigger the cut-off $\mathcal{M}$ will be (cf. fig. IV.5). In the end, the bigger the energy shift ϵ is the longer the simulation time. There is then a compromise to be found.

Figure IV.4 shows the convergence to the ground-state value of the superfluid

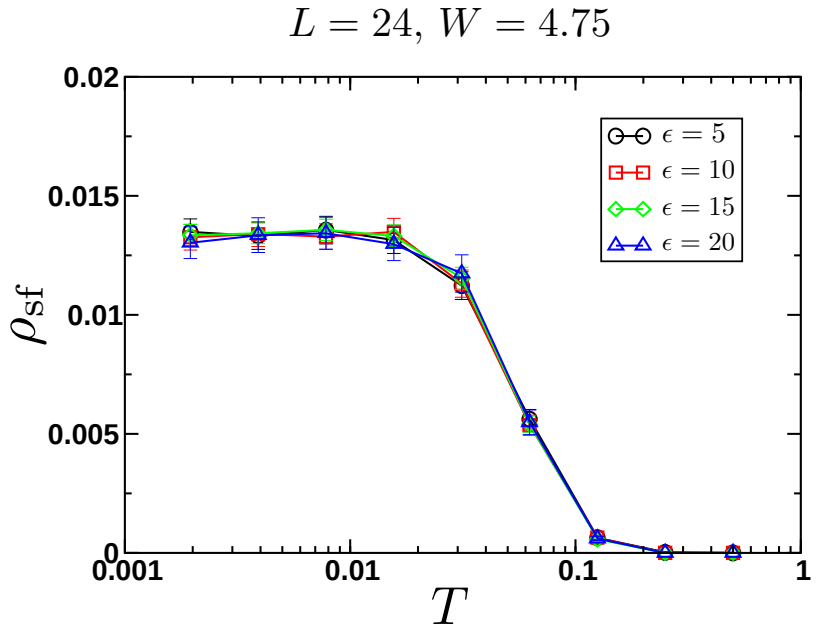

Figure IV.4: *Temperature dependance of the superfluid density for different values of the energy shift ϵ for a system of size $L = 24$ at a disorder strength of $W = 4.75$. All values of the energy shift considered give the same expectation values at all temperatures T. The chosen shift for the simulations is $\epsilon = 10$ (see text).*

density of a system of size $N = 24 \times 24$ at disorder strength $W = 4.75$ for different values of the energy shift ϵ. The data for the biggest values of ϵ have bigger error bars because the number of realizations of disorder is lower because every simulation takes a longer time. We check that the value of the shift does not affect the expectation value of the physical observable being measured for our range of ϵ, this means that our lowest value $\epsilon = 5$ is already big enough to ensure the stochasticity of the simulation. In all the simulations that will be discussed in the following sections of this manuscript, we chose the intermediate shift of $\epsilon = 10$ so as to help the closing of the loops but not be penalized by too long simulation times.

2.2 β-doubling scheme and convergence to the ground-state

2.2.1 Equilibration and thermalization

A QMC SSE simulation involves a cut-off in the Taylor expansion of the partition function, as described in the previous section. It is of paramount importance to assure that this cut-off $\mathcal{M}$ is high enough for the neglected terms of higher order in the expansion effectively do not contribute to the trace in the partition function (IV.7). If this condition is met, the corresponding Monte Carlo configuration is said to be equilibrated and physical observables will be reliably measured. At the same time, the cut-off $\mathcal{M}$ is the length of the operator string $S_{\mathcal{M}}$ and the bigger it is, the longer the simulation will be. The need to find an appropriate value for $\mathcal{M}$ becomes evident since it has to be big but not too much so. During the diagonal update, the number of non-identity operators n in the operator string $S_{\mathcal{M}}$ is changed. This quantity can

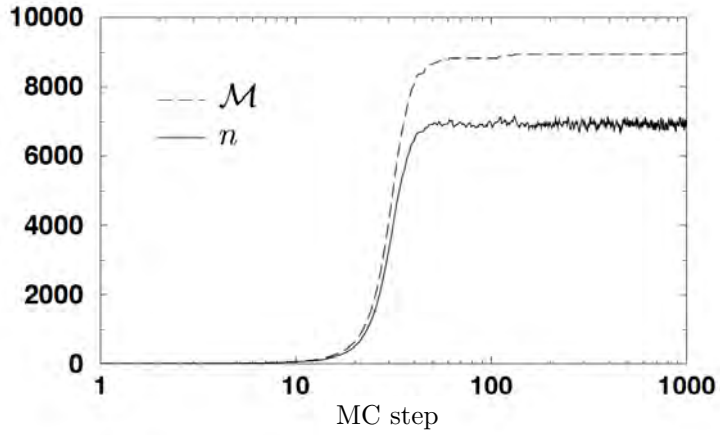

Figure IV.5: *Evolution of the number of non-identity operators n (full line) and the cut-off $\mathcal{M}$ (dashed line) as a function of the number of Monte Carlo steps for a clean XXX chain of spins $\frac{1}{2}$ of length $L = 100$ at the an inverse temperature of $\beta = 100$. Taken from reference [268].*

be used to dynamically adjust the the cut-off $\mathcal{M}$ as follows. The initial $\mathcal{M}_{\text{init}}$ is a small number and at first $n_{\text{init}} = 0$ because we start from an empty operator string. One appropriate way to ensure that during the simulation $\mathcal{M}$ is high enough is to fix the criterion that if $n > 0.8 \times \mathcal{M}$, the cut-off is dynamically readjusted to the new value $\mathcal{M} \to 1.25 \times n$. An equilibrated configuration is obtained when the cut-ff $\mathcal{M}$ reaches a saturation value after a certain number of Monte Carlo steps. This procedure is illustrated in figure IV.5 where both $\mathcal{M}$ and n are plotted versus the number of Monte Carlo steps. It is then convenient to do a number of equilibration Monte Carlo steps N_{eq} where no measurement is made before the actual measurement steps. In the example illustrated in figure IV.5 some $N_{\text{eq}} = 100$ steps are sufficient for the equilibration of the configuration.

2.2.2 Description of the β-doubling scheme

The Superfluid - Bose glass transition is a quantum ($T = 0$) phase transition. We have to ensure we are simulating the ground-state of our system. However, the SSE algorithm works at finite inverse temprature β. The β-doubling scheme was first introduced by Sanvik [216] for the study of the ground-state properties of the site diluted Heisenberg model. It is a very powerful technique allows us to reach extremely low temperatures fairly quickly and at the same time reduce the necessary equilibration steps.

The β-doubling scheme starts by simulating a random disordered sample at high temperature $\beta_1 = 2^1 = 2$. N_{eq} equilibration steps followed (if necessary) by the N_{m} measurement steps are performed, after what the final Monte Carlo configuration at the inverse temperature β_1 is given by a state $|\alpha\rangle$ and an operator string $S_{\mathcal{M}} = [a_1, b_1], \cdots, [a_{\mathcal{M}}, b_{\mathcal{M}}]$. Next, the inverse temperature is doubled so $\beta = \beta_2 = 2^2 = 4$. Let us now note that since the average number of non-identity operators in the string scales as $\langle n \rangle \sim \beta N$, the operator string at β_2 will approximatively be twice as long as the one at β_1. Hence, a very good starting point for the operator string at $\beta_2 = 2\beta_1$ is obtained by doubling and inverting the equilibrated string at β_1:

$$S_{2\mathcal{M}} = [a_1, b_1], \cdots, [a_{\mathcal{M}}, b_{\mathcal{M}}], [a_{\mathcal{M}}, b_{\mathcal{M}}], \cdots, [a_1, b_1] \tag{IV.35}$$

This procedure is repeated until a high inverse temperature $\beta_{h_{max}} = 2^{h_{max}}$ is reached for every disordered sample. During the cooling, the Monte Carlo configuration becomes increasingly equilibrated since the number of equilibration steps taken at a given β_h is effectively $N_{eq}(h) = h(N_{\text{eq}} + N_{\text{m}})$.

Figure IV.6 shows the convergence to the ground-state expectation value of the superfluid and Bose condensed densities calculated for our model (IV.1) for various system sizes at two different disorder strengths (the extremal ones). It is clear that the average expectation values are converged within error bars at different inverse temperatures depending on the system size and the disorder strength. This enables

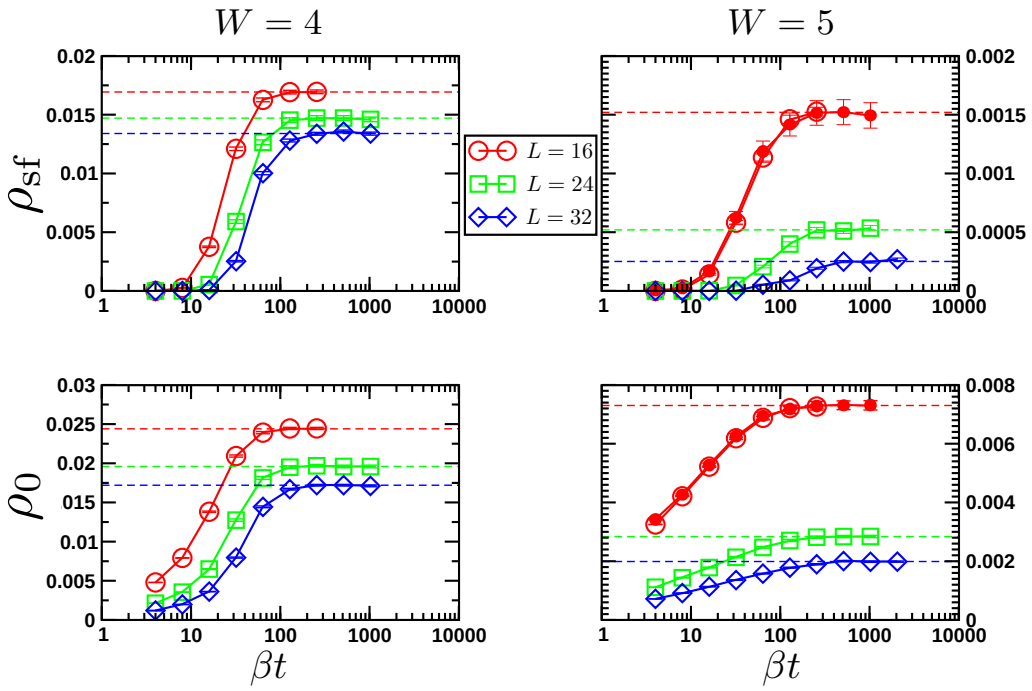

Figure IV.6: *Convergence of the superfluid and Bose condensed densities to the ground-state during the β-doubling procedure for different system sizes and two different disorder strengths. The full red circles in the right panels ($L = 16, W = 5$) are data for a $N_m = 10^4$ measurement Monte Carlo steps, all the other data was obtained with $N_m 10^3$ measurement steps and are in perfect agreement regardless of the number of steps. The dashed lines indicate the β-converged values of the superfluid and BEC densities for every system size and disorder strength.*

us to chose our inverse temperature for the production runs, namely $\beta t = 2^7$ for $L = 12$ and up to $\beta t = 2^9$ for $L = 32$. The same inverse temperatures are enough for all considered disorder strengths for each system size. The best strategy to simulate our model (IV.1) consists then in performing the β-doubling scheme with no measurement steps up to the inverse temperature that ensures ground-state convergence for the given system size and disorder strength and an equilibrated Monte Carlo configuration with $N_{\mathrm{eq}} = 200$ equilibration steps and a dynamically adjusted number of measurement steps N_{m}, as will be explained in more detail in section 2.4.

2.2.3 Actual ground-state convergence

The issue of ground-state convergence is actually a very subtle one. Contributions from low energy excited states strongly depends on the measured physical observable, therefore the actual convergence temperature can be different for different physical

quantities. Furthermore, the convergence to the ground-state achieved with the β-doubling scheme is a an average convergence. As a matter of fact, it is practically impossible to ensure that every individual disordered sample is effectively in its ground-state, *i.e.* the temperature is below the sample's finite-size gap. This comes from the fact that some samples present a finite-size gap smaller than the average one, and actually there can be some samples with extremely low finite-size gaps, meaning that the corresponding temperature for this sample to be in its ground-state is also extremely low.

Figures IV.7 and IV.8 show the evolution of the average compressibility κ, the superfluid density ρ_{sf} and the condensate density ρ_0 during the β-doubling procedure for a disorder strength of $W = 5$ and two different system sizes $L = 8$ and $L = 16$. The compressibility in figure IV.7 follows the expected Curie law at high temperature, saturates to finite value at an inverse temperature of $\beta t = 4$ for both system sizes $L = 8$ and $L = 16$ and only starts to reach its ground-state value of zero (because the finite-size gap renders incompressible the finite-size sample) for very low temperatures around $\beta t \geq 128$ for $L = 8$ and $\beta t \geq 512$ for $L = 16$. The average compressibility is still not strictly vanishing and there are still samples that are not in their ground-

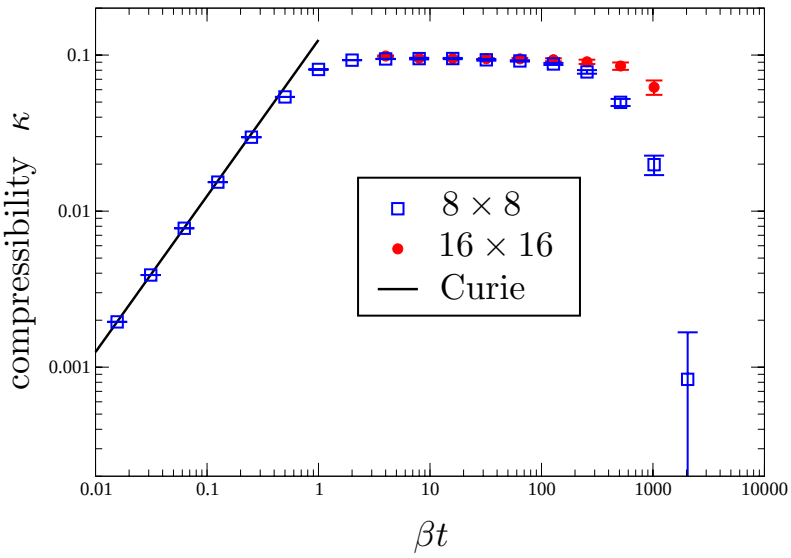

Figure IV.7: *Compressibility of the system as a function of the inverse temperature, during the β-doubling scheme, for two system sizes $L = 8$ and $L = 16$ at disorder strength $W = 5$, inside the Bose glass phase. The data is well described by the Curie law (linear growth in βt) and saturates to finite value of ≈ 0.095 before dropping down to its vanishing ground-state value at low temperatures due to finite-size effects (see text).*

state. On another hand, the superfluid and Bose condensed densities in fig. IV.8 saturate to their ground-state values at a much lower temperature $\beta t = 128$.

The total number of bosons $N_{\text{bosons}} = \langle \sum_i n_i \rangle = \langle N\rho \rangle$ being a good quantum number,it is conserved and can only take integer values in the ground-state. It is then a good observable for determining if a sample effectively is in its ground-state. The right panel of figure IV.8 shows the histogram of N_{bosons} for a system of size $L = 8$ at disorder strength $W = 5$ (BG). We can see that the peaks around the integer values of bossing occupation are rounded, a purely thermal effect. The inset shows the fraction of N-locked samples as a function of the inverse temperature, which is only around 30% for $\beta t = 128$, which amounts to at least some 70% of the samples not being in their ground-state while the average ρ_{sf} and ρ_0 densities appear converged to their ground-state values at that temperature.

Summing up, reaching the actual ground-state for all the disordered samples requires extremely low temperatures ($\beta t \geq 1024$), but fortunately the average estimates of ρ_0 and ρ_{sf} converge to their ground-state values at much higher temperatures and can safely be interpreted as $T = 0$ ones for the temperatures chosen by the β-doubling scheme for studying the quantum Superfluid - Bose glass transition.

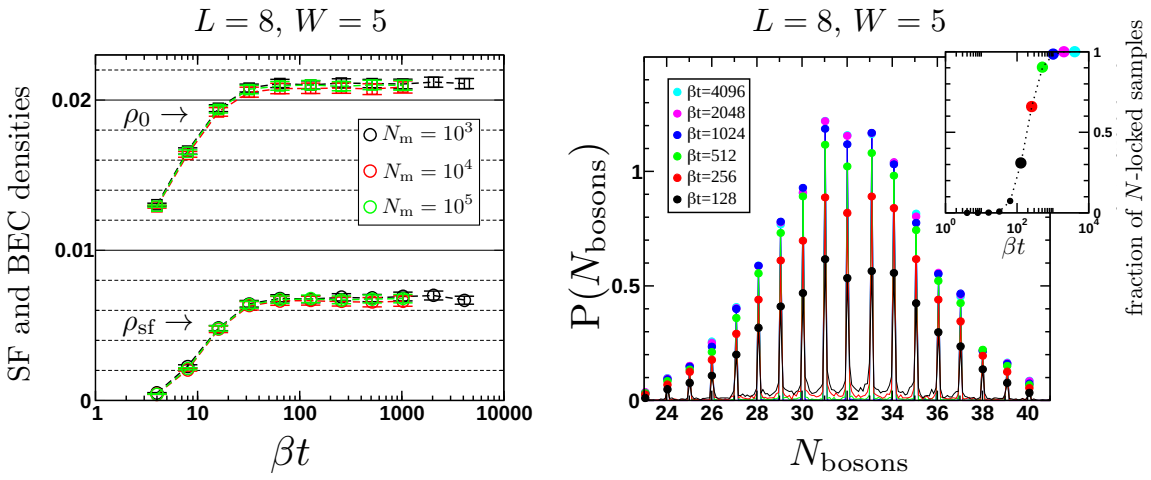

Figure IV.8: *Left panel: Convergence of the superfluid* (○) *and Bose condensed* (□) *average densities to the GS for a system of size* $N = 8 \times 8$ *at disorder strength* $W = 5$ *for different number of measurement steps* N_m*, using* $\mathcal{N}_s \sim \mathcal{O}(10^3)$ *disordered samples. It is clear that the number of measurement steps* N_m *has no effect and the smallest one can be used. Right panel: Distribution of the number of bosons for different inverse temperatures* βt*. Inset: Fraction of samples actually in their ground-state.*

2.3 Estimation of errors: Disorder and Monte Carlo error bars

Any Monte Carlo expectation value is by definition an average of measurements over Monte Carlo configurations and hence inherently presents statistical errors. They can be reduced by generating longer Markov chains, *i.e.* by performing a larger number of measurement steps N_{m} and an exact result would be found in the limit of infinite Monte Carlo measurement steps $N_{\mathrm{m}} \to \infty$. In addition, disordered sample-to-sample fluctuations are another source of statistical errors. Adding more disorder realizations (bigger $\mathcal{N}_{\mathrm{s}}$) is the only way to reduce them. However, the computational time at our disposition is finite meaning that an optimized strategy to obtain the smaller possible final uncertainties needs to be set in action. We already discussed how to choose the proper temperatures in an optimized fashion and this section will address the determination of the dominant source of uncertainties between Monte Carlo and disorder statistical errors and how to achieve the best possible precision in our final results.

2.3.1 Monte Carlo fluctuations vs disorder fluctuations

We try to determine a hierarchy between Monte Carlo and disorder statistical fluctuations to gain more insight on this problem, which means we need to quantify both of them. In order to do so, we take 10 representative disordered samples of a system of size $N = 16 \times 16$ at a disorder strength of $W = 4.6$ inside the SF phase and perform the β-doubling scheme to reduce equilibration times, using N_{eq} steps. 10 independent bins of measurement using N_{m} measurement steps are carried out for each sample, and we use three different values of $N_{\mathrm{m}} = 10^2,\ 10^3$ and 10^4, keeping a constant ratio $N_{\mathrm{m}}/N_{\mathrm{eq}} = 5$. The results for the superfluid stiffness ρ_{sf} and the BEC density ρ_0 are plotted in figure IV.9. On one hand, for $N_{\mathrm{m}} = 100$ (black circles) the estimates from a bin of measurement to another one (*i.e.* the Monte Carlo fluctuations) have a spread of the same order of magnitude as the spread of the estimates for different samples. On the other hand, for a number of measurement steps $N_{\mathrm{m}} \geq 1000$, the Monte Carlo fluctuations are smaller than the disorder fluctuations.

We can partially conclude that at least 1000 measurement steps are needed to make the fluctuations due to the Monte Carlo sampling to be negligible as compared to disorder fluctuations. In order to check if 1000 indeed are enough we plot in figure IV.10, for a system of size $L = 16$ and a disorder strength $W = 5$ inside the Bose glass phase, the full distribution of the logarithm of the superfluid response $\ln(\rho_{\mathrm{sf}})$ using $\mathcal{N}_{\mathrm{s}} \approx 20000$ independent disorder realizations together with the distributions of the same quantity for 5 representative samples using $N_{\mathrm{m}} = 1000$. For each one of these samples around $300 - 400$ independent Monte Carlo estimates with $N_{\mathrm{m}} = 1000$ were carried out. The full distribution over disordered samples was multiplied by a factor of 20 for graphical reasons. The distribution for different Monte Carlo mea-

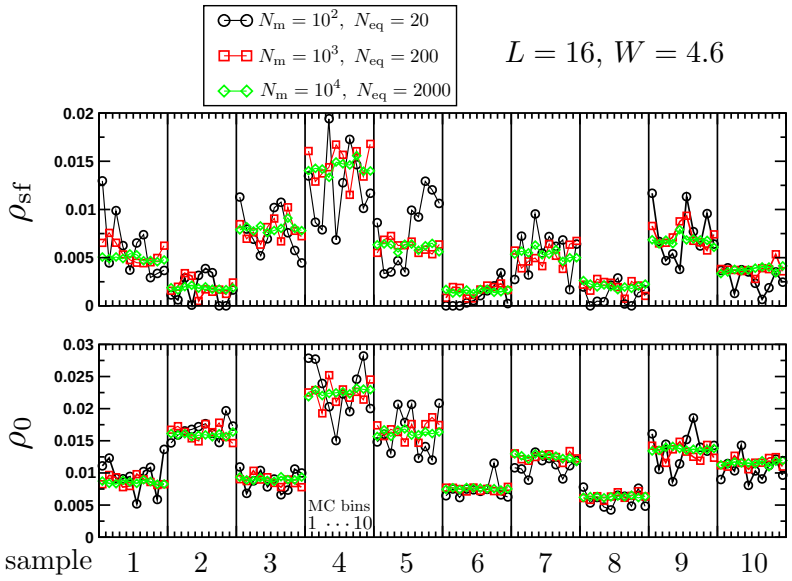

Figure IV.9: *Superfluid and Bose condensed densities for a system of size* $N = 16 \times 16$ *at disorder strength* $W = 4.6$. *The estimates for 10 independent disordered samples are presented. For each one of them, the* β*-doubling procedure using* N_{eq} *equilibration steps was used, followed by 10 independent bins of measurement, each with* N_m *measurement steps, performed only at the lowest temperature* $\beta t = 2^8$. *The 10 computed expectation values for a given sample and number of measurement steps is represented by a data point.*

surements with 1000 steps inside a single disorder realization is clearly much narrower than the full distribution, specially so for the samples exhibiting big values of the stiffness. At most, the spread over Monte Carlo measurements is around one third of the spread of the disorder distribution (red distribution in figure IV.10). This corresponds to the samples with the lowest superfluid response, for which a larger number of measurement steps may be necessary since autocorrelation times for ρ_{sf} are the longest precisely for these samples (*cf.* section 2.4).

As a conclusion, the fluctuations are vastly dominated by the disorder fluctuations and the best strategy to reduce the overall uncertainty of our results is to perform a large amount of disorder realizations using at least 1000 measurement steps, which usually are much larger than the autocorrelation times for the observables of interest, namely the superfluid stiffness ρ_{sf} and the BEC condensate ρ_0. As a matter of fact, there are some samples that present very large autocorrelation times for the superfluid stiffness ρ_{sf}, and 1000 measurement steps are not enough in this case. This issue will be addressed further along in section 2.4.

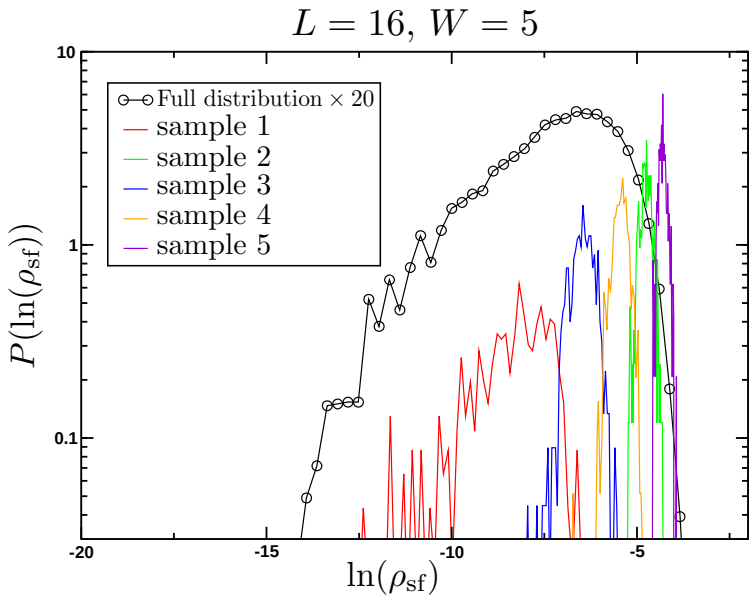

Figure IV.10: *Distribution of* $\ln(\rho_{sf})$ *for a system of size* $N = 16 \times 16$ *at disorder strength* $W = 5$*, inside the Bose glass phase. The black circles curve is the full distribution over* ≈ 20000 *disordered samples, multiplied by a factor of 20 for graphical reasons. The colored lines are the histograms of* $\sim 300 - 400$ *MC measurements made using* $N_m = 10^3$ *steps, shown for 5 representative disordered samples. The spread of the MC measurements distributions is clearly much smaller than the spread stemming from disordered samples.*

2.3.2 Obtaining disorder-converged estimates

Now that we have determined that disorder fluctuations are dominant in our problem, we have to tackle how to reduce them. As stated before, the only way to do so is by adding more disordered samples, keeping in mind that the total computation time grows with the number of disorder realizations (see eq. (IV.34)). In figure IV.10 it can be seen that the distributions of $\ln(\rho_{sf})$ are very wide and need a very large number of disorder realizations to be properly sampled so, a large enough number of samples is needed. In addition, Lin *et al.* found that, for the superfluid-insulator transition in the related model of quantum rotors, around 1000 samples do not give converged estimates [276]. So we may need to use the biggest possible number of samples as possible, without it being too large. To find a good compromise between these two constraints we plotted in figure IV.11 the cumulative averages of the superfluid stiffness ρ_{sf} and the BEC density ρ_0 upon increasing the number of included disorder realizations for two different system sizes $L = 16$ and $L = 32$ and several disorder strengths. The averages drift slowly towards their converged value and it becomes apparent that for the smaller size at least $\mathcal{N}_s \sim 10^4$ disorder samples

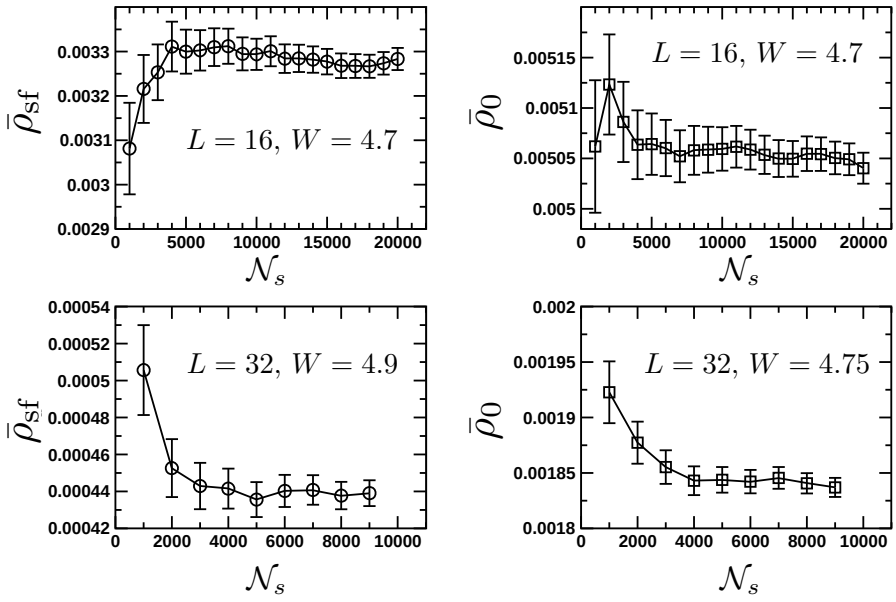

Figure IV.11: *Estimated averages of the superfluid stiffness ρ_{sf} and the Bose condensed density ρ_0 as a function of the number of disordered samples $\mathcal{N}_{\rm s}$ for different system sizes ($N = 16 \times 16,\ 32 \times 32$) and disorder strengths. A very large number of samples ($\mathcal{N}_{\rm s} \gg 1000$) is needed to achieve disorder-converged averages, like in the discussion for a related model [276].*

are needed to achieve a converged estimate and at least $\mathcal{N}_{\rm s} \approx 5000$ for the bigger size. Since the distributions of $\ln(\rho_{\rm sf})$ are very wide (as will be discussed in details in section 4) we choose an even bigger number of samples: for the smaller sizes $L \leq 22$, $\mathcal{N}_{\rm s} \sim 20000$ and for the bigger sizes $L \leq 24$, $\mathcal{N}_{\rm s} \sim 10000$.

2.4 Large autocorrelation times

In section 2.3.1 we determined our best strategy to simulate the Superfluid - Bose glass transition to be using a relatively small number of measurement MC steps $N_{\rm m} = 10^3$ and a big number of disorder realizations. While $N_{\rm m} = 10^3$ is usually much larger than the autocorrelation times for both the superfluid stiffness $\rho_{\rm sf}$ and the Bose Einstein condensate density ρ_0, there are some disordered samples for which the autocorrelation time of $\rho_{\rm sf}$ can reach a few hundreds or even thousands of steps. These samples correspond to the ones with the smallest superfluid densities. A consequence of such long autocorrelation times is that for these samples, the measured stiffness,which is calculated in SSE by the fluctuations of the winding numbers of worldlines (see equation (IV.31)) the change from the zero winding number sector to nonzero winding numbers requires more Monte Carlo steps and using only 1000

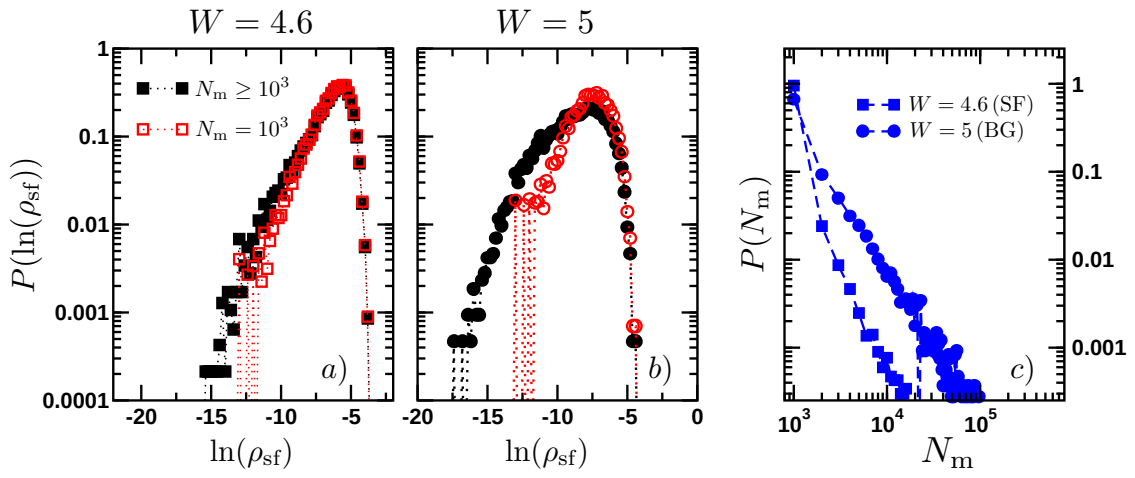

Figure IV.12: *a) Distribution of* $\ln(\rho_{sf})$ *for a system of size* $N = 24 \times 24$ *at disorder strength* $W = 4.6$ *(SF phase)) with 1000 measurement steps (red) and with the dynamical adjustment of the measurement steps (black). b) Distribution of the same quantity for the same size inside the Bose glass phase (*$W = 5$*). The dynamical adjustment procedure allows for the measurement of much smaller superfluid densities, specially inside the Bose glass phase. c) Distribution of the number of Monte Carlo measurement steps* N_m *needed for the two disorder strengths in panels a) and b). In the superfluid phase only* 10% *of the disordered samples required more than* 10^3 *measurement steps, this goes up to around* 30% *inside the Bose glass phase.*

measurement steps will yield a zero estimate for $\rho_{\rm sf}$. As a matter of fact, a vanishing superfluid response is a physically impossible result for a finite-size system even in the Bose glass phase (we remind the reader that in the BG phase the superfluid response vanishes only at the thermodynamic limit $N \to \infty$). It is hence necessary to perform more Monte Carlo measurement steps for these samples, but only for them so as to optimize the computing time. We decide to dynamically adjust, for these cases, the number of measurement steps by performing additional blocks of 1000 Monte Carlo steps until the autocorrelation time is much lower than the simulation time and the computed $\rho_{\rm sf}$ estimate is reliable. This is actually a dynamical adjustment of the stiffness Markov chain length.

We set a maximum limit of $N_{\rm m} = 10^5$ measurement steps for obvious computational time reasons. There are still some rare disorder realizations that need even more steps to leave the zero winding number sector and their superfluid response will be wrongly evaluated to zero. These samples cannot be included for the evaluation of distributions of $\ln(\rho_{\rm sf})$ nor the typical stiffness. They may or may not be included for the evaluation of the average stiffness though, and this should be done with caution since a bias may be added in both cases! A careful discussion on this subject will be held in section 3.1.2.

To illustrate the effect of our dynamic Markov chain length adjustment method, figure IV.12 shows the distributions of $\ln(\rho_{\rm sf})$ for a system of size $L = 24$ at two different disorder strengths, one inside the superfluid phase $W = 4.6$ (panel a) and the other in the Bose glass phase $W = 5$ (panel b), with a fixed number of measurement steps $N_{\rm m} = 10^3$ (in red) and with the dynamic adjustment method (in black). The fact that for $W = 4.6$ the system is in the superfluid phase and for $W = 5$ in the Bose glass phase will become clear in section 3.1.4. A low cut-off in the measured superfluid response is present when only 1000 steps are used and the implementation of our dynamic adjustment method clearly shifts this cut-off to lower stiffness values, specially in the BG regime. This is of paramount importance for the qualitative and quantitative studies of these distributions (cf. section 4) since they could not have been properly sampled.

In order to quantify the incidence of need of our method, we show in panel c) of figure IV.12 the distribution of the number of measurement steps $N_{\rm m}$ required to obtain the distributions in panels a and b. In the SF phase around 5% of the disorder realizations used more than 1000 measurement steps and $\mathcal{O}(10^4)$ seems to be the largest number of steps that were needed. In the BG phase around 33% of the realizations used more than 1000 steps and our maximal limit of 10^5 measurement steps was reached, although very few samples did.

Now that the technical details of our simulations have been presented, we can proceed to the presentation of our results for the superfluid - Bose glass transition.

3 Critical exponents of the SF-BG phase transition

The ground-breaking work of Fisher *et al.* [6], extended the Josephson relations [172] for classical phase transitions driven by thermal fluctuations to get a hyperscaling relation for quantum ($T = 0$) phase transitions where quantum fluctuations drive the system from one phase to the other. Some bounds for the critical exponents were derived [6](see first line in table IV.2) and have ever since been tested but no general consensus has been reached, particularly over the equality $z = d$ [6, 157, 160, 176, 178–182, 270, 271]. This section shows how we extracted estimates for these critical exponents from the Quantum Monte Carlo simulations described in the previous sections using finite-size scaling analysis and bootstraping for evaluation of errors.

3.1 Critical exponents for average quantities

We focus our attention on the scaling properties of the average superfluid response $\rho_{\rm sf}$ and the Bose Einstein condensate density ρ_0 with system size in order to extract

the critical exponents and critical disorder strength for the Superfluid - Bose glass transition with our model (IV.1).

3.1.1 Finite size scaling analysis

The derivation of the scalings with system size was treated in section 2.3.2 of the Introduction chapter I, here we just remind the important results.

The superfluid response is shown to scale, for simulations on a finite lattice of size L, as [6]:

$$\rho_{\rm sf}(L) = L^{-(d+z-2)}\ \mathcal{G}_{\rm sf}[L^{1/\nu}(W - W_c)], \tag{IV.36}$$

where z is the dynamical critical exponent, ν the correlation length exponent, W_c the critical disorder, and $\mathcal{G}_{\rm sf}$ a universal function. So in the vicinity of the 2D quantum critical point, the finite-size scaling of the SF density is:

$$\rho_{\rm sf}(L) = L^{-z}\ \mathcal{G}_{\rm sf}[L^{1/\nu}(W - W_c)]. \tag{IV.37}$$

The actual order parameter for the transition is the Bose Einstein condensate density which displays a critical scaling:

$$\rho_0(L) = L^{-(d+z+\eta-2)}\ \mathcal{G}_0[L^{1/\nu}(W - W_c)], \tag{IV.38}$$

with η the anomalous exponent. In our 2D case this yields the scaling:

$$\rho_0(L) = L^{-(z+\eta)}\ \mathcal{G}_0[L^{1/\nu}(W - W_c)]. \tag{IV.39}$$

Before performing the scaling analysis, we need to correctly compute the estimate of the average with its error bar for each system size and disorder strength. While the estimate of the average is simply given by the average over disorder realizations of the Monte Carlo averages, the error bar estimation is more complex. In fact, since the distributions have special shapes the central limit theorem estimate of the error bar as $\sigma_{\rm sf|0}/\sqrt{\mathcal{N}_s}$ is not reliable. The best way to estimate the error bars is then to perform a bootstrap analysis [253]. For this, we generate a set of bootstrap samples by randomly selecting a subset $\{i_{BS}\}$ from the $\mathcal{N}_s$ realizations with replacement (*i.e.* we select in total $\mathcal{N}_s$ realizations from the total data set with the possibility to choose the same data point several times) which we then average over $\{i_{BS}\}$. This is repeated approximatively 1000 times and the standard deviation of such calculated averages is indeed an accurate estimator of the error bar [253].

We can now do the scaling analysis by fitting our average estimates of $\rho_{\rm sf}$ and ρ_0 (with their respective error bars) to the scaling forms (IV.37) and (IV.39) respectively, where we have Taylor expanded the scaling functions $\mathcal{G}_{\rm sf}$ and $\mathcal{G}_0$ to an order high enough so that the qualities of the fit are acceptable (see table IV.1 and equation (IV.41)), namely to third order in $L^{1/\nu}(W - W_c)$. We get the best estimates of the critical disorder strength W_c and the critical exponents z, ν and η. To extract error bars on our best estimates of the critical parameters we perform a

gaussian resampling of our data for ρ_{sf} and ρ_0 within the error bars determined by the bootstrap analysis and perform the same scaling fits multiple times, typically 100 times are enough since the uncertainties for each window of size and disorder strength is very small compared to the ones coming from different windows, specially in system size (*cf.* figure IV.14). The standard deviation of such fit results represent the statistical error of the final results.

As a means for quantifying the quality of our fits, we calculate the sum of squared residuals

$$\chi^2 = \sum_i \left((\rho^i_{\mathrm{sf}|0} - \mathrm{fit}(W_i, L))/\sigma_i \right)^2 \tag{IV.40}$$

and the probability Q of finding a χ^2 greater or equal than this value given the fit by

$$Q = \frac{1}{\Gamma(n_{\mathrm{dof}}/2)} \int_{\chi^2/2}^{\infty} \mathrm{d}y y^{n_{\mathrm{dof}}/2-1} \mathrm{e}^{-y}, \tag{IV.41}$$

following Young [253].

In order to take into account possible systematic effects, we apply this procedure for different windows of system size and disorder strengths. Our final estimates and their error bars are determined by the total fluctuations of all the fit results which will be presented further along in section 3.1.4 (see figure IV.14).

3.1.2 Inclusion of samples with long autocorrelation times

As discussed in section 2.4, our dynamical adjustment of the Markov chain length so as to properly estimate very low stiffness values, was imposed a maximum number of measurement steps of 10^5 for computational time reasons and the rare realizations of disorder which needed more steps are evaluated to zero stiffness. This result is not possible for a finite-size system, even inside the Bose glass phase. However, plainly neglecting such samples for our analysis may introduce a bias. It is worth noting that our analysis leads us to speculate that these samples have actually been simulated out of their ground-state at too high a temperature. We will now discuss how to include them in a careful way that does not also induce a systematic bias.

First, simply adding these samples to the analysis explained in section 3.1.1 would necessarily introduce a bias since the added values are not physical. This would amount to approximating the distribution of ρ_{sf} by a distribution with a cut-off (*i.e.* the lowest measured stiffness for each system size and disorder strength) and a δ-peak in zero. This is obviously wrong because the real distribution vanishes at zero stiffness and the delta peak due to not long enough simulations at too high temperatures.

Another way consists try to extrapolate the distribution of $\ln(\rho_{\mathrm{sf}})$ for each couple (L, W) to zero by a power law tail, which seems justified. However, its most negative part is the least properly sampled one, therefore a good reliable extrapolation cannot be obtained. In other words, any extrapolation one could try would not be justified.

A third solution, consists in replacing the non physical zero values by half the value of the cut-off (*i.e.* the minimal computed stiffness for every couple (L, W)) and adding them to the data set. This is equivalent to approximating the real distribution by a distribution with a cut-off (the same as for the first possibility) and a box distribution below it which is only justified by the fact that the approximated part of the distribution has a very small weight. We chose this solution and performed the data analysis procedure to check for the stability of our results. We find that the inclusion of these samples does not change our final results. This is illustrated in figure IV.14 in section 3.1.4, along with all the estimates of the critical parameters.

3.1.3 Correction of systematic errors

Despite our efforts for reducing the source of uncertainty (see section 2), some systematic errors may still be present. Two of them are known and expected to have low influence in the final results (see section 2), namely, problems in convergence to the ground-state (*i.e.* thermal errors) and the fluctuations of the Monte Carlo statistical estimates. We will now describe how to deal with errors.

i) Thermal errors

In spite of the fact that our careful β-doubling procedure was carried out to ensure the convergence to the ground-state (see section 2.2.2), it cannot be ensured that all samples are effectively in their ground-state (see section 2.2.3). Hence one should still pay attention to potential systematic bias that may be introduced by the rare disorder realizations that may have not fully converged to their ground-state values for $\rho_{\rm sf}$ and ρ_0. To do so, we fit the β-doubling curves of $\rho_{\rm sf|0}$ as a function of temperature to the following form

$$\rho_{\rm sf|0}(\beta) = \rho_{\rm sf|0}(\beta \to \infty) - A_{\rm sf|0} \exp\left(-\beta/\beta_{\rm sf|0}\right), \tag{IV.42}$$

which turns out to describe quite well our results near the convergence inverse temperature with the following fitting parameters

$$\begin{cases} A_{\rm sf} \approx \dfrac{2}{L^2}, \\ A_0 \approx \dfrac{1}{L^2}, \\ \beta_{\rm sf} = \beta_0 \approx 0.1 L^2, \end{cases} \tag{IV.43}$$

as shown in figure IV.13 three different system sizes ($L = 16, 24, 32$) at disorder strength $W = 5$. The fits (thick dashed curves) are particularly good near the convergence which justifies using them to correct the systematic thermal errors.

The phenomenological law (IV.42), allows us to estimate the corrected average stiffness and Bose condensate densities estimates to get the the ground-state converged values and then perform the full scaling analysis for a comparison of the

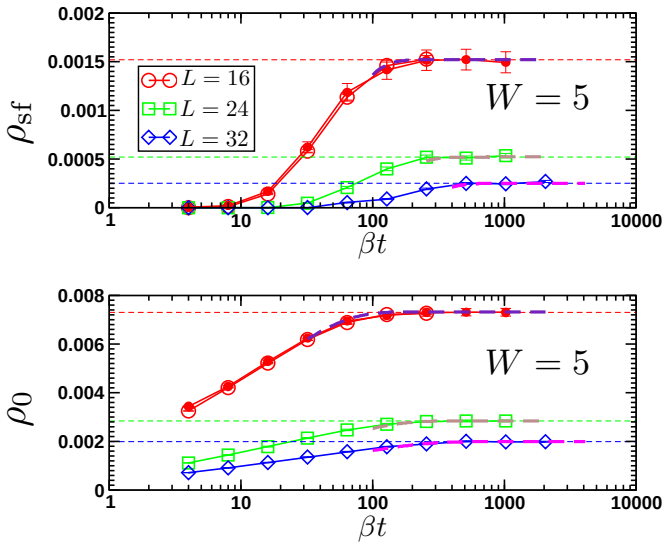

Figure IV.13: *β-doubling curves for the average superfluid response ρ_{sf} and the Bose condensed density ρ_0 for three different system sizes $N = 256, 576$ and 1024 at disorder strength $W = 5$. The fits to the phenomenological law* (IV.42) *using the parameters* (IV.43)*, represented by the thick dashed color lines, describe the curves particularly well near the convergence.*

results and provide a check of their stability (see figure IV.14 in section 3.1.4) and conclude that their inclusion does not change our final estimates.

ii) Monte Carlo fluctuations

In section 2.3.1 we showed how Monte Carlo fluctuations are much smaller than those brought about by different independent disorder realizations (see figures IV.10 and IV.9), however completely neglecting them could induce some systematic bias. In order to take this contribution into account in the calculation of the error bars for each system size and disorder strength, we add one step to the bootstrap analysis, namely, we dram a Gaussian random number distributed according to

$$p(x) = \frac{1}{\sqrt{2\pi}\sigma_{\mathrm{MC}}} \mathrm{e}^{-(x-\rho)^2/(2\sigma^2_{\mathrm{MC}})} \tag{IV.44}$$

around the Monte Carlo estimate , with standard deviation equal to the standard deviation of the Monte Carlo configurations σ_{MC} for each selected sample, which we then average over $\{i_B\}$. The final estimates for the critical parameters remain unchanged when adding such corrections as can be seen in figure IV.14.

3.1.4 Critical parameter estimates

The previous sections described the simulation details and the data analysis scheme for our model for the superfluid - Bose glass transition. We now discuss the estimates we get by applying said schemes, including all the subtleties and corrections described earlier. Figure IV.14 shows the best estimates for the four critical parameters (the critical threshold W_c, the dynamical exponent z, the correlation length exponent ν and the order parameter exponent η) for different windows of size $[L_{\min}; 32]$ and different included disorder strengths (different colors). The estimates obtained by the scaling of the Bose condensed density ρ_0 are represented by circles and those obtained via the superfluid stiffness ρ_{sf} by squares. Full symbols depict

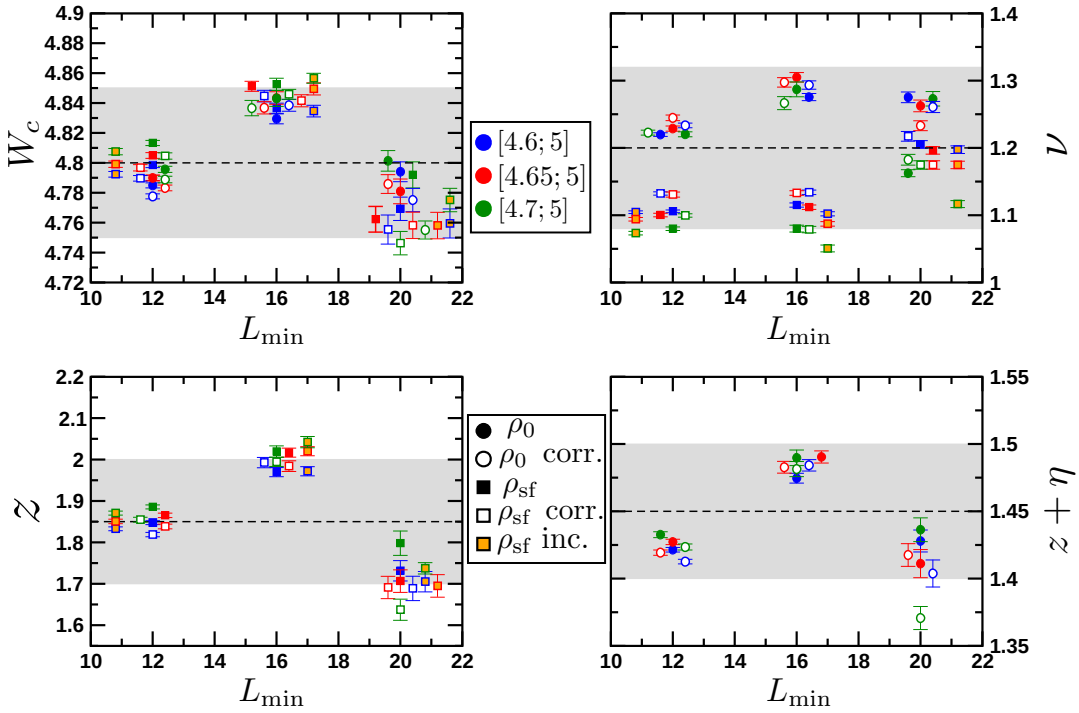

Figure IV.14: *Bootstrap estimates of the critical exponents for different disorder and system size windows. Different colors represent the estimates for different windows of disorder. Circles depict estimates obtained with the scaling of the BEC density ρ_0 and squares those obtained via the superfluid density ρ_{sf}. Full symbols correspond to critical parameter estimates when no systematic error correction is added and open symbols estimates where both the Monte Carlo and temperature systematic error corrections are included. Orange-filled squares are the estimates when the samples with too long auto-correlation times for the stiffness are included (cf. section 3.1.2). The dashed line gives the final best estimates and the shaded area the final uncertainties.*

the final bootstrap results when the systematic errors from temperature and Monte Carlo fluctuations are completely neglected while open symbols are the results with the inclusion of corrections to these errors as discussed in section 3.1.3. Finally, orange-filled squares correspond to estimates obtained via the stiffness when including the rare samples with too long auto-correlation times as discussed in section 3.1.2. Clearly, the estimates and their error bars are not affected by the inclusion of long auto-correlation times samples and corrections to thermal effects and Monte Carlo fluctuations. Hence, we decided to neglect all these effects. It is worth noticing that neglecting the zero stiffness samples allows us to treat on equal footing the typical and average stiffness. Despite our best efforts, some systematic size effects are still present, as can be seen from the fact that estimates have strong fluctuations when changing the fit window in size, which translates to quite big error bars on the final estimates.

	Q_0 ($\times 100$)			Q_{sf} ($\times 100$)		
L_{min}	$[4.6;5]$	$[4.65;5]$	$[4.7;5]$	$[4.6;5]$	$[4.65;5]$	$[4.7;5]$
12	8.7	13.3	16.2	4.5	4.25	11
16	7	15.2	13.5	4	5	9.2
20	21.3	39.75	33.8	37.5	39.25	39.5

Table IV.1: *Quality of the fits of the critical parameters from the Bose condensed density (Q_0) and from the superfluid density (Q_{sf}), corresponding to the parameters shown in figure IV.14 for different windows of disorder and of system size* $[L_{\mathrm{min}};32]$*, neglecting corrections due to thermal effects and Monte Carlo fluctuations as well as the zero stiffness samples.*

Table IV.1 shows the qualities of fit for all windows in system size and disorder strength where all systematic corrections have been neglected. We see that the qualities for the the window $[L_{\mathrm{min}};32]$ are systematically higher, as expected since reducing the number of system sizes included in the analysis while keeping the bigger sizes means that there is less size dynamics, hence the fact that no drift term is included in the fits becomes more justified. Secondly, the bigger system sizes have slightly bigger relative error bars so the corresponding χ^2 is smaller and the quality of fit Q larger as these two quantities are very sensible to the error bars.

Our final estimates with their (quite large) error bars are shown in table IV.2 along with the estimates from previous works for the SF-BG transition in 2D, with different models. We stress the fact that the superfluid stiffness and the BEC condensate vanish at exactly the same critical point $W_c = 4.80(5)$, which was not clear from semi-classical results (*cf.* section 3.1 of chapter III and Ref. [271]). Our results are in agreement within error bars with the estimates of Ref. [179] for the same model

z	ν	η	W_c	Reference
2	≥ 1	≤ 0		Fisher *et al.* [6]
1.7	1.4	n.a.	n.a.	Zhang *et al.* [181]
2.0(1)	0.9(1)	n.a.	n.a.	Sørensen *et al.* [178]
0.5(1)	2.2(2)	n.a.	2.5	Makivić *et al.* [160]
2.0(4)	0.90(13)	n.a.	4.95(20)	Zhang *et al.* [179]
1.93	1.38	n.a.	n.a.	Herbut [157]
1.40(2)	1.10(4)	−0.22(6)	4.42(2)	Priyadarshee *et al.* [182]
1.80(5)	1.15(3)	−0.3(1)	n.a.	Meier *et al.* [270]
1.88(8)	0.99(3)	−0.16(8)	4.79(3)	Ng and Sørensen [277]
1.85(15)	1.20(12)	−0.40(15)	4.80(5)	Álvarez Zúñiga *et al.* [247]

Table IV.2: *Various estimates of critical exponents and disorder strength W_c for the Superfluid–Bose glass transition of different models in 2D. The results are shown in chronological order.* n.a. *= not available.*

although much more precise due to the fact that the system sizes available to us were much larger. There is also a very good agreement with the results of Ref. [277] also on the same model, and the estimates of Ref. [270] for the closely linked model of quantum rotors [144]. The results of references [160] and [182] most probably suffer from small system sizes, finite temperature effects or not sufficient disorder averaging.

Concerning the boundaries predicted by Fisher *et al.* [6] (*cf.* first line of table IV.2), our best estimates satisfy both the Harris criterion $\nu \geq 2/d = 1$ [173–175] and the boundary for the anomalous exponent $\eta \leq 0$. As for the dynamical exponent, the much debated equality $z = d = 2$ is still compatible within our error bars but our best estimate is lower, indicating that $z < d$, in agreement with Ref. [270] and the theoretical arguments in Ref. [176].

In order to show that our data is very well described by the scaling relations (IV.37) and (IV.39), we plot in figure IV.15 the curves of $\rho_{\mathrm{sf}} \times L^z$ and $\rho_0 \times L^{z+\eta}$ for all system sizes L as function of disorder strength with our best estimates for the shown window in sizes $[12; 32]$ and disorder strengths $W \in [4.6; 5]$, $z \simeq 1.85$, $W_c^{\mathrm{sf}} \simeq 4.8$, $W_c^0 \simeq 4.79$, $z + \eta \simeq 1.42$, $\nu_{\mathrm{sf}} \simeq 1.1$, $\nu_0 \simeq 1.2$, and the Taylor expansion of the universal scaling functions $\mathcal{G}_{\mathrm{sf}|0}$ is to third order polynomial in $L^{1/\nu}(W - W_c)$. An excellent crossing with no sizeable drift is achieved with the critical parameters for this window. Irrelevant corrections to scaling are practically absent, contrary to the scaling of the typical stiffness (*cf.* figure IV.16 in section 3.2). The insets show the same curves *vs.* the rescaled length $L/\xi = L|W - W_c|^\nu$ where an almost perfect collapse of the data further justifies our scaling forms and results.

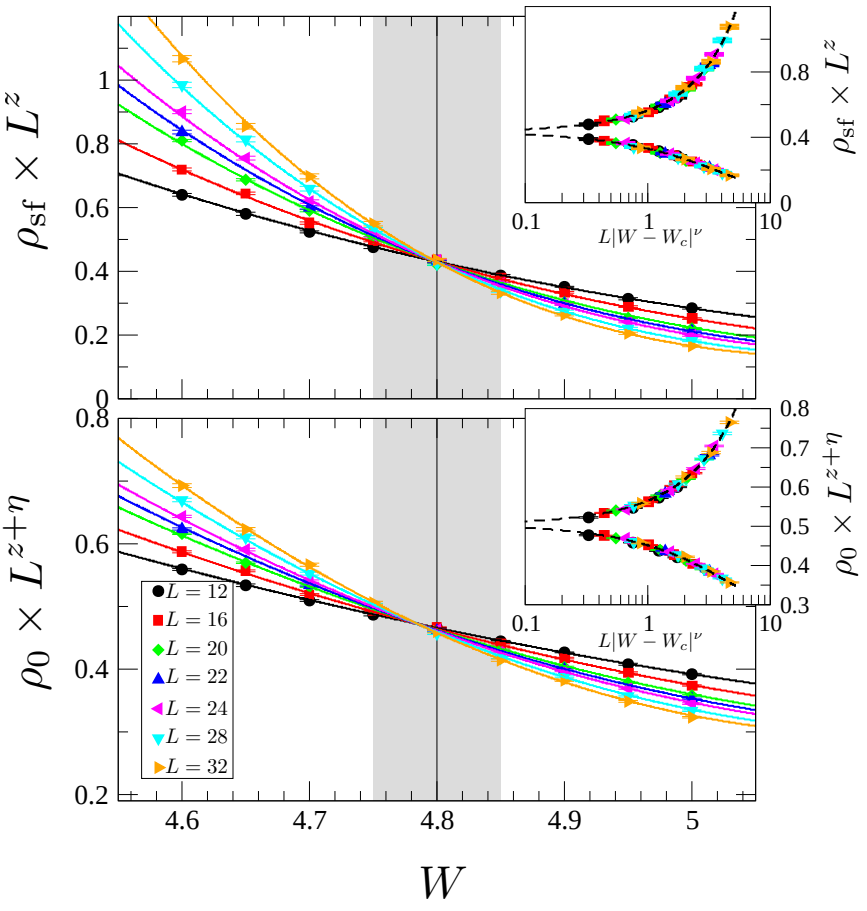

Figure IV.15: *Example of the scaling analysis of the SF ρ_{sf} (top) and BEC ρ_0 (bottom) densities including all system sizes $L \in [12; 32]$ and disorder strengths $W \in [4.6; 5]$. Solid lines depict the best fits to the universal scaling functions eqs.* (IV.37) *and* (IV.39) *yielding $z \simeq 1.85$, $W_c^{\rm sf} \simeq 4.8$, $W_c^0 \simeq 4.79$, $z + \eta \simeq 1.42$, $\nu_{\rm sf} \simeq 1.1$, $\nu_0 \simeq 1.2$, and $\mathcal{G}_{sf|0}$ 3rd order polynomials. The final estimate of the critical point $W_c = 4.80(5)$ is shown by the grey areas. Insets: data collapse when rescaling the system size L by $1/\xi = |W - W_c|^\nu$ with $\nu = 1.2$ and $W_c = 4.8$. The collapse is almost perfect.*

3.2 Critical exponents for the typical stiffness

The distinction between the typical and average quantities can be very important. While the former refers to the most likely value of a physical quantity, the latter is just an ensemble average. Some early studies on the random bond model made the confusion between the two [278], making the comparison to, for instance, neutron scattering experiments which can only access *average* quantities, impossible. The typical and average behaviours of the order parameter or other interesting quantities have been found in some cases to be very different. For example, in a very meticulous

study of the random transverse-field Ising chains by real-space strong disorder renormalization group, Daniel Fisher found that the critical exponent of the correlation length for typical and mean spin-spin correlations are different, namely $\nu_{\rm typ} = 1$ and $\nu_{\rm avg} = 2$ [279]. It is then worthwhile investigating also the typical stiffness defined by

$$\rho_{\rm sf}^{\rm typ} = \exp(\overline{\ln(\rho_{\rm sf})}) \tag{IV.45}$$

where $\overline{(.)}$ denotes the average over disorder realizations, so as to compare its scaling with the average one. We stress the fact that only the typical stiffness will be considered since the BEC density ρ_0 as defined in SSE (*cf.* equations (IV.33)) is the average over the entire sample of the plus-minus Green's functions. Therefore, the typical BEC density is cannot be accessed in this framework.

The typical stiffness can be described by a similar scaling hypothesis than the average one, eventually including irrelevant corrections, such that [280, 281]

$$\rho_{\rm sf}^{\rm typ}(L) = L^{-z}\left(\mathcal{G}_{\rm sf}^{\rm typ}[L^{1/\nu}(W - W_c)] + cL^{-y}\right). \tag{IV.46}$$

When performing the same data analysis procedure than with the average stiffness using a Taylor expansion of the universal scaling function $\mathcal{G}_{\rm sf}^{\rm typ}$ up to third order, the fits are very unstable due to the irrelevant corrections. A way to check if the scaling for the typical stiffness is the same as for the average one consists in fixing the parameters to our best estimates for the average quantities, $z_{\rm typ} = 1.85$, $\nu_{\rm typ} = 1.2$ and $W_c^{\rm typ} = 4.8$, and extract the remaining irrelevant parameters with our data analysis scheme. This is represented in panel *a*) in figure IV.16 where a sizeable drift to the critical point is visible, well described in that window of disorder by the scaling function with irrelevant corrections in eq. (IV.46) with parameters $c = 1.13(8)$ and $y = 0.97(4)$.

Perhaps, a more convincing way to check whether the critical exponents are really the same for the typical and the average stiffness is to divide $\rho_{\rm sf}^{\rm typ}$ by its value at W_c, in order to cancel out the irrelevant corrections $\sim L^{-y}$, and plot it against the system size L rescaled by the correlation length $\xi = |W - W_c|^{-\nu}$ with $\nu = 1.2$ and $W_c = 4.8$ (estimated from the average stiffness). This is shown in figure IV.16 (b) for $4.0 \leq W \leq 5.5$ and all available system sizes $12 \leq L \leq 32$, where an almost perfect collapse without any additional adjustable parameters is achieved. This demonstrates that the quantum critical behaviours of average and typical superfluid densities are similar, specially their critical exponents $z_{\rm avg} = z_{\rm typ} = 1.85(15)$, a smaller value than $d = 2$ although still compatible within error bars; and $\nu_{\rm typ} = \nu_{\rm avg} = 1.20(12)$ which fulfils the Harris criterion $\nu \geq 2/d = 1$ [173–175].

In addition, the study of the distributions of $\ln(\rho_{\rm sf})$ at criticality shows that for different system sizes the distributions are similar up to a shift $z\ln(L)$, further verifying that typical and average superfluid densities have the *same* critical scalings (*cf.* figures IV.18 and IV.19 in section 4).

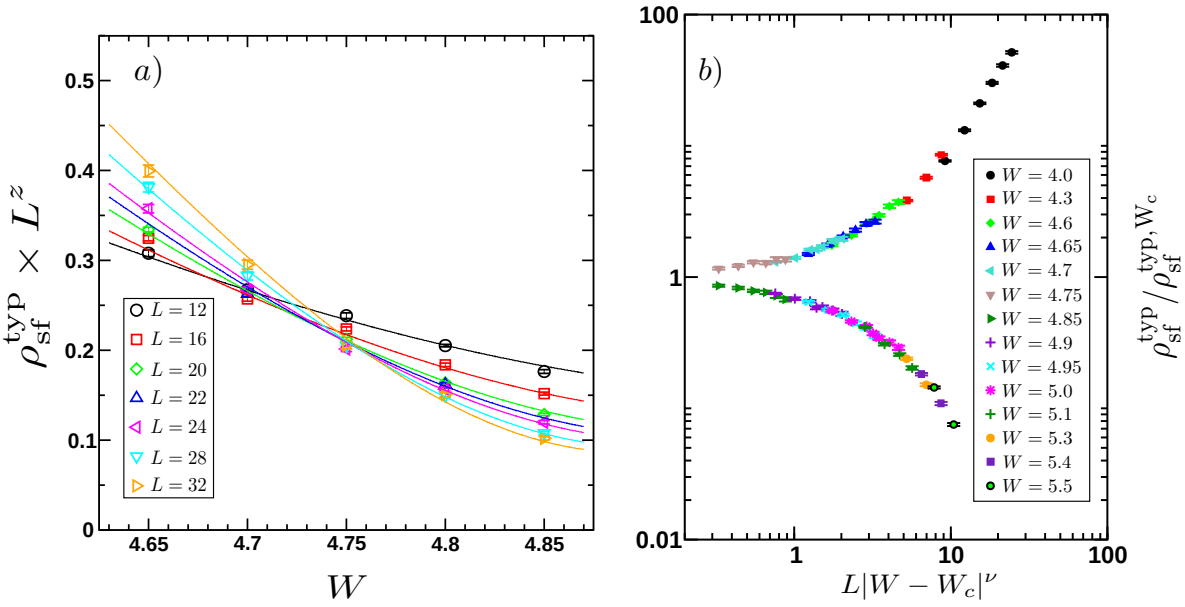

Figure IV.16: *Panel a) Scaling of the typical SF density plotted as* $\rho_{\rm sf}^{\rm typ} \times L^z$ *against disorder strength with fixed* $W_c = 4.8$, $\nu = 1.2$ *and* $z = 1.85$. *The scaling form* (IV.46) *yields an estimated irrelevant exponent* $y = 0.97(4)$. *Panel b):* $\rho_{\rm sf}^{\rm typ} / \rho_{\rm sf}^{\rm typ, W_c}$ *plotted against* $L|W - W_c|^\nu$, *with fixed* $\nu = 1.2$. *The data exhibit an almost perfect collapse for* $4 \leq W \leq 5.5$ *and* $12 \leq L \leq 32$ *with no additional parameters.*

4 Distributions of the superfluid response

The issue of self-averaging is closely linked to fluctuations in the considered thermodynamic phase, a self-averaging phase having its fluctuations governed by the central limit theorem. If this is not the case there is a breakdown of self-averaging which necessarily means that any physical quantity has a finite variance in the thermodynamic limit, as shown by Aharony and Harris [282]. Hence, the broadening (or lack thereof) of the finite-size distributions with growing system sizes is a distinct character of the lack of (or presence of) self-averaging. Motivated by the fact that the study of the inhomogeneous properties of the different present phases via the distributions of the order-parameter or of relevant energy scales has improved the understanding of the microscopic nature of the concerned thermodynamical phases, *e.g.* for 3D dilute Ising models [283], random transverse-field Ising spin chains (1D) [279, 284] and strongly disordered superconductors [25, 30]; and that the Bose glass phase has been predicted to break self-averaging [272, 285] but never studied using exact numerical methods, we carry out such a study. It will be presented in this section first qualitatively then in a more quantitative manner.

4.1 The issue of self averaging: qualitative results

The relevant quantity for this study is the natural logarithm of the superfluid response $\ln(\rho_{\rm sf})$, since at the thermodynamic limit, $\rho_{\rm sf}$ vanishes exactly at the critical point $W = 4.80(5)$(*cf.* table IV.2 in section 3.1.4), separating the superfluid phase where $\rho_{\rm sf}$ is finite and the Bose glass phase with $\rho_{\rm sf} = 0$. However, another test for self-averaging is comparing the average and typical superfluid stiffness. Indeed, in a self-averaging phase these two quantities are identical at the thermodynamic limit $N \to \infty$ whereas they will be different if self-averaging breaks down. In figure IV.17 we plotted the ratio of these two quantities $\mathcal{R} = \rho_{\rm sf}^{\rm avg}/\rho_{\rm sf}^{\rm typ}$ *vs.* system size in both the SF (a) and BG (b) phase as well as at the QCP (c). Deep inside the SF phase we recover the known result that the SF phase is self-averaging, because the ratio $\mathcal{R}$ tends to one with increasing system size. Self-averaging breaks down at the quantum critical point (QCP) and inside the BG phase: while the ratio $\mathcal{R}$ increases with system size in both cases, it saturates to a finite value larger than one value at the transition.

It is worth noticing that $\mathcal{R}$ is always bigger than one, which translates to $\rho_{\rm sf}^{\rm typ} < \rho_{\rm sf}^{\rm avg}$, meaning that the distributions of $\ln(\rho_{\rm sf})$ are asymmetric with more weight on the lower values of $\ln(\rho_{\rm sf})$ as can be seen in figures IV.18, IV.10 or IV.12. On the one hand, when $\mathcal{R}$ decreases with system size like in the SF phase (*cf.* fig. IV.17

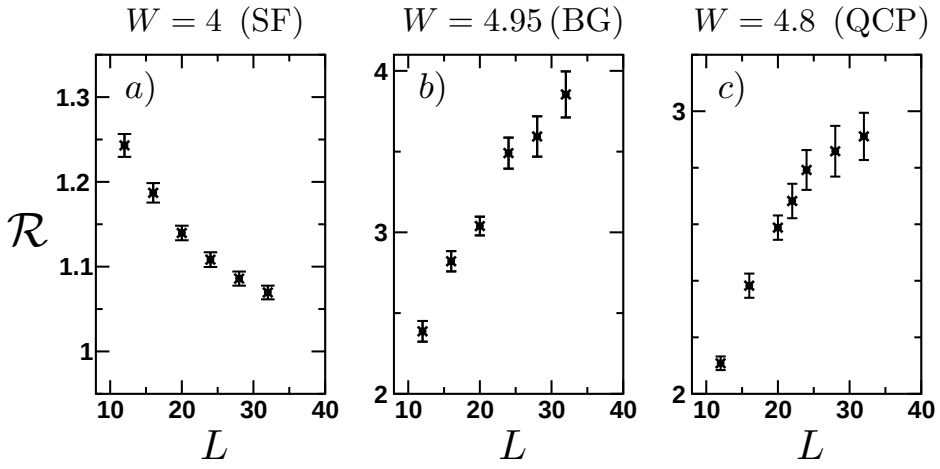

Figure IV.17: *Evolution of $\mathcal{R} = \rho_{\rm sf}^{\rm avg}/\rho_{\rm sf}^{\rm typ}$ with system size L inside the different phases and at criticality. Panel a: In the SF phase $W = 4$, $\mathcal{R}$ tends to 1 for increasing system size L, signalling a self-averaging SF phase. Panel b: Inside the BG phase ($W = 4.95$) $\mathcal{R}$ increases with system size indicating a lack of self-averaging. Panel c: At criticality, the ratio $\mathcal{R}$ seems to saturate for big system sizes to a finite value > 1, i.e. the critical point is not self-averaging but has different nature than the BG phase.*

a), the typical stiffness is closer and closer to the average one as L increases and the distributions of $\ln(\rho_{\rm sf})$ are becoming more and more symmetric. On the other hand, if $\mathcal{R}$ increases with L, like in the BG phase, the typical stiffness gets smaller and smaller compared to the average one with increasing L and the distributions of $\ln(\rho_{\rm sf})$ get more and more asymmetric towards the most negative values of $\ln(\rho_{\rm sf})$, signalling a break-down in self-averaging.

Figure IV.18 complements this analysis by showing the distributions of $\ln(\rho_{\rm sf})$ which clearly shrink with increasing system size in the SF phase (panel a) confirming that it is self-averaging (as expected for a *global* quantity). In the Bose glass phase (panel b) these distributions broaden with increasing L undoubtably stating the lack of self-averaging in the BG phase. As far as the QCP is concerned, the distributions broaden until $L = 20$ and then appear identical to one another but shifted, which

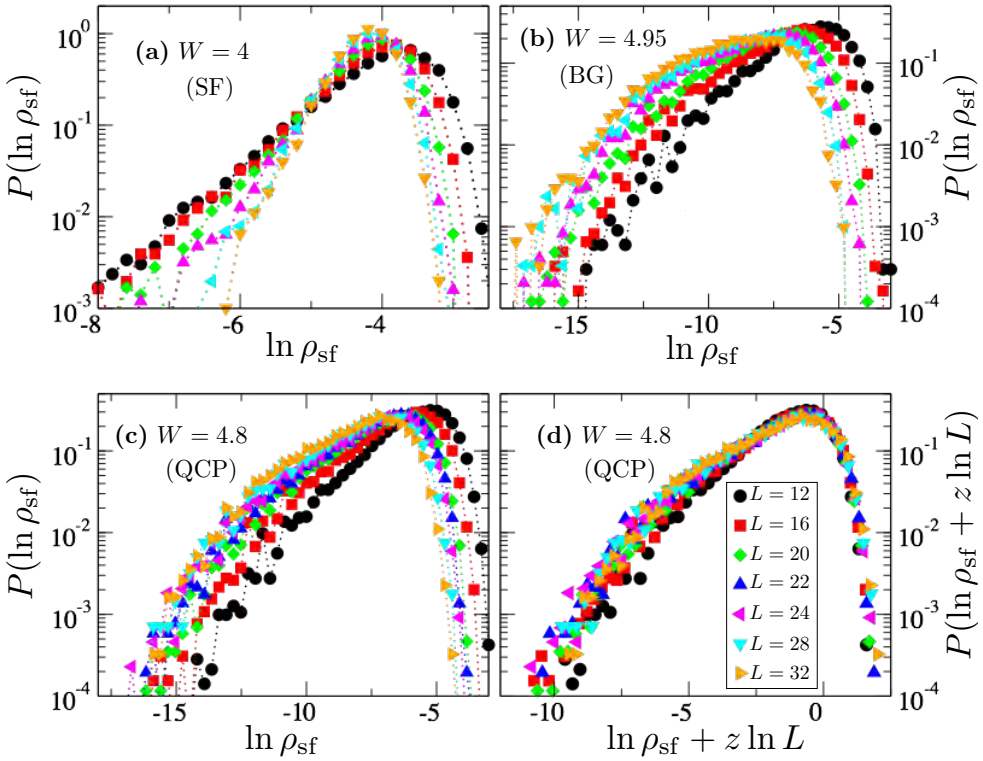

Figure IV.18: *Distribution of* $\ln(\rho_{sf})$ *for all available system sizes at three different disorder strengths inside the SF phase (a), the BG phase (b) and at criticality (c−d). In the SF phase (panel a* $W = 4$*) the distributions shrink with increasing system size* L*, indicating self-averaging. In the BG phase (panel b* $W = 4.95$*) they broaden as* L *grows, a clear signature of lack of self-averaging. At criticality (panel c* $W = 4.8$*) the distributions are similar to one another specially for* $L \geq 20$*, and an excellent collapse is achieved by shifting them by* $z \ln(L)$ *using* $z = 1.85$ *(panel d).*

means that the fluctuations of $\ln(\rho_{\rm sf})$ at the thermodynamic limit is finite, *i.e.* self-averaging breaks down at criticality. The distributions can be shifted by $z\ln(L)$ (as plotted in panel *d*) to obtain a very convincing collapse specially for $L \geq 20$, using our best estimate for the dynamical exponent $z = 1.85$. Such a collapse of the full distributions using the best estimate for the *average* stiffness further confirms the fact that the critical scalings of typical and average stiffness are the same, and the irrelevant corrections to the scaling, *cf.* eq. (IV.46), are responsible for the transient broadening for the smallest sizes, as already discussed in section 3.2 (see figure IV.16).

4.2 Variance of $\ln(\rho_{\rm sf})$

In order to further investigate the inhomogeneous properties of our model (IV.1) and specially in the Bose glass phase a more quantitative study of the broadening (shrinking) of the distributions of $\ln(\rho_{\rm sf})$ is necessary. It is worth mentioning that the dynamical adjustment of the number of measurement steps described in section 2.4 (*cf.* figure IV.12) reveals crucial for the quantitative study of the broadening of the distributions in the Bose glass phase. As a matter of fact, this method allows us to properly sample the full distribution specially inside the Bose glass phase, where the broadening of the distributions of $\ln(\rho_{\rm sf})$ would not have been seen even qualitatively as in figure IV.18.

Noting that self-averaging was shown to imply a finite variance of any physical thermodynamic quantity [282], a natural quantity to observe is the standard deviation of $\ln(\rho_{\rm sf})$. However, the presence of irrelevant corrections to scalings is responsible for the transient broadening of distributions at criticality (*cf.* figure IV.18 in section 4.1). As a means of eliminating such effects, we compute the corrected standard deviation of $\ln(\rho_{\rm sf})$ for each system size L defined by:

$$\tilde{\sigma}_{\ln\rho_{\rm sf}}(W,L) = \sigma_{\ln\rho_{\rm sf}}(W,L) - \sigma^c(L), \tag{IV.47}$$

where $\sigma^c(L) = \sigma_{\ln\rho_{\rm sf}}(W_c,L)$ is the standard deviation of $\ln\rho_{\rm sf}$ at the critical point $W_c = 4.8$ which saturates to a value σ^c for $L \geq 20$ (see figure IV.18 in section 4.1).

We plot $\tilde{\sigma}_{\ln\rho_{\rm sf}}$ against the system size in units of the localization length $L/\xi = L|W - W_c|^\nu$ with our best estimate $\nu = 1.2$ in figure IV.19. A very good collapse of the data is found once again confirming that our estimate for the correlation length exponent is consistent with our data. Inside the superfluid phase the corrected standard deviation decreases and tends to $-\sigma^c$ as $1/\sqrt{N}$ meaning that the standard deviation goes to zero as $1/\sqrt{N}$. The fluctuations are then dominated by the central limit theorem confirming the self-averaging nature of the superfluid phase, which was expected for the superfluid stiffness as defined and computed in SSE is a *global* quantity.

Inside the Bose glass phase ($W > 4.8$) the corrected standard deviation grows with system size and the data is very well described by a power law growth of the form

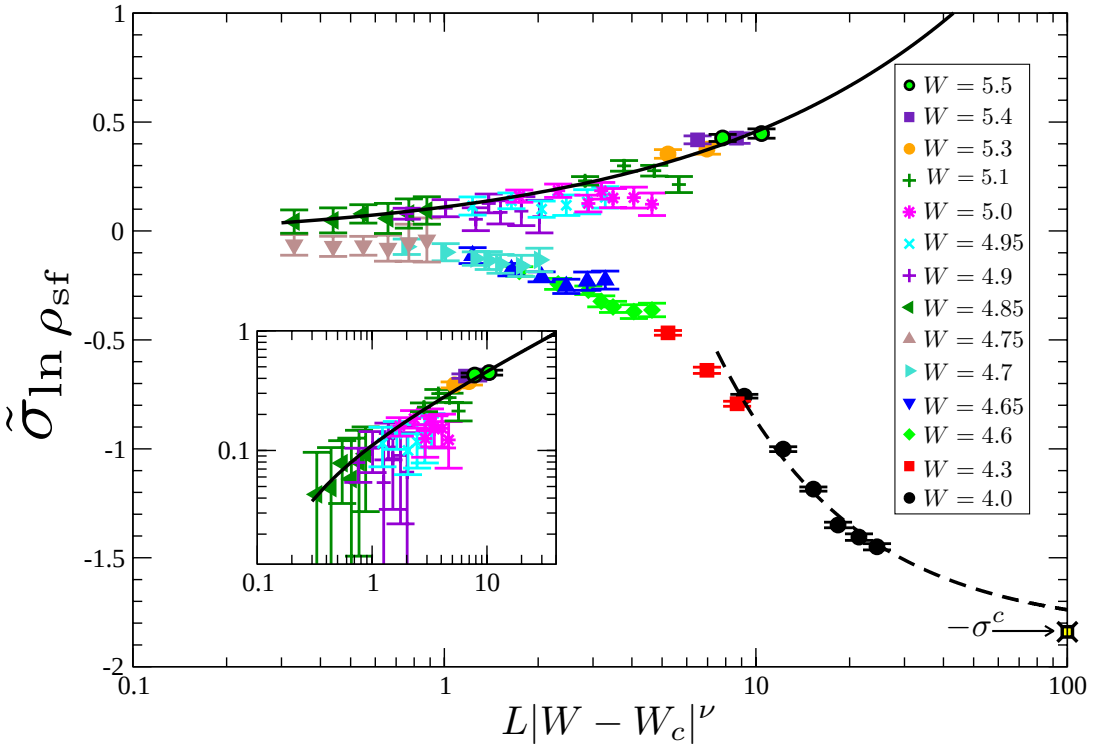

Figure IV.19: *Evolution of the corrected standard deviation* $\tilde{\sigma}_{\ln \rho_{sf}}$ *of eq.* (IV.47) *with system size rescaled by the correlation length* $L/\xi = L|W - W_c|^{\nu}$*, with* $\nu = 1.2$*, for all disorder strengths from* $W = 4.0$ *to* $W = 5.5$*. In the SF phase* ($W < 4.8$) *it drops down to* $-\sigma^c$ *as* $1/\sqrt{N}$ *(black dashed line), a consequence of self-averaging. In the BG phase* ($W > 4.8$) *it increases as* $(L/\xi)^{\omega}$ *with* $\omega = 0.5(2)$ *(full black line). The inset shows a zoom in the BG phase parameter region.*

$(L/\xi)^{\omega}$ with an exponent $\omega = 0.5(2)$. This confirms the break-down of self-averaging inside the Bose glass phase.

The physical scenario we extract from this is the following. First, the Bose glass phase was predicted to bear a partial analogy with the disordered (paramagnetic) phase of the transverse-field Ising model (TFIM) [30, 195, 279], as supported by recent 1D results with a strong disorder renormalisation-group approach [286]. Additionally, such a paramagnetic phase in the TFIM was shown to follow directed polymer physics in dimension $D = (d-1)$ by Monthus and Garel [207]. In our $d = 2$ case this means 1D directed polymer physics for which it is known that the distributions of local quantities broaden with size as L^{ω} with $\omega = 1/3$ [287] in agreement with our estimate. Furthermore, Seibold *et al.* showed that the stiffness is dominated by quasi 1D percolating paths at strong disorder [204], *i.e.* in the BG phase the global superfluid response of the system can be seen as a purely local quantity.

5 Absence of percolation in the SF-BG phase transition

Throughout the years, the understanding of the Bose glass phase has evolved and developed as the interplay of disorder and interactions became subject of an increasing interest. The theorem of inclusions [166] put an end to the controversy of whether the Bose glass phase always intervenes between the Superfluid and Mott Insulating phases, which it does. This theorem rules out any transition driven by disorder between a gapped and a gapless phase, unless it is driven by rare region effects (*cf.* section 2.2 in the Introduction chapter I). A rather widely spread description of the critical region of the SF-BG transition states the existence of superfluid regions inside the BG phase, where the local order parameter is almost uniform. Hence the emerging picture of the Bose glass as consisting in disconnected superfluid droplets (or clusters), with coherent inter-droplet tunneling inhibited by Anderson localization (hence the insulating nature) while the exchange of bosons between different droplets is costless (explaining the finite compressibility). Then, the onset of superfluidity at criticality is realized with the appearance of a SF cluster percolating through the system, yielding a percolation scenario for the SF-BG transition [83, 171, 185, 187, 188].

While discussing the break-down of self-averaging inside the BG phase (*cf.* section 4.2) we pointed out the existing analogy of the BG phase in our XY model with the paramagnetic phase of the transverse-field Ising model (TFIM). The critical regime of the TFIM was extensively studied and was shown to be of the Griffiths type with exponentially large rare regions of the ordered phase inside the disordered phase [279]. However, Yu and Müller showed that upon approaching the critical regime the analogy breaks down [111] as could be inferred by the completely different nature of the critical points for the XY model and the TFIM. Indeed, Fisher showed that the critical point of the TFIM is an infinite randomness fixed point with a formally infinite dynamical exponent $z = \infty$ [279], while we have shown that our XY model has a conventional fixed point with $z = 1.85(15)$. Another difference is the breaking of the continuous U(1) symmetry in the TFIM and its conservation for the XY model. As a consequence, the ordering transition can only happen at the thermodynamic limit and never in a finite-size sample, hence the locally ordered regions inside the disordered phase cannot exist. This can be explained by a simple argument: we have seen that for finite-size systems at $T = 0$ the compressibility vanishes because of the finite-size gap (*cf.* fig. IV.7 of section 2.2.3) and the system has no particle number fluctuations $\Delta N = 0$, hence its conjugate operator, the phase operator, has diverging fluctuations in virtue of Heisenberg's uncertainty principle and the spins in the XY plane cannot be ordered (*i.e.* have zero phase fluctuations). In the thermodynamic limit the particle number operator has non vanishing fluctuations ($\kappa \neq 0$ when $N \to \infty$) and ordering is then possible.

The percolation scenario of the transition is then worth questioning. In order to do so, we perform QMC simulations to compute the local density profiles of systems of relatively small sizes $N = 64$ and 256. To ensure ground-state properties are being investigated, the simulations are carried out at very low temperatures $\beta t = 2^9$, for which the number of bosons does not fluctuate (*cf.* figure IV.8 in section 2.2.3). We compute, inside the BG ($W = 5$) the local densities $\rho_i = \langle b_i^\dagger b_i \rangle$ (*cf.* equation IV.22 for its expression in SSE), which requires a much bigger number of MC steps than the average superfluid stiffness or BEC density, namely $N_{\rm mc} = 10^5$, for being properly estimated (so that the directed loops visit all sites). Such values for $N_{\rm mc}$ and βt make the simulations much longer (*cf.* equation IV.34), limiting the available sizes. Furthermore, we restrict the number of disorder realizations to $\mathcal{N}_s = 150$, since for $L = 16$ we already have $16^2 * 150 = 38400$ values of ρ_i.

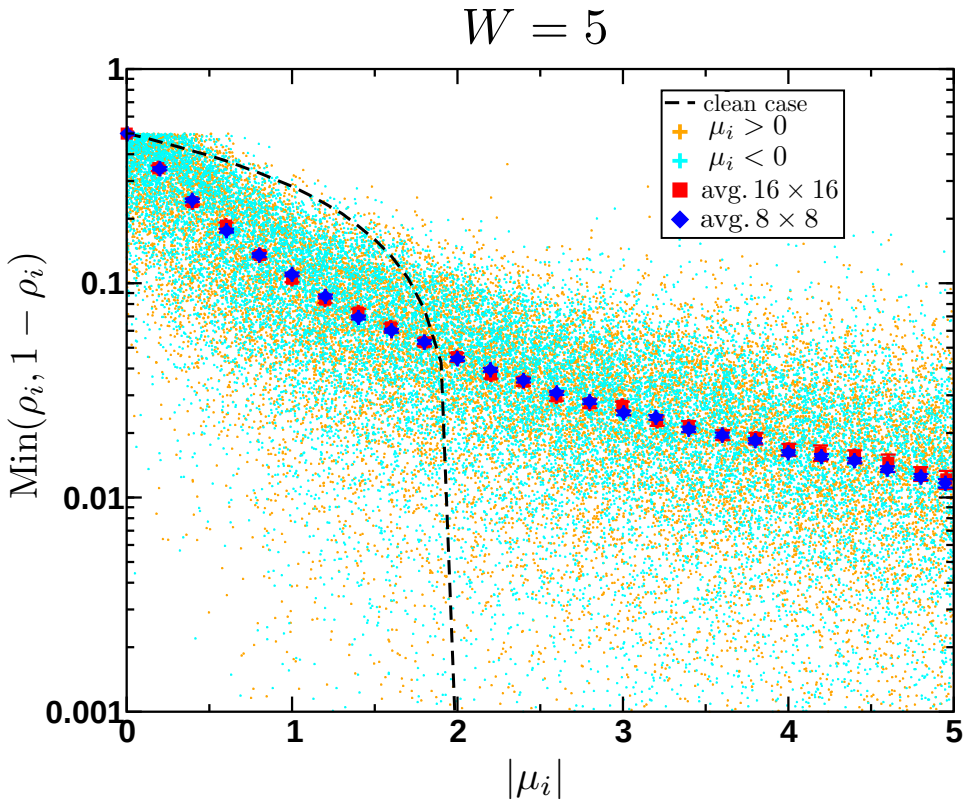

Figure IV.20: *Effective local density Min($\rho_i, 1-\rho_i$) inside the BG phase ($W = 5$) as a function of the local chemical potential $|\mu_i|$ for a system of size $L = 16$ (small crosses). $\mathcal{N}_S = 150$ disorder realizations were simulated at $\beta t = 1024$ using $N_{mc} = 10^5$ MC steps. The average density over windows in chemical potential $[\bar{\mu}-0.1; \bar{\mu}+0.1]$ are represented by red (blue) data points for $N = 256$ ($N = 64$). The black dashed line is the result for the disorder-free system (taken from Ref. [246]).*

The obtained results are represented in figure IV.20 as the effective local density $\mathrm{Min}(\rho_i, 1-\rho_i)$ (we remind the reader that if $\rho_i < 1/2$ the bosons are superfluid and if $\rho_i > 1/2$ the holes with density $1-\rho_i$ are superfluid owing to time reversal symmetry) *vs.* the local chemical potential $|\mu_i|$ for $L = 16$. The symmetry between positive and negative local chemical potentials for the effective local densities is clear *i.e.* half-filling is indeed restored on average [164]. The averages over windows of local chemical potential $\bar{\mu} - 0.1 \leq \mu_i \leq \bar{\mu} + 0.1$ are also plotted as red squares. For comparison the average data for $L = 8$ is also shown as blue diamonds, but the effective local densities are not shown for this size for graphical reasons. The dashed black line represents the average density of the clean system $W = 0$ obtained in Ref. [246], which vanishes for chemical potentials outside the band $|\mu_i| \geq 2$, indicating an incompressible behavior. In contrast, the average behavior is always compressible inside the BG even for outside the band $|\mu_i| \geq 2$.

Figure IV.21 shows the distribution of the local densities for the two previously considered system sizes using different number of MC steps $N_{\mathrm{mc}} = 10^4$ and 10^5 (panel

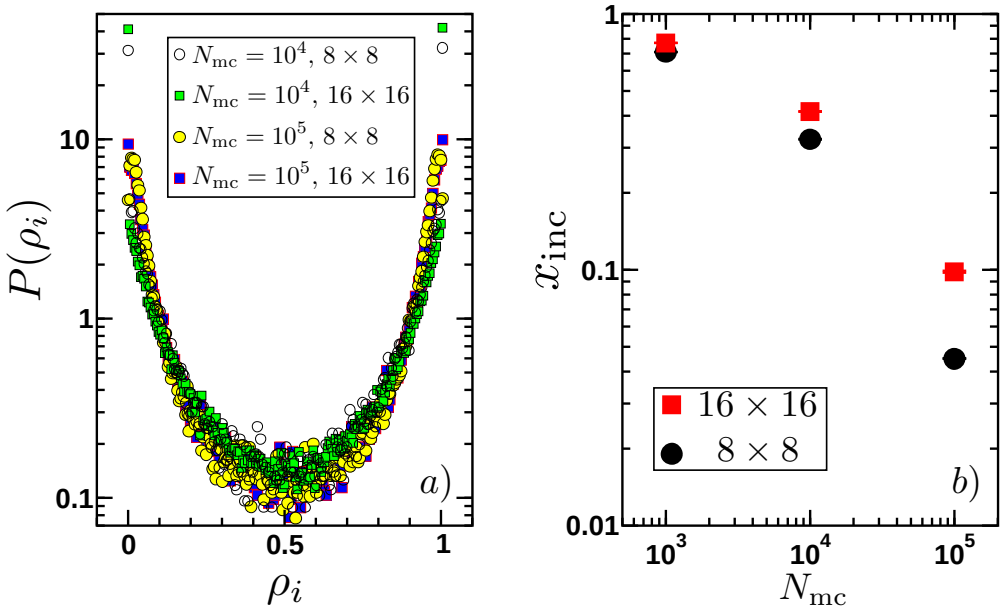

Figure IV.21: *Panel a: Distribution of the local density ρ_i for two system sizes $L = 8$ and $L = 16$, and different number of Monte Carlo steps N_{mc} in the simulations with $\mathcal{N}_s = 150$ disordered samples at $\beta t = 2^9$. The weight of the peaks at $\rho_i = 0$ and 1 diminishes as N_{mc} grows. Panel b: Evolution of the fraction of incompressible sites x_{inc} with increasing number of Monte Carlo steps N_{mc} for the same system sizes. The fraction drastically drops as N_{mc} increases and presumably vanishes at the exact limit $N_{mc} \to \infty$. Error bars are represented but are smaller than the symbol size.*

a) and $x_{\rm inc}$ the corresponding fraction of incompressible sites presenting $\rho_i = 0$ or 1 as a function of $N_{\rm mc}$ (panel *b*). Qualitatively, the distribution $P(\rho_i)$ has two peaks at 0 and 1 but their weight decreases as $N_{\rm mc}$ is cranked up. More quantitatively, the fraction of incompressible sites $x_{\rm inc}$ is reduced by at least one order of magnitude upon increasing the number of MC steps in the simulations and it is already well below the percolation threshold. In addition, $x_{\rm inc}$ seems to vanish at the exact limit of infinite MC steps, yielding the fact that all sites are compressible inside the BG phase. Hence, the scenario of the BG phase as disconnected SF clusters inside an insulating background is wrong for the insulating background is never realized: there is always a percolation through compressible sites ruling out a percolation-related scenario of the SF-BG transition.

This is further justified by the fact that according to percolation theory, the superfluid density should vanish close to the critical point as a power-law on the distance to the critical point (*cf.* equation (II.19)) [216, 222, 224–228], with an exponent $t = 1.310(1)$ [228]. However, we have shown that close to the critical point the superfluid density vanishes as:

$$\rho_{\rm sf} \sim L^{-z} \underset{W \to W_c}{\sim} \xi^{-z} \sim |W - W_c|^{z\nu}, \tag{IV.48}$$

and our best estimates for the critical parameters yield $z\nu \approx 1.85(15) \times 1.20(12) = 2.2(4) \neq 1.31$, so that a percolation scenario for the superfluid – Bose glass transition is definitely ruled out.

Chapter V

Conclusion and perspectives

The Superfluid - Insulator transition remains one of the most active fields of research in condensed matter physics, even a quarter of a century after its discovery. In particular, the Superfluid - Bose glass transition keeps puzzling theoreticians and experimentalists alike. This manuscript tackled this transition in the somewhat special case of two dimensional hard-core bosons with on-site disordered chemical potentials. This model, though quite simple, is able to capture the essential elements of the physics and is pertinent in the context of superconductors, spin dimers and cold atoms. The bimodal distribution and the box distribution of disorder were considered throughout this work. After presenting some of the different theoretical and experimental results obtained thus far, a purely classical approach to the transition was developed in chapter II. There we provide the first calculations of the classical superfluid density (thus far only the order-parameter, *i.e.* the Bose-Einstein condensate fraction had been considered), which we priorly tested on the Heisenberg model to ascertain the validity of our method. The importance of phase relaxation was evidenced and the complete neglecting of the quantum fluctuations in our Mean-Field approach led it to fail to capture the glassy physics of the problem, despite some precursor effects on classical transport properties. In addition, we give compelling arguments disproving the long-standing findings of Ma *et al.* concerning the break-down of the Mean-Field theory for the considered transition.

In chapter III, quantum fluctuations were introduced by means of Linear Spin-Wave Theory which we showed to capture the Superfluid – Bose glass transition. The ground-state critical parameters of the transition were estimated for the two different disorder distributions, with different estimates for the dynamical exponent, one in agreement with the predicted $z = d$ equality (bimodal distribution) and one that clearly violates it (box distribution). Furthermore, the excitation spectrum in the case of the bimodal disorder distribution presents a very rich physics with a localization transition of the one-particle spin-wave excited states at a finite mobility edge inside the Superfluid phase, and a vanishing mobility edge inside the Bose glass, although some more recent results by Lemarié would indicate otherwise.

Finally, chapter IV focused on the large-scale Quantum Monte Carlo simulations of the hard-core bosons with on-site box disorder model, extracting by a careful procedure the ground-state critical properties. The critical disorder strength for the transition into the Bose glass from the superfluid phase is in good numerical agreement with our spin-wave estimate, the 2D cavity Mean-Field estimate of Lemarié *et al.* and the QMC estimate of Ng and Sørensen for the same model. The extracted dynamical exponent is different than the spin-wave one and though it is smaller than the dimensionality, $z = d$ cannot be ruled out for sure. We also provide estimates for the correlation length exponent ν and the anomalous exponent η in agreement with their theoretical bounds and other recent estimates. The inhomogeneous properties of the system were also discussed. The absence of self-averaging inside the Bose glass phase was demonstrated and the percolation scenario for the transition was shown to not be relevant, in contradiction with a well spread idea given by previous theoretical and experimental findings.

These results call for further investigations. The study of the inhomogeneous local properties of the system for both distributions of disorder on the one hand, as well as that of the excitation properties in the case of the box distributed disorder and and how it is affected by an external magnetic field in both cases on the other hand, are perfectly suited to be carried out by Linear Spin-Wave theory. The Quantum Monte Carlo simulations of the model with bimodal disorder so as to extract precise estimates of the its ground-state critical properties and compare them with the spin-wave ones constitute another direction to follow. Performing similar studies on the infinite dimensional Bethe lattice to see the effects of dimensionality, considering the Ising model instead of the XY model for hard-core bosons or including temperature effects are all possible lines of work to be tackled in the future.

Appendices

Appendix A

Iterative Mean-Field

1 Hard-core bosons on the square lattice

1.1 Periodic boundary conditions

The Iterative Mean-Field approach treats the spin-$\frac{1}{2}$ as a quantum spin with two levels, contrary the Mean-Field approach consisting in replacing the spin-$\frac{1}{2}$ operators classical spins with a minimization of the energy. Mean-Field theory is included by applying the common Mean-Field decoupling to the Hamiltonian (A.1). Starting from the XY Hamiltonian with periodic boundary conditions which by rotational symmetry around the z-axis can be simplified to restrict the spins to the XZ plane:

$$H_{\text{class}} = -\sum_i \mu_i S_i^z - 2t \sum_{\langle i,j \rangle} S_i^x S_j^x, \tag{A.1}$$

with μ_i the local disordered chemical potential and $\langle i, j \rangle$ a couple of nearest-neighbour sites. Applying the standard Mean-Field decoupling to the kinetic term

$$S_i^x S_j^x = S_i^x \langle S_j^x \rangle + \langle S_i^x \rangle S_j^x - \langle S_i^x \rangle \langle S_j^x \rangle, \tag{A.2}$$

we obtain for the Hamiltonian

$$H_{\text{class}} = -\sum_i [\mu_i S_i^z + 2t S_i^x \sum_{\langle j \rangle_i} \langle S_j^x \rangle] + 2t \sum_{\langle i,j \rangle} \langle S_i^x \rangle \langle S_j^x \rangle. \tag{A.3}$$

The sum $\sum_{\langle j \rangle_i}$ runs over all sites j that are nearest-neighbours of site i. This Hamiltonian can be rewritten as

$$H_{\text{class}} = \sum_i h_i + 2t \sum_{\langle i,j \rangle} \langle S_i^x \rangle \langle S_j^x \rangle \tag{A.4}$$

where we have defined the local Mean-Field Hamiltonian on each site i:

$$h_i = -\mu_i S_i^z - 2t S_i^x \sum_{\langle j \rangle_i} \langle S_j^x \rangle = -\mu_i S_i^z - B_i S_i^x. \tag{A.5}$$

This last step of calculation allows us to define the local fields B_i as

$$B_i = 2t \sum_{\langle j \rangle_i} \langle S_j^x \rangle. \tag{A.6}$$

The local Mean-Field Hamiltonians (A.5) can be expressed in matrix notation using the Pauli matrices so that, in the $\{|\uparrow\rangle, |\downarrow\rangle\}$ basis representation the h_i are written:

$$h_i = \begin{pmatrix} -\frac{\mu_i}{2} & \frac{B_i}{2} \\ \frac{B_i}{2} & \frac{\mu_i}{2} \end{pmatrix}, \tag{A.7}$$

which has the eigenvalues $\lambda_i = \pm\frac{1}{2}\sqrt{\mu_i^2 + B_i^2}$. The ground-state wave-function, *i.e.* the eigenvector corresponding to the lowest eigenvalue $\lambda_i = -\frac{1}{2}\sqrt{\mu_i^2 + B_i^2}$, is straightforwardly obtained in the $\{|\uparrow\rangle, |\downarrow\rangle\}$ basis:

$$|\Psi_i\rangle = \frac{x_i}{B_i} \begin{pmatrix} B_i \\ \\ \sqrt{\mu_i^2 + B_i^2} - \mu_i \end{pmatrix}, \tag{A.8}$$

and the x_i coefficient is a real number constrained so as to make the wave-function normalized, which yields:

$$x_i^2 = \frac{B_i^2}{2\sqrt{\mu_i^2 + B_i^2}(\sqrt{\mu_i^2 + B_i^2} - \mu_i)}. \tag{A.9}$$

Finally, one can calculate the ground-state expectation values of S_i^x, S_i^z and therefore h_i:

$$\begin{cases} \langle S_i^x \rangle = \langle \Psi_i | S_i^x | \Psi_i \rangle = \dfrac{B_i}{2\sqrt{\mu_i^2 + B_i^2}} \\ \langle S_i^z \rangle = \langle \Psi_i | S_i^y | \Psi_i \rangle = \dfrac{\mu_i}{2\sqrt{\mu_i^2 + B_i^2}} \\ \\ \langle h_i \rangle = \langle \Psi_i | h_i | \Psi_i \rangle = -\dfrac{\sqrt{\mu_i^2 + B_i^2}}{2}. \end{cases} \tag{A.10}$$

Replacing the expectation values (A.10) into the definition of the local fields (A.6) one obtains the self-consistency relation for the fields

$$B_i = t \sum_{\langle j \rangle_i} \frac{B_j}{\sqrt{\mu_j^2 + B_j^2}}. \tag{A.11}$$

Doing the same for the ground-state expectation value of the full Hamiltonian (A.4) one gets the ground-state energy:

$$\langle H_{\text{class}} \rangle = -\sum_i \frac{\sqrt{\mu_i^2 + B_i^2}}{2} + \frac{t}{2} \sum_{\langle i,j \rangle} \frac{B_i B_j}{\sqrt{(\mu_i^2 + B_i^2)(\mu_j^2 + B_j^2)}}. \tag{A.12}$$

1.2 Twisted boundary conditions

When a twist Φ is applied to the boundary conditions, the spins are no longer restricted to the XZ plane and a y component is inevitable. The starting Hamiltonian is under such conditions

$$H_{\text{class}}(\Phi) = -\sum_i \mu_i S_i^z - 2t \sum_{\langle i,j \rangle} \left(S_i^x S_j^x + S_i^y S_j^y \right). \tag{A.13}$$

The standard Mean-Field decoupling has now to be applied on *both* parts of the kinetic term such that

$$S_i^{x/y} S_j^{x/y} = S_i^{x/y} \langle S_j^{x/y} \rangle + \langle S_i^{x/y} \rangle S_j^{x/y} - \langle S_i^{x/y} \rangle \langle S_j^{x/y} \rangle. \tag{A.14}$$

Under such a decoupling, the Hamiltonian becomes

$$\begin{aligned} H_{\text{class}}(\Phi) = & -\textstyle\sum_i [\mu_i S_i^z + 2t S_i^x \sum_{\langle j \rangle_i} \langle S_j^x \rangle + 2t S_i^y \sum_{\langle j \rangle_i} \langle S_j^y \rangle] + \\ & 2t \textstyle\sum_{\langle i,j \rangle} \left\{ \langle S_i^x \rangle \langle S_j^x \rangle + \langle S_i^y \rangle \langle S_j^y \rangle \right\} \\ = & \textstyle\sum_i h_i + 2t \sum_{\langle i,j \rangle} \left\{ \langle S_i^x \rangle \langle S_j^x \rangle + \langle S_i^y \rangle \langle S_j^y \rangle \right\} \end{aligned} \tag{A.15}$$

where we have once again defined the local Mean-Field Hamiltonians:

$$h_i = -\mu_i S_i^z - 2t S_i^x \sum_{\langle j \rangle_i} \langle S_j^x \rangle - 2t S_i^y \sum_{\langle j \rangle_i} \langle S_j^y \rangle = -\mu_i S_i^z - B_i^x S_i^x - B_i^y S_i^y. \tag{A.16}$$

The sum $\sum_{\langle j \rangle_i}$ runs over sites j that are nearest-neighbours with site i. The last step in equation (A.16) allows us to define the local fields:

$$B_i^{x/y} = 2t \sum_{\langle j \rangle_i} \langle S_j^{x/y} \rangle. \tag{A.17}$$

Using the Pauli matrices again, we can write, in the $\{|\uparrow\rangle, |\downarrow\rangle\}$ basis representation, the h_i as the matrix:

$$h_i = \begin{pmatrix} -\frac{\mu_i}{2} & \frac{-B_i^x + \imath B_i^y}{2} \\ \frac{-B_i^x - \imath B_i^y}{2} & \frac{\mu_i}{2} \end{pmatrix}, \tag{A.18}$$

which has the eigenstates $\lambda_i = \pm \frac{1}{2} \sqrt{\mu_i^2 + B_i^{x\,2} + B_i^{y\,2}}$. The ground-state wave-function, *i.e.* the eigenvector corresponding to the lowest eigenvalue which in this case is $\lambda_i = -\frac{1}{2} \sqrt{\mu_i^2 + B_i^{x\,2} + B_i^{y\,2}}$, is in the $\{|\uparrow\rangle, |\downarrow\rangle\}$ basis

$$|\Psi_i\rangle = a_i |\uparrow\rangle + b_i |\downarrow\rangle. \tag{A.19}$$

Solving the eigenvalue problem yields for the ground-state yields the relation:

$$b_i = \frac{a_i}{B_i^x - \imath B_i^y} \left(\sqrt{\mu_i^2 + B_i^{x\,2} + B_i^{y\,2}} - \mu_i \right). \tag{A.20}$$

Hence, the ground-state eigenvector reads:

$$|\Psi_i\rangle = \frac{a_i}{B_i^x - \imath B_i^y} \begin{pmatrix} B_i^x - \imath B_i^y \\ \sqrt{\mu_i^2 + B_i^{x2} + B_i^{y2}} - \mu_i \end{pmatrix}, \tag{A.21}$$

and enforcing the normalization condition on the ground-state eigenvector gives the constraint:

$$|a_i|^2 = \frac{B_i^{x2} + B_i^{y2}}{2\sqrt{\mu_i^2 + B_i^{x2} + B_i^{y2}}\left(\sqrt{\mu_i^2 + B_i^{x2} + B_i^{y2}} - \mu_i\right)}. \tag{A.22}$$

Finally, one can calculate the ground-state expectation values of S_i^x, S_i^y, S_i^z and therefore that of the local Mean-Field Hamiltonian h_i:

$$\begin{cases} \langle S_i^x \rangle = \langle \Psi_i | S_i^x | \Psi_i \rangle = \dfrac{B_i^x}{2\sqrt{\mu_i^2 + B_i^{x2} + B_i^{y2}}} \\ \\ \langle S_i^y \rangle = \langle \Psi_i | S_i^y | \Psi_i \rangle = \dfrac{B_i^y}{2\sqrt{\mu_i^2 + B_i^{x2} + B_i^{y2}}} \\ \\ \langle S_i^z \rangle = \langle \Psi_i | S_i^z | \Psi_i \rangle = \dfrac{\mu_i}{2\sqrt{\mu_i^2 + B_i^{x2} + B_i^{y2}}} \\ \\ \langle h_i \rangle = -\dfrac{\sqrt{\mu_i^2 + B_i^{x2} + B_i^{y2}}}{2} \end{cases} \tag{A.23}$$

Replacing the expectation values (A.23) into the definition of the local fields (A.17) gives the self-consistency equations of the fields:

$$\begin{cases} B_i^x = t \sum\limits_{\langle j \rangle_i} \dfrac{B_j^x}{\sqrt{\mu_j^2 + B_j^{x2} + B_j^{y2}}} \\ \\ B_i^y = t \sum\limits_{\langle j \rangle_i} \dfrac{B_j^y}{\sqrt{\mu_j^2 + B_j^{x2} + B_j^{y2}}}. \end{cases} \tag{A.24}$$

Doing the same for the ground-state expectation value of the full Hamiltonian (A.15) we obtain

$$\langle H_{\text{class}}(\Phi) \rangle = -\sum_i \frac{\sqrt{\mu_i^2 + B_i^{x2} + B_i^{y2}}}{2} + \frac{t}{2} \sum_{\langle i,j \rangle} \frac{B_i^x B_j^x + B_i^y B_j^y}{\sqrt{(\mu_i^2 + B_i^{x2} + B_i^{y}.^2)(\mu_j^2 + B_j^{x2} + B_j^{y2})}}. \tag{A.25}$$

1.3 Periodic boundary conditions with complex hopppings

As will be shown in section 2 of appendix B, the calculation of the superfluid density can be carried out either by applying a twist Φ to the boundary conditions or by distributing the twist along the bonds. The Iterative Mean-Field approach for the former was discussed in section 1.2 and now we turn to the latter.

Starting from the Hamiltonian in this case

$$\begin{aligned} H_{\text{class}}(\Phi) = &- \sum_i \frac{\mu_i}{2} - \sum_i \mu_i S_i^z - 2t \sum_i (S_i^x S_{i+\hat{y}}^x + S_{i+\hat{y}}^y S_i^y) \\ &- 2t \cos(\frac{\Phi}{L}) \sum_i (S_i^x S_{i+\hat{x}}^x + S_i^y S_{i+\hat{x}}^y) \\ &- 2t \sin(\frac{\Phi}{L}) \sum_i (S_i^y S_{i+\hat{x}}^x - S_i^x S_{i+\hat{x}}^y), \end{aligned} \tag{A.26}$$

we apply the standard Mean-Field decoupling (A.14) to all the terms in the Hamiltonian, which then becomes:

$$\begin{aligned} H_{\text{class}}(\Phi) = - \sum_i \Bigg\{ & \mu_i S_i^z + 2t S_i^x \Bigg[\langle S_{i+\hat{y}}^x \rangle + \langle S_{i-\hat{y}}^x \rangle + \cos(\frac{\Phi}{L})(\langle S_{i+\hat{x}}^x \rangle + \langle S_{i-\hat{x}}^x \rangle) \\ & \qquad + \sin(\frac{\Phi}{L})(\langle S_{i-\hat{x}}^y \rangle - \langle S_{i+\hat{x}}^y \rangle) \Bigg] \\ & + 2t S_i^y \Bigg[\langle S_{i+\hat{y}}^y \rangle + \langle S_{i-\hat{y}}^y \rangle + \cos(\frac{\Phi}{L})(\langle S_{i+\hat{x}}^y \rangle + \langle S_{i-\hat{x}}^y \rangle) \\ & \qquad + \sin(\frac{\Phi}{L})(\langle S_{i+\hat{x}}^x \rangle - \langle S_{i-\hat{x}}^y \rangle) \Bigg] \Bigg\} \\ + 2t \sum_i \Bigg\{ & \langle S_i^x \rangle \left[\langle S_{i+\hat{y}}^x \rangle + \cos(\frac{\Phi}{L}) \langle S_{i+\hat{x}}^x \rangle - \sin(\frac{\Phi}{L}) \langle S_{i+\hat{x}}^y \rangle \right] \\ & + \langle S_i^y \rangle \left[\langle S_{i+\hat{y}}^y \rangle + \cos(\frac{\Phi}{L}) \langle S_{i+\hat{x}}^y \rangle + \sin(\frac{\Phi}{L}) \langle S_{i+\hat{x}}^x \rangle \right] \Bigg\}. \end{aligned} \tag{A.27}$$

This Hamiltonian can be rewritten into the form

$$\begin{aligned} H_{\text{class}}(\Phi) = \sum_i h_i + 2t \sum_i \Bigg\{ & \langle S_i^x \rangle \left[\langle S_{i+\hat{y}}^x \rangle + \cos(\frac{\Phi}{L}) \langle S_{i+\hat{x}}^x \rangle - \sin(\frac{\Phi}{L}) \langle S_{i+\hat{x}}^y \rangle \right] \\ & + \langle S_i^y \rangle \left[\langle S_{i+\hat{y}}^y \rangle + \cos(\frac{\Phi}{L}) \langle S_{i+\hat{x}}^y \rangle + \sin(\frac{\Phi}{L}) \langle S_{i+\hat{x}}^x \rangle \right] \Bigg\} \end{aligned} \tag{A.28}$$

by defining the local Mean-Field Hamiltonians:

$$\forall i, h_i = -\mu_i S_i^z - B_i^x S_i^x - B_i^y S_i^y, \tag{A.29}$$

and the local fields

$$\begin{cases} B_i^x = 2t \left[\langle S_{i+\hat{y}}^x \rangle + \langle S_{i-\hat{y}}^x \rangle + \cos(\frac{\Phi}{L})(\langle S_{i+\hat{x}}^x \rangle + \langle S_{i-\hat{x}}^x \rangle) + \sin(\frac{\Phi}{L})(\langle S_{i-\hat{x}}^y \rangle - \langle S_{i+\hat{x}}^y \rangle) \right] \\ B_i^y = 2t \left[\langle S_{i+\hat{y}}^y \rangle + \langle S_{i-\hat{y}}^y \rangle + \cos(\frac{\Phi}{L})(\langle S_{i+\hat{x}}^y \rangle + \langle S_{i-\hat{x}}^y \rangle) + \sin(\frac{\Phi}{L})(\langle S_{i+\hat{x}}^x \rangle - \langle S_{i-\hat{x}}^y \rangle) \right]. \end{cases} \tag{A.30}$$

At this point, we note that though the definitions of the local fields are different, the expression of the local Mean-Field Hamiltonian h_i is formally the same as that of iterative Mean-Field approach for the twisted boundary conditions problem with real hoppings studied in section 1.2. Therefore, the expressions of the ground-state wave-function (A.21) and its normalization constraint (A.22) are also the same and we end up with the same expressions for the expectation values of S_i^x, S_i^y, S_i^z and h_i, namely:

$$\begin{cases} \langle S_i^x \rangle = \dfrac{B_i^x}{2\sqrt{\mu_i^2 + B_i^{x\,2} + B_i^{y\,2}}} \\ \langle S_i^y \rangle = \dfrac{B_i^y}{2\sqrt{\mu_i^2 + B_i^{x\,2} + B_i^{y\,2}}} \\ \langle S_i^z \rangle = \dfrac{\mu_i}{2\sqrt{\mu_i^2 + B_i^{x\,2} + B_i^{y\,2}}} \\ \langle h_i \rangle = -\dfrac{\sqrt{\mu_i^2 + B_i^{x\,2} + B_i^{y\,2}}}{2}. \end{cases} \tag{A.31}$$

Entering these expectation values into the ground-state expectation value of the full Hamiltonian (A.28) yields the ground-state energy:

$$\begin{aligned}\langle H_{\text{class}}(\Phi)\rangle = &-\sum_i \frac{\sqrt{\mu_i^2 + {B_i^x}^2 + {B_i^y}^2}}{2} \\ &+ \frac{t}{2}\sum_i \left\{ \frac{B_i^x}{\sqrt{\mu_i^2 + {B_i^x}^2 + {B_i^y}^2}} \left[\frac{B_{i+\hat{y}}^x}{\sqrt{\mu_{i+\hat{y}}^2 + {B_{i+\hat{y}}^x}^2 + {B_{i+\hat{y}}^y}^2}} \right.\right. \\ &\left. + \cos(\frac{\Phi}{L}) \frac{B_{i+\hat{x}}^x}{\sqrt{\mu_{i+\hat{x}}^2 + {B_{i+\hat{x}}^x}^2 + {B_{i+\hat{x}}^y}^2}} - \sin(\frac{\Phi}{L}) \frac{B_{i+\hat{x}}^y}{\sqrt{\mu_{i+\hat{x}}^2 + {B_{i+\hat{x}}^x}^2 + {B_{i+\hat{x}}^y}^2}} \right] \\ &+ \frac{B_i^y}{\sqrt{\mu_i^2 + {B_i^x}^2 + {B_i^y}^2}} \left[\frac{B_{i+\hat{y}}^y}{\sqrt{\mu_{i+\hat{y}}^2 + {B_{i+\hat{y}}^x}^2 + {B_{i+\hat{y}}^y}^2}} \right. \\ &\left.\left. + \cos(\frac{\Phi}{L}) \frac{B_{i+\hat{x}}^y}{\sqrt{\mu_{i+\hat{x}}^2 + {B_{i+\hat{x}}^x}^2 + {B_{i+\hat{x}}^y}^2}} + \sin(\frac{\Phi}{L}) \frac{B_{i+\hat{x}}^x}{\sqrt{\mu_{i+\hat{x}}^2 + {B_{i+\hat{x}}^x}^2 + {B_{i+\hat{x}}^y}^2}} \right] \right\}. \end{aligned} \tag{A.32}$$

Despite the fact that the resolution is identical to that of the real hopping under twisted boundary conditions problem, this energy is different from the one in that case (A.25). Similarly, plugging the expectation values (A.31) into the definitions of the local fields (A.30) one ends up with the different self-consistency equations:

$$\begin{cases} B_i^x = t \left[\dfrac{B_{i+\hat{y}}^x}{\sqrt{\mu_{i+\hat{y}}^2 + {B_{i+\hat{y}}^x}^2 + {B_{i+\hat{y}}^y}^2}} + \dfrac{B_{i-\hat{y}}^x}{\sqrt{\mu_{i-\hat{y}}^2 + {B_{i-\hat{y}}^x}^2 + {B_{i-\hat{y}}^y}^2}} \right. \\ \quad + \cos(\dfrac{\Phi}{L}) \left(\dfrac{B_{i+\hat{x}}^x}{\sqrt{\mu_{i+\hat{x}}^2 + {B_{i+\hat{x}}^x}^2 + {B_{i+\hat{x}}^y}^2}} + \dfrac{B_{i-\hat{x}}^x}{\sqrt{\mu_{i-\hat{x}}^2 + {B_{i-\hat{x}}^x}^2 + {B_{i-\hat{x}}^y}^2}} \right) \\ \quad \left. + \sin(\dfrac{\Phi}{L}) \left(\dfrac{B_{i-\hat{x}}^y}{\sqrt{\mu_{i-\hat{x}}^2 + {B_{i-\hat{x}}^x}^2 + {B_{i-\hat{x}}^y}^2}} - \dfrac{B_{i+\hat{x}}^y}{\sqrt{\mu_{i+\hat{x}}^2 + {B_{i+\hat{x}}^x}^2 + {B_{i+\hat{x}}^y}^2}} \right) \right] \\ B_i^y = t \left[\dfrac{B_{i+\hat{y}}^y}{\sqrt{\mu_{i+\hat{y}}^2 + {B_{i+\hat{y}}^x}^2 + {B_{i+\hat{y}}^y}^2}} + \dfrac{B_{i-\hat{y}}^y}{\sqrt{\mu_{i-\hat{y}}^2 + {B_{i-\hat{y}}^x}^2 + {B_{i-\hat{y}}^y}^2}} \right. \\ \quad + \cos(\dfrac{\Phi}{L}) \left(\dfrac{B_{i+\hat{x}}^y}{\sqrt{\mu_{i+\hat{x}}^2 + {B_{i+\hat{x}}^x}^2 + {B_{i+\hat{x}}^y}^2}} + \dfrac{B_{i-\hat{x}}^y}{\sqrt{\mu_{i-\hat{x}}^2 + {B_{i-\hat{x}}^x}^2 + {B_{i-\hat{x}}^y}^2}} \right) \\ \quad \left. + \sin(\dfrac{\Phi}{L}) \left(\dfrac{B_{i+\hat{x}}^x}{\sqrt{\mu_{i+\hat{x}}^2 + {B_{i+\hat{x}}^x}^2 + {B_{i+\hat{x}}^y}^2}} - \dfrac{B_{i-\hat{x}}^x}{\sqrt{\mu_{i-\hat{x}}^2 + {B_{i-\hat{x}}^x}^2 + {B_{i-\hat{x}}^y}^2}} \right) \right]. \end{cases} \tag{A.33}$$

2 Heisenberg model on the square lattice

The second model considered in this thesis is the Heisenberg model with either random exchange couplings or site dilution. In both cases the equations are the same since the only difference is the numerical values of the exchange couplings which can be taken from a probability distribution in the former case, or be either 0 or 1 in the site dilution case. Hence, there is only one formulation of the Iterative Mean-Field approach which we develop in the following.

The starting point is the Heisenberg Hamiltonian:

$$H_r = \sum_{\langle i,j \rangle} J_{ij} \hat{S}_i \hat{S}_j. \tag{A.34}$$

As seen in chapter II, we are interested in computing the superfluid stiffness and in order to do so, a twist to the boundary conditions along the x direction is applied, the relevant quantity to compute being the energy cost carried about by this twist. Since the twist only couples to the XY part of the Hamiltonian at the Mean-Field level, the z component is not affected by it and it generates no energy cost. In this sense, it is natural to neglect the z components of the spin operators in the following, leaving the Hamiltonian:

$$H = \sum_{\langle i,j \rangle} J_{ij} (S_i^x S_j^x + S_i^y S_j^y). \tag{A.35}$$

At this point, this XY Hamiltonian is equivalent to the spin-XY Hamiltonian obtained by applying the Matsubara-Matsuda transformation to the hard-core boson Hamiltonian, *i.e.* to the one in equation (A.1), with the correspondence between the two given by:

$$\begin{cases} 2t \longleftrightarrow J_{ij} \\ \mu_i \longleftrightarrow 0. \end{cases} \tag{A.36}$$

This means that the ground-state expectation value of the energy and the self-consistency equations both in the presence of a twist or under periodic boundary conditions, are deduced from those of the hard-core bosons model discussed in section 1 by applying the transformation (A.36).

Appendix B

Equivalencies of diverse methods

1 Equivalency between Mean-Field approaches

In chapter (II) we used two classical Mean-Field approaches that *a priori* seem completely different. On the one hand, we have the replacement of the spin-$\frac{1}{2}$ operators by 3D classical vectors such that:

$$\vec{S}_i = \frac{1}{2}\begin{pmatrix}\sin\theta_i\cos\varphi_i\\ \sin\theta_i\sin\varphi_i\\ \cos\theta_i\end{pmatrix}. \tag{B.1}$$

On the other hand, we have the iterative Mean-Field solution described in detail in Appendix A for which a set of self-consistency equations is solved iteratively in order to get the local fields in terms of which we can compute the physical observables of interest. Here we will see that they are in fact equivalent in the sense that they both try to solve the same equations of minimization of the classical energy, with the only difference that the problem is formulated in a different way. We will start from the minimization of the classical energy in terms of the classical angles defined in equation (B.1), in the case of an applied magnetic field along the x direction, and derive the self-consistency equations (II.33).

The Hamiltonian obtained by replacing spin operators by classical vectors in the hard-core boson Hamiltonian reads:

$$\begin{aligned} H_{class}(\Phi) = \; & -\textstyle\sum_i \frac{\mu_i}{2} - \sum_i \frac{\mu_i}{2}\cos\theta_i - \frac{t}{2}\sum_i \sin\theta_i \sin\theta_{i+\hat{y}}\cos(\varphi_i - \varphi_{i+\hat{y}}) \\ & -\tfrac{t}{2}\cos(\tfrac{\Phi}{L})\textstyle\sum_i \sin\theta_i\sin\theta_{i+\hat{x}}\cos(\varphi_i - \varphi_{i+\hat{x}}) \\ & -\tfrac{t}{2}\sin(\tfrac{\Phi}{L})\textstyle\sum_i \sin\theta_i\sin\theta_{i+\hat{x}}\sin(\varphi_i - \varphi_{i+\hat{x}}), \end{aligned} \tag{B.2}$$

where μ_i is the local chemical potential on site i through which disorder is put in the system. Deriving the Hamiltonian with respect to the θ_i angles we get some relations

that need to be respected for the ground-state angles:

$$\begin{aligned}\frac{\partial H_{class}(\Phi)}{\partial \theta_i} =&\mu_i \sin\theta_i - t\cos\theta_i \sin\theta_{i+\hat{y}} \cos\varphi_i \cos\varphi_{i+\hat{y}} - t\cos\theta_i \sin\theta_{i+\hat{y}} \sin\varphi_i \sin\varphi_{i+\hat{y}} \\ &- t\cos\theta_i \sin\theta_{i-\hat{y}} \cos\varphi_i \cos\varphi_{i-\hat{y}} - t\cos\theta_i \sin\theta_{i-\hat{y}} \sin\varphi_i \sin\varphi_{i-\hat{y}} \\ &- t\cos(\frac{\Phi}{L})\cos\theta_i \sin\theta_{i+\hat{x}} \cos\varphi_i \cos\varphi_{i+\hat{x}} - t\cos(\frac{\Phi}{L})\cos\theta_i \sin\theta_{i+\hat{x}} \sin\varphi_i \sin\varphi_{i+\hat{x}} \\ &- t\sin(\frac{\Phi}{L})\cos\theta_i \sin\theta_{i+\hat{x}} \sin\varphi_i \cos\varphi_{i+\hat{x}} + t\sin(\frac{\Phi}{L})\cos\theta_i \sin\theta_{i+\hat{x}} \cos\varphi_i \sin\varphi_{i+\hat{x}} \\ &- t\cos(\frac{\Phi}{L})\cos\theta_i \sin\theta_{i-\hat{x}} \cos\varphi_i \cos\varphi_{i-\hat{x}} - t\cos(\frac{\Phi}{L})\cos\theta_i \sin\theta_{i-\hat{x}} \sin\varphi_i \sin\varphi_{i-\hat{x}} \\ &- t\sin(\frac{\Phi}{L})\cos\theta_i \sin\theta_{i-\hat{x}} \cos\varphi_i \sin\varphi_{i-\hat{x}} + t\sin(\frac{\Phi}{L})\cos\theta_i \sin\theta_{i-\hat{x}} \sin\varphi_i \cos\varphi_{i-\hat{x}} \\ &= 0\end{aligned}$$

which can be rearranged to take the form:

$$\begin{aligned}\mu_i \tan\theta_i =& t\cos\varphi_i \Big[\sin\theta_{i+\hat{y}} \cos\varphi_{i+\hat{y}} + \sin\theta_{i-\hat{y}} \cos\varphi_{i-\hat{y}} \\ &+ \cos(\frac{\Phi}{L}) \left(\sin\theta_{i+\hat{x}} \cos\varphi_{i+\hat{x}} + \sin\theta_{i-\hat{x}} \cos\varphi_{i-\hat{x}}\right) \\ &+ \sin(\frac{\Phi}{L}) \left(-\sin\theta_{i+\hat{x}} \sin\varphi_{i+\hat{x}} + \sin\theta_{i-\hat{x}} \sin\varphi_{i-\hat{x}}\right)\Big] \\ &+ t\sin\varphi_i \Big[\sin\theta_{i+\hat{y}} \sin\varphi_{i+\hat{y}} + \sin\theta_{i-\hat{y}} \sin\varphi_{i-\hat{y}} \\ &+ \cos(\frac{\Phi}{L}) \left(\sin\theta_{i+\hat{x}} \sin\varphi_{i+\hat{x}} + \sin\theta_{i-\hat{x}} \sin\varphi_{i-\hat{x}}\right) \\ &+ \sin(\frac{\Phi}{L}) \left(\sin\theta_{i+\hat{x}} \cos\varphi_{i+\hat{x}} - \sin\theta_{i-\hat{x}} \cos\varphi_{i-\hat{x}}\right)\Big] .\end{aligned} \tag{B.3}$$

Both Mean-Field approaches give an estimate of the ground-state expectation values of the spin operators. These are straightforwardly given in the case of classical vectors by the vector components themselves (B.1), while for the iterative resolution they are non-trivial but determined by the local fields $B_i^{x/y}$ via the expressions in equation (A.23). These expectation values have to be equal for the to methods to

be equivalent, so:

$$\begin{cases} \langle S_i^x \rangle = \dfrac{B_i^x}{2\sqrt{\mu_i^2 + B_i^{x2} + B_i^{y2}}} = \dfrac{1}{2}\sin\theta_i \cos\varphi_i \\ \\ \langle S_i^y \rangle = \dfrac{B_i^y}{2\sqrt{\mu_i^2 + B_i^{x2} + B_i^{y2}}} = \dfrac{1}{2}\sin\theta_i \sin\varphi_i \\ \\ \langle S_i^z \rangle = \dfrac{\mu_i}{2\sqrt{\mu_i^2 + B_i^{x2} + B_i^{y2}}} = \dfrac{1}{2}\cos\theta_i \end{cases} \tag{B.4}$$

and we get a direct link between the classical angles of the 3D vectors $\{\theta_i, \varphi_i\}$ and the local fields $B_i^{x/y}$ on each site i.

$$\begin{cases} \tan\theta_i = \dfrac{\sqrt{B_i^{x2} + B_i^{y2}}}{\mu_i} \\ \cos\varphi_i = \dfrac{B_i^x}{\sqrt{B_i^{x2} + B_i^{y2}}} \\ \sin\varphi_i = \dfrac{B_i^y}{\sqrt{B_i^{x2} + B_i^{y2}}}. \end{cases} \tag{B.5}$$

Now, we can rewrite the expression obtained by the minimization of the Hamiltonian written in terms of the classical vectors angles of equation (B.3) in terms of the local fields of the iterative Mean-Field approach framework. We will see that upon a simple definition the self-consistency relations which determine the local fields are recovered.

Replacing the expressions (B.5) in equation (B.3) we obtain after a few simple manipulations

$$
\begin{aligned}
B_i^{x2} + B_i^{y2} =& B_i^x t \left[\frac{B^x_{i+\hat{y}}}{\sqrt{\mu^2_{i+\hat{y}} + {B^x_{i+\hat{y}}}^2 + {B^y_{i+\hat{y}}}^2}} + \frac{B^x_{i-\hat{y}}}{\sqrt{\mu^2_{i-\hat{y}} + {B^x_{i-\hat{y}}}^2 + {B^y_{i-\hat{y}}}^2}} \right. \\
&+ \cos(\frac{\Phi}{L}) \left(\frac{B^x_{i+\hat{x}}}{\sqrt{\mu^2_{i+\hat{x}} + {B^x_{i+\hat{x}}}^2 + {B^y_{i+\hat{x}}}^2}} + \frac{B^x_{i-\hat{x}}}{\sqrt{\mu^2_{i-\hat{x}} + {B^x_{i-\hat{x}}}^2 + {B^y_{i-\hat{x}}}^2}} \right) \\
&\left. + \sin(\frac{\Phi}{L}) \left(\frac{B^y_{i-\hat{x}}}{\sqrt{\mu^2_{i-\hat{x}} + {B^x_{i-\hat{x}}}^2 + {B^y_{i-\hat{x}}}^2}} - \frac{B^y_{i+\hat{x}}}{\sqrt{\mu^2_{i+\hat{x}} + {B^x_{i+\hat{x}}}^2 + {B^y_{i+\hat{x}}}^2}} \right) \right] \\
&+ B_i^y t \left[\frac{B^y_{i+\hat{y}}}{\sqrt{\mu^2_{i+\hat{y}} + {B^x_{i+\hat{y}}}^2 + {B^y_{i+\hat{y}}}^2}} + \frac{B^y_{i-\hat{y}}}{\sqrt{\mu^2_{i-\hat{y}} + {B^x_{i-\hat{y}}}^2 + {B^y_{i-\hat{y}}}^2}} \right. \\
&+ \cos(\frac{\Phi}{L}) \left(\frac{B^y_{i+\hat{x}}}{\sqrt{\mu^2_{i+\hat{x}} + {B^x_{i+\hat{x}}}^2 + {B^y_{i+\hat{x}}}^2}} + \frac{B^y_{i-\hat{x}}}{\sqrt{\mu^2_{i-\hat{x}} + {B^x_{i-\hat{x}}}^2 + {B^y_{i-\hat{x}}}^2}} \right) \\
&\left. + \sin(\frac{\Phi}{L}) \left(\frac{B^x_{i+\hat{x}}}{\sqrt{\mu^2_{i+\hat{x}} + {B^x_{i+\hat{x}}}^2 + {B^y_{i+\hat{x}}}^2}} - \frac{B^x_{i-\hat{x}}}{\sqrt{\mu^2_{i-\hat{x}} + {B^x_{i-\hat{x}}}^2 + {B^y_{i-\hat{x}}}^2}} \right) \right],
\end{aligned}
\tag{B.6}
$$

from which we can deduce for the local fields on site i that

$$
\begin{cases}
B_i^x = t \left[\frac{B^x_{i+\hat{y}}}{\sqrt{\mu^2_{i+\hat{y}} + {B^x_{i+\hat{y}}}^2 + {B^y_{i+\hat{y}}}^2}} + \frac{B^x_{i-\hat{y}}}{\sqrt{\mu^2_{i-\hat{y}} + {B^x_{i-\hat{y}}}^2 + {B^y_{i-\hat{y}}}^2}} \right. \\
\quad + \cos(\frac{\Phi}{L}) \left(\frac{B^x_{i+\hat{x}}}{\sqrt{\mu^2_{i+\hat{x}} + {B^x_{i+\hat{x}}}^2 + {B^y_{i+\hat{x}}}^2}} + \frac{B^x_{i-\hat{x}}}{\sqrt{\mu^2_{i-\hat{x}} + {B^x_{i-\hat{x}}}^2 + {B^y_{i-\hat{x}}}^2}} \right) \\
\quad \left. + \sin(\frac{\Phi}{L}) \left(\frac{B^y_{i-\hat{x}}}{\sqrt{\mu^2_{i-\hat{x}} + {B^x_{i-\hat{x}}}^2 + {B^y_{i-\hat{x}}}^2}} - \frac{B^y_{i+\hat{x}}}{\sqrt{\mu^2_{i+\hat{x}} + {B^x_{i+\hat{x}}}^2 + {B^y_{i+\hat{x}}}^2}} \right) \right] \\
B_i^y = t \left[\frac{B^y_{i+\hat{y}}}{\sqrt{\mu^2_{i+\hat{y}} + {B^x_{i+\hat{y}}}^2 + {B^y_{i+\hat{y}}}^2}} + \frac{B^y_{i-\hat{y}}}{\sqrt{\mu^2_{i-\hat{y}} + {B^x_{i-\hat{y}}}^2 + {B^y_{i-\hat{y}}}^2}} \right. \\
\quad + \cos(\frac{\Phi}{L}) \left(\frac{B^y_{i+\hat{x}}}{\sqrt{\mu^2_{i+\hat{x}} + {B^x_{i+\hat{x}}}^2 + {B^y_{i+\hat{x}}}^2}} + \frac{B^y_{i-\hat{x}}}{\sqrt{\mu^2_{i-\hat{x}} + {B^x_{i-\hat{x}}}^2 + {B^y_{i-\hat{x}}}^2}} \right) \\
\quad \left. + \sin(\frac{\Phi}{L}) \left(\frac{B^x_{i+\hat{x}}}{\sqrt{\mu^2_{i+\hat{x}} + {B^x_{i+\hat{x}}}^2 + {B^y_{i+\hat{x}}}^2}} - \frac{B^x_{i-\hat{x}}}{\sqrt{\mu^2_{i-\hat{x}} + {B^x_{i-\hat{x}}}^2 + {B^y_{i-\hat{x}}}^2}} \right) \right],
\end{cases}
\tag{B.7}
$$

which are none other than the self-consistency equations of the Iterative Mean-Field approach for the starting Hamiltonian (B.2), given in equation (II.33).

It is worth mentioning that a similar calculation can be carried out with all the starting Hamiltonians considered in this thesis, be it the Heisenberg model, the hard-

core boson Hamiltonian or its XY counterpart in the presence of a twist Φ to the boundary conditions and real hoppings, or with periodic boundary conditions. In all cases, the minimization of the classical energy with respect to the set of angles $\{\theta_i\}$ can be rearranged so that by using the relations (B.5) one finally deduces the self-consistency equations for the iterative solution.

2 Equivalency between Twisted boundary conditions with real hoppings and periodic ones with complex hoppings

We will show the equivalency between the two approaches to compute the $1/S$-corrected superfluid density, namely by simply adding a small twist Φ to the boundary conditions, or by keeping periodic boundary conditions and adding a magnetic field, with circulation along a bond Φ/L, along the twist direction which translates the replacement $t \mapsto te^{-\imath\frac{\Phi}{L}}$. In order to do so, we will show that for the clean system (no disorder, $W = 0$) the Holstein-Primakoff Hamiltonian to be diagonalized is exactly the same. We restrict to the clean case because it is the only one where we can derive analytical expressions for the diagonalized Holstein-Primakoff Hamiltonian, since we know the basis which diagonalizes it is the momentum $\{\mathbf{k}\}$.

We start from the part to be diagonalized in the Holstein-Primakoff Hamiltonian (III.34) for the complex hopping and periodic boundary conditions problem:

$$\begin{aligned} H_2 = &- \sum_i \epsilon_i(\Phi) n_i + \sum_i \{(t_{ii+\hat{y}}(\Phi) a_i^\dagger a_{i+\hat{y}} + h.c.) + (\overline{t}_{ii+\hat{y}}(\Phi) a_i a_j + h.c.)\} \\ &+ \sum_i \{(t_{ii+\hat{x}}(\Phi) a_i^\dagger a_{i+\hat{x}} + h.c.) + (\overline{t}_{ii+\hat{x}}(\Phi) a_i a_{i+\hat{x}} + h.c.)\} \end{aligned} \tag{B.8}$$

with the same coefficients given by equations (III.35) and (III.36). In the absence of disorder, *i.e.* that $\forall i, \varphi_i = 0$, $\cos\theta_i = \cos\theta$ and $\mu_i = \mu$, these coefficients simplify to:

$$\begin{cases} t_{ii+\hat{y}}(\Phi) = t_{ii-\hat{y}}(\Phi) = -\dfrac{t}{2}\left[1+\cos^2\theta\right] = t^y \\ \overline{t}_{ii+\hat{y}}(\Phi) = \overline{t}_{ii-\hat{y}}(\Phi) = \dfrac{t}{2}\left[1-\cos^2\theta\right] = \overline{t^y} \\ t_{ii+\hat{x}}(\Phi) = t_{ii+\hat{x}}(\Phi) = -\dfrac{t}{2}\cos\left(\dfrac{\Phi}{L}\right)\left[1+\cos^2\theta\right] = t^x = t^y\cos\left(\dfrac{\Phi}{L}\right) \\ \overline{t}_{ii+\hat{x}}(\Phi) = \overline{t}_{ii-\hat{x}}(\Phi) = \dfrac{t}{2}\cos(\dfrac{\Phi}{L})\left[1-\cos^2\theta\right] = \overline{t^x} = \overline{t^y}\cos\left(\dfrac{\Phi}{L}\right) \\ \epsilon_i(\Phi) = -\mu\cos\theta - 2t\sin^2\theta\left(1+\cos(\dfrac{\Phi}{L})\right) = \epsilon. \end{cases} \tag{B.9}$$

Let us diagonalize this Hamiltonian by applying the Fourier Transform defined as

$$\begin{cases} b_i = \dfrac{1}{\sqrt{N}} \sum\limits_{\mathbf{k}} e^{\imath \mathbf{R_i}.\mathbf{k}} b_{\mathbf{k}} \\ b_i^\dagger = \dfrac{1}{\sqrt{N}} \sum\limits_{\mathbf{k}} e^{-\imath \mathbf{R_i}.\mathbf{k}} b_{\mathbf{k}}^\dagger, \end{cases} \tag{B.10}$$

on each part of the Hamiltonian separately, for clarity issues. In the curse of the calculations here forth described, the equality

$$\sum_i e^{-\imath(\mathbf{k}-\mathbf{k}')\mathbf{R_i}} = N\delta(\mathbf{k}-\mathbf{k}'). \tag{B.11}$$

will be used several times. Let us begin by the diagonal part of Hamiltonian (B.8):

$$\sum_i \epsilon(\Phi) n_i = \frac{1}{N} \sum_{\mathbf{k}} \sum_{\mathbf{k}'} \epsilon b_{\mathbf{k}}^\dagger b_{\mathbf{k}'} \sum_i e^{-\imath(\mathbf{k}-\mathbf{k}')\mathbf{R_i}} = \sum_{\mathbf{k}} \epsilon b_{\mathbf{k}}^\dagger b_{\mathbf{k}} = \sum_{\mathbf{k}} \frac{\epsilon}{2} (b_{\mathbf{k}}^\dagger b_{\mathbf{k}} + b_{-\mathbf{k}}^\dagger b_{-\mathbf{k}}). \tag{B.12}$$

where we have used the equality (B.11).

Moving on to the off-diagonal part of the Holstein-Primakoff Hamiltonian (B.8). The two sums in it are formally the same, but with different coefficients t^x and t^y defined in (B.9) accounting for the twist (or magnetic field) being applied only along the x direction. The r index can be either $r = x$ or $r = y$. The off-diagonal part reads:

$$\begin{aligned} \sum_{\langle ij \rangle r} (t_{ij}^r a_i^\dagger a_{ij} + h.c.) =& \frac{1}{2N} t^r \sum_{\mathbf{k}} \sum_{\mathbf{k}'} \left\{ b_{\mathbf{k}}^\dagger b_{\mathbf{k}'} \left(e^{\imath k_r} \sum_i e^{-\imath(\mathbf{k}-\mathbf{k}')\mathbf{R_i}} + e^{-\imath k_r} \sum_i e^{-\imath(\mathbf{k}-\mathbf{k}')\mathbf{R_i}} \right) \right. \\ & \left. + b_{\mathbf{k}} b_{\mathbf{k}'}^\dagger \left(e^{\imath k_r} \sum_i e^{\imath(\mathbf{k}-\mathbf{k}')\mathbf{R_i}} + e^{-\imath k_r} \sum_i e^{\imath(\mathbf{k}-\mathbf{k}')\mathbf{R_i}} \right) \right\} \\ & + \frac{1}{2N} \overline{t^r} \sum_{\mathbf{k}} \sum_{\mathbf{k}'} \left\{ b_{\mathbf{k}}^\dagger b_{\mathbf{k}'}^\dagger \left(e^{\imath k_r} \sum_i e^{\imath(\mathbf{k}+\mathbf{k}')\mathbf{R_i}} + e^{-\imath k_r} \sum_i e^{\imath(\mathbf{k}+\mathbf{k}')\mathbf{R_i}} \right) \right. \\ & \left. + b_{\mathbf{k}} b_{\mathbf{k}'} \left(e^{\imath k_r} \sum_i e^{-\imath(\mathbf{k}+\mathbf{k}')\mathbf{R_i}} + e^{-\imath k_r} \sum_i e^{-\imath(\mathbf{k}+\mathbf{k}')\mathbf{R_i}} \right) \right\} \\ =& \frac{t^r}{2N} \sum_{\mathbf{k}} \left\{ 2N \cos(k_r) b_{\mathbf{k}}^\dagger b_{\mathbf{k}} + 2N \cos(k_r) b_{-\mathbf{k}}^\dagger b_{-\mathbf{k}} \right\} \\ & + \frac{\overline{t^r}}{2N} \sum_{\mathbf{k}} \left\{ 2N \cos(k_r) b_{\mathbf{k}}^\dagger b_{-\mathbf{k}}^\dagger + 2N \cos(k_r) b_{\mathbf{k}} b_{-\mathbf{k}} \right\}. \end{aligned} \tag{B.13}$$

Now, putting together the results of equations (B.12) and (B.13), we obtain the

Fourier space-diagonalized Holstein-Primakoff Hamiltonian:

$$\begin{aligned} H_2 =& t^y \sum_{\mathbf{k}} (\cos k_y + \cos(\frac{\Phi}{L}) \cos k_x)(b^\dagger_{\mathbf{k}} b_{\mathbf{k}} + b^\dagger_{-\mathbf{k}} b_{-\mathbf{k}}) \\ &+ \overline{t^y} \sum_{\mathbf{k}} (\cos k_y + \cos(\frac{\Phi}{L}) \cos k_x)(b^\dagger_{\mathbf{k}} b^\dagger_{-\mathbf{k}} + b_{\mathbf{k}} b_{-\mathbf{k}}) \\ &- \frac{\epsilon}{2} \sum_{\mathbf{k}} b^\dagger_{\mathbf{k}} b_{\mathbf{k}} + b^\dagger_{-\mathbf{k}} b_{-\mathbf{k}}, \end{aligned} \tag{B.14}$$

which can be finally contracted as

$$H_2 = \sum_{\mathbf{k}} \left[A_{\mathbf{k}} (b^\dagger_{\mathbf{k}} b_{\mathbf{k}} + b^\dagger_{-\mathbf{k}} b_{-\mathbf{k}}) + B_{\mathbf{k}} (b^\dagger_{\mathbf{k}} b^\dagger_{-\mathbf{k}} + b_{\mathbf{k}} b_{-\mathbf{k}}) \right] \tag{B.15}$$

where we have defined the k-dependent coefficients

$$\begin{cases} A_{\mathbf{k}} = -\frac{t}{2}(1+\cos^2\theta)(\cos k_y + \cos(\frac{\Phi}{L})\cos k_x) + \frac{\mu}{2}\cos\theta + t\sin^2\theta(1+\cos(\frac{\Phi}{L})) \\ B_{\mathbf{k}} = \frac{t}{2}\sin^2\theta(\cos k_y + \cos(\frac{\Phi}{L})\cos k_x). \end{cases} \tag{B.16}$$

This can be further simplified by using the minimization of the classical energy (B.2), which in the clean case gives the equation

$$\frac{\mu}{2}\sin\theta - t\cos\theta\sin\theta - t\cos\theta\sin\theta\cos(\frac{\Phi}{L}) = 0 \tag{B.17}$$

which yields for the angle θ:

$$\Rightarrow \begin{cases} \cos\theta = \dfrac{\mu}{2t(1+\cos(\frac{\Phi}{L}))} \\ \sin\theta = \pm\sqrt{1 - \dfrac{\mu^2}{4t^2(1+\cos(\frac{\Phi}{L}))^2}}. \end{cases} \tag{B.18}$$

We end up with the diagonal Holstein-Primakoff Hamiltonian (B.15) with the coefficients

$$\begin{cases} A_{\mathbf{k}} = -\frac{t}{2}(1+\cos^2\theta)(\cos k_y + \cos(\frac{\Phi}{L})\cos k_x) + t(1+\cos(\frac{\Phi}{L})) \\ B_{\mathbf{k}} = \frac{t}{2}\sin^2\theta(\cos k_y + \cos(\frac{\Phi}{L})\cos k_x). \end{cases} \tag{B.19}$$

These expressions are similar to those obtained by Coletta *et al.* [246] for the diagonalized Holstein-Primakoff Hamiltonian for the same model of hard-core bosons in the presence of a twist to the boundary conditions with the difference that in their case they have put the twist in *both* x and y directions and our result is for the complex hoppings along the x direction alone, but if we applied the magnetic field along the y direction as well we would obtain identical results.

Bibliography

[1] L. Pitaevskii and S. Stringari, *Bose-Einstein Condensation* (Clarendon Press, Oxford, 2003).

[2] A. J. Leggett, *Quantum Liquids: Bose Condensation and Cooper Pairing in Condensed-Matter Systems* (Oxford University Press, Oxford, 2006).

[3] P. W. Anderson, "Theory of dirty superconductors", *Journal of Physics and Chemistry of Solids* **11**, 26 (1959).

[4] F. Evers and A. Mirlin, "Anderson transitions", *Reviews of Modern Physics* **80**, 1355 (2008).

[5] A. Lagendijk, B. v. Tiggelen, and D. S. Wiersma, "Fifty years of Anderson localization", *Physics Today* **62**, 24 (2009).

[6] M. P. A. Fisher, P. B. Weichman, G. Grinstein, and D. S. Fisher, "Boson localization and the superfluid-insulator transition", *Physical Review B* **40**, 546 (1989).

[7] J. D. Reppy, "Superfluid helium in porous media", *Journal of Low Temperature Physics* **87**, 205 (1992).

[8] M. Ma and P. A. Lee, "Localized superconductors", *Physical Review B* **32**, 5658 (1985).

[9] M. Ma, B. I. Halperin, and P. A. Lee, "Strongly disordered superfluids: Quantum fluctuations and critical behavior", *Physical Review B* **34**, 3136 (1986).

[10] T. Giamarchi and H. J. Schulz, "Localization and interaction in one-dimensional quantum fluids", *Europhysics Letters* **3**, 1287 (1987).

[11] T. Giamarchi and H. J. Schulz, "Anderson localization and interactions in one-dimensional metals", *Physical Review B* **37**, 325 (1988).

[12] D. S. Fisher and M. P. A. Fisher, "Onset of superfluidity in random media", *Physical Review Letters* **61**, 1847 (1988).

[13] J. F. Allen and H. Jones, "New Phenomena Connected with Heat Flow in Helium II", *Nature* **141**, 243 (1938).

[14] D. Finotello, K. A. Gillis, A. Wong, and M. H. W. Chan, "Sharp Heat-Capacity Signature at the Superfluid Transition of Helium Films in Porous Glasses", *Physical Review Letters* **61**, 1954 (1988).

[15] A. M. Goldman and Y. Liu, "The two-dimensional superconductor-insulator transition", *Physica D: Nonlinear Phenomena* **83**, 163 (1995).

[16] B. C. Crooker, B. Hebral, E. N. Smith, Y. Takano, and J. D. Reppy, "Superfluidity in a dilute Bose gas", *Physical Review Letters* **51**, 666 (1983).

[17] P. A. Crowell, J. D. Reppy, S. Mukherjee, J. Ma, M. H. W. Chan, and D. W. Schaefer, "Critical behavior of superfluid He^4 films adsorbed in aerogel glass", *Physical Review B* **51**, 12721 (1995).

[18] P. A. Crowell, F. W. Van Keuls, and J. D. Reppy, "Onset of superfluidity in He 4 films adsorbed on disordered substrates", *Physical Review B* **55**, 12620 (1997).

[19] P. Levitz, G. Ehret, S. Sinha, and J. Drake, "Porous vycor glass:The microstructure as probed by electron miscroscopy,direct energy transfer, small angle scattering and molecular adsorption", *Journal of Chemical Physics* **95**, 6151 (1991).

[20] D. W. Schaefer and K. D. Keefer, "Structure of random porous materials: silica aerogel", *Physical Review Letters* **56**, 2199 (1986).

[21] R. Vacher, T. Woignier, J. Pelous, and E. Courtens, "Structure and self-similarity of silica aerogels", *Physical Review B* **37**, 6500 (1988).

[22] E. L. Andronikashvili, *Zh. Eksp. Teor. Fiz.* **16**, 780 (1946).

[23] D. Shahar and Z. Ovadyahu, "Superconductivity near the mobility edge", *Physical Review B* **46**, 10917 (1992).

[24] B. Sacépé, C. Chapelier, T. Baturina, V. Vinokur, M. Baklanov, and M. Sanquer, "Disorder-Induced Inhomogeneities of the Superconducting State Close to the Superconductor-Insulator Transition", *Physical Review Letters* **101**, 157006 (2008).

[25] B. Sacépé, T. Dubouchet, C. Chapelier, M. Sanquer, M. Ovadia, D. Shahar, M. Feigel'man, and L. Ioffe, "Localization of preformed Cooper pairs in disordered superconductors", *Nature Physics* **7**, 239 (2011).

[26] E. F. C. Driessen, P. C. J. J. Coumou, R. R. Tromp, P. J. de Visser, and T. M. Klapwijk, "Strongly Disordered TiN and NbTiN s-Wave Superconductors Probed by Microwave Electrodynamics", *Physical Review Letters* **109**, 107003 (2012).

[27] D. Dochev, V. Desmaris, A. Pavolotsky, D. Meledin, Z. Lai, A. Henry, E. Janzén, E. Pippel, J. Woltersdorf, and V. Belitsky, "Growth and characterization of epitaxial ultra-thin NbN films on 3C-SiC/Si substrate for terahertz applications", *Superconductor Science and Technology* **24**, 035016 (2011).

[28] Y. Noat, V. Cherkez, C. Brun, T. Cren, C. Carbillet, F. Debontridder, K. Ilin, M. Siegel, A. Semenov, H.-W. Hübers, and D. Roditchev, "Unconventional superconductivity in ultrathin superconducting NbN films studied by scanning tunneling spectroscopy", *Physical Review B* **88**, 014503 (2013).

[29] M. Mondal, A. Kamlapure, S. C. Ganguli, J. Jesudasan, V. Bagwe, L. Benfatto, and P. Raychaudhuri, "Enhancement of the finite-frequency superfluid response in the pseudogap regime of strongly disordered superconducting films", *Scientific Reports* **3**, 1357 (2013).

[30] G. Lemarié, A. Kamlapure, D. Bucheli, L. Benfatto, J. Lorenzana, G. Seibold, S. C. Ganguli, P. Raychaudhuri, and C. Castellani, "Universal scaling of the order-parameter distribution in strongly disordered superconductors", *Physical Review B* **87**, 184509 (2013).

[31] Z. Ovadyahu, "Some finite temperature aspects of the Anderson transition", *Journal of Physics C: Solid State Physics* **19**, 5187 (1986).

[32] D. Kowal and Z. Ovadyahu, "Disorder induced granularity in an amorphous superconductor", *Solid State Communications* **90**, 783 (1994).

[33] N. Hadacek, M. Sanquer, and J.-C. Villégier, "Double reentrant superconductor-insulator transition in thin TiN films", *Physical Review B* **69**, 024505 (2004).

[34] T. Baturina, A. Mironov, V. Vinokur, M. Baklanov, and C. Strunk, "Localized Superconductivity in the Quantum-Critical Region of the Disorder-Driven Superconductor-Insulator Transition in TiN Thin Films", *Physical Review Letters* **99**, 257003 (2007).

[35] D. Kowal and Z. Ovadyahu, "Scale dependent superconductor-insulator transition", *Physica C* **468**, 322 (2005).

[36] G. Sambandamurthy, L. Engel, A. Johansson, and D. Shahar, "Superconductivity-Related Insulating Behavior", *Physical Review Letters* **92**, 107005 (2004).

[37] G. Sambandamurthy, L. Engel, A. Johansson, E. Peled, and D. Shahar, "Experimental Evidence for a Collective Insulating State in Two-Dimensional Superconductors", *Physical Review Letters* **94**, 017003 (2005).

[38] V. M. Vinokur, T. I. Baturina, M. V. Fistul, A. Y. Mironov, M. R. Baklanov, and C. Strunk, "Superinsulator and quantum synchronization", *Nature* **452**, 613 (2008).

[39] V. F. Gantmakher, M. V. Golubkov, J. G. S. Lok, and A. K. Geim, "Giant negative magnetoresistance of semi-insulating amorphous indium oxide films in strong magnetic fields", *Zh. Eksp. Teor. Fiz* **109**, 1765 (1996).

[40] T. Baturina, C. Strunk, M. Baklanov, and A. Satta, "Quantum Metallicity on the High-Field Side of the Superconductor-Insulator Transition", *Physical Review Letters* **98**, 127003 (2007).

[41] M. Feigel'man, L. Ioffe, V. Kravtsov, and E. Yuzbashyan, "Eigenfunction Fractality and Pseudogap State near the Superconductor-Insulator Transition", *Physical Review Letters* **98**, 027001 (2007).

[42] A. M. Finkel'shtein, "Superconducting transition temperature in amorphous films", *JETP Letters* **45**, 46 (1987).

[43] V. F. Gantmakher and V. T. Dolgopolov, "Superconductor - Insulator quantum phase transition", *Physics-Uspekhi* **53**, 1 (2010).

[44] J. Bardeen, L. N. Cooper, and J. R. Schrieffer, "Theory of superconductivity", *Physical Review* **108**, 1175 (1957).

[45] I. Giaever, "Energy gap in superconductors measured by electron tunneling", *Physical Review Letters* **5**, 147 (1960).

[46] Ø. Fischer, M. Kugler, I. Maggio-Aprile, C. Berthod, and C. Renner, "Scanning tunneling spectroscopy of high-temperature superconductors", *Reviews of Modern Physics* **79**, 353 (2007).

[47] D. R. Nelson and V. M. Vinokur, "Boson localization and pinning by correlated disorder in high-temperature superconductors", *Physical Review Letters* **68**, 2398 (1992).

[48] D. R. Nelson and V. M. Vinokur, "Boson localization and correlated pinning of superconducting vortex arrays", *Physical Review B* **48**, 13060 (1993).

[49] A. J. Leggett, "What DO we know about high T_c?", *Nature Physics* **2**, 134 (2006).

[50] V. J. Emery and S. Kivelson, "Importance of phase fluctuations in superconductor with small superfluid density", *Nature* **374**, 434 (1995).

[51] F. Dalfovo, S. Giorgini, L. P. Pitaevskii, and S. Stringari, "Theory of Bose-Einstein condensation in trapped gases", *Reviews of Modern Physics* **71**, 463 (1999).

[52] W. Ketterle, D. S. Durfee, and D. M. Stamper-Kurn, "Bose-Einstein Condensation in Atomic Gases", in *Proc. of the International School of Physics "Enrico Fermi", Course CXL*, edited by M. Inguscio, S. Stringari, and C. E. Wieman IOP Press 1998.

[53] W. Ketterle and M. W. Zwierlein, "Ultra-cold Fermi Gases", in *Proc. of the International School of Physics "Enrico Fermi", Course CLXIV*, edited by M. Inguscio, W. Ketterle, and C. Salomon IOP Press 2008.

[54] S. Giorgini and S. Stringari, "Theory of ultracold atomic Fermi gases", *Reviews of Modern Physics* **80**, 1215 (2008).

[55] N. Trivedi, "Quantum Phase Transition in Disordered Systems: What are the Issues?", in *Proceedings of the 20th International Workshop on Condensed Matter Theories* volume 12 pp. 141–157 Plenum Press 1997.

[56] M. Lewenstein, A. Sanpera, V. Ahufinger, B. Damski, A. Sen(De), and U. Sen, "Ultracold atomic gases in optical lattices: mimicking condensed matter physics and beyond", *Advances in Physics* **56**, 243 (2007).

[57] L. Sanchez-Palencia and M. Lewenstein, "Disordered quantum gases under control", *Nature Physics* **6**, 87 (2010).

[58] M. H. Anderson, J. R. Ensher, M. R. Matthews, C. E. Wieman, and E. A. Cornell, "Observation of Bose-Einstein Condensation in a Dilute Atomic Vapor", *Science* **269**, 14 (1995).

[59] K. B. Davis, M. O. Mewes, M. R. Andrews, N. J. van Druten, D. S. Durfee, D. M. Kurn, and W. Ketterle, "Bose-Einstein Condensation in a Gas of Sodium Atoms", *Physical Review Letters* **75**, 3969 (1995).

[60] L. P. Pitaevskii, "Vortex lines in an imperfect Bose gas", *Soviet Physics Journal of Experimental and Theoretical Physics (USSR)* **13**, 646 (1961).

[61] E. Gross, "Structure of a quantized vortex in boson systems", *Il Nuovo Cimento Series 10* **20**, 454 (1961).

[62] R. C. Kuhn, C. Miniatura, D. Delande, O. Sigwarth, and C. A. Müller, "Localization of Matter Waves in Two-Dimensional Disordered Optical Potentials", *Physical Review Letters* **95**, 250403 (2005).

[63] G. Roati, C. D'Errico, L. Fallani, M. Fattori, C. Fort, M. Zaccanti, G. Modugno, M. Modugno, and M. Inguscio, "Anderson localization of a non-interacting Bose-Einstein condensate", *Nature* **453**, 895 (2008).

[64] J. Billy, V. Josse, Z. Zuo, A. Bernard, B. Hambrecht, P. Lugan, D. Clément, L. Sanchez-Palencia, P. Bouyer, and A. Aspect, "Direct observation of Anderson localization of matter waves in a controlled disorder", *Nature* **453**, 891 (2008).

[65] J. Chabé, G. Lemarié, B. Grémaud, D. Delande, P. Szriftgiser, and J. C. Garreau, "Experimental Observation of the Anderson Metal-Insulator Transition with Atomic Matter Waves", *Physical Review Letters* **101**, 255702 (2008).

[66] M. Greiner, O. Mandel, T. Esslinger, T. W. Hänsch, and I. Bloch, "Quantum phase transition from a superfluid to a Mott insulator in a gas of ultracold atoms", *Nature* **415**, 39 (2002).

[67] T. Stöferle, H. Moritz, C. Schori, M. Köhl, and T. Esslinger, "Transition from a Strongly Interacting 1D Superfluid to a Mott Insulator", *Physical Review Letters* **92**, 130403 (2004).

[68] F. Gerbier, A. Widera, S. Fölling, O. Mandel, T. Gericke, and I. Bloch, "Interference pattern and visibility of a Mott insulator", *Physical Review A* **72**, 053606 (2005).

[69] F. Gerbier, A. Widera, S. Fölling, O. Mandel, T. Gericke, and I. Bloch, "Phase Coherence of an Atomic Mott Insulator", *Physical Review Letters* **95**, 050404 (2005).

[70] I. Spielman, W. Phillips, and J. Porto, "Mott-Insulator Transition in a Two-Dimensional Atomic Bose Gas", *Physical Review Letters* **98**, 080404 (2007).

[71] I. Spielman, W. Phillips, and J. Porto, "Condensate Fraction in a 2D Bose Gas Measured across the Mott-Insulator Transition", *Physical Review Letters* **100**, 120402 (2008).

[72] I. Bloch, J. Dalibard, and W. Zwerger, "Many-body physics with ultracold gases", *Reviews of Modern Physics* **80**, 885 (2008).

[73] D. Jaksch, C. Bruder, J. I. Cirac, C. W. Gardiner, and P. Zoller, "Cold bosonic atoms in optical lattices", *Physical Review Letters* **81**, 3108 (1998).

[74] P. Courteille, R. S. Freeland, D. J. Heinzen, F. A. Van Abeelen, and B. J. Verhaar, "Observation of a Feshbach resonance in cold atom scattering", *Physical Review Letters* **81**, 69 (1998).

[75] S. Inouye, M. R. Andrews, J. Stenger, H.-J. Miesner, D. M. Stamper-Kurn, and W. Ketterle, "Observation of Feshbach resonances in a Bose - Einstein condensate", *Nature* **392**, 151 (1998).

[76] J. Lye, L. Fallani, M. Modugno, D. Wiersma, C. Fort, and M. Inguscio, "Bose-Einstein Condensate in a Random Potential", *Physical Review Letters* **95**, 070401 (2005).

[77] D. Clément, A. F. Varón, M. Hugbart, J. A. Retter, P. Bouyer, L. Sanchez-Palencia, D. M. Gangardt, G. V. Shlyapnikov, and A. Aspect, "Suppression of Transport of an Interacting Elongated Bose-Einstein Condensate in a Random Potential", *Physical Review Letters* **95**, 170409 (2005).

[78] C. Fort, L. Fallani, V. Guarrera, J. E. Lye, M. Modugno, D. S. Wiersma, and M. Inguscio, "Effect of Optical Disorder and Single Defects on the Expansion of a Bose-Einstein Condensate in a One-Dimensional Waveguide", *Physical Review Letters* **95**, 170410 (2005).

[79] T. Schulte, S. Drenkelforth, J. Kruse, W. Ertmer, J. Arlt, K. Sacha, J. Zakrzewski, and M. Lewenstein, "Routes Towards Anderson-Like Localization of Bose-Einstein Condensates in Disordered Optical Lattices", *Physical Review Letters* **95**, 170411 (2005).

[80] M. White, M. Pasienski, D. McKay, S. Q. Zhou, D. Ceperley, and B. DeMarco, "Strongly Interacting Bosons in a Disordered Optical Lattice", *Physical Review Letters* **102**, 055301 (2009).

[81] M. Pasienski, D. McKay, M. White, and B. DeMarco, "A disordered insulator in an optical lattice", *Nature Physics* **6**, 677 (2010).

[82] S. Krinner, D. Stadler, J. Meineke, J.-P. Brantut, and T. Esslinger, "Superfluidity with disorder in a thin film of quantum gas", *Physical Review Letters* **110**, 100601 (2013).

[83] S. Krinner, D. Stadler, J. Meineke, J.-P. Brantut, and T. Esslinger, "Direct Observation of Fragmentation in a Disordered, Strongly Interacting Fermi Gas", *arXiv:1311.5174* (2013).

[84] R. Roth and K. Burnett, "Phase diagram of bosonic atoms in two-color superlattices", *Physical Review A* **68**, 023604 (2003).

[85] B. Damski, J. Zakrzewski, L. Santos, P. Zoller, and M. Lewenstein, "Atomic Bose and Anderson Glasses in Optical Lattices", *Physical Review Letters* **91**, 080403 (2003).

[86] L. Fallani, J. E. Lye, V. Guarrera, C. Fort, and M. Inguscio, "Ultracold Atoms in a Disordered Crystal of Light: Towards a Bose Glass", *Physical Review Letters* **98**, 130404 (2007).

[87] B. Deissler, M. Zaccanti, G. Roati, C. D'Errico, M. Fattori, M. Modugno, G. Modugno, and M. Inguscio, "Delocalization of a disordered bosonic system by repulsive interactions", *Nature Physics* **6**, 354 (2010).

[88] C. D'Errico, E. Lucioni, L. Tanzi, L. Gori, G. Roux, I. P. McCulloch, T. Giamarchi, M. Inguscio, and G. Modugno, "Observation of a Disordered Bosonic Insulator from Weak to Strong Interactions", *Physical Review Letters* **113**, 095301 (2014).

[89] P. Vignolo, Z. Akdeniz, and M. P. Tosi, "The transmittivity of a Bose-Einstein condensate on a lattice: interference from period doubling and the effect of disorder", *Journal of Physics B: Atomic, Molecular and Optical Physics* **36**, 4535 (2003).

[90] U. Gavish and Y. Castin, "Matter-Wave Localization in Disordered Cold Atom Lattices", *Physical Review Letters* **95**, 020401 (2005).

[91] S. Ospelkaus, C. Ospelkaus, O. Wille, M. Succo, P. Ernst, K. Sengstock, and K. Bongs, "Localization of Bosonic Atoms by Fermionic Impurities in a Three-Dimensional Optical Lattice", *Physical Review Letters* **96**, 180403 (2006).

[92] G. Roux, T. Barthel, I. P. McCulloch, C. Kollath, U. Schollwöck, and T. Giamarchi, "Quasiperiodic Bose-Hubbard model and localization in one-dimensional cold atomic gases", *Physical Review A* **78**, 023628 (2008).

[93] E. G. Baytev and L. S. Braginskii, "Antiferrornagnet in a strong magnetic field: analogy with Bose gas", *Journal of Experimental and Theoretical Physics* **60**, 781 (1984).

[94] T. Giamarchi and A. M. Tsvelik, "Coupled ladders in a magnetic field", *Physical Review B* **59**, 11398 (1999).

[95] T. Giamarchi, C. Ruegg, and O. Tchernyshyov, "Bose-Einstein condensation in magnetic insulators", *Nature Physics* **4**, 198 (2008).

[96] V. Zapf, M. Jaime, and C. Batista, "Bose-Einstein condensation in quantum magnets", *Reviews of Modern Physics* **86**, 563 (2014).

[97] B. R. Patyal, B. L. Scott, and R. D. Willett, "Crystal-structure, magnetic-susceptibility, and EPR studies of bis (piperidinium) tetrabromocuprate (II): A novel monomer system showing spin diffusion", *Physical Review B* **41**, 1657 (1990).

[98] H. Manaka, I. Yamada, and K. Yamaguchi, "Ferromagnetic-Dominant Alternating Heisenberg Chains with Ferromagnetic and Antiferromagnetic Interactions Formed in $(CH_3)_2CHNH_3CuCl_3$", *Journal of the Physical Society of Japan* **72**, 564 (1997).

[99] M. B. Stone, I. Zaliznyak, D. H. Reich, and C. Broholm, "Frustration-induced two-dimensional quantum disordered phase in piperazinium hexachlorodicuprate", *Physical Review B* **64**, 144405 (2001).

[100] M. Fujisawa, J.-I. Yamaura, H. Tanaka, H. Kageyama, Y. Narumi, and K. Kindo, "Crystal Structure and Magnetic Properties of the Quasi-One-Dimensional Quantum Spin System Cu $_2$ Cl $_4$ ·H $_8$ C $_4$ SO $_2$", *Journal of the Physical Society of Japan* **72**, 694 (2003).

[101] M. Azuma, Y. Fujishiro, M. Takano, M. Nohara, and H. Takagi, "Switching of the gapped singlet spin-liquid state to an antiferromagnetically ordered state in $Sr(Cu_{1-x}Zn_x)_2O_3$", *Physical Review B* **55**, 8658(R) (1997).

[102] Y. Uchiyama, Y. Sasago, I. Tsukada, K. Uchinokura, A. Zheludev, T. Hayashi, N. Miura, and P. Böni, "Spin-vacancy-induced long-range order in a new haldane-gap antiferromagnet", *Physical Review Letters* **83**, 632 (1999).

[103] J. Bobroff, N. Laflorencie, L. Alexander, A. Mahajan, B. Koteswararao, and P. Mendels, "Impurity-Induced Magnetic Order in Low-Dimensional Spin-Gapped Materials", *Physical Review Letters* **103**, 047201 (2009).

[104] T. Shiroka, F. Casola, V. Glazkov, A. Zheludev, K. Prša, H.-R. Ott, and J. Mesot, "Distribution of NMR Relaxations in a Random Heisenberg Chain", *Physical Review Letters* **106**, 137202 (2011).

[105] M. Thede, F. Xiao, C. Baines, C. Landee, E. Morenzoni, and A. Zheludev, "Ordering in weakly coupled random singlet spin chains", *Physical Review B* **86**, 180407 (2012).

[106] C. Rüegg, B. Normand, M. Matsumoto, A. Furrer, D. McMorrow, K. Krämer, H. Güdel, S. Gvasaliya, H. Mutka, and M. Boehm, "Quantum Magnets under Pressure: Controlling Elementary Excitations in $TlCuCl_3$", *Physical Review Letters* **100**, 205701 (2008).

[107] D. Hüvonen, S. Zhao, M. Månsson, T. Yankova, E. Ressouche, C. Niedermayer, M. Laver, S. N. Gvasaliya, and A. Zheludev, "Field-induced criticality in a gapped quantum magnet with bond disorder", *Physical Review B* **85**, 100410 (2012).

[108] D. Hüvonen, S. Zhao, G. Ehlers, M. Månsson, S. N. Gvasaliya, and A. Zheludev, "Excitations in a quantum spin liquid with random bonds", *Physical Review B* **86**, 214408 (2012).

[109] B. Náfrádi, T. Keller, H. Manaka, U. Stuhr, A. Zheludev, and B. Keimer, "Bond randomness induced magnon decoherence in a spin-$\frac{1}{2}$ ladder compound", *Physical Review B* **87**, 020408(R) (2013).

[110] M. Vojta, "Excitation Spectra of Disordered Dimer Magnets Near Quantum Criticality", *Physical Review Letters* **111**, 097202 (2013).

[111] X. Yu and M. Müller, "Localization of disordered bosons and magnets in random fields", *Annals of Physics* **337**, 55 (2013).

[112] C. Hess, B. Büchner, U. Ammerahl, L. Colonescu, F. Heidrich-Meisner, W. Brenig, and A. Revcolevschi, "Magnon Heat Transport in Doped La_2CuO_4", *Physical Review Letters* **90**, 197002 (2003).

[113] N. Hlubek, P. Ribeiro, R. Saint-Martin, S. Nishimoto, A. Revcolevschi, S.-L. Drechsler, G. Behr, J. Trinckauf, J. E. Hamann-Borrero, J. Geck, B. Büchner, and C. Hess, "Bond disorder and breakdown of ballistic heat transport in the spin-1/2 antiferromagnetic Heisenberg chain as seen in Ca-doped $SrCuO_2$", *Physical Review B* **84**, 214419 (2011).

[114] A. Zheludev and T. Roscilde, "Dirty-boson physics with magnetic insulators", *Comptes Rendus Physique* **14**, 740 (2013).

[115] Y. Endoh, G. Shirane, R. J. Birgeneau, P. M. Richards, and S. L. Holt, "Dynamics of an S=1/2, One-Dimensional Heisenberg Antiferromagnet", *Physical Review Letters* **32**, 170 (1974).

[116] P. P. Mitra and B. I. Halperin, "Understanding far-infrared absorption in the S= 1 antiferromagnetic chain compound NENP", *Physical Review Letters* **72**, 912 (1994).

[117] R. Chitra and T. Giamarchi, "Critical properties of gapped spin-chains and ladders in a magnetic field", *Physical Review B* **55**, 5816 (1997).

[118] Z. Honda, H. Asakawa, and K. Katsumata, "Magnetic field versus temperature phase diagram of a quasi-one-dimensional $S = 1$ Heisenberg antiferromagnet", *Physical Review Letters* **81**, 2566 (1998).

[119] A. Oosawa, H. Katori, and H. Tanaka, "Specific heat study of the field-induced magnetic ordering in the spin-gap system $TlCuCl_3$", *Physical Review B* **63** (2001).

[120] T. Hong, R. Custelcean, B. Sales, B. Roessli, D. Singh, and A. Zheludev, "Synthesis and structural characterization of 2Dioxane·2H_2O·$CuCl_2$: Metal-organic compound with Heisenberg antiferromagnetic $S = 1/2$ chains", *Physical Review B* **80**, 132404 (2009).

[121] P. Hammar and D. Reich, "Cu_2(1,4-diazacycloheptane)$_2Cl_4$, a quasi-one-dimensional $S = \frac{1}{2}$ spin liquid system", *Journal of applied physics* **79**, 5392 (1996).

[122] G. Chaboussant, P. A. Crowell, L. P. Lévy, O. Piovesana, A. Madouri, and D. Mailly, "Experimental phase diagram of $Cu_2(C_5H_{12}N_2)_2Cl_4$: A quasi-one-dimensional antiferromagnetic spin-Heisenberg ladder", *Physical Review B* **55**, 3046 (1997).

[123] P. R. Hammar, D. H. Reich, C. Broholm, and F. Trouw, "Spin gap in a quasi-one-dimensional S= 1 2 antiferromagnet: Cu_2(1, 4-diazacycloheptane)$_2Cl_4$", *Physical Review B* **57**, 7846 (1998).

[124] M. Hagiwara, H. A. Katori, U. Schollwöck, and H.-J. Mikeska, "Specific heat of an $S = 1/2$ Heisenberg ladder compound $Cu_2(C_5H_{12}N_2)_2Cl_4$ under magnetic fields", *Physical Review B* **62**, 1051 (2000).

[125] B. Watson, V. Kotov, M. Meisel, D. Hall, G. Granroth, W. Montfrooij, S. Nagler, D. Jensen, R. Backov, M. Petruska, G. Fanucci, and D. Talham, "Magnetic Spin Ladder $(C_5H_{12}N)_2CuBr_4$: High-Field Magnetization and Scaling near Quantum Criticality", *Physical Review Letters* **86**, 5168 (2001).

[126] T. Masuda, A. Zheludev, H. Manaka, L.-P. Regnault, J.-H. Chung, and Y. Qiu, "Dynamics of Composite Haldane Spin Chains in IPA-$CuCl_3$", *Physical Review Letters* **96**, 047210 (2006).

[127] M. Stone, C. Broholm, D. Reich, O. Tchernyshyov, P. Vorderwisch, and N. Harrison, "Quantum Criticality in an Organic Magnet", *Physical Review Letters* **96**, 257203 (2006).

[128] C. Rüegg, D. McMorrow, B. Normand, H. Rønnow, S. Sebastian, I. Fisher, C. Batista, S. Gvasaliya, C. Niedermayer, and J. Stahn, "Multiple Magnon Modes and Consequences for the Bose-Einstein Condensed Phase in $BaCuSi_2O_6$", *Physical Review Letters* **98**, 017202 (2007).

[129] S. Krämer, R. Stern, M. Horvatić, C. Berthier, T. Kimura, and I. Fisher, "Nuclear magnetic resonance evidence for a strong modulation of the Bose-Einstein condensate in $BaCuSi_2O_6$", *Physical Review B* **76**, 100406 (2007).

[130] V. V. Mazurenko, M. V. Valentyuk, R. Stern, and A. A. Tsirlin, "Nonfrustrated Interlayer Order and its Relevance to the Bose-Einstein Condensation of Magnons in $BaCuSi_2O_6$", *Physical Review Letters* **112**, 107202 (2014).

[131] U. Tutsch, B. Wolf, S. Wessel, L. Postulka, Y. Tsui, H. Jeschke, I. Opahle, T. Saha-Dasgupta, R. Valentí, A. Brühl, K. Remović-Langer, T. Kretz, H.-W.

Lerner, M. Wagner, and M. Lang, "Evidence of a field-induced Berezinskii-Kosterlitz-Thouless scenario in a two-dimensional spin-dimer system", *Nature Communications* **5**, 5169 (2014).

[132] A. Oosawa, M. Ishii, and H. Tanaka, "Field-induced three-dimensional magnetic ordering in the spin-gap system $TiCuCl_3$", *J. Phys.: Condens. Matter* **11**, 265 (1999).

[133] V. Garlea, A. Zheludev, L.-P. Regnault, J.-H. Chung, Y. Qiu, M. Boehm, K. Habicht, and M. Meissner, "Excitations in a Four-Leg Antiferromagnetic Heisenberg Spin Tube", *Physical Review Letters* **100**, 037206 (2008).

[134] B. T. M. Willis and C. J. Carlile, *Experimental neutron scattering* (Oxford University Press Oxford, 2009).

[135] H. Manaka, I. Yamada, Z. Honda, H. A. Katori, and K. Katsumata, "Field-Induced Magnetic Long-Range Order in the Ferromagnetic-Antiferromagnetic Alternating Heisenberg Chain System (CH 3) 2CHNH 3CuCl 3 Observed by Specific Heat Measurements", *Journal of the Physical Society of Japan* **67**, 3913 (1998).

[136] H. Manaka, I. Yamada, M. Hagiwara, and M. Tokunaga, "High-field and high-frequency ESR study of the Haldane state formed in the ferromagnetic and antiferromagnetic alternating Heisenberg chain system $(CH_3)_2CHNH_3CuCl_3$", *Physical Review B* **63**, 144428 (2001).

[137] V. Garlea, A. Zheludev, T. Masuda, H. Manaka, L.-P. Regnault, E. Ressouche, B. Grenier, J.-H. Chung, Y. Qiu, K. Habicht, K. Kiefer, and M. Boehm, "Excitations from a Bose-Einstein Condensate of Magnons in Coupled Spin Ladders", *Physical Review Letters* **98**, 167202 (2007).

[138] A. Zheludev, V. Garlea, T. Masuda, H. Manaka, L.-P. Regnault, E. Ressouche, B. Grenier, J.-H. Chung, Y. Qiu, K. Habicht, K. Kiefer, and M. Boehm, "Dynamics of quantum spin liquid and spin solid phases in IPA-CuCl3 under an applied magnetic field studied with neutron scattering", *Physical Review B* **76**, 054450 (2007).

[139] B. Náfrádi, T. Keller, H. Manaka, A. Zheludev, and B. Keimer, "Low-Temperature Dynamics of Magnons in a Spin-1/2 Ladder Compound", *Physical Review Letters* **106**, 177202 (2011).

[140] T. Hong, A. Zheludev, H. Manaka, and L.-P. Regnault, "Evidence of a magnetic Bose glass in $(CH_3)_2CHNH_3Cu(Cl_{0.95}Br_{0.05})_3$ from neutron diffraction", *Physical Review B* **81**, 060410 (2010).

[141] T. Hong, Y. H. Kim, C. Hotta, Y. Takano, G. Tremelling, M. M. Turnbull, C. P. Landee, H.-J. Kang, N. B. Christensen, K. Lefmann, K. P. Schmidt, G. S. Uhrig, and C. Broholm, "Field-Induced Tomonaga-Luttinger Liquid Phase of a Two-Leg Spin-1/2 Ladder with Strong Leg Interactions", *Physical Review Letters* **105**, 137207 (2010).

[142] R. Yu, L. Yin, N. S. Sullivan, J. S. Xia, C. Huan, A. Paduan-Filho, N. F. Oliveira Jr, S. Haas, A. Steppke, C. F. Miclea, F. Weickert, R. Movshovich, E.-D. Mun, B. L. Scott, V. S. Zapf, and T. Roscilde, "Bose glass and Mott glass of quasiparticles in a doped quantum magnet", *Nature* **489**, 379 (2012).

[143] R. Yu, C. F. Miclea, F. Weickert, R. Movshovich, A. Paduan-Filho, V. S. Zapf, and T. Roscilde, "Quantum critical scaling at a Bose-glass/superfluid transition: Theory and experiment for a model quantum magnet", *Physical Review B* **86**, 134421 (2012).

[144] S. Sachdev, *Quantum Phase Transitions* (Cambridge University Press, 1999).

[145] M. P. A. Fisher and G. Grinstein, "Quantum Critical Phenomena in Charged Superconductors", *Physical Review Letters* **60**, 208 (1988).

[146] I. F. Herbut, "Critical behavior at superconductor-insulator phase transitions near one dimension", *Physical Review B* **58**, 971 (1998).

[147] F. Pázmándi and G. T. Zimányi, "Direct Mott insulator-to-superfluid transition in the presence of disorder", *Physical Review B* **57**, 5044 (1998).

[148] J. Wu and P. Phillips, "Minimal model for disorder-induced missing moment of inertia in solid He^4", *Physical Review B* **78**, 014515 (2008).

[149] W. Krauth, N. Trivedi, and D. Ceperley, "Superfluid-insulator transition in disordered boson systems", *Physical Review Letters* **67**, 2307 (1991).

[150] J.-W. Lee, M.-C. Cha, and D. Kim, "Phase Diagram of a Disordered Boson Hubbard Model in Two Dimensions", *Physical Review Letters* **87**, 247006 (2001).

[151] R. V. Pai, R. Pandit, H. R. Krishnamurthy, and S. Ramasesha, "One-Dimensional Disordered Bosonic Hubbard Model: A Density-Matrix Renormalization Group Study", *Physical Review Letters* **76**, 2937 (1996).

[152] K. G. Singh and D. S. Rokhsar, "Real-space renormalization study of disordered interacting bosons", *Physical Review B* **46**, 3002 (1992).

[153] F. Pázmándi, G. Zimányi, and R. Scalettar, "Mean-field theory of the localization transition of hard-core bosons", *Physical Review Letters* **75**, 1356 (1995).

[154] U. Bissbort and W. Hofstetter, "Stochastic mean-field theory for the disordered Bose-Hubbard model", *EPL (Europhysics Letters)* **86**, 50007 (2009).

[155] J. K. Freericks and H. Monien, "Strong-coupling expansions for the pure and disordered Bose-Hubbard model", *Physical Review B* **53**, 2691 (1996).

[156] I. F. Herbut, "Dual Superfluid-Bose-Glass Critical Point in Two Dimensions and the Universal Conductivity", *Physical Review Letters* **79**, 3502 (1997).

[157] I. F. Herbut, "Dual theory of the superfluid-Bose-glass transition in the disordered Bose-Hubbard model in one and two dimensions", *Physical Review B* **57**, 13729 (1998).

[158] B. V. Svistunov, "Superfluid – Bose-glass transition in weakly disordered commensurate one-dimensional system", *Physical Review B* **54**, 16131 (1996).

[159] R. Scalettar, G. Batrouni, and G. Zimanyi, "Localization in interacting, disordered, Bose systems", *Physical Review Letters* **66**, 3144 (1991).

[160] M. Makivić, N. Trivedi, and S. Ullah, "Disordered bosons: Critical phenomena and evidence for new low energy excitations", *Physical Review Letters* **71**, 2307 (1993).

[161] M. Wallin, E. S. Sørensen, S. M. Girvin, and A. P. Young, "Superconductor-insulator transition in two-dimensional dirty boson systems", *Physical Review B* **49**, 12115 (1994).

[162] J. Kisker and H. Rieger, "Bose-glass and Mott-insulator phase in the disordered boson Hubbard model", *Physical Review B* **55**, R11981 (1997).

[163] N. Prokof'ev and B. Svistunov, "Superfluid-Insulator Transition in Commensurate Disordered Bosonic Systems: Large-Scale Worm Algorithm Simulations", *Physical Review Letters* **92**, 015703 (2004).

[164] P. Weichman and R. Mukhopadhyay, "Particle-hole symmetry and the dirty boson problem", *Physical Review B* **77**, 214516 (2008).

[165] P. B. Weichman, "Dirty Bosons: Twenty Years Later", *Modern Physics Letters B* **22**, 2623 (2008).

[166] L. Pollet, N. V. Prokof'ev, B. V. Svistunov, and M. Troyer, "Absence of a Direct Superfluid to Mott Insulator Transition in Disordered Bose Systems", *Physical Review Letters* **103**, 140402 (2009).

[167] L. D. Landau and E. M. Lifshitz, *Statistical Physics,* volume 5, 3rd ed. (Butterworth-Heinemann, 1980).

[168] L. Pollet, "A review of Monte Carlo simulations for the Bose-Hubbard model with diagonal disorder", *Comptes Rendus Physique* **14**, 712 (2013).

[169] R. Griffiths, "Nonanalytic Behavior Above the Critical Point in a Random Ising Ferromagnet", *Physical Review Letters* **23**, 17 (1969).

[170] B. M. McCoy, "Incompleteness of the critical exponent description for ferromagnetic systems containing random impurities", *Physical Review Letters* **23**, 383 (1969).

[171] V. Gurarie, L. Pollet, N. V. Prokof'ev, B. V. Svistunov, and M. Troyer, "Phase diagram of the disordered Bose-Hubbard model", *Physical Review B* **80**, 214519 (2009).

[172] B. D. Josephson, "Relation between the superfluid density and order parameter for superfluid He near Tc", *Physics Letters* **21**, 608 (1966).

[173] A. B. Harris, "Effect of random defects on the critical behaviour of Ising models", *Journal of Physics C: Solid State Physics* **7**, 1671 (1974).

[174] J. Chayes, L. Chayes, D. Fisher, and T. Spencer, "Finite-Size Scaling and Correlation Lengths for Disordered Systems", *Physical Review Letters* **57**, 2999 (1986).

[175] F. Pázmándi, R. Scalettar, and G. Zimányi, "Revisiting the Theory of Finite Size Scaling in Disordered Systems: ν Can Be Less than $2/d$", *Physical Review Letters* **79**, 5130 (1997).

[176] P. B. Weichman and R. Mukhopadhyay, "Critical Dynamics of the Dirty Boson Problem: Revisiting the Equality z=d", *Physical Review Letters* **98**, 245701 (2007).

[177] M. E. Fisher, M. N. Barber, and D. Jasnow, "Helicity Modulus, Superfluidity, and Scaling in Isotropic Systems", *Physical Review A* **8**, 1111 (1973).

[178] E. S. Sørensen, M. Wallin, S. M. Girvin, and A. P. Young, "Universal conductivity of dirty bosons at the superconductor-insulator transition", *Physical Review Letters* **69**, 828 (1992).

[179] S. Zhang, N. Kawashima, J. Carlson, and J. E. Gubernatis, "Quantum Simulations of the Superfluid-Insulator Transition for Two-Dimensional, Disordered, Hard-Core Bosons", *Physical Review Letters* **74**, 1500 (1995).

[180] Z. Yao, K. P. C. da Costa, M. Kiselev, and N. Prokof'ev, "Critical Exponents of the Superfluid–Bose-Glass Transition in Three Dimensions", *Physical Review Letters* **112**, 225301 (2014).

[181] L. Zhang and M. Ma, "Real-space renormalization-group study of hard-core dirty bosons", *Physical Review B* **45**, 4855 (1992).

[182] A. Priyadarshee, S. Chandrasekharan, J.-W. Lee, and H. U. Baranger, "Quantum Phase Transitions of Hard-Core Bosons in Background Potentials", *Physical Review Letters* **97**, 115703 (2006).

[183] H. Rieger, "Critical and off-critical singularities in disordered quantum magnets", *Annalen der Physik* **7**, 564 (1998).

[184] K. Sheshadri, H. R. Krishnamurthy, R. Pandit, and T. V. Ramakrishnan, "Superfluid and insulating phases in an interacting-boson model: mean-field theory and the RPA", *Europhysics Letters* **22**, 257 (1993).

[185] G. Falco, T. Nattermann, and V. Pokrovsky, "Weakly interacting Bose gas in a random environment", *Physical Review B* **80**, 104515 (2009).

[186] L. Dell'Anna and M. Fabrizio, "How localized bosons manage to become superfluid", *Journal of Statistical Mechanics: Theory and Experiment* **2011**, P08004 (2011).

[187] A. E. Niederle and H. Rieger, "Superfluid clusters, percolation and phase transitions in the disordered, two-dimensional Bose-Hubbard model", *New Journal of Physics* **15**, 075029 (2013).

[188] A. Barman, S. Dutta, A. Khan, and S. Basu, "Understanding the Bose glass phase via a percolation scenario", *The European Physical Journal B* **86**, 1 (2013).

[189] M. Gouker and F. Family, "Evidence for classical critical behavior in long-range site percolation", *Physical Review B* **28**, 1449 (1983).

[190] M. B. Isichenko, "Percolation, statistical topography, and transport in random media", *Reviews of Modern Physics* **64**, 961 (1992).

[191] P. Buonsante, F. Massel, V. Penna, and A. Vezzani, "Gutzwiller approach to the Bose-Hubbard model with random local impurities", *Physical Review A* **79**, 013623 (2009).

[192] H. Kuroyanagi, M. Tsukamoto, and M. Tsubota, "Study of Kosterlitz - Thouless Transition of Bose Systems Governed by a Random Potential Using Quantum Monte Carlo Simulations", *Journal of the Physical Society of Japan* **80**, 034603 (2011).

[193] J. Saliba, P. Lugan, and V. Savona, "Superfluid-insulator transition of two-dimensional disordered Bose gases", *Physical Review A* **90**, 031603 (2014).

[194] L. B. Ioffe and M. Mézard, "Disorder-Driven Quantum Phase Transitions in Superconductors and Magnets", *Physical Review Letters* **105**, 037001 (2010).

[195] M. V. Feigel'man, L. B. Ioffe, and M. Mézard, "Superconductor-insulator transition and energy localization", *Physical Review B* **82**, 184534 (2010).

[196] R. J. Hamers and D. F. Padowitz, "Scanning Probe Microscopy and Spectroscopy: Theory, Techniques, and Applications"„ in *Methods of Tunneling Spectroscopy with the STM*, edited by D. A. Bonnell New York: Wiley-VCH, Inc. , 2nd ed. 2001.

[197] H. J. Zandvliet and A. van Houselt, "Scanning Tunneling Spectroscopy", *Annual Review of Analytical Chemistry* **2**, 37 (2009).

[198] B. Sacépé, C. Chapelier, T. I. Baturina, V. M. Vinokur, M. R. Baklanov, and M. Sanquer, "Pseudogap in a thin film of a conventional superconductor", *Nature Communications* **1**, 140 (2010).

[199] M. Mondal, A. Kamlapure, M. Chand, G. Saraswat, S. Kumar, J. Jesudasan, L. Benfatto, V. Tripathi, and P. Raychaudhuri, "Phase fluctuations in a strongly disordered s-wave NbN superconductor close to the metal-insulator transition", *Physical review letters* **106**, 047001 (2011).

[200] M. Chand, G. Saraswat, A. Kamlapure, M. Mondal, S. Kumar, J. Jesudasan, V. Bagwe, L. Benfatto, V. Tripathi, and P. Raychaudhuri, "Phase diagram of the strongly disordered s-wave superconductor NbN close to the metal-insulator transition", *Physical Review B* **85** (2012).

[201] K. Bouadim, Y. L. Loh, M. Randeria, and N. Trivedi, "Single- and two-particle energy gaps across the disorder-driven superconductor-insulator transition", *Nature Physics* **7**, 884 (2011).

[202] P. G. de Gennes, *Superconductivity in Metals and Alloys* (Benjamin, New York, 1966).

[203] A. Ghosal, M. Randeria, and N. Trivedi, "Inhomogeneous pairing in highly disordered s-wave superconductors", *Physical Review B* **65**, 014501 (2001).

[204] G. Seibold, L. Benfatto, C. Castellani, and J. Lorenzana, "Superfluid Density and Phase Relaxation in Superconductors with Strong Disorder", *Physical Review Letters* **108**, 207004 (2012).

[205] C. Monthus and T. Garel, "Random transverse field Ising model in dimensions $d = 2$, 3: infinite disorder scaling via a non-linear transfer approach", *Journal of Statistical Mechanics: Theory and Experiment* **2012**, P01008 (2012).

[206] M. Prähofer and H. Spohn, "Universal distributions for growth processes in 1+ 1 dimensions and random matrices", *Physical review letters* **84**, 4882 (2000).

[207] C. Monthus and T. Garel, "Random transverse field Ising model in dimension $d > 1$: scaling analysis in the disordered phase from the directed polymer model", *Journal of Physics A: Mathematical and Theoretical* **45**, 095002 (2012).

[208] D. A. Huse, "Ground-state staggered magnetization of two-dimensional quantum Heisenberg antiferromagnets", *Physical Review B* **37**, 2380 (1988).

[209] J. D. Reger and A. P. Young, "Monte Carlo simulations of the spin-(1/2 Heisenberg antiferromagnet on a square lattice", *Physical Review B* **37**, 5978 (1988).

[210] S. Chakravarty, B. I. Halperin, and D. R. Nelson, "Two-dimensional quantum Heisenberg antiferromagnet at low temperatures", *Physical Review B* **39**, 2344 (1989).

[211] R. R. P. Singh, "Thermodynamic parameters of the T=0, spin-1/2 square-lattice Heisenberg antiferromagnet", *Physical Review B* **39**, 9760(R) (1989).

[212] E. Manousakis, "The spin-$1/2$ Heisenberg antiferromagnet on a square lattice and its application to the cuprous oxides", *Reviews of Modern Physics* **63**, 1 (1991).

[213] B. B. Beard and U.-J. Wiese, "Simulations of discrete quantum systems in continuous Euclidean time", *Physical Review Letters* **77**, 5130 (1996).

[214] H. Schulz, T. A. Ziman, and D. Poilblanc, "Magnetic Order and Disorder in the Frustrated Quantum Heisenberg Antiferromagnet in Two Dimensions", *J. Phys. I France* **6**, 675 (1996).

[215] A. W. Sandvik, "Finite-size scaling of the ground-state parameters of the two-dimensional Heisenberg model", *Physical Review B* **56**, 11678 (1997).

[216] A. W. Sandvik, "Classical percolation transition in the diluted two-dimensional $S = \frac{1}{2}$ Heisenberg antiferromagnet", *Physical Review B* **66**, 024418 (2002).

[217] N. Laflorencie, S. Wessel, A. Läuchli, and H. Rieger, "Random-exchange quantum Heisenberg antiferromagnets on a square lattice", *Physical Review B* **73**, 060403 (2006).

[218] K. Kato, S. Todo, K. Harada, N. Kawashima, S. Miyashita, and H. Takayama, "Quantum Phase Transition of the Randomly Diluted Heisenberg Antiferromagnet on a Square Lattice", *Physical Review Letters* **84**, 4204 (2000).

[219] A. Sandvik, "Comment on "Quantum Phase Transition of the Randomly Diluted Heisenberg Antiferromagnet on a Square Lattice"", *Physical Review Letters* **86**, 3209 (2001).

[220] W. H. Press, S. A. Teukolsky, W. T. Vetterling, and B. P. Flannery, *Numerical Recipes in FORTRAN: The Art of Scientific Computing*volume 6 (Cambridge University Press, 1992).

[221] A. Paramekanti, N. Trivedi, and M. Randeria, "Upper bounds on the superfluid stiffness of disordered systems", *Physical Review B* **57**, 11639 (1998).

[222] D. Stauffer and A. Aharony, *Introduction to percolation theory*, 2nd ed. (Taylor and Francis, London, 1992).

[223] M. E. J. Newman and R. M. Ziff, "Efficient Monte Carlo algorithm and high-precision results for percolation", *Physical Review Letters* **85**, 4104 (2000).

[224] A. B. Harris and T. C. Lubensky, "Randomly diluted xy and resistor networks near the percolation threshold", *Physical Review B* **35**, 6964 (1987).

[225] C. J. Lobb and D. J. Frank, "A large-cell renormalisation group calculation of the percolation conduction critical exponent", *Journal of Physics C: Solid State Physics* **12**, L827 (1979).

[226] C. J. Lobb and D. J. Frank, "Percolative conduction and the Alexander-Orbach conjecture in two dimensions", *Physical Review B* **30**, 4090 (1984).

[227] S. Feng, P. N. Sen, B. I. Halperin, and C. J. Lobb, "Percolation on two-dimensional elastic networks with rotationally invariant bond-bending forces", *Physical Review B* **30**, 5386 (1984).

[228] P. Grassberger, "Conductivity exponent and backbone dimension in 2-d percolation", *Physica A: Statistical Mechanics and its Applications* **262**, 251 (1999).

[229] T. Matsubara and H. Matsuda, "A Lattice Model of Liquid Helium, I", *Progress of Theoretical Physics* **16**, 569 (1956).

[230] K. Bernardet, G. G. Batrouni, J.-L. Meunier, G. Schmid, M. Troyer, and A. Dorneich, "Analytical and numerical study of hardcore bosons in two dimensions", *Physical Review B* **65**, 104519 (2002).

[231] M. Mézard, G. Parisi, and M. A. Virasoro, "SK Model: The Replica Solution without Replicas", *Europhysics Letters* **1**, 77 (1986).

[232] D. Sherrington and S. Kirkpatrick, "Solvable model of a spin-glass", *Physical Review Letters* **35**, 1792 (1975).

[233] D. J. Thouless, P. W. Anderson, and R. G. Palmer, "Solution of "Solvable model of a spin glass"", *Philosophical Magazine* **35**, 593 (1977) http://dx.doi.org/10.1080/14786437708235992.

[234] G. Parisi, "A sequence of approximated solutions to the SK model for spin glasses", *Journal of Physics A: Mathematical and General* **13**, L115 (1980).

[235] G. Parisi, "The order parameter for spin glasses: A function on the interval 0-1", *Journal of Physics A: Mathematical and General* **13**, 1101 (1980).

[236] Mézard, M., Parisi, G., Sourlas, N., Toulouse, G., and Virasoro, M., "Replica symmetry breaking and the nature of the spin glass phase", *J. Phys. France* **45**, 843 (1984).

[237] A. J. Bray and M. A. Moore, "Metastable states in spin glasses", *Journal of Physics C: Solid State Physics* **13**, L469 (1980).

[238] G. Parisi, "Order parameter for spin-glasses", *Physical Review Letters* **50**, 1946 (1983).

[239] Mézard, M., Parisi, G., and Virasoro, M.A., "Random free energies in spin glasses", *J. Physique Lett.* **46**, 217 (1985).

[240] O. Dimitrova and M. Mézard, "The cavity method for quantum disordered systems: from transverse random field ferromagnets to directed polymers in random media", *Journal of Statistical Mechanics: Theory and Experiment* **2011**, P01020 (2011).

[241] C. Laumann, A. Scardicchio, and S. L. Sondhi, "Cavity method for quantum spin glasses on the Bethe lattice", *Physical Review B* **78**, 134424 (2008).

[242] A. Chernyshev, Y. Chen, and A. Castro Neto, "Diluted quantum antiferromagnets: Spin excitations and long-range order", *Physical Review B* **65**, 104407 (2002).

[243] E. R. Mucciolo, A. H. Castro Neto, and C. Chamon, "Excitations and quantum fluctuations in site-diluted two-dimensional antiferromagnets", *Physical Review B* **69**, 214424 (2004).

[244] A. Szallas and A. Jagannathan, "Spin waves and local magnetizations on the Penrose tiling", *Physical Review B* **77**, 104427 (2008).

[245] S. Wessel and I. Milat, "Quantum fluctuations and excitations in antiferromagnetic quasicrystals", *Physical Review B* **71**, 104427 (2005).

[246] T. Coletta, N. Laflorencie, and F. Mila, "Semiclassical approach to ground-state properties of hard-core bosons in two dimensions", *Physical Review B* **85**, 104421 (2012).

[247] J. P. Álvarez Zúñiga, D. J. Luitz, G. Lemarié, and N. Laflorencie, "Critical Properties of the Superfluid – Bose Glass Transition in Two Dimensions", 2014 arXiv:1412.5595.

[248] T. Holstein and H. Primakoff, "Field dependence of the intrinsic domain magnetization of a ferromagnet", *Physical Review* **58**, 1098 (1940).

[249] E. Anderson, Z. Bai, C. Bischof, S. Blackford, J. Demmel, J. Dongarra, J. Du Croz, A. Greenbaum, S. Hammarling, A. McKenney, and D. Sorensen, *LAPACK Users' Guide*, Third ed. (Society for Industrial and Applied Mathematics, Philadelphia, PA, 1999).

[250] N. Laflorencie and F. Mila, "Theory of the Field-Induced BEC in the Frustrated Spin-12 Dimer Compound $BaCuSi_2O_6$", *Physical Review Letters* **102**, 060602 (2009).

[251] N. Laflorencie and F. Mila, "Condensate-Free Superfluid Induced by the Frustrated Proximity Effect", *Physical Review Letters* **107**, 037203 (2011).

[252] S. Krämer, N. Laflorencie, R. Stern, M. Horvatić, C. Berthier, H. Nakamura, T. Kimura, and F. Mila, "Spatially resolved magnetization in the Bose-Einstein condensed state of $BaCuSi_2O_6$: Evidence for imperfect frustration", *Physical Review B* **87**, 180405(R) (2013).

[253] P. Young, "Everything you wanted to know about Data Analysis and Fitting but were afraid to ask", 2012 arXiv:1210.3781.

[254] C. Monthus and T. Garel, "Anderson localization of phonons in dimension d=1,2,3: Finite-size properties of the inverse participation ratios of eigenstates", *Physical Review B* **81** (2010).

[255] A. Amir, J. J. Krich, V. Vitelli, Y. Oreg, and Y. Imry, "Emergent Percolation Length and Localization in Random Elastic Networks", *Physical Review X* **3** (2013).

[256] T. Cea, "Superconduttori fortemente disordinati in prossimità della transizione superconduttore-isolante",, Master's thesis Università La Sapienza di Roma 2012.

[257] M. Müller, "Purely electronic transport and localization in the Bose glass", *Annalen der Physik* **18**, 849 (2009).

[258] G. Lemarié, private communication 2015.

[259] E. Abrahams, P. W. Anderson, D. C. Licciardello, and T. V. Ramakrishnan, "Scaling theory of localization: absence of quantum diffusion in two dimensions", *Physical Review Letters* **42**, 673 (1979).

[260] P. W. Anderson, "An Approximate Quantum Theory of the Antiferromagnetic Ground State", *Physical Review* **86**, 694 (1952).

[261] B. Bernu, P. Lecheminant, C. Lhuillier, and L. Pierre, "Exact spectra, spin susceptibilities, and order parameter of the quantum Heisenberg antiferromagnet on the triangular lattice", *Physical Review B* **50**, 10048 (1994).

[262] A. Dorneich and M. Troyer, "Accessing the dynamics of large many-particle systems using the stochastic series expansion", *Physical Review E* **64**, 066701 (2001).

[263] A. W. Sandvik and J. Kurkijärvi, "Quantum Monte Carlo simulation method for spin systems", *Physical Review B* **43**, 5950 (1991).

[264] A. Sandvik, "A generalization of Handscomb's quantum Monte Carlo scheme-application to the 1D Hubbard model", *Journal of Physics A: Mathematical and General* **25**, 3667 (1992).

[265] A. W. Sandvik, "Stochastic series expansion method with operator-loop update", *Physical Review B* **59**, 14157(R) (1999).

[266] O. F. Syljuåsen and A. W. Sandvik, "Quantum Monte Carlo with directed loops", *Physical Review E* **66**, 046701 (2002).

[267] F. Alet, *Étude numérique de systèmes magnétiques et supraconducteurs*, PhD thesis, Université Paul Sabatier, Toulouse (2002).

[268] N. Laflorencie, *Influence des impuretés et du désordre dans des systèmes magnétiques de basse dimensionnalité*, PhD thesis, Université Paul Sabatier, Toulouse (2004).

[269] *The Monte Carlo Method in the Physical Sciences: Celebrating the 50th Anniversary of the Metropolis Algorithm* (2003).

[270] H. Meier and M. Wallin, "Quantum Critical Dynamics Simulation of Dirty Boson Systems", *Physical Review Letters* **108**, 055701 (2012).

[271] J. P. Álvarez Zúñiga and N. Laflorencie, "Bose-glass Transition and Spin-Wave Localization for 2D Bosons in a Random Potential", *Physical Review Letters* **111**, 160403 (2013).

[272] A. Hegg, F. Krüger, and P. Phillips, "Breakdown of self-averaging in the Bose glass", *Physical Review B* **88**, 134206 (2013).

[273] D. C. Handscomb, "The Monte Carlo method in quantum statistical mechanics", *Mathematical Proceedings of the Cambridge Philosophical Society* **58**, 594 (1962).

[274] P. Henelius, A. W. Sandvik, C. Timm, and S. M. Girvin, "Monte Carlo study of a two-dimensional quantum ferromagnet", *Physical Review B* **61**, 364 (2000).

[275] A. W. Sandvik, R. R. P. Singh, and D. K. Campbell, "Quantum Monte Carlo in the interaction representation: Application to a spin-Peierls model", *Physical Review B* **56**, 14510 (1997).

[276] F. Lin, E. Sørensen, and D. Ceperley, "Superfluid-insulator transition in the disordered two-dimensional Bose-Hubbard model", *Physical Review B* **84**, 094507 (2011).

[277] R. Ng and E. Sørensen, "Critical Properties of the Superfluid – Bose Glass Transition in Two Dimensions", 2015 arXiv:1501.05981.

[278] R. Shankar and G. Murthy, "Nearest-neighbor frustrated random-bond model in *d=2*: Some exact results", *Physical Review B* **36**, 536 (1987).

[279] D. Fisher, "Critical behavior of random transverse-field Ising spin chains", *Physical Review B* **51**, 6411 (1995).

[280] A. Rodriguez, L. J. Vasquez, K. Slevin, and R. A. Römer, "Critical Parameters from a Generalized Multifractal Analysis at the Anderson Transition", *Physical Review Letters* **105**, 046403 (2010).

[281] A. Rodriguez, L. J. Vasquez, K. Slevin, and R. A. Römer, "Multifractal finite-size scaling and universality at the Anderson transition", *Physical Review B* **84**, 134209 (2011).

[282] A. Aharony and A. Harris, "Absence of Self-Averaging and Universal Fluctuations in Random Systems near Critical Points", *Physical Review Letters* **77**, 3700 (1996).

[283] S. Wiseman and E. Domany, "Finite-Size Scaling and Lack of Self-Averaging in Critical Disordered Systems", *Physical Review Letters* **81**, 22 (1998).

[284] A. P. Young and H. Rieger, "Numerical study of the random transverse-field Ising spin chain", *Physical Review B* **53**, 8486 (1996).

[285] F. Krüger, S. Hong, and P. Phillips, "Two distinct Mott-insulator to Bose-glass transitions and breakdown of self-averaging in the disordered Bose-Hubbard model", *Physical Review B* **84**, 115118 (2011).

[286] H. Javan Mard, J. A. Hoyos, E. Miranda, and V. Dobrosavljević, "Strong-disorder renormalization-group study of the one-dimensional tight-binding model", *Physical Review B* **90** (2014).

[287] D. A. Huse, C. L. Henley, and D. S. Fisher, "Huse, henley, and fisher respond", *Physical Review Letters* **55**, 2924 (1985).

List of Publications

[1] J.P. Álvarez Zúñiga and N. Laflorencie, "Bose-glass Transition and Spin-Wave Localization for 2D Bosons in a Random Potential", *Physical Review Letters* **111**, 160403 (2013).

[2] J.P. Álvarez Zúñiga, G. Lemarié, and N. Laflorencie, "Spin wave theory for 2D disordered hard-core bosons", *AIP Conf. Proc. 1610*, pp. 102–107 (2014).

[3] J.P. Álvarez Zúñiga, D. J. Luitz, G. Lemarié, and N. Laflorencie, "Critical Properties of the Superfluid – Bose Glass Transition in Two Dimensions", *Physical Review Letters* **114**, 155301 (2015).

Resumé

1 Introduction

La physique des systèmes de matière condensée a attiré un grand intérêt tout au long de son histoire. Ces systèmes, où les propriétés de basse énergie sont étudiées, présentent une quantité importante de phénomènes spectaculaires qui défient l'intuition physique et constituent donc un excellent terrain pour les recherches fondamentales, à la fois expérimentalement et théoriquement, comme la superfluidité, supraconductivité ou la condensation de Bose-Einstein [1, 2]. Les régimes à basse énergie sont devenus accessibles au début du 20ème siècle, les progrès technologiques ayant permis l'exploration des températures de plus en plus basses. Dans ce régime, les effets quantiques deviennent importants et donnent lieu à une nouvelle physique jamais vue dans les expériences, qui devait être expliquée par la théorie. Il a vite été compris que les effets à plusieurs corps étaient responsables de certaines de ces étonnantes caractéristiques, c'est-à-dire que les interactions jouent un rôle énorme et ne peuvent être négligées. Ceci est également le cas pour certains systèmes classiques.

En même temps, le désordre, c'est-à-dire les impuretés, est intrinsèque à tout système réaliste. Bien que les premières théories développées négligeaient complètement les effets du désordre, ceux-ci sont inévitables dans les expériences et donnent lieu à de nouveaux phénomènes tels que la localisation d'Anderson [3–5] parmi d'autres. Il est connu que les électrons qui n'interagissent pas sont localisés par un désordre arbitrairement faible à une et deux dimensions, mais des interactions répulsives peuvent stabiliser un état délocaliséen deux dimensions [5, 6]. Les effets conjoints des interactions et du désordre ont reçu beaucoup d'attention dans les années suivantes.

La question de bosons désordonnés interagissants a été portée au premier plan par des expériences sur l'hélium superfluide dans les milieux poreux [7]. La perte de la superfluidité dans ces systèmes a soulevé de nouvelles questions théoriques. Une série d'études théoriques suivi [6, 8–12], découvrant que l'apparition quantique ($T = 0$) de la superfluidité dans les milieux aléatoires doit être traitée comme une transition de phase quantique régie par les fluctuations entre un superfluide délocalisé et une phase de verre Bose localisée. Le modèle de Bose-Hubbard est ainsi devenu le modèle paradigmatique pour étudier les effets conjoints des interactions et

du désordre. D'énormes efforts théoriques et expérimentaux ont été effectués pour déterminer le diagramme de phases de ce modèle à une, deux et trois dimensions. À deux dimensions, a été montré que les bosons avec interactions répulsives présentent une superfluidité robuste au désordre faible [6].

La transition de phases quantique entre le superfluide et le verre de Bose à deux dimensions est étudiée dans ce manuscrit à l'aide de trois approches différentes. En premier lieu, on montre comment les fractions superfluide et du condensat de Bose-Einstein sont affectées par le désordre dans une approximation de Champ Moyen qui, bien qu'incapable de capturer la transition, donne accès à des caractéristiques qualitatives intéressantes. En se basant sur cette solution Champ Moyen, on introduit les fluctuations quantiques à travers une théorie d'ondes de spin linéaires dans l'espace réel qui capture la transition et dévoile un comportement non trivial du spectre d'excitations. Finalement, on explore minutieusement la région critique quantique par des simulations de Monte Carlo Quantique à l'état de l'art, menant à une évaluation précise des exposants critiques et à une surprenante absence d'auto-moyennation dans le régime du verre de Bose.

2 Théorie de Champ Moyen pour la transition SF-VB

On étudie la transition Superfluide – Verre de Bose des bosons de coeur-dur sur réseau carré à deux dimensions de taille $N = L \times L$. Le système est décrit par le Hamiltonien:

$$H = -t \sum_{\langle i,j \rangle} \left(b_i^\dagger b_j + b_j^\dagger b_i \right) - \sum_i \mu_i n_i, \tag{1}$$

où $\sum_{\langle i,j \rangle}$ représente la somme sur toutes les paires de plus proches voisins, t est l'amplitude de saut entre sites voisins, μ_i est potentiel chimique sur le site i, $b_i^\dagger$ and b_i sont, respectivement, les opérateurs bosoniques de création et annihilation sur le $i^{\text{ème}}$ site et $n_i = b_i^\dagger b_i$ est l'opérateur de nombre, qui suit la contrainte de coeur-dur $n_i = 0$ ou 1. Ce Hamiltonien est équivalent, par la transformation de Matsubara-Matsuda [229] (*cf.* éq. (II.21)), au Hamiltonien XY:

$$H_{XY} = -\frac{1}{2} \sum_i \mu_i - 2t \sum_{\langle i,j \rangle} (S_i^x S_j^x + S_j^y S_i^y) - \sum_i \mu_i S_i^z. \tag{2}$$

Le paramètre d'ordre pour la transition est l'aimantation dans le plan XY m_{XY} qui est liée à la densité du condensat de Bose-Einstein dans le langage bosonique par $\rho_0 = m_{XY}^2$, et est calculé par l'expression (II.29). On peut résoudre le problème par deux méthodes de Champ Moyen équivalentes: d'une part, considérer les opérateurs de spin comme des vecteurs 3D (*cf.* éq (II.5)) et minimiser numériquement le Hamiltonien (II.23) qui en résulte (ce qui permet la relaxation de la phase), et d'autre part introduire le découplage Champ Moyen (II.13) et résoudre les équations

d'auto-cohérence (II.30) qui en résultent de façon itérative pour calculer l'énergie. On peut utiliser les deux méthodes dans le cas de conditions au bords périodiques et dans le cas de conditions au bords en présence d'un twist, pour calculer la densité superfluide (II.4).

2.1 Modèle XY avec désordre bimodal

Dans le cas d'un désordre bimodal le potentiel chimique sur un site i vaut $\mu_i = \pm W$, avec W la force du désordre. Dans ce cas le problème avec conditions périodiques a une solution analytique donnée par les équations (II.25) et (II.29). Pour calculer la densité superfluide on applique un "twist" aux conditions aux bords et on calcule la différence en énergie que cela entraine. Elle est minimale à dans l'état fondamental ce qui donne finalement les équations couplées décrivant la relaxation de la phase:

$$\forall i,\ \ t \sum_{\langle j \rangle_i} \sin\theta_i \sin\theta_j (\varphi_i - \varphi_j) = 0. \tag{3}$$

Ce système est résolu à l'aide de subroutines de la Réf. [220]. On reporte les résultats pour les densités superfluide et condensée sur la figure 1 où l'on voit que les deux densités sont identiques et ne s'annulent que quand le désordre est en dehors de la bande de conduction $W/t \geq 4$ et le système est dans une phase isolante et gappée. Il n'y a pas de phase de verre de Bose à ce niveau d'approximation.

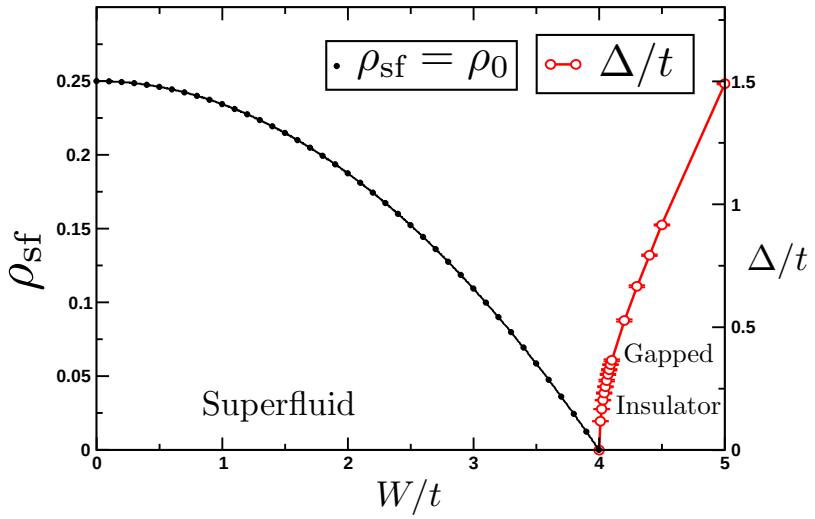

Figure 1: *Evolution des densités superfluide et condensés vs. la force du désordre W/t pour une distribution bimodale du désordre. Une seule taille du système est représentée puisqu'il n'y a pas d'effets de taille finie. Les deux densités sont égales et diminuent avec le désordre de leur valeur dans le cas pur* 0.25 *s'annulant pour une force du désordre égale à la largeur de bande $W/t = 4$. Pour des désordres plus forts le système est dans une phase isolante et gappée.*

2.2 Modèle XY avec désordre boite

Dans le cas d'un désordre uniforme $\mu_i \in [-W;W]$ il n'y a pas de solution analytique et la minimisation doit se faire par la méthode du découplage Champ Moyen (II.13) suivit d'une résolution itérative des équations d'auto-cohérence (qui incluent implicitement la relaxation de la phase) avec conditions aux bords périodiques (*cf.* éq. (II.30)) ainsi que "twistées" (*cf.* éq. (II.33)).

2.2.1 Absence de transition de phases SF – VB

Dans le formalisme Champ Moyen itératif, la densité condensée est donnée en fonction des champs locaux B_i obtenus de façon auto-cohérente, par l'expression (II.36). On reporte les résultats pour les densités superfluide et condensée en fonction du désordre pour des systèmes de taille $L = 8, \ldots, 36$ sur la figure 2. Bien que différentes ($\rho_{\rm sf} < \rho_0$), les deux densités sont compatibles à fort désordre avec une diminution soit exponentielle, soit en loi de puissance, ce qui indique qu'elles ne s'annulent qu'à la limite du désordre infini $W \to \infty$, c'est-à-dire qu'il n'y a pas de phase verre de Bose présente, au niveau Champ Moyen.

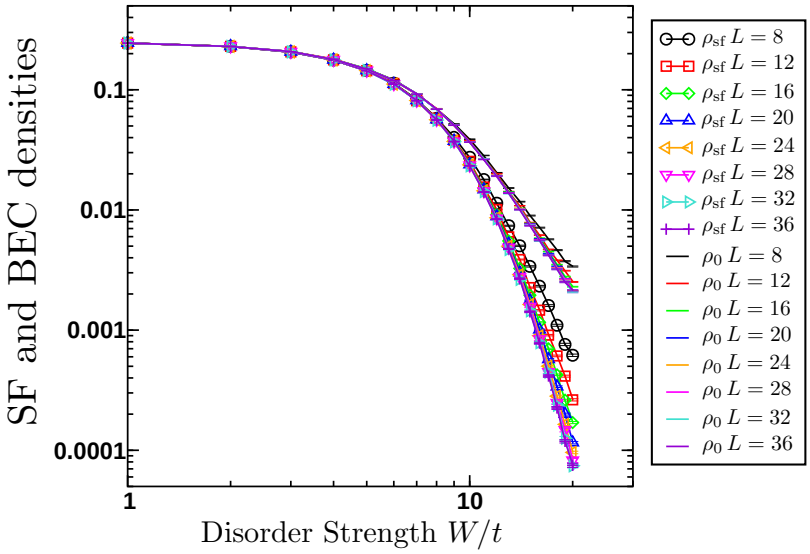

Figure 2: *Evolution des densités superfluide (ρ_{sf}) et Bose condensée (ρ_0) vs. la force du désordre en unités du paramètre de saut W/t pour la distribution de désordre uniforme $\mu_i \in [-W;W]$. Même au niveau Champ Moyen les deux densités sont différentes: $\rho_{sf} < \rho_0$. Les deux densités montrent une dépendance linéaire avec le désordre en échelle Log-Log ou log-normale (non représenté): les données sont compatibles à la fois avec une diminution en loi exponentielle et en loi de puissance. De ce fait, les deux quantités ne s'annulent qu'à la limite du désordre infini $W \to \infty$ indiquant une absence de transition vers une phase de verre Bose à ce niveau d'approximation.*

2.2.2 Distributions des courants

Les propriétés de transport du système sont étudiées à travers les courants locaux induits par le "twist" aux conditions de bord Φ. Celui-ci est appliqué selon la direction X seulement. L'on peut donc définir les courants transverses (selon Y) et longitudinaux (selon X) par

$$J^y_{i\to i+\hat{y}} = 2(S^x_i S^y_{i+\hat{y}} - S^y_i S^x_{i+\hat{y}}) \tag{4}$$

et

$$J^x_{i\to i+\hat{x}} = 2\sin(\frac{\Phi}{L})(S^x_i S^x_{i+\hat{x}} + S^y_i S^y_{i+\hat{x}}) + 2\cos(\frac{\Phi}{L})(S^x_i S^y_{i+\hat{x}} - S^y_i S^x_{i+\hat{x}}). \tag{5}$$

Le panneau du haut de la figure 3 illustre l'évolution avec le désordre de la valeur moyenne de ces courants divisée par le courant moyen dans le cas pur pour un système de taille $L = 32$, et le panneau du bas montre l'écart-type de ces courants divisé par leur valeur moyenne en fonction du désordre. Il est clair que le transport passe d'être

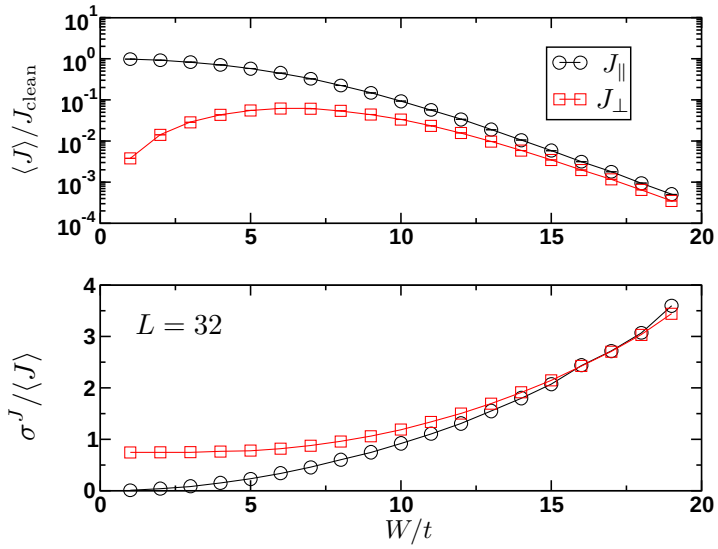

Figure 3: *Haut: Courants longitudinal ($J_\parallel$) et transverse ($J_\perp$) pour un système de taille $L = 32$ vs. la force du désordre W/t pour la distribution du désordre uniforme $\mu_i \in [-W; W]$, renormalisés par la valeur du courant dans le pur $\bar{J}_{clean} = \frac{1}{2}\bar{\rho}_{sf}\frac{\Phi}{L}$. À faible désordre, le transport longitudinal est plusieurs ordres de grandeur plus grand quel le transport transverse. À fort désordre ($W \geq 10t$) les courrants longitudinal et transverse sont du même ordre de grandeur. Les barres d'erreur sont plus petites que les symboles. Bas: Écart-type des courrants longitudinal et transverse divisé par leur valeur moyenne, en fonction du désordre. The transverse currents have a wider relative spread at low disorders but it becomes equivalent to the longitudinal current spread at strong disorders $W > 10t$.*

unidirectionnel à faible désordre à être isotrope à fort désordre, un effet précurseur de la transition vers le verre de Bose, et ce malgré l'absence de transition à ce niveau d'approximation.

3 Au-delà du Champ Moyen: Approche semi-classique

On développe un approche semi-classique à travers la théorie des ondes de spin linéaires. Cette théorie se base sur le résultat Champ Moyen et y ajoute les fluctuations quantiques décrites par des bosons selon la transformation de Holstein-Primakoff (III.3) [248] linéarisée. Pour un spin S ceci permet d'obtenir les quantités corrigés à l'ordre $1/S$ après la diagonalisation dans l'espace réel du Hamiltonien en termes des bosons de Holstein-Primakoff (III.6) qui en résulte pour notre problème désordonné.

3.1 Propriétés critiques de l'état fondamental

3.1.1 Désordre bimodal

On a calculé la densité superfluide ρ_{sf} et la fraction du condensat de Bose-Einstein ρ_0 corrigées à l'ordre $1/S$, ainsi que le gap dans le spectre des excitations pour des systèmes de taille $L = 12, \ldots, 32$ et une distribution du désordre bimodale $\mu_i = \pm W$. Les extrapolations à la limite thermodynamique $L \to \infty$ de ces quantités sont tracées sur la figure 4. Dans le cas pur, la densité superfluide est augmentée par les fluctuations quantiques pendant que la densité du BEC est réduite. En augmentant la force du désordre les deux quantités diminuent jusqu'à s'annuler à deux points différents $W_0 < W_{\text{sf}} < 4t$. L'extrapolation à la limite thermodynamique du gap dans le spectre d'excitations Δ est nulle jusqu'au bord de bande et devient finie pour $W \geq 4t$.

Il existe donc une fenêtre finie du désordre, $W_0 < W < W_{\text{sf}}$, dans laquelle le système est dans une phase superfluide sans fraction condensée. Bien que ceci est possible dans des systèmes frustrées tels que $BaCuSi_2O_6$ [250–252], il est possible que cette fenêtre ne survive pas aux fluctuations quantiques d'ordre supérieur, ce qui est serait résolu à l'aide de simulations QMC dans le futur. Dans tous les cas, il reste une fenêtre finie de désordre $W_{\text{sf}} < W < 4t$ pour laquelle une phase isolante ($\rho_{\text{sf}} = 0$) et gapless ($\Delta = 0$) est stable, c'est-à-dire, une phase de verre de Bose est stabilisée par les fluctuations quantiques à l'ordre $1/S$.

Pour déterminer la valeur pour laquelle la densité superfluide s'annule, on utilise la théorie de taille finie décrite dans la section 2.3.2 du chapitre I du manuscrit. Selon celle-ci, les courbes en fonction du désordre de $\rho_{\text{sf}} \times L^z$, où z est l'exposant

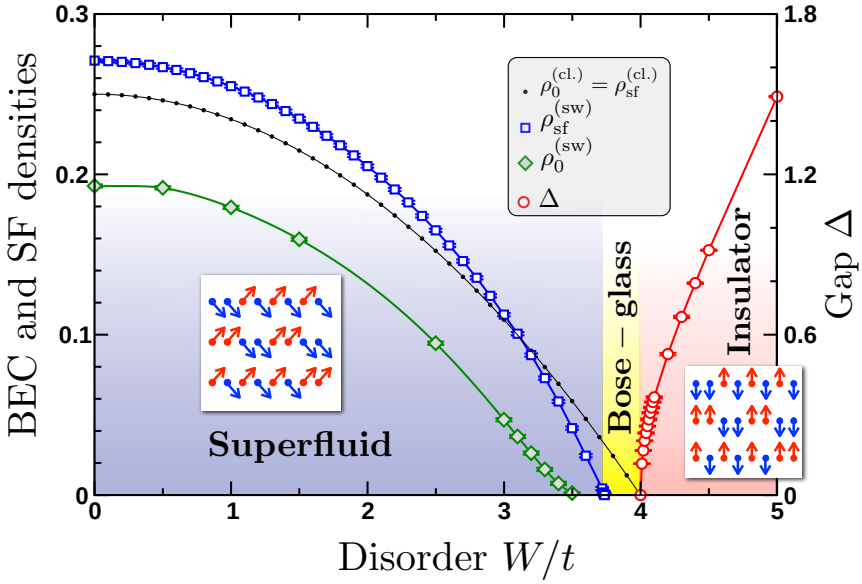

Figure 4: *Evolution des extrapolations à la limite thermodynamique de la densité superfluide ρ_{sf}, la densité du condensat de Bose-Einstein ρ_0 et le gap dans le spectre des excitations Δ aver la force du désordre W/t. Les densities classiques ($\bullet$) sont égales et s'annulent au bord de la bande $W = 4t$. Les quantités corrigées par les ondes de spin $\rho_{sf}^{(sw)}$ ($\square$) et $\rho_0^{(sw)}$ ($\diamond$) s'annulent à des points différents $W_0 < W_{sf} < 4t$, laissant place à une phase gapless verre de Bose (BG) sur une fenêtre finie du désordre, avant l'apparition de l'isolant gappé pour $W > 4t$. Les vignettes montrent les phases superfluide et isolantes dans la représentation des pseudo-spins. Les moyennes sur le désordre ont été faites sur plusieurs centaines d'échantillons désordonnés. La ligne verte est un guide visuel.*

dynamique décrivant la transition, pour différentes tailles du système L doivent se croiser au point critique. Ceci est visible sur le panneau (a) de la figure 5 où un très bon croisement est obtenu pour des tailles de système $L = 12, \ldots, 32$ avec une valeur de l'exposant dynamique $z = 2.0(1)$ en bon accord avec la prédiction théorique de Fisher *et al.* [6] $z = d = 2$. Le point critique correspondant est estimé à $W_{sf}/t = 3.738(1)$.

Le cas de la densité du condensant de Bose-Einstein est un peu différent. En effet la présence d'une cohérence macroscopique dans le langage bosonique (*i.e.* d'un condensat) est liée à la présence d'un ordre transverse dans le plan XY dans le langage des spins par $\rho_0 = m_{xy}^2$, avec $m_{xy} = \overline{\langle S^x \rangle}$ l'aimantation transverse. L'analyse de taille finie de m_{xy} est présentée dans le panneau (b) de la figure 5 où l'on voit que l'extrapolation à taille infinie du paramètre d'ordre XY devient négative, ce qui est interprété comme un ordre XY nul. Ceci arrive pour une valeur de la force du désordre $W_0/t = 3.55(5)$.

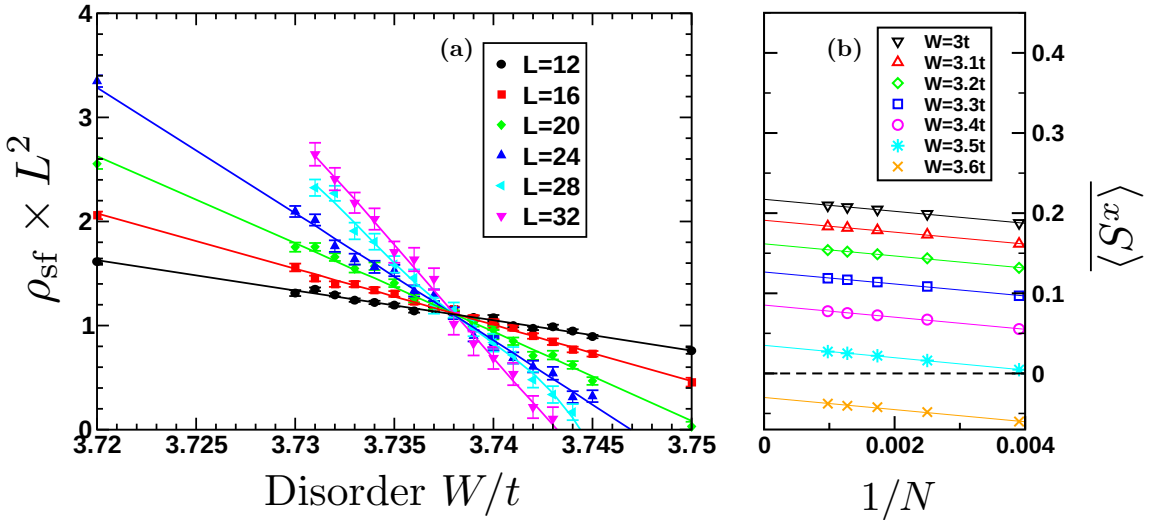

Figure 5: *Panneau a: Croisement des courbes de $\rho_{sf} \times L^z$ pour des systèmes de tailles allant de $L = 12$ à $L = 32$. Un très bon croisement best obtenu aver un exponent dynamique $z = 2.0(1)$ et le point de croisement est estimé à $W_{sf}/t = 3.738(1)$. Les traits pleins montrent des fits de degré 2. Panneau b: Analyse de taille finie de l'aimantation transverse corrigée par ondes de spin $m_{xy} = \overline{\langle S^x \rangle}$ à différentes forces du désordre. Les extrapolations à taille infinie négatives sont interprétées comme étant nulles. Le paramètre d'ordre XY s'annule à une force du désordre $W_0/t = 3.55(5)$.*

3.1.2 Désordre uniforme

On calcule de façon similaire la densité superfluide corrigée à l'ordre $1/S$ pour le cas d'une distribution du désordre uniforme sur le potentiel chimique $\mu_i \in [-W; W]$. Dans le cas pur les résultats sont en accord avec les résultats analytiques de Coletta *et al.* [246]: les fluctuations quantiques augmentent la superfluidité par rapport au résultat classique (Champ Moyen). Le désordre fait diminuer la densité superfluide $\rho_{\rm sf}$ corrigée par les ondes de spin de façon monotone jusqu'à ce qu'elle s'annule pour une force du désordre avoisinant $W = 10t$.

Pour évaluer avec précision le point critique et l'exposant dynamique z qui gouverne la transition de phases vers le verre de Bose on utilise le fait que la densité superfluide doit suivre la forme $\rho_{\rm sf} \sim L^{-z}$. On trace donc sur le panneau (a) de la figure 6 en échelle log-log la densité superfluide corrigée à l'ordre $1/S$ en fonction de l'inverse de la taille du système $1/L$ pour différentes valeurs du désordre autour de $W = 10t$. On trouve un point critique $W_c/t = 10.00(5)$ et un exposant dynamique $z = 1.43(1)$ en désaccord avec l'égalité $z = d = 2$ de Fisher *et al.* [6]. Le panneau (b) de la figure 6 montre le croisement des courbes de $\rho_{\rm sf} \times L^z$ pour différentes taille du système $L = 24, \ldots, 48$ obtenu en utilisant la valeur de $z = 1.43(1)$ trouvée par l'analyse précédente. En effet, un très bon croisement apparait pour une valeur du désordre critique $W_c/t = 10.00(5)$, ce qui confirme l'estimation pour z.

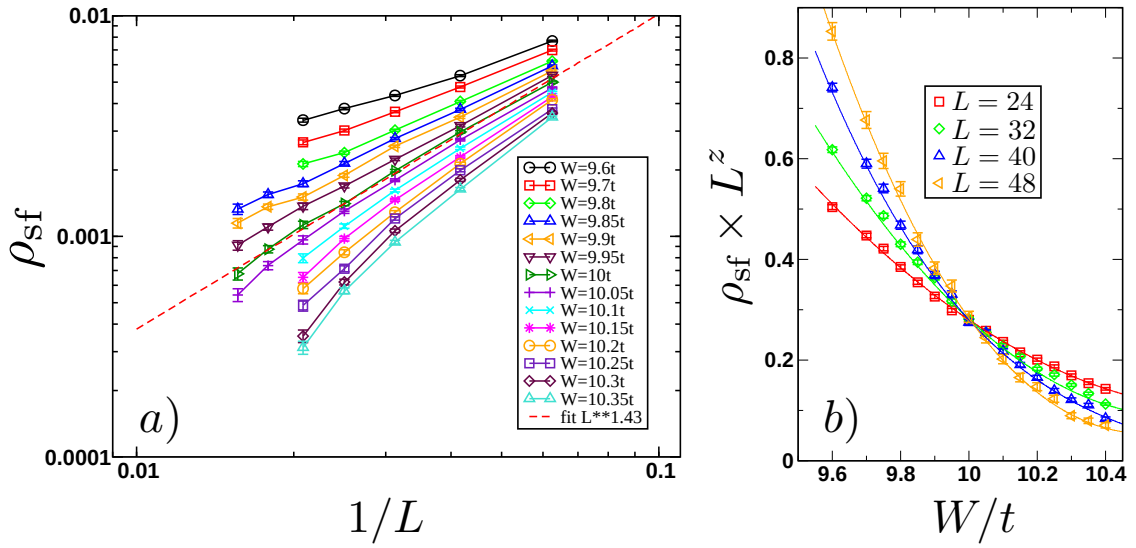

Figure 6: *Panneau a: Densité superfluide corrigée par les ones de spin ρ_{sf} vs. l'inverse de la taille du sytème pour différentes valeur du désordre. La ligne pointillée rouge est un fit en loi de puissance de la forme $\rho_{sf} \sim L^{-z}$ avec $z = 1.43$, qui decrypt les données à $W = 10t$. Les données pour les autres valeurs du désordre suivent un loi similaire pour les petites tailles mais l'inclusion des tailles les plus grandes les fait dévier de ce comportement, sauf pour $W/t = 9.95$ et $W/t = 10.05$. Panneau b: Croisement des courbes de $\rho_{sf} \times L^z$ pour des systèmes de taille allant de $L = 24$ à $L = 48$. U/n très bon croisement est obtenu avec la valeur de l'exposant critique de $z = 1.43(1)$ et le point de croisement est à $W_c/t = 10.00(5)$. Les traits pleins montrent des fits polynomiaux au troisième ordre.*

3.2 Propriétés du spectre des excitations

On étudie le spectre des excitations à une particule produites par les ondes de spin dans le cas d'un désordre bimodal. On a vu sur la figure 4 qu'il y a trois phases dans le diagramme de phases dans ce cas: un phase superfluide à faible désordre, une phase verre de Bose pour $W_{\rm sf} < W < 4t$, et un isolant gappé pour $W > 4t$. Les deux premières sont gapless et l'on étudie les propriétés de localization de ces transitions à travers les Inverse Participation Ratios (IPR) des états propres du Hamiltonien, en suivant les travaux de Monthus et Garel [254] et de l'équipe de Castellani à Rome [256]. Les IPRs à une fréquence donnée Ω sont définis, pour un état propre normalisé et indexé par p, par:

$$\mathrm{IPR}_p = \sum_{i=1}^{N} |a_i^p|^4. \tag{6}$$

Les IPRs se comportent comme pour la transition de Anderson [4, 254]:

$$\begin{cases} \text{IPR} \sim \dfrac{1}{N}, & \text{si l'état est délocalisé} \\ \text{IPR} \sim \dfrac{1}{L^{D_2}}, & \text{à la transition de localisation-délocalisation} \\ \text{IPR} \sim \dfrac{1}{\xi^2}, & \text{si l'état est localisé avec une longueur de localisation } \xi \end{cases} \tag{7}$$

ce qui définit l'exposant multifractal D_2. Comme les spectres onde de spin sont discrets pour des systèmes de taille finie et que pour chaque échantillon désordonné les énergies propres sont proches mais pas identiques, on étudie les IPRs moyennés sur des tranches de fréquences de largeur $\delta\Omega/v_0 = 1/20$ (avec $v_0 = 2t$ la vitesse des ondes de spin dans le cas pur). D'après l'équation (7), les courbes des IPR$\times L^{D_2}$ en fonction de la fréquence pour différentes tailles du système doivent se croiser au seuil de mobilité Ω_c, et ce pour chaque valeur du désordre. On obtient en effet un très bon croisement pour $W = 3.4t$ (dans la phase superfluide) en utilisant un exposant multifractal $D_2 = 1.48$ comme l'illustre la figure 7. Le même exposant multifractal donne des bons croisements à d'autres valeurs du désordre, surtout dans la phase superfluide.

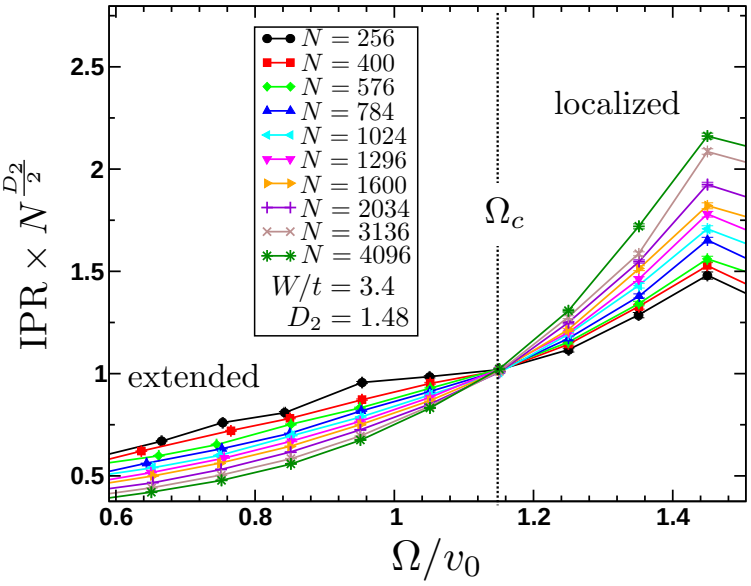

Figure 7: *Croisement des courbes des Inverse Participation Ratio pour des systèmes de taille $L = 16, \ldots, 64$ et multipliés par L^{D_2} avec un exposant multifractal $D_2 = 1.48$ pour use force du désordre de $W = 3.4t$ dans la phase superfluide. Un croisement convaincant best obtenu à use fréquence fine $\Omega_c/v_0 \approx 1.15$ séparant des états delocalisés à fable énergie ($\Omega < \Omega_c$) et des états localizés à haute énergie ($\Omega > \Omega_c$). Les barres d'erreur sont représentées mais sont plus petites que la taille des symboles.*

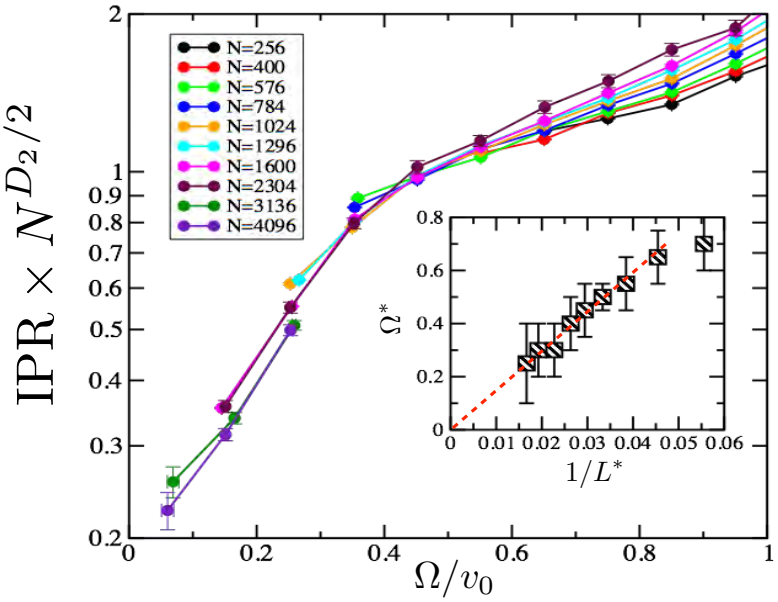

Figure 8: *Croisement des courbes des Inverse Participation Ratio pour des systèmes de taille* $L = 16, \ldots, 64$ *et multipliés par* L^{D_2} *avec un exposant multifractal* $D_2 = 1.48$ *pour use force du désordre de* $W = 3.4t$ *dans la phase verse de Bose. Une grande dérive des points de croisement est présente . La vignette montre les points de croisement successifs* Ω^* *entre une paire de tailles de système successives* L_1 *and* L_2 *en fonction de l'inverse de* $L^* = (L_1 + L_2)/2$. Ω^* *tend vers zéro lorsque* L^* *tend vers l'infini, indiquant que le seuil de mobilité* $\Omega_c = 0$.

Dans la phase verre de Bose, les points de croisement des courbes de tailles successives L_1 et L_2 dérivent vers des fréquences de plus en plus faibles, comme illustré dans la figure 8 pour une force du désordre de $W = 3.9t$. La vignette montre les valeurs des points de croisement successifs Ω^* en fonction de l'inverse de la taille $L^* = (L_1 + L_2)/2$. Le point de croisement s'annule à la limite où L^* tend vers l'infini, ce qui signale un seuil de mobilité nul.

En faisant la même étude pour toutes les valeurs du désordre, on peut dresser le diagramme de phases de la figure 9 qui montre l'évolution du seuil de mobilité en fonction du désordre. Le seuil de mobilité (losanges jaunes) est fini et a des barres d'erreur plutôt grandes dans la phase superfluide. Le seuil décroit et les barres d'erreur augmentent avec le désordre, et finalement le seuil semble s'annuler exactement à la transition entre le superfluide et le verre de Bose (indiqué par l'astérique bleu), c'est-à-dire que dans le verre de Bose toutes les excitations sont localisées.

Cependant, ces résultats sont contraires à des résultats récents de Lemarié [258] pour le même modèle à deux dimensions sur réseau carré et utilisant aussi les ondes de spin, avec des tailles de système beaucoup plus grandes qui sembleraient indiquer que le seuil de mobilité est nul même dans la phase superfluide. Cette étude nécessite donc de résultats supplémentaires pour permettre de conclure.

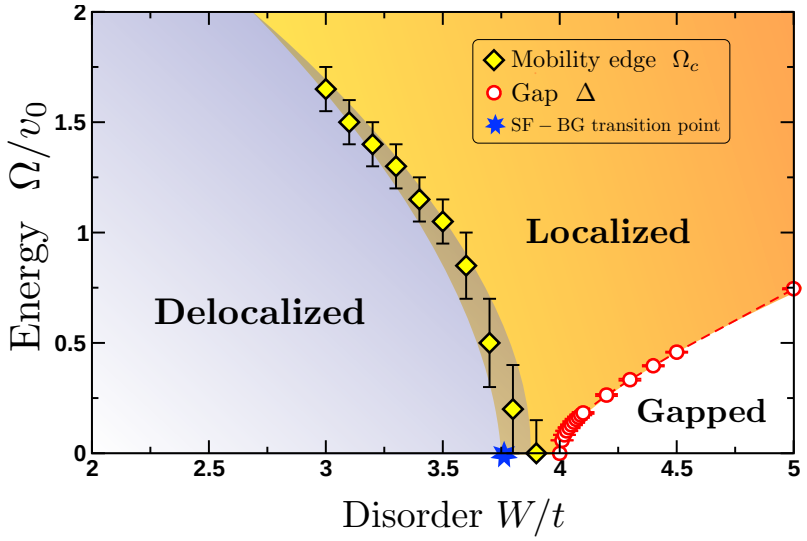

Figure 9: *Spectre des excitations ondes de spin renormalisé par $v_0 = 2t$ et tracé en fonction de la force du désordre W/t. Les états excités sont délocalisés en dessous du seuil de mobilité Ω_c (losanges jaunes) et localisés au dessus. Ω_c, qui détermine la frontière entre états localisés et delocalisés (zone grisée) aver des barres d'erreur assez grandes proche de la transition superfluide - verre de Bose (astérisque bleu), semble s'annuler au point de transition $W_{sf}/t = 3.738(1)$ et tous les états sont localisés dans la phase verre de Bose. L'isolant gappé ne présente aucun état en dessous du gap Δ (cercles rouges) tous les états sont localisés en dessus du gap.*

4 Étude avec le Monte Carlo Quantique

On fait l'étude des propriétés critiques de notre modèle de bosons de coeur-dur sur réseau carré bidimensionel avec désordre sur site suivant une distribution uniforme $\mu_i \in [-W; W]$ à travers le Monte Carlo Quantique (QMC) à l'état de l'art, plus précisément avec la technique dite *Stochastic Series Expansion* (SSE). Celle-ci travaille à température inverse β finie et l'étude de la transition de phases quantique (*i.e.* à $T = 0$) nécessite d'une température inverse assez grande pour que la simulation concerne seulement la physique de l'état fondamental. Cependant, pour optimiser le temps de simulation, on utilise la technique dite de β-doubling dans laquelle pour chaque échantillon désordonné une augmentation progressive de la température inverse est utilisée en prenant comme point de départ la configuration Monte Carlo convergée pour la température précédente. Ceci réduit le temps de d'équilibration de la simulation QMC et on augmente la température jusqu'à ce que la quantité que l'on veut mesurer n'évolue plus quand on change β, *i.e.* l'observable mesurée a atteint sa valeur dans l'état fondamental. Un exemple de cette procédure est montré pour les densités superfluide et du condensat de Bose-Einstein pour différentes tailles et différentes valeurs du désordre dans la figure 10.

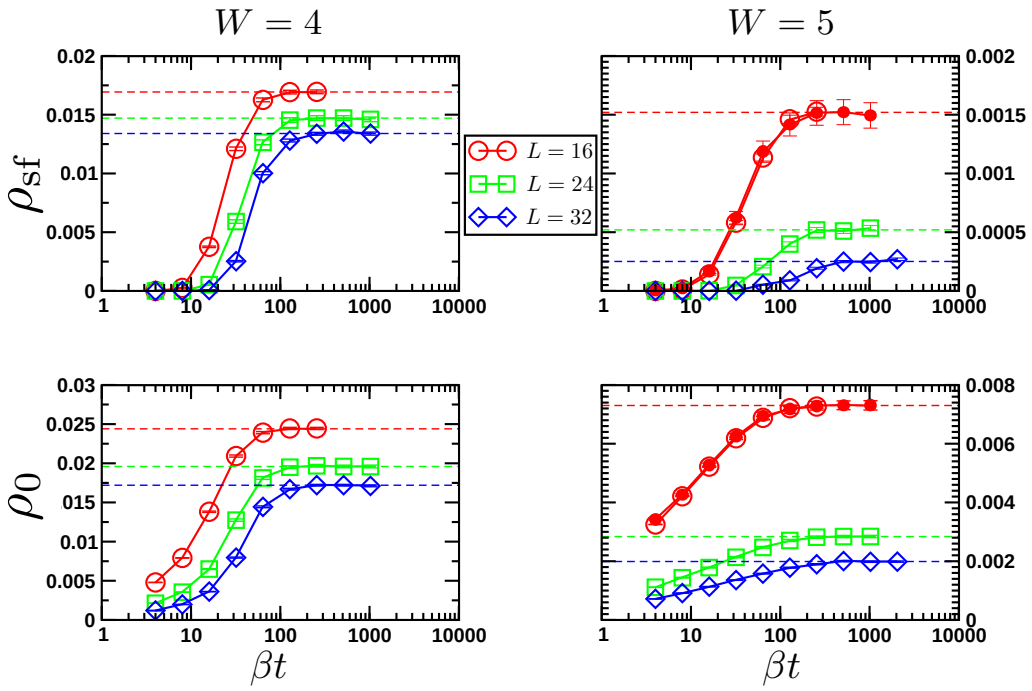

Figure 10: *Convergence des densités superfluide et du condensed de Bose-Einstein vers leurs valeur à l'état fondamental pendant la procedure de β-doubling differences tails du système et deux forces du désordre. Les cercles remplis dans les panneaux de droite ($L = 16, W = 5$) sont les données pour $N_m = 10^4$pas de mesure Monte Carlo, toutes les autres données étant obtenues avec $N_m 10^3$ pas de mesure sont en parfait accord avec celles obtenues avec plus de pas. Les lignes pointillées indiquent les valeurs convergées en β des densités superfluide et du BEC pour chaque taille et chaque valeur du désordre.*

En plus de la température, le nombre de pas Monte Carlo utilisés pour faire les mesures est très important. Il faut qu'il soit assez grand pour s'assurer de minimiser les erreurs statistiques intrinsèques à la méthode Monte Carlo. On a vérifié que 1000 pas de mesures étaient suffisants dans la plupart des échantillons, néanmoins une fraction des échantillons ont des temps d'autocorrélation plus longs et nécessitent plus de pas de mesure, à défaut de quoi on mesure une densité superfluide nulle, ce qui est impossible pour un système de taille finie. On traite ces échantillons en ajustant dynamiquement le nombre de pas, *i.e.* en ajoutant 1000 pas supplémentaires et vérifiant que les résultats sont fiables et le temps d'autocorrélation beaucoup plus petit que le temps total de simulation. On fixe une limite maximale de 10^5 pas pour des raisons de temps de calcul fini.

Un grand nombre d'échantillons est aussi nécessaire pour atteindre une moyenne sur le désordre convergée et donc fiable. On utilise $\sim$ 20000 échantillons pour les

plus petites tailles $L \leq 22$ et ~ 10000 pour les plus grandes afin de s'assurer que les moyennes sont convergées tout en gardant des temps de simulation accessibles. Les barres d'erreur sont estimées à l'aide d'une procédure de bootstrap accolée à un rééchantillonage suivant une gaussienne des données pour chaque taille et chaque force du désordre. Présentons maintenant les résultats obtenus.

4.1 Exposants critiques de a transition SF–VB

4.1.1 Quantités moyennées

Pour extraire les exposants critiques de le désordre critique pour la transition sur les données moyennées, on utilise les formes de loi d'échelle que doivent suivre la densité superfluide et la fraction condensée:

$$\rho_{\mathrm{sf}}(L) = L^{-(z)}\, \mathcal{G}_{\mathrm{sf}}[L^{1/\nu}(W - W_c)] \tag{8}$$

et

$$\rho_0(L) = L^{-(z+\eta)}\, \mathcal{G}_0[L^{1/\nu}(W - W_c)]. \tag{9}$$

avec z l'exposant dynamique, ν l'exposant critique de la longueur de corrélation, W_c le désordre critique, η l'exposant anormal et $\mathcal{G}_0$ et $\mathcal{G}_{\mathrm{sf}}$ des fonctions universelles qui sont approchées par un polynôme du troisième degré. On effectue donc des fits des données QMC sur ces formes sur différentes fenêtres du désordre et de tailles du système incluses. Nous vérifions aussi la stabilité de notre analyse si l'on corrige des possibles effets de température finie ou en incluant les échantillons qui donnent des densités superfluides nulles. Nos résultats finaux prennent en compte toutes ces

z	ν	η	W_c	Reference
2	≥ 1	≤ 0		Fisher *et al.* [6]
1.7	1.4	n.d.	n.d.	Zhang *et al.* [181]
2.0(1)	0.9(1)	n.d.	n.d.	Sörensen *et al.* [178]
0.5(1)	2.2(2)	n.d.	2.5	Makivić *et al.* [160]
2.0(4)	0.90(13)	n.d.	4.95(20)	Zhang *et al.* [179]
1.93	1.38	n.d.	n.d.	Herbut [157]
1.40(2)	1.10(4)	−0.22(6)	4.42(2)	Priyadarshee *et al.* [182]
1.80(5)	1.15(3)	−0.3(1)	n.d.	Meier *et al.* [270]
1.88(8)	0.99(3)	−0.16(8)	4.79(3)	Ng *et al.* [277]
1.85(15)	1.20(12)	−0.40(15)	4.80(5)	Álvarez Zúñiga *et al.* [247]

Table 1: *Différentes estimations des exposants critiques et du désordre critique W_c de la transition Superfluide–verre de Bose sur différents modèles à deux dimensions. Les résultats sont montrés dans l'ordre chronologique.* n.d. *= non disponible.*

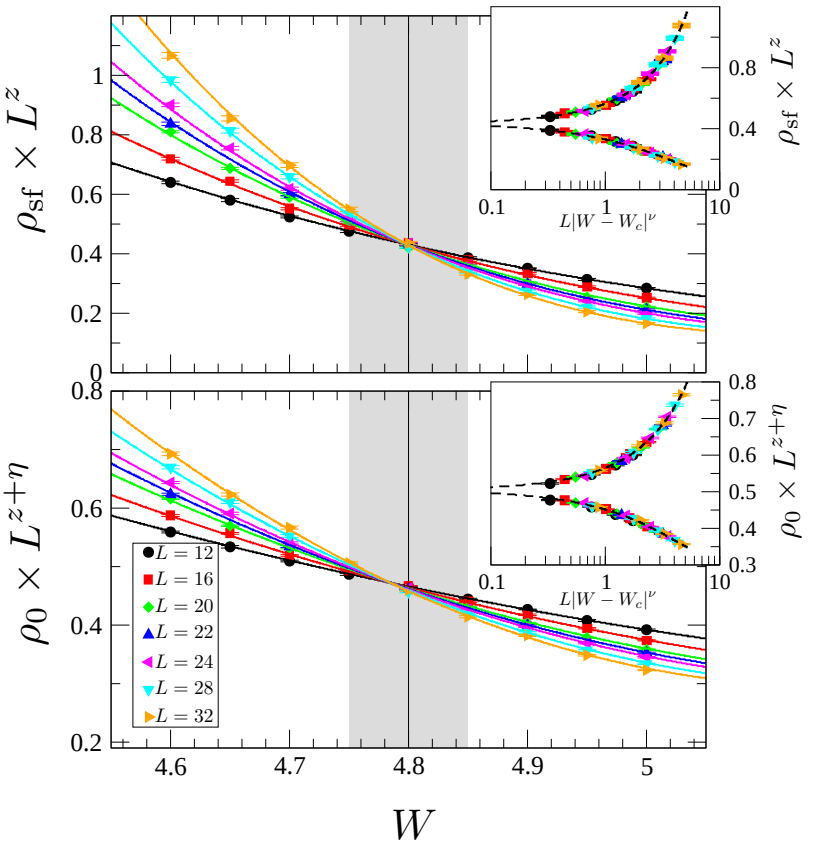

Figure 11: *Exemple de l'analyse de scaling des densités SF ρ_{sf} (haut) et du BEC ρ_0 (bas) en incluant toutes les tailles de système $L \in [12; 32]$ et toutes les forces du désordre $W \in [4.6; 5]$. Les traits pleins montrent les meilleurs fits aux formes universelles des éqs.* (8) *et* (9) *qui donnent $z \simeq 1.85$, $W_c^{\rm sf} \simeq 4.8$, $W_c^0 \simeq 4.79$, $z + \eta \simeq 1.42$, $\nu_{\rm sf} \simeq 1.1$, $\nu_0 \simeq 1.2$, et $\mathcal{G}_{sf|0}$ des polynômes du 3$^{\rm ème}$ ordre. L'estimation finale du point critique $W_c = 4.80(5)$ best montrée par les zones grisées. Vignettes: Collapse des données obtenu en renormalisant la taille du système L par $1/\xi = |W - W_c|^\nu$ avec $\nu = 1.2$ et $W_c = 4.8$. Le collapse est presque parfait.*

sources d'erreur et donnent donc des barres d'erreur finales assez grandes. Ces résultats sont consignés avec différentes estimations de la littérature dans le tableau 1. Un exemple des fits obtenus sur la fenêtre du désordre $W \in [4.6; 5]$ et en incluant toutes les tailles ($L \in [12; 32]$) est montré sur la figure 11 pour les densités superfluide et condensée. Un excellent croisement est obtenu, ainsi que qu'un collapse des données presque parfait lorsqu'on renormalise la taille du système par la longueur de corrélation $L \mapsto L/\xi$, où $\xi = |W - W_c|^{-\nu}$ avec $W_c = 4.8$ et $\nu = 1.2$, ce qui confirme nos meilleures estimations. Celles-ci respectent les bornes théoriques pour ν et η, mais notre meilleure estimation pour l'exposant dynamique $z = 1.85(15)$ est légèrement inférieure à $d = 2$ bien que l'égalité reste dans la barre d'erreur.

4.1.2 Densité superfluide typique

Les propriétés critiques de la densité superfluide typique et moyenne ne sont pas forcément les mêmes [279]. La densité typique est définie par:

$$\rho_{\rm sf}^{\rm typ} = \exp(\overline{\ln(\rho_{\rm sf})}) \tag{10}$$

avec $\overline{(.)}$ la moyenne sur les échantillons désordonnés. On se concentre sur la densité superfluide typique puisque en SSE la densité condensée est calculée comme la moyenne des densités condensées locales et la densité condensée typique ne peut donc pas être obtenue en SSE. La densité SF typique suit une loi d'échelle similaire à celle de la densité moyenne, et peut contenir aussi des corrections non pertinentes [280, 281]:

$$\rho_{\rm sf}^{\rm typ}(L) = L^{-z}\left(\mathcal{G}_{\rm sf}^{\rm typ}[L^{1/\nu}(W-W_c)] + cL^{-y}\right). \tag{11}$$

Bien que l'analyse identique à celle sur la densité moyenne n'est pas stable lorsqu'utilisée pour la densité typique, on peut vérifier que les résultats obtenus pour la moyenne sont compatibles avec la densité typique en fixant les paramètres aux valeurs de nos meilleures estimations: $z_{\rm typ} = 1.85$, $\nu_{\rm typ} = 1.2$ et $W_c^{\rm typ} = 4.8$. On obtient ainsi un croisement avec une dérive grande du point de croisement décrite par les

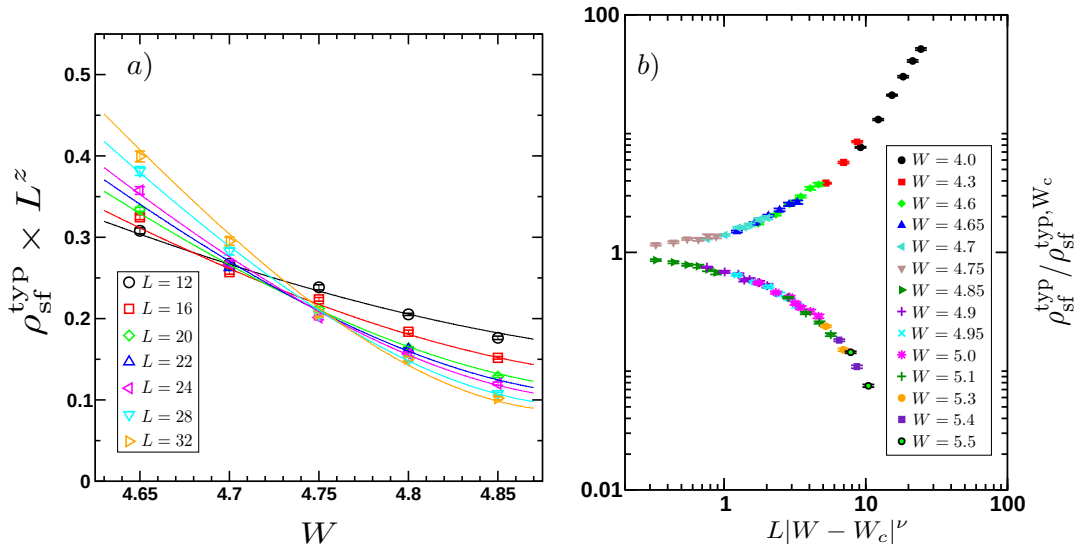

Figure 12: *Panneau a) Analyse de la densité SF typique tracée comme* $\rho_{\rm sf}^{\rm typ} \times L^z$ *en fonction du désordre, en fixant* $W_c = 4.8$, $\nu = 1.2$ *et* $z = 1.85$. *La from universelle de l'éq.* (11) *donne un exposant non pertinent* $y = 0.97(4)$. *Panneau b):* $\rho_{\rm sf}^{\rm typ}/\rho_{\rm sf}^{\rm typ,W_c}$ *en fonction de* $L|W-W_c|^\nu$, *en fixant* $\nu = 1.2$. *Les données collapse parfaitement sur toute la plage de désordre* $4 \leq W \leq 5.5$ *et taille* $12 \leq L \leq 32$ *sans aucun paramètre supplémentaire.*

paramètres non pertinents dans l'éq (11) $c = 1.13(8)$ et $y = 0.97(4)$, comme le montre la figure 12 panneau (a). Si on divise la densité typique par sa valeur au point critique $\rho_{\rm sf}^{\rm typ}/\rho_{\rm sf}^{{\rm typ},W_c}$ pour éliminer les corrections non pertinentes, lorsqu'on effectue une renormalisation de la taille du système par la longueur de corrélation $L \mapsto L/\xi = L|W - W_c|^{\nu}$, en fixant les paramètres critiques aux meilleures estimations pour la densité moyenne, un collapse presque parfait des données est obtenu sans aucun autre paramètre ajustable, ce qui confirme que la densité superfluide typique a la mêmes propriétés critiques que la densité moyenne.

4.2 Distribution du logarithme de la réponse superfluide

Pour étudier les propriétés d'auto-moyennation des phases superfluide et verre de Bose (*i.e.* des fluctuations dans les phases considérées), on étudie les distributions pour différentes tailles du système du logarithme de la réponse superfluide. La figure 13 montre ces distributions pour trois valeurs de la force du désordre: $W = 4t$

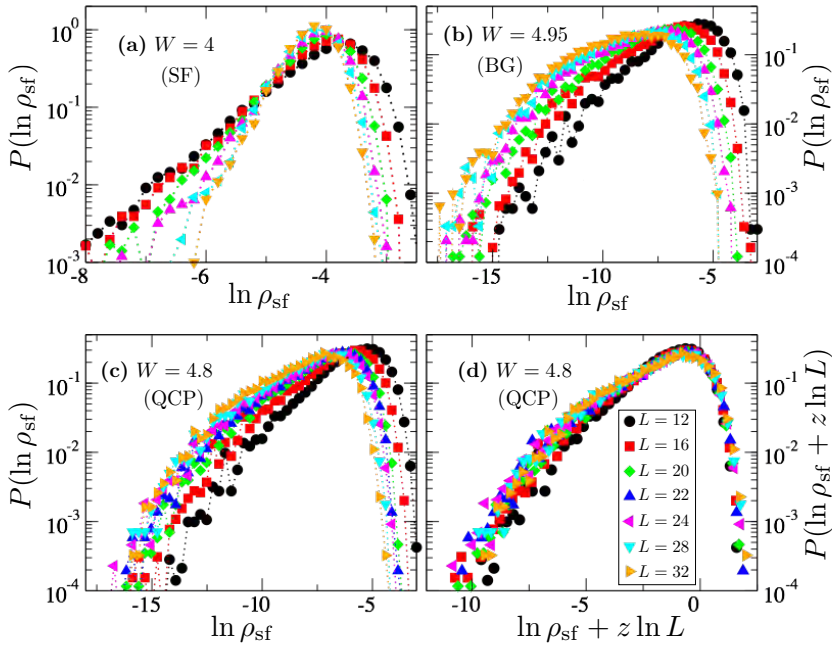

Figure 13: *Distribution de* $\ln(\rho_{sf})$ *pour toutes les tailles du système à trois forces du désordre différentes, une dans la phase SF (a), autre dans le verre de Bose (b) et au point critique* $(c - d)$*. Dans la phase SF (panneau a* $W = 4$*) les distributions rétrécissent lorsque la taille augmente* L*, un signe d'auto-moyennation. Dans le verre de Bose (panel b* $W = 4.95$*) elles s'élargissent lorsque* L *croît, un indice clair du manque d'auto-moyennation dans le verre de Bose. Au point critique (panneau c* $W = 4.8$*) les distributions se ressemblent, particulièrement pour* $L \geq 20$*, et un excellent collapse est obtenu en les décalant par* $z \ln(L)$ *avec* $z = 1.85$ *(panneau d).*

dans la phase superfluide, $W = 4.95t$ dans la phase verre de Bose et $W = 4.8t = W_c$ au point critique. Dans la phase superfluide les distributions de $\ln(\rho_{\rm sf})$ sont de moins en moins larges pour des tailles de plus en plus grandes, ce qui indique que la phase superfluide est auto-moyennante, comme il était déjà connu. Dans la phase verre de Bose les distributions s'élargissent avec taille croissante, indiquant une absence d'auto-moyennation dans cette phase, en accord avec Réfs. [272, 285]. Au point critique $W = W_c = 4.8t$, les distributions sont similaires pour toutes les tailles, spécialement pour $L \geq 20$, et un excellent collapse est obtenu en les décalant par $z \ln(L)$ avec $z = 1.85$, ce qui confirme une fois de plus nos meilleures estimations pour z et W_c.

On peut étudier ceci de façon plus quantitative en utilisant la variance de $\ln(\rho_{\rm sf})$ [282]. On peut éliminer les corrections non pertinentes responsables de l'élargissement transitoire des distributions au point critique pour les petites tailles en calculant l'écart-type corrigé $\tilde{\sigma}_{\ln\rho_{\rm sf}}(W,L) = \sigma_{\ln\rho_{\rm sf}}(W,L) - \sigma^c(L)$, avec $\sigma^c(L) = \sigma_{\ln\rho_{\rm sf}}(W_c,L)$ l'écart-type au point critique. Sur la figure 14 on trace les résultats de $\tilde{\sigma}_{\ln\rho_{\rm sf}}(W,L)$ pour différentes forces du désordre en fonction de la taille renormalisée $L/\xi = L|W-W_c|^\nu$, et on obtient un très bon collapse des données. Dans la phase superfluide ($W < 4.8t$), l'écart-type tend vers $-\sigma^c$ comme $1/\sqrt{N}$, comme attendu pour la phase auto-

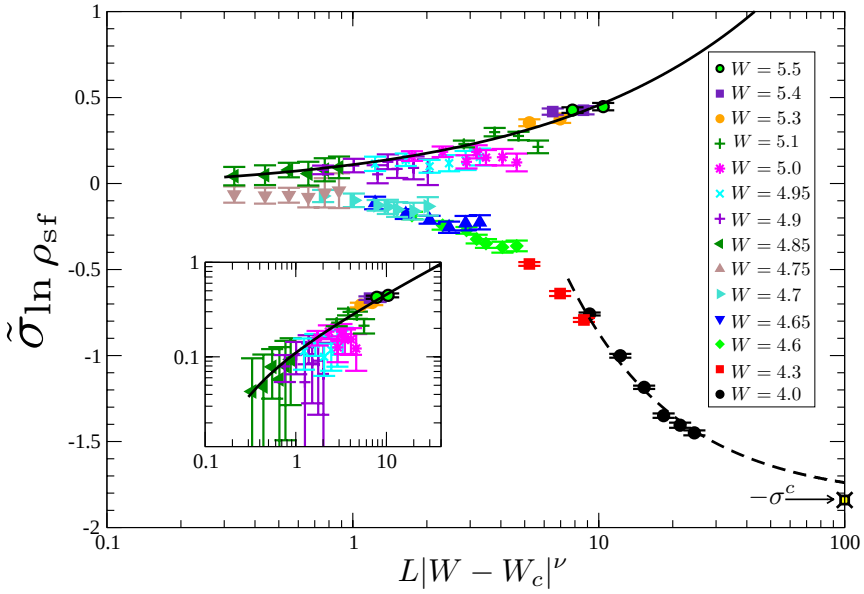

Figure 14: *Evolution de l'écart-type corrigé $\tilde{\sigma}_{\ln\rho_{sf}}$ avec la taille du système renormalisée par la longueur de corrélation $L/\xi = L|W-W_c|^\nu$, avec $\nu = 1.2$, pour routes les forces du désordre de $W = 4.0$ à $W = 5.5$. Dans la phase SF ($W < 4.8$) il diminue et tend vers $-\sigma^c$ comme $1/\sqrt{N}$ (ligne pointillée noire), une conséquence de l'auto-moyennation. Dans la phase verre de Bose ($W > 4.8$) il augmente suivant $(L/\xi)^\omega$ avec $\omega = 0.5(2)$ (trait plein noir). La vignette montre un zoom de la région de paramètres dans le verre de Bose.*

moyennante. Dans le verre de Bose ($W > 4.8t$), l'écart-type corrigé augmente suivant $(L/\xi)^{\omega}$ avec un exposant $\omega = 0.5(2)$, en accord avec les prédictions que la phase verre de Bose est gouvernée par une physique de polymères dirigés à dimension 1+1 [30, 195, 207, 279, 286], ce qui donne $\omega = 1/3$ [287], et la réponse superfluide globale se comporte comme une quantité purement locale dans cette phase, en accord avec Seibold *et al.* [204].

4.3 Absence d'un scénario de percolation

Dans la littérature, la phase de verre de Bose est souvent décrite comme étant composée de régions superfluides déconnectées incrustées dans un fond isolant. La transition vers la phase superfluide correspond dans ce contexte à la percolation de la plus grande de ces régions à travers tout le système [83, 171, 185, 187, 188].

On se propose de vérifier si la transition SF–VB suit bien un scénario de percolation. Pour ce faire, on réalise des simulations QMC à très haute température inverse $\beta t = 1024$ avec un très grand nombre de pas de mesure Monte Carlo $N_{\rm mc} = 10^5$ sur

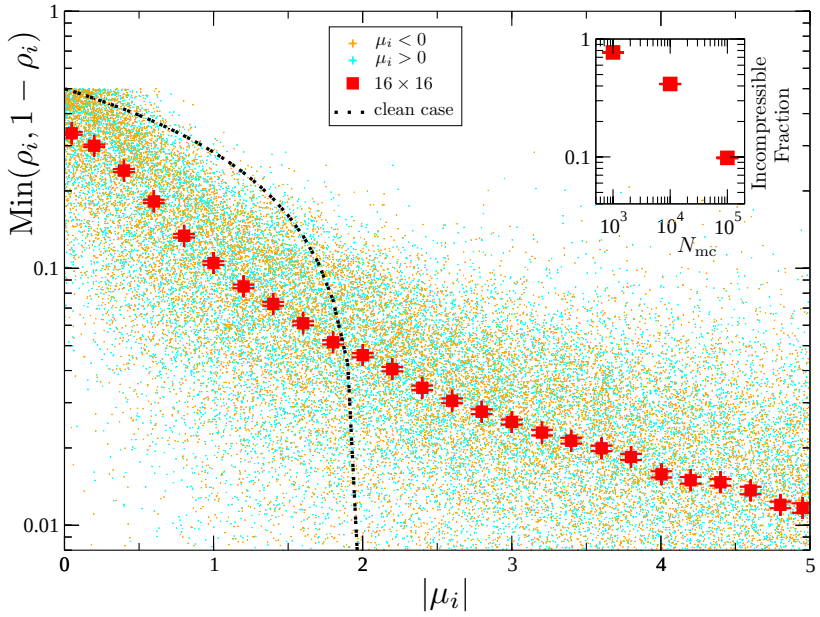

Figure 15: *Densité locale effective $Min(\rho_i, 1-\rho_i)$ dans la phase verse de Bose ($W = 5$) en fonction du potentiel chimique local $|\mu_i|$ pour un système de taille $L = 16$ (croix). Des simulations de $\mathcal{N}_S = 150$ échantillons désordonnés ont été effectuées à $\beta t = 1024$ avec $N_{mc} = 10^5$ pas de mesure Monte Carlo. La densité moyennée sur des fenêtres du potential chimique $[\bar{\mu} - 0.1; \bar{\mu} + 0.1]$ est représentée par les points rouges. Le trait pointillé noir est le résultat de la densité moyenne dans le cas pur (extrait de la Réf. [246]). La vignette montre comment la fraction de sites incompressibles tombe à zéro quand le nombre de pas de mesure augmente.*

un système de taille $N = 16\times16$, et on calcule la densité locale effective $\mathrm{Min}(\rho_i, 1-\rho_i)$ à l'intérieur de la phase verre de Bose ($W = 5t$). Les résultats des densités locales efficaces en fonction du potentiel chimique local sont présentés sur la figure 15 par les étoiles de couleurs. La symétrie particule-trou est bien évidente puisque les résultats sont symétriques par rapport à l'axe $\mu = 0$. On effectue des moyennes sur des tranches de potentiel chimique $[\bar{\mu} - 0.1; \bar{\mu} + 0.1]$ (carrés rouges) et le comportement moyen est toujours compressible, même en dehors de la bande de conduction ($|\mu_i| > 2t$), contrairement au cas pur (ligne noire pointillée). En vignette on voit la fraction de sites incompressibles (*i.e.* qui ont $\rho_i = 0$ ou 1) x_{inc} en fonction du nombre de pas de mesure Monte Carlo utilisés, et il est clair que dans la limite exacte du nombre de pas infini la fraction de sites incompressibles qui forment le fond isolant tend vers zéro. Ceci montre qu'il y a toujours percolation de sites compressibles même à l'intérieur de la phase verre de Bose et un scénario de percolation pour la transition n'est donc pas pertinent. De plus, la théorie de percolation dit que la densité superfluide devrait s'annuler proche du seuil de percolation x^* comme $\rho_{\mathrm{sf}} \sim |x - x^*|^t$ avec $t = 1.310(1)$ [222], mais dans notre cas elle s'annule comme $\rho_{\mathrm{sf}} \sim L^{-z}$ qui proche de la transition peut s'écrire $\rho_{\mathrm{sf}} \sim \xi^{-z} \sim |W - W_c|^{z\nu}$. Or on trouve que $z\nu \approx 1.85 \times 1.2 \approx 2.2$. Tout ceci nous sert à conclure que le scénario de transition de percolation ne s'applique pas pour la transition de phases superfluide – verre de Bose.

4.4 Conclusion

La transition Superfluide – Isolant reste un des domaines de recherche en physique de la matière condensée les plus actifs, même un quart de siècle après sa découverte. On a ici étudié la transition de phases Superfluide – verre de Bose à deux dimensions à travers trois approches différentes. La première est purement classique et donne le premier calcul de la densité superfluide classique, d'abord testée sur le modèle de Heisenberg. L'importance de la relaxation de phase ainsi que celle des fluctuations quantiques pour pouvoir décrire la transition ont été mises en évidence. En suite, une approche semi-classique a permis d'introduire les fluctuations quantiques à travers la théorie des ondes de spins linéaires, permettant d'observer la transition SF–VB. On a déterminé l'exposant critique z pour deux modèles différents du désordre, trouvant deux résultats différents, l'un en accord et l'autre en désaccord avec la prédiction $z = d$. D'autre part, pour le désordre bimodal, une très riche physique du spectre des excitation est trouvée, avec une transition de localisation des états excités à un seuil de mobilité non-nul dans la phase superfluide qui s'annule à la transition vers le verre de Bose. Ces derniers résultats ont été récemment mis en question par une étude de Lemarié.

Finalement, on a employé des simulations de Monte Carlo Quantique dans le cas du désordre uniforme et extrait les propriétés critiques de l'état fondamental. L'estimation du point critique est en accord avec celle obtenue par les ondes spin et

le cavity Mean-Field. L'exposant dynamique obtenu est légèrement plus petit que d mais l'égalité ne peut être exclue. On obtient aussi des estimations des exposants critiques de la longueur de corrélation ν et l'exposant anormal η qui sont en accord avec les bornes théoriques et d'autres estimations récentes. On a montré aussi l'absence d'auto-moyennation dans la phase verre de Bose, ainsi que le fait qu'un scénario liant la transition de phase SF–VB à une transition de percolation n'est pas pertinent, en désaccord avec certains résultats théoriques et expérimentaux précédents.

"Music gives a soul to the universe, wings to the mind, flight to the imagination and life to everything. "

Plato

"I have a friend who's an artist and has sometimes taken a view which I don't agree with very well. He'll hold up a flower and say "look how beautiful it is," and I'll agree. Then he says "I as an artist can see how beautiful this is but you as a scientist take this all apart and it becomes a dull thing," and I think that he's kind of nutty. First of all, the beauty that he sees is available to other people and to me too, I believe. Although I may not be quite as refined aesthetically as he is ... I can appreciate the beauty of a flower. At the same time, I see much more about the flower than he sees. I could imagine the cells in there, the complicated actions inside, which also have a beauty. I mean it's not just beauty at this dimension, at one centimeter; there's also beauty at smaller dimensions, the inner structure, also the processes. The fact that the colors in the flower evolved in order to attract insects to pollinate it is interesting; it means that insects can see the color. It adds a question: does this aesthetic sense also exist in the lower forms? Why is it aesthetic? All kinds of interesting questions which the science knowledge only adds to the excitement, the mystery and the awe of a flower. It only adds. I don't understand how it subtracts."

Richard P. Feynman

Analytical and numerical study of the Superfluid - Bose glass transition in two dimensions

The interplay of disorder (*i.e.* impurities) and interactions is one of the most fundamental questions in Condensed Matter Physics that has received a lot attention in the past couple of decades. The quantum phase transition from Superfluid to Bose glass driven by disorder has puzzled theoreticians and experimentalists alike, leaving unresolved questions despite their best efforts. The work presented in this thesis addresses some of these questions for two models of disordered hard-core bosons in two dimensions. In particular, the values of the critical exponents governing the transition, the inhomogeneous properties of the competing phases, the physical scenario at criticality and the bosonic excitations' localization properties are investigated. Three different approaches to the transition are used to explore this problem. We first show how Bose-condensate and superfluid fractions are affected by disorder in a Mean-Field approximation, which is unable to capture a transition, but reveals interesting qualitative features. Building on such a Mean-Field solution, quantum fluctuations are then introduced using a linear spin-wave theory in real space which does capture the transition and furthermore unveils a non-trivial behavior for the excitation spectrum. Finally, the quantum criticality is explored in great detail using state-of-the-art Quantum Monte Carlo simulations, leading to a precise evaluation of the critical exponents and a surprising absence of self-averaging in the Bose glass regime.

Keywords: Disorder, interactions, Bose glass, superfluid, hard-core bosons

Étude analytique et numérique de la transition Superfluide - verre de Bose à deux dimensions

Les effets conjoints du désordre (*i.e.* des impuretés) et des interactions constituent une des questions les plus fondamentales de la Physique de la Matière Condensée qui a reçu énormément d'attention dans les dernières décennies. La transition de phase quantique du Superfluide vers le verre de Bose déclenchée par le désordre s'est révélée énigmatique tant pour les théoriciens que pour les expérimentateurs et des questions restent ouvertes malgré tous leurs efforts. Les travaux présentés dans ce manuscrit abordent certaines de ces questions pour deux modèles de bosons de coeur dur désordonnés à deux dimensions : valeurs des exposants critiques qui gouvernent la transition ; propriétés inhomogènes des phases en compétition ; scénario physique au point critique ; propriétés de localisation des excitations bosoniques. On utilise trois approches différentes pour la transition afin d'explorer ce problème. En premier lieu, on montre comment les fractions superfluide et du condensat de Bose-Einstein sont affectées par le désordre dans une approximation de Champ Moyen qui, bien qu'incapable de capturer la transition, donne accès à des caractéristiques qualitatives intéressantes. En se basant sur cette solution Champ Moyen, on introduit les fluctuations quantiques à travers une théorie d'ondes de spin linéaires dans l'espace réel qui capture la transition et dévoile un comportement non trivial du spectre d'excitations. Finalement, on explore minutieusement la région critique quantique par des simulations de Monte Carlo Quantique à l'état de l'art, menant à une évaluation précise des exposants critiques et à une surprenante absence d'auto-moyennation dans le régime du verre de Bose.

Mots-Clés : Désordre, interactions, verre de Bose, superfluide, bosons de coeur dur